

ABSTRACT

Title of Document: GASIFICATION AND COMBUSTION OF
LARGE CHAR PARTICLES AND TAR

Henry Molintas, Doctor of Philosophy 2015

Directed By: Dr. Ashwani K. Gupta
Department of Mechanical Engineering

Although diffusion is known to play an important role for gasification and combustion of large char particles, their effects on conversion rates, kinetic parameters and other relevant factors have not been thoroughly analyzed. Similarly, tar reduction is not yet well understood. Central to these challenges is the shortage of experimental data for reduction of tar and large char particles. Likewise, analytical models for reduction processes have not been systematically examined.

In this study, large char particles between 1.5 to 7 mm are gasified and combusted non-isothermally with initial temperatures up to 1000 °C using various oxidants. Tar is also reduced with steam and vitiated air continuously and non-isothermally. In the absence of mathematical tools for large particle reduction analysis, models are proposed and derived in this study. Carbon and large near-spherically or irregularly shaped particles are modeled as large disk-shaped and spherically-shaped particles, respectively. One-film ash segregated core and random pore models are explored to analyze char reduction data and these are found to

provide consistent and inconsistent results, respectively. Thiele analysis is also used and it indicates that less porous particles are consumed more externally at the surface than internally. For $C + O_2 \rightarrow CO_2$ reductions, disk-shaped particles ignite when reactor temperature reaches 584 °C and these processes are purely kinetic controlled for 1.5 mm thick samples. Reduction of spherically-shaped particles shows that O_2 enrichment as compared to a 50 degree °C rise in reactor temperature substantially improves conversion. Oxygen enrichment with steam also significantly increases conversion of 5.5 mm thick disk-shaped particle up to 600 % under identical reactor conditions. For $C + CO_2 \rightarrow 2CO$ reductions, conversion rates increased five-fold when reactor temperature is increased from 850 to 1000 °C. Increasing initial reactor temperatures and O_2 enrichment provide an increase in char reactivity, diffusional rate, conversion, reduction rate and surface temperature.

Most of the large particle reductions investigated here operate near kinetic-diffusion controlled regime. Calculated total energy released during combustion is within the range of Dulong's empirical formula. At higher tar concentrations, CO and H_2 production moderately increase between 814 to 875 °C.

GASIFICATION AND COMBUSTION OF LARGE CHAR PARTICLES AND
TAR

By

Henry Molintas

Dissertation submitted to the Faculty of the Graduate School of the
University of Maryland, College Park, in partial fulfillment
of the requirements for the degree of
Doctor of Philosophy
2015

Advisory Committee:

Professor Ashwani K. Gupta, Chair

Dr. Nam Sun Wang, Associate Professor, Dean's Representative

Dr. Gary A. Pertmer, Associate Professor

Dr. Bao Yang, Associate Professor

Dr. Chandra Thamire, Senior Lecturer

© Copyright by
Henry Molintas
2015

Dedication

I would like to dedicate this work to The Father via Our Savior, Jesus Christ. He gets all the glory and honor because only through Him, with Him and by Him that I am able to withstand the rigors and challenges of completing a PhD in engineering part time. I also like to dedicate this work to my beloved wife, Marvi Perla for her relentless patience and unconditional love in completing this project. Thirdly, I also dedicate this work to my son, Henrik for his patient understanding. This work is also dedicated to my father (Moreno B. Molintas) and mother (Felisa J. Molintas), who went ahead to be with the Father in October 2009. Last but not the least, this work is also dedicated to those who sacrificially gave their lives for our great nation, the United States of America so that we can all enjoy peace and have liberty and freedom to pursue our God-inspired dreams and aspirations.

Acknowledgements

I would like to express my deepest gratitude to my PhD advisor Professor Ashwani K. Gupta for the opportunity to work with him at the Combustion Laboratory, University of Maryland. His guidance, patience, flexibility and unwavering support have made my PhD completion a delightful experience.

The encouragements of Mr. Peter McGraw (NAVSEA 05P, US Navy Technical Warrant Holder for Environmental Systems and Hazardous Material Management) and Mr. Christopher Chiodo (Branch Head, Advanced Propulsor Manufacturing) to start and finish my PhD studies are also greatly acknowledged.

The financial supports provided by Dr. Steve McElvany (Program Manager, Office of Naval Research Code 332) and Mr. William Sudduth (Director of Science and Technology, Naval Surface Warfare Center Carderock Division Code 60) are also instrumental for the completion of this work.

I would like also to gratefully acknowledge the members of Mechanical Engineering Combustion Laboratory at UMD, especially Mr. Alex Huang, Mr. Krishna Trehan, Ms. Danica Gordon, Ms. Rachel Kang and Dr. Islam Ahmed for their assistance.

Finally, I owe my deepest gratitude to my siblings (Myrna, Dolores and Josephine) and close friends at the Philippine International Bible Church (Pastor Arnel, Brother John Rillera, Brother Joel Nicolas and Brother Neil Manalo) for their prayers.

Table of Contents

Dedication	ii
Acknowledgements	iii
Table of Contents	iv
List of Tables	vii
List of Figures	viii
Nomenclature	xi
Chapter 1: Introduction	1
1.1 Objectives and Motivation	2
1.2 Thesis Approach and Hypothesis.....	10
1.3 Thesis Organization	14
Chapter 2: Literature Review	17
2.1 Char Reduction Process	18
2.1.1 Char reduction conversion curves.....	20
2.1.2 Uncertainties on calculated kinetic parameters.....	21
2.2 Char Reactions	24
2.3 Heterogeneous Char Reductions.....	27
2.3.1 Initial specific surface areas of char particles	29
2.3.2 Effective and bulk diffusion.....	31
2.3.2 Char reactivity and pore structure	33
2.4 Char Reduction Models	34
2.4.1 Random pore model for spherical shaped chars	35
2.4.2 One-film ASCM for disk-shaped char particles	38
2.4.3 One-film ASCM for spherically shaped chars.....	44
2.4.4 Energy conservation models	49
2.4 Tar Reduction Process	52
Chapter 3: Experimental Setup and Conditions.....	58
3.1 Disk-shaped Large Particles	58
3.2 Spherical Wood Char Particles	65
3.3 Irregular Shaped Coal Char Particles.....	69
3.4 Tar Reduction.....	72
Chapter 4: Results and Discussion.....	75
4.1 Reduction of Disk-shaped Carbon Particles with O ₂	75

4.1.1	Effect of different injection temperatures on conversion	75
4.1.2	Effect of injection temperatures on char surface temperatures.....	77
4.1.3	Effect of air and partial CO ₂ gasification models during preheating.....	81
4.1.4	Effect of temperatures in calculating the kinetic parameters.....	82
4.1.5	Summary of experimental and modeling.....	96
4.2	Reduction of Disk-shaped Carbon Particles with Steam, Air and O ₂	97
4.2.1	Summary of experimental results	100
4.3	Reduction of Spherical Oak Wood Char Particles.....	100
4.3.1	Effect of ash on char reduction	101
4.3.2	Effect of different temperatures and oxidizing agents on reduction regimes.....	105
4.3.3	Effect of reactor temperatures on weight and other variables	106
4.3.4	Kinetic Parameters via the ASCM and RPM.....	110
4.3.5	External reactions and pore diffusion rates.....	113
4.3.6	Effects of conversion parameters on activation energies.....	117
4.3.7	Summary of experimental and modeling results	118
4.4	Reduction of Irregular Shaped Coal Char Particles.....	120
4.4.1	Effects of different amounts of air and number of particles at 900 °C .	120
4.4.2	Effects of different number of particles on CO ₂ gasification at 900 °C	121
4.4.3	Effects of different temperatures on CO ₂ gasification.....	125
4.4.4	Effect of greater CO ₂ flow rates at 900 °C.....	129
4.4.5	Effects of air and CO ₂ on coal char reduction	130
4.4.6	Calculated kinetic parameters	130
4.4.7	Effects of diffusional parameters on X, Ea and <i>m</i>	133
4.4.8	Summary of experimental and modeling results	134
4.4	Thermal Reduction of Tar.....	136
4.4.1	Effect of residence time on syngas produced	136
4.4.2	Effect of steam-to-tar mass ratio (S/T) on syngas evolution	137
4.4.3	Effect of temperature on syngas production	139
4.4.4	Summary of experimental results	139
	Chapter 5: Analysis of Results.....	141
5.1	Comparison of Results with Literature Studies	141
5.1.1	Arrhenius plot of large particle reduction	141
5.1.2	Sherwood number	143
5.1.3	Combustion and gasification surface temperatures	147
5.1.4	Kinetic parameters	148
5.2	Thiele modulus, effectiveness factor, Sh and R _{kin} /R _{diff}	152
5.3	Energy Analysis	156
5.3.1	Absorbed peak and total energy during gasification.....	156
5.3.2	Peak and total energy releases during combustion	157
5.3.3	System thermal efficiencies	159
	Chapter 6: Conclusions	162
6.1	Large Disk-Shaped Char Particle Reduction	162
6.2	Large Spherical Char Particles.....	165

6.3	Large Irregular Shaped Char Particles	166
6.4	Tar	168
6.5	Modeling Analysis Results	169
	Chapter 7: Contributions.....	173
	Chapter 8: Recommendations for Future Work.....	176
8.1	Experimental Recommendations	176
8.2	Modeling Recommendations	179
8.3	Energy Balance Calculations	180
	Appendices.....	181
	Appendix I. Derivation of One-film ASCM for Disk-shaped Char.....	181
	Appendix II. Derivation of Energy Equation for Disk-Shaped Char Particle	185
	Appendix III. Sample of Numerical Method to Fit Models to Experimental Data	189
	A3.1 Accounting mass changes at $t = k$ using Euler Explicit Method	189
	A3.2 Accounting of equivalent radius at $t = k$ using Euler Explicit Method ..	189
	Appendix IV. Derivation of Energy Equation for Gasified Spherical Particle.....	191
	Appendix V. Sensitivity Analysis of Estimated Char Surface Temperatures	193
	Appendix VI. Standard Deviations of Experimental Data with Models	197
	A6.1 Disk-shaped char.....	197
	A6.2 Spherical oakwood and coal char particles	200
	Appendix VII. Other Char Reduction Models for Zone I Regime Analysis	203
	A7.1 Chemical equilibrium.....	203
	A7.2 Coats and Redfern Model and its modifications.....	204
	A7.3 Homogenous model	207
	A7.4 Arrhenius-type model	208
	Appendix VIII. Error Analysis	209
	A8.1 Systematic errors.....	211
	A8.2 Random errors.....	212
	Bibliography	213

List of Tables

Table 2-1. Reactor and surface particle temperatures of char	19
Table 2-2. Categories of Tar [53]	52
Table 2-3. Chemical Components of Gasifier Tars [53].....	53
Table 2-4. Syngas Quality Requirements for Energy Generation [54].....	53
Table 3-1. Physical properties of commercial carbon black.....	58
Table 3-2. Carbon particles with steam and its combination with air and O ₂	65
Table 3-3. Test matrix used for wood char particles	69
Table 3-4. Proximate and ultimate analysis of coal chars particles.....	72
Table 3-5. Experimental test matrix used in the investigation for coal char particles	72
Table 3-6. Physical and Chemical Properties of Examined O-cresol.....	73
Table 4-1. Modeling results for KPs at various injection temperatures (IT)	94
Table 4-2. Overall modeling results during preheating	95
Table 4-3. Overall modeling results during combustion	95
Table 4-4. Percent weight [18], melting points and boiling points of oakwood.....	102
Table 4-5. Summary of the linear fit derived kinetic parameters	113
Table 4-6. Chemical reaction rates with external diffusion rates	117
Table 4-7. Chemical reaction rates with pore diffusion rates	117
Table 4-8. Relationships of activation energies with other reduction parameters....	118
Table 4-9. DLF obtained kinetic parameters via ASCM and RPM.....	133
Table 4-10. Effects of diffusional parameters on X, E _a and m	134
Table 5-1. Average combustion and gasification surface temperatures	148
Table 5-2. KPs and other parameters for the combustion of large char particles.....	151
Table 5-3. KPs and other parameters for the gasification of large char particles.....	152
Table 5-4. Average diffusional properties of combusted large char particles	155
Table 5-5. Diffusional properties of gasified large char particles	156
Table 5-6. Peak and total energies absorbed.....	157
Table 5-7. Peak and total energies releases	159
Table 5-8. Combustion system thermal efficiencies.....	160
Table 5-9. Gasification system thermal efficiencies.....	161
Table A5-1. Sensitivity of calculated surface temperatures	196
Table A5-2. SDs of the average values for wood char	201
Table A5-3. SDs of the average values for coal char	202

List of Figures

Figure 1-1. Typical gasifier for coal, biomass or solid wastes	4
Figure 1-2. Reduction of carbonaceous materials.....	5
Figure 1-3. Rate-controlling zones for heterogeneous char oxidation.....	7
Figure 2-1. Arrhenius plot of combusted particles for $d_p < 0.15$ mm	17
Figure 2-2. Arrhenius plot of CO ₂ gasified particles for $0.057 < d_p < 0.2$ mm.....	18
Figure 2-3. Typical char conversion, of solid-gas reactions.	20
Figure 2-4. Typical low and high temperature Arrhenius plot	23
Figure 2-5. Expose thin disk-shaped disk model	44
Figure 2-6. ASCM for a char undergoing a reduction process	45
Figure 2-7. Air-ejector and tar cracking device [63]	57
Figure 3-1. SEM images of fisher lampblack [66]	59
Figure 3-2. (A) Forces on a single particle char and (B) Forces acting on multiple particles	62
Figure 3-3. Typical char conversion in thin disk-shaped chars	63
Figure 3-4. Experimental schematic diagram	65
Figure 3-5. (A) Raw spherical oakwood and (B) 0.076 g spherical oakwood char....	66
Figure 3-6. SEM micrographs of oakwood char particles	67
Figure 3-7. Experimental system	68
Figure 3-8. Particle mesh screen container	70
Figure 3-9. Irregular shaped char samples	70
Figure 3-10. Bench Scale Experimental Setup used for Tar Reduction	74
Figure 4-1. Char conversion of 0.2 g sample with 4 cmph O ₂	76
Figure 4-2. Char surface temperature profile for injection temperature at 644 °C	79
Figure 4-3. Char surface temperature profile for injection temperature at 584 °C	80
Figure 4-4. Char surface temperature profile for injection temperature at 504 °C	80
Figure 4-5. Modeling weight loss for 0.2 g char at IT= 644 °C with DNLR.....	85
Figure 4-6. Ash formation at the top layer of char particles	85
Figure 4-7. Modeling weight loss for 0.2 g char at IT= 584.6 °C with DNLR.....	86
Figure 4-8. Modeling weight loss for 0.2 g char at IT = 504 °C with DNLR.....	88
Figure 4-9. Modeling weight loss for 0.2 g char at IT = 644 °C with DLR.....	89
Figure 4-10. Modeling weight loss for 0.2 g char at IT = 584 °C with DLR	90
Figure 4-11. Modeling 0.2 g char reduction (IT = 504 °C) with DLR °C	92
Figure 4-12. R_{kin}/R_{diff} ratios during non-accelerated region for IT = 504 °C	92
Figure 4-13. Oxygen enrichment of steam char gasification.....	99
Figure 4-14. (A) Char inside reactor and (B) Ash leftover for Test No. 1	104
Figure 4-15. Five second images of spherical char particles (Test Nos. 3 & 4).....	105
Figure 4-16. Resistance ratios of kinetic and diffusion rates.....	106
Figure 4-17. Raw data for weight (A) and diameters (B) versus reaction time.....	107
Figure 4-18. Conversion curves of spherical char particles.....	108
Figure 4-19. Normalized diameter reductions of spherical char particles	109
Figure 4-20. Estimated char surface temperatures.....	110
Figure 4-21. Activation energies using ASCM.....	111
Figure 4-22. Ratio of activation energies (ASCM) to amount of char converted.....	112

Figure 4-23. Thiele modulus versus reaction times	114
Figure 4-24. Effectiveness factors versus reaction times.....	115
Figure 4-25. Thiele modulus versus effectiveness factors.....	116
Figure 4-26. Effects of different amounts of air and number of particles at 900 °C	121
Figure 4-27. Effect of different no. of particles on 900 °C and 0.05 gram	122
Figure 4-28. Leftover ash for test case nos. 1, 2 and 3	123
Figure 4-29. Effect of different no. of particles at 900 °C for 3 cmph of CO ₂	124
Figure 4-30. Leftover ash for tests 8 and 9	125
Figure 4-31. Effects of 850, 900 and 1000 °C on CO ₂ gasification (2 pcs).....	126
Figure 4-32. Leftover ash for tests nos. 10 and 11.....	127
Figure 4-33. Effects of 800 and 930 °C on CO ₂ gasification (3 pcs).....	128
Figure 4-34. Leftover ash for tests 5 and 6	128
Figure 4-35. Effect of greater CO ₂ flow rates at 900 °C	129
Figure 4-36. Effect of air and CO ₂ on conversion at 900 °C	130
Figure 4-37. Syngas produced when doubling residence time	137
Figure 4-38. Evolution of syngas at S/T = 1.7.....	138
Figure 4-39. Evolution of syngas at S/T = 0.865.....	138
Figure 4-40. Temperature effect on syngas produced	139
Figure 5-1. Arrhenius plot of large wood and coal char particles	142
Figure 5-2. CO ₂ gasification of large coal char particles	143
Figure 5-3. Sh for the CO ₂ gasification of coal chars with literature data.....	144
Figure 5-4. Sh for combusted wood char particles with petroleum coke spheres [71]	145
Figure 5-5. Sh of combusted wood and coal char particles	146
Figure 5-6. Sh. of combusted and gasified coal char particles	146
Figure 5-7. Sh of combusted and gasified coal char particles	147
Figure 5-8. Average Thiele and EFs of wood and coal char	154
Figure 5-9. Relationship of the activation energy and the total energy absorbed.....	157
Figure 5-10. Relationship of the activation energy and the total energy released....	159
Figure A1-1. One film diffusion model combustion of disk-shaped char particle ...	181
Figure A2-2. Energy flows at surface of burning flat-shaped char.....	185
Figure A2-3. 1D steady-state energy analysis of energy conservation.....	186
Figure A3-4. Nonlinear regression on experimental data	190
Figure A4-5. Energy flows at the surface of gasified particle	191
Figure A5-6. One-dimensional steady-state energy analysis.....	194
Figure A5-7. Estimated T _s based on emissivity from 0.7 to 1.0	195
Figure A5-8. Estimated T _s based on H from 0.25H to H	195
Figure A5-9. Estimated T _s based on the T _s (0.25 to 1.0) and T _{inf} (0 to 0.75)	196
Figure A5-10. SDs of modeling results versus experimental data at 644 °C.....	198
Figure A5-11. SDs of modeling results versus experimental data at 584 °C.....	199
Figure A5-12. SDs of modeling results versus experimental at 504 °C	200
Figure A5-13. SDs of the exp. data and the two models used for wood char.....	201
Figure A5-14. SDs of exp. data and the two models used for coal char.....	202
Figure A8-15. 5 percent error on measured values and exponential fits	210
Figure A8-16. Percent error based on nonlinear best fit.....	211

Nomenclature

A	frequency factor, m/s or l/s
b	heating rate, K/s
B	reactant B
Bo, m	transfer number
C or $C(s)$	char or carbon
c_{pg}	specific heat, $J/kg\cdot K$
d_p	particle diameter, m
D or D_{eff}	Effective diffusion coefficient, m^2/s
D_k	Knudsen diffusion coefficient, m^2/s
Ω	dimensionless collision integral
ε or ε_s	emissivity
E_a	activation energy, kJ/mol
F	forces on a particle, n
f_v , $F(X)$ or $G(X)$	linearized value of integration
H	height of stagnant layer
h	convective heat transfer coefficient, W/m^2K or char thickness
Δhc	heat of combustion or gasification, J/kg
IT	injection temperature, $^{\circ}C$ or K
k_B	Boltzman constant, J/K
Kn	Knudsen number
k_j or k or k_c	rate coefficient of reaction “ j ”, m/s or l/s

kg	gas thermal conductivity, $W/m.K$
k_o	random pore model pre-exponential factor, l/s
L_o	pore length
m	mass of char
MW	molecular weight
Nav	Avogadro's number, l/mol
n or m	order of reaction
η	effectiveness factor
O	oxidant or gasifying agents (O_2 or CO_2)
Pr	Prandtl number
Q	heat energy
r	particle radius
r_f	roughness factor
R	resistance
Re	Reynolds number
R_{reac}	char reactivity, $sec-l$
R_u or R	universal gas constant
S_{gc}	specific surface area, m^2/g
Sh	Sherwood number
So	pore surface area, m^2
T	temperature, K
TR	reactor or freestream temperature, K
ν_I	stoichiometric coefficient

V	specific volume, m^3/g
W	weight of remaining sample at time “t”
W_o	initial dry ash-free (daf) weight
X	degree of conversion or mole fraction
Y	mass fraction

Greek alphabets

θ	porosity
ρ	density
σ	hard sphere dia. or Stefan-Boltzman constant, W/m^2K^4
\emptyset	Thiele modulus
τ	tortuosity
φ	parameter that describes pore structure
u	oxidant velocity, m/s
ν	kinematic viscosity, m^2/s

Subscripts

A	anchoring
a	activation
c	carbon or char
D	dimensionless, drag
L	lift
$mix\ or\ tot$	gas mixture or bulk gas
0	initial value
$inf\ or\ \infty$	free stream condition

<i>K</i>	Knudsen diffusion
<i>k</i>	time marching symbol
<i>m</i>	number of molecules in carbon
<i>n</i>	number of molecules in H ₂
<i>ox</i>	oxidant (O ₂ or CO ₂)
<i>rad</i>	radiation
<i>s</i>	surface
<i>s-f</i>	surface to flame or diffused gas area
<i>s-i</i>	surface to inside or conduction
<i>sur</i>	surrounding condition
∞	freestream
<i>kin</i>	kinetic
<i>diff</i>	diffusion
<i>i</i> or <i>j</i>	species (reactants or products) or reactions
<i>0</i>	starting point
<i>tot</i>	bulk gas or gas mixtures

Chapter 1: Introduction

Biomass fuel for generating heat and power has captured the interest of energy researchers because it is renewable and with low ash and sulfur content. Co-firing biomass and coal large char particles is also a good approach to further reduce fossil fuel depletion and air pollution. Typically, depending on the type of processor, biomass particles are much larger than pulverized coal particles. For updraft or downdraft packed bed processors, biomass particles are used between 5 to 100 mm either as received or with some preprocessing to reduce size [1]. With fluidized-bed gasifiers and combustors, biomass fuels are pelletized between 2 to 5 mm or sometimes larger depending on fluidization conditions [2]. Biomass or coal reduction processes can undergo different processes such as drying, devolatilization, solid-gas reactions and gas-phase reactions. As a result, these processes are inherently complex especially when particles are larger than 1 mm. The reduction of small char particles with less than 0.25 mm in diameter is usually purely kinetic controlled based on analyses of abundant experimental data that have been thoroughly investigated using various kinetic models available in literature [3, 14, 15, 16, 17, 23, 24, 25]. In contrast, the reduction of large particles greater than 1 mm in thickness or diameter is known to be influenced with diffusional effects. However, specific extents on how diffusion rates directly affect conversion rates, kinetic parameters, char porosity, char shapes, type of oxidants and energy parameters have not been thoroughly evaluated. Because kinetic data of small char particles (< 0.25 mm) are available, most reduction modeling studies for large particles greater than 1 mm use char kinetic data for small particles. As a result, state-of-the-art modeling studies do not agree well with

experimental data [26, 27]. Hence, gasifiers and combustors that are intended to process large particles are often designed iteratively via a trial and error approach. This approach is the rule rather than the exception even at this present, causing such processors to be oversized, unstable and inefficient. Along with these challenges, tars (mostly heavy polycyclic aromatic hydrocarbons) that are processed during gasification and combustion are not well understood [3, 4, 5]. Although tar reductions can be analyzed with gas chromatography [6], effects of various oxidants, particularly steam has not been examined for various types of tars. Central to most of these challenges is that there is a dearth of experimental data for reduction of large char particles and tars. Therefore, the objective of this research is to provide experimental data and underscore operating regimes, extent of diffusion (external and pore) and energy parameters (absorbed and released) for reduction of large char particles between 1.5 mm to 7 mm at temperatures between 500 to 1000 °C with O₂ enrichment, steam, CO₂, vitiated air, air and some combination of these oxidants. This research is further extended to provide tar reduction experimental data using steam and vitiated air as an oxidant for continuously-fed, non-isothermal and non-catalyzed reactions. In the absence of suitable analytical tools, some mathematical models are also proposed, derived, developed, explored and presented in this work.

1.1 Objectives and Motivation

Energy derived from biomass and biomass-based municipal solid wastes are promising eco-friendly alternative energy resources to coal or other fossil liquid and gaseous fuels. Unlike coal, biomass produces no harmful sulfur or mercury emissions and has significantly less nitrogen content, which is the main culprit of acid rain and

smog. Coals and other fossil fuels (mined natural gas and liquid fuels) need expensive CO₂ sequestration systems to enhance their environmental quality performance. Conversely, biomass energy resources do not need such systems because biomass CO₂ emissions are rapidly absorbed back from atmosphere through plant growth and regeneration. Hence, co-firing coal and biomass large char particles may also need some consideration to reduce fossil fuel depletion and pollution. Although biomass energy is recognized as an important ingredient in increasing the contribution of renewable energy profile worldwide, biomass utilization is still limited mainly because of significant technical and logistical challenges that are inherently associated with it as a mainstay energy resource. In 2013, biomass energy provides only about 10 percent of the global energy portfolio [7]. With this perspective, perhaps a viable approach to advance biomass energy utilization is to increase the use of efficient small scale and compact biomass-based gasifiers or combustors in locations where such resources are readily available. However, this approach requires the development of efficient compact and small scale biomass gasifiers or combustors. Such processors are also expected to be very ideal and attractive for special applications such as ships (cargo, military and cruise) that generate biomass-based wastes or remote rural areas in developing and developed countries where biomass energy resources are plentiful and accessible. Other application of interest for compact and small scale processors may include a manned space station in deep space, an isolated peacekeeping military contingent operating away from main energy grid centers and isolated villages in rural areas of developed and developing countries.

Syngas from biomass resources may be used as a fuel for gas turbines and other energy conversion devices such as gas engines for propulsion, electricity generation, space heating, or other applications, see Figure 1-1.

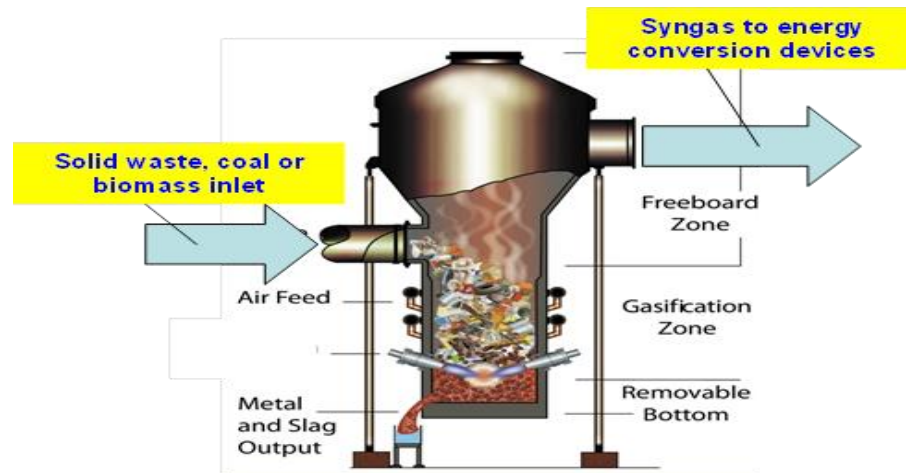


Figure 1-1. Typical gasifier for coal, biomass or solid wastes

Nevertheless, large char particle reduction is considered a major determining or controlling step in most combustion and gasification processes because normally these require longest time to complete. To improve and obtain more efficient energy conversion, coal char particles are generally pulverized to less than 0.2 mm in diameter. This approach ensures that the reduction processes are purely kinetic controlled (oxidant gas diffusion is infinitely fast). Intrinsically controlled reduction processes are extensively studied and therefore these are well understood and predictable. However, the use of pulverizing equipment and large preprocessing equipment are not practical for space constrained environments and remote locations. Additionally, the reduction of larger particles (diameter > 1 mm) is not generally kinetic controlled because diffusional effects also play an important role.

Char reduction processes can also undergo different processes such as drying, devolatilization, gas-phase reactions, gasification and combustion. Some of these processes can also overlap because particle sizes and shapes can change along with surface temperatures as particles are consumed via gasification and combustion. The gasification and combustion of carbonaceous materials are divided into two major processes (see Figure 1-2) [3]:

1. Drying and pyrolysis and
2. Char and tar reduction (combustion and gasification)

Drying and pyrolysis occur fast accompanied with the release of pyrolysis gases, tars and other compounds resulting to the formation of a carbon rich solid residue called char. However, char reduction is very slow and the rate-controlling step in the overall process.

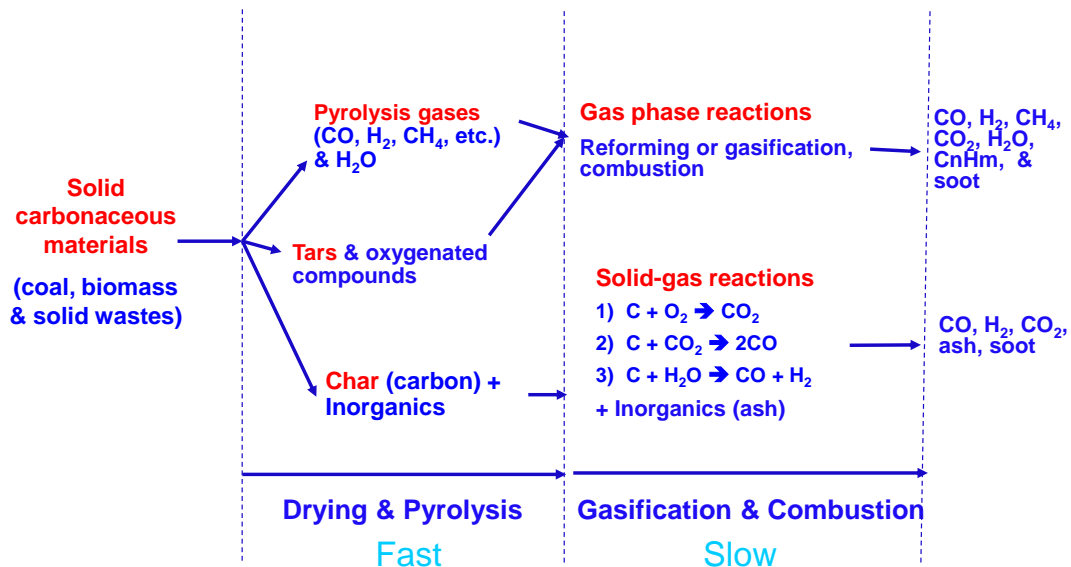


Figure 1-2. Reduction of carbonaceous materials

Additionally, the reduction of tars is cumbersome and challenging [4, 5]. Van Paasen and Kiel [5] determined that harmful tars are those that cannot be detected

with gas chromatography. Harmful tars can plug reforming catalysts, disable sulfur removal systems, corrode or damage off-gas systems, such as, heat recovery boilers, induced draft fans, pumps, compressors, heat exchangers, gas turbines and other off-gas downstream systems.

Char reduction of small particles is usually analyzed using Arrhenius plot (see Figure 1-3) via appropriate kinetic models. This plot provides direction relationship between reaction rate coefficient (k_c) natural logarithm and char surface temperature (T_s) reciprocal [6]. Three regimes are used to describe char reduction processes: (a) kinetic controlled or Zone I, (b) diffusion-kinetic controlled or Zone II and (c) diffusion controlled or Zone III (see Figure 2-2) [6]. Zone I occurs when chemical reaction rate is significantly slow as compared to the diffusion rate (i.e. at low temperature and for small particles). Zone II is equally controlled by both chemical reaction (kinetics) and diffusion. Zone III occurs usually at high temperatures and it is characterized by slow diffusional rates at external boundary layer of particles. Large particles generally operate somewhere between Zone I and Zone III. However, this has not been thoroughly examined for various particle sizes. The three zones regimes are conveniently determined by the by the ratio of kinetic rate resistance (R_{kin}) to external diffusion rate resistance (R_{diff}) values [8]. When $R_{kin} / R_{diff} > >1$, reduction is kinetically controlled (Zone I or diffusion rate is infinitely fast). When R_{kin} and R_{diff} are nearly identical, reduction is under kinetic-diffusion controlled regime or Zone II. On the other extreme case when $R_{kin} / R_{diff} < <1$, reduction is called diffusion controlled (Zone III or kinetic rate is infinitely fast).

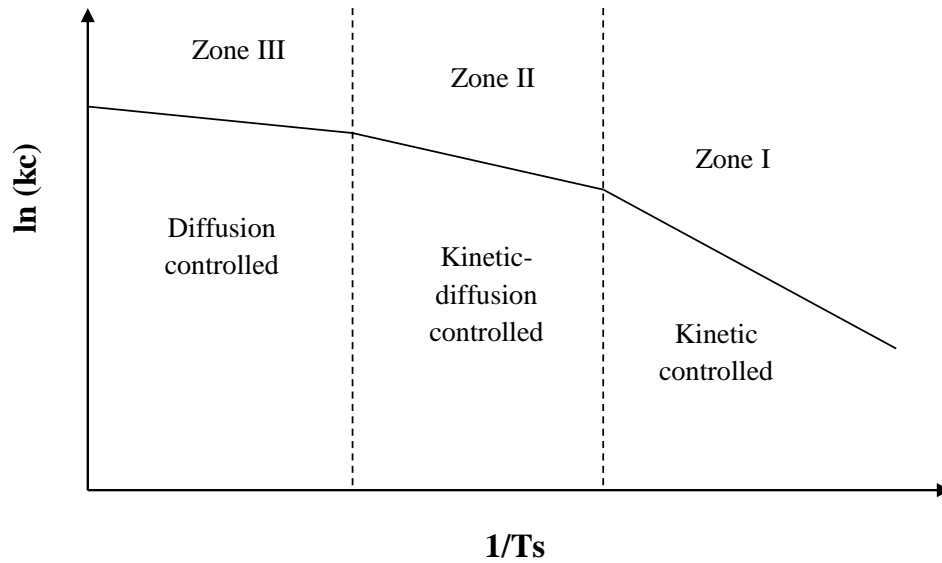


Figure 1-3. Rate-controlling zones for heterogeneous char oxidation

For large particles, diffusion effects are expected to play a major role in the overall process and these should be considered when analyzing reduction (i.e. gasification and/or combustion) experimental data. Unfortunately, experimental data for reduction of large particles are very limited. Therefore, the reduction of large char particles is performed in this study along with the use of novel and state-of-the-art analytical tools to analyze and estimate the following reduction parameters:

1. Apparent activation energy and frequency factor
2. Thiele modulus – Ratio of external reaction rates to pore (internal) diffusion rates [9]
3. Effectiveness Factor – Ratio of observed reaction rate to maximum possible reaction rate [9]
4. Sherwood number – Ratio of convective mass transfer coefficient to diffusive mass transfer coefficient [10,11]

The thesis objectives are to:

1. Provide experimental reduction data for large char particles particularly between 1.5 mm thick up to 6.8 mm in diameter
2. Experimentally characterize the reduction behavior of large disk-shaped carbon and near-spherically shaped large char (from oak wood and coal) particles at 1 atm for temperatures between 500 to 1000 °C by determining specific effects of the following on conversion:
 - a. O₂ at different reactor temperatures for combustion of carbon particles
 - b. Steam with or without air and O₂ for carbon particles
 - c. Air with or without O₂ enrichment at different temperatures for oak wood char particles
 - d. Air combustion and CO₂ gasification at specified temperatures for coal char particles
 - e. Use of vitiated air to preheat and gasify carbon particles at low temperatures
3. Perform experimental data analysis to characterize diffusional effects (R_{kin}/R_{diff} , ϕ and Sherwood numbers) and their associated kinetic parameters using:
 - a. One-film ASCM at discrete time periods to account decreasing particle sizes via Euler explicit method (EEM)
 - b. Thiele modulus (ϕ) and effectiveness factor (η) for large particles with diameters (d_p) > 4 mm at discrete times while considering changes in particle sizes and char porosities during reduction

4. Provide tar experimental reduction data using steam and vitiated air as oxidizers and characterize these for a continuously fed non-isothermal reactor at $800\text{ }^{\circ}\text{C} < T < 1000\text{ }^{\circ}\text{C}$ under 1 atm by determining the effects of the following:
 - a. Residence time or reaction time
 - b. Reactor temperatures
 - c. Steam to tar mass ratios between 1 and 2

Non-isothermal reduction analysis is also considered here to simulate real world operation of gasifiers and combustors. Additionally, this work is motivated to investigate reduction of harmful tars with concentrations that simulate the operation of updraft and fluidized bed gasifiers using steam as oxidant.

To achieve these objectives, gasification and combustion of nearly pure carbon particles arranged in large disk-shaped configuration and spherical modeled char particles are investigated. Disk-shaped arranged carbon black particles (1.5 to 5.5 mm thick) are used as model particles of disk-shaped or flat-shaped biomass-based solid waste feed stocks (mostly paper and cardboard) and other biomass waste materials (e.g. seasonal fallen leaves from trees, yard trimmings and industrial wastes from food processing industries). Large spherical biomass and coal char particles with diameters ranging from 4 to 7 mm are investigated to analyze particles of various ash contents (for low ash wood char particles and high ash coal char particles). O-cresol ($\text{C}_7\text{H}_8\text{O}$) is used as a tar model to simulate large concentrations of phenol based tars that are normally produced during steam gasification processes.

A one film (assumes no flame at the reaction boundary layer) ash segregated core model (ASCM) and random pore model (RPM) with a first order global reaction rate are proposed and used to analyze experimental reduction (combustion and gasification) data of large char particles. Simplified steady-state energy processes are also considered to calculate energy requirements and char surface temperatures. In the absence of any suitable mathematical tools to characterize large char particle reduction, energy equations and reduction model equations (i.e. for carbon particles arranged in disk shaped configurations) are featured, derived and presented in this work (see Appendices I and II). Analysis results are also provided in Chapter 5 as well as in Appendices V and VII. For all experiments, I have used mostly non-isothermal conditions to mimic real world temperature conditions of gasifiers and combustors. All model equations used for analysis of experimental data are valid only for single particles and therefore, the effects of intra-particle and inter-particle phenomena are not considered.

1.2 Thesis Approach and Hypothesis

Experiments are first performed to investigate the reduction behavior of tar as well as carbon and large char (from oak wood and coal) particles at 1 atm for temperatures between 500 to 1000 °C. Particle sample weights and reactor temperatures are measured continuously using a data acquisition system, starting from their initial conditions up to their final conditions. For nearly identical sample weights and geometrical sizes (i.e. diameters and thicknesses), different types and amounts of oxidants (i.e. air, CO₂, steam, O₂ and different combinations of these) are used to gasify and combust test particles. Liquid o-cresol (C₇H₈O) is modeled as tar,

which is injected at room temperature into an evaporator inside the reactor that is maintained between 800 to 900 °C at 1 atm. Gas chromatography is used to measure the resulting product gas concentrations for H₂, CO, O₂, CO₂ and C_nH_m (hydrocarbons) at reactor outlet when using steam and vitiated air as a oxidizing agents.

Experimental data analysis for specific experimental conditions is subsequently performed using a single step global reaction rate via one film (no chemical reaction at the boundary layer) ash segregated core model (ASCM) which relates measured char burning rates to external char surface areas. One-film kinetic-diffusion ASCM is used to analyze experimental data. ASCM is also used to determine the time dependent reduction parameters (kinetics and diffusion) for carbon and char reduction conditions using air, O₂ and CO₂. Additionally, random pore model (RPM) is used to analyze the reduction of oakwood and large coal char particles. However, data modeling analysis of steam char gasification processes and tar reduction is not performed in this work due to the complexity of tertiary gas reactions (i.e., $C + H_2O \rightarrow H_2$ and CO) when these are applied on the one-film ASCM and global gas reaction rates, respectively. Energy equations are used to calculate particle surface temperatures, energy released and energy absorbed based on measured gas reactor temperatures. Char surface temperatures are calculated with the use of energy models for a convergence criteria of + or - 1 % of the total energy released (combustion) or absorbed (gasification). The ASCM, RPM, Thiele modulus, effectiveness factor and energy equations are solved at discrete time periods with via Euler explicit method (EEM) to account for the changes in particle diameters and

porosities during reduction. Because the reduction of large particles is the focus of this work, Thiele modulus and effectiveness factor analyses are also performed to examine the relationships between surface reaction rates and internal diffusion rates. Sherwood numbers are also estimated to characterize transfer of oxidants to surface of gasified and combusted particles. With these analytical tools, it is anticipated that relative diffusional effects (both external and internal) are characterized with their relationships to surface reaction rates.

Diffusional effects are known to play a vital role for the combustion and gasification of large porous char particles [13, 14, 15]. However, the severity and extent of diffusional effects have not been clearly understood, particularly their effects to kinetic parameters and energy properties, which are useful in predicting char reduction rates. In an attempt to determine intrinsic kinetic parameters and energy properties for reduction of disk-shaped char particles, a collection of tiny carbon particles with an average diameter of $0.06\text{ }\mu\text{m}$ is arranged in a disk-shaped configuration during the first phase of this work (see section 3.1). External diffusion rates are expected to be very fast during reduction of thin disk-shaped particles when these are placed in a shallow stainless steel container. As a result, derived one-film ASCM is expected to directly analyze reduction data whether it is purely kinetic controlled or not. A shallow container is used to ensure that the concentration of oxidants at the bulk region is the same as the concentration of oxidants at the char surfaces. Relevant models are proposed and provided (some are derived and some are taken from literature) to capture elementary physics of reduction phenomena when using specific types of oxidants during reduction process. Char particles with

different porosities and ash content are also studied to characterize reduction kinetic parameters, diffusional effects and energy requirements (see Chapter 3). Tar reduction experiments are also performed to determine the role and effect of steam as a primary oxidant (see section 3.4).

Global (i.e. CO to CO₂) and elementary reactions occurring inside the particle boundary layer are neglected. This approach is to reduce computational complexities that are associated with time dependent char reduction conditions at the boundary layer. Nonetheless, simplified model equations conveniently couple external contributions of diffusion and chemical reactions such that char reduction operating regimes can be discriminated by fitting these into experimental data for analysis. Transient and discrete time conditions are all evaluated using Euler Explicit Method on reduction models (ASCM and RPM) and energy model equations being investigated. Thiele modulus and effectiveness factors are estimated to determine the relationship of external surface reaction rates and pore diffusion rates. In summary, sample test materials and shapes are combusted and gasified under atmospheric pressure for the following conditions:

1. Tiny carbon black particles arranged in a disk-shaped configuration up to 5.5 mm in thickness
2. Large spherical wood char particles between 6.7 to 6.8 mm in diameters and
3. Irregular shaped particles packed together to form equivalent diameters between 4 to 7 mm

With this approach, the following are the hypothesis:

1. Char reduction regimes (Zones I, II and III) can be determined consistently with a simple one dimensional single-film ash segregated core model (ASCM) for one-step global reaction.
2. Intrinsic kinetic parameters for disk-shaped arranged carbon particles can be obtained at temperatures between 500 to 650 °C.
3. Up to specific sizes, large particles up to 6.8 mm in diameters can have intrinsic kinetic parameters at reactor temperatures between 800 to 1000 °C during combustion and gasification with air, pure O₂ and pure CO₂.
4. Pure kinetic model using random pore model (RPM) can provide reasonable kinetic parameters for large char particle reduction.
5. Released and absorbed energies during combustion and gasification can be predicted and calculated

1.3 Thesis Organization

The first phase of this research is the experimentation and data analysis of disk-shaped carbon black particle combustion and gasification using O₂, steam, steam plus air and steam plus O₂ as oxidants between 500 to 800 °C. Moderate reactor temperatures are used to investigate the lowest input energy possible and determine lowest temperatures that carbon particles can be gasified or combusted at 1 atm. Thin disk-shaped carbon black particles are used to ensure that conversion is purely kinetically controlled during oxidation, allowing external surface diffusion rates to be very fast. The disk-shaped char particles are also made of carbon black materials which contains only about 2.2 % ash by weight with very low amount of volatile matter (tar).

The second part of this thesis work is the experimental and data analysis for combustion of large semi-spherically shaped wood char particles with pure air and O₂ enrichment between 800 and 850 °C. Identical residence time of 40 seconds is used for all experiments. It is anticipated that diffusion will play a vital role during char conversion.

Thirdly, irregular shaped coal char particles are combusted and gasified with the use of air and CO₂ for particles with equivalent diameters between 4 mm to 7 mm in size. It is anticipated that diffusion will also play a vital role during char reduction.

The fourth phase is to experimentally perform tar reduction in a non-isothermal reactor operated between 800 and 900 °C under 1 atm using steam and vitiated air.

The fifth phase is to analyze the results by determining the following (see section 5):

1. Sensitivity analysis of estimated char surface temperatures
2. Standard deviations of experimental data and modeling results
3. Comparison of results with previous studies in literature
4. Characterize extent of diffusion rates on wood and coal char particles
5. Energy analysis for combustion and gasification of large char particles
6. Explore the use of one-film ash segregated core and random pore models to analyze large particle reduction data and determine extents of diffusional effects on reduction
7. Explore the use of Thiele modulus and Sherwood number analyses on large reduction data

8. Perform error analysis of experimental data
9. Determine suitable future work to advance large char particle reduction

Some derivations (see Appendices I, II and IV) are performed to provide additional analysis tools for gasification and combustion of coal char and disk-shaped particles. The last part of this work deliberates the major conclusions, contributions and recommendations for future work.

Chapter 2: Literature Review

Currently, most studies on char particles are based on small particles less than 0.2 mm in diameter [14, 15, 16, 17, 18, 19, 20, 21, 22]. Majority of these studies are primarily geared towards the utilization of pulverized coal char particles. Because pulverized particles are also small, it is well established that the main reduction regime is intrinsically kinetic controlled or diffusional rates are extremely fast. Figures 2-1 and 2-2 show the Arrhenius plots of experimentally obtained data for the combustion and gasification of small particles, respectively. Arrhenius plots conveniently provide the relationship between the reaction rate coefficient (k_c) and char surface temperature (T_s). This relationship gives insight about the activation energy and frequency factor of char reductions which are key parameters in developing design guidelines for gasifiers and combustors.

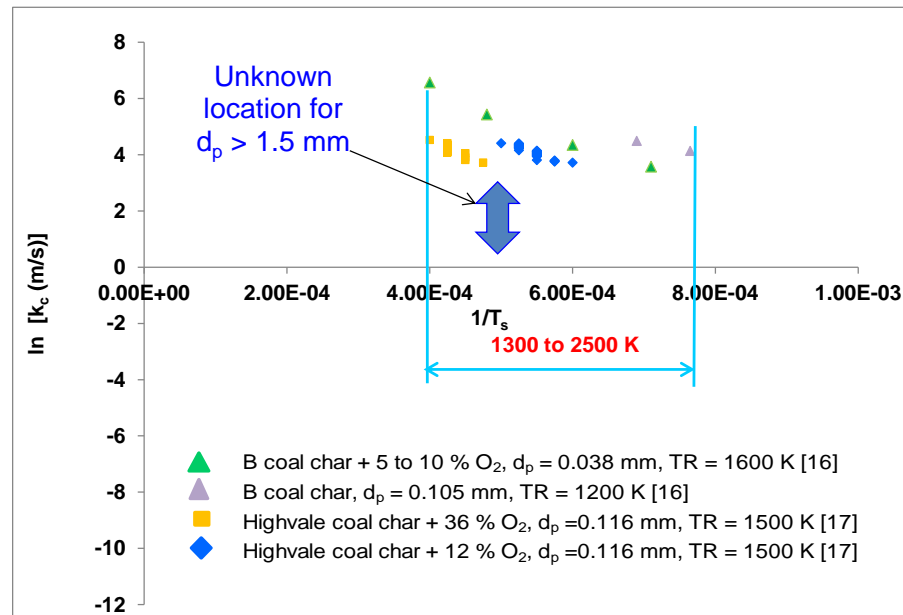


Figure 2-1. Arrhenius plot of combusted particles for $d_p < 0.15$ mm

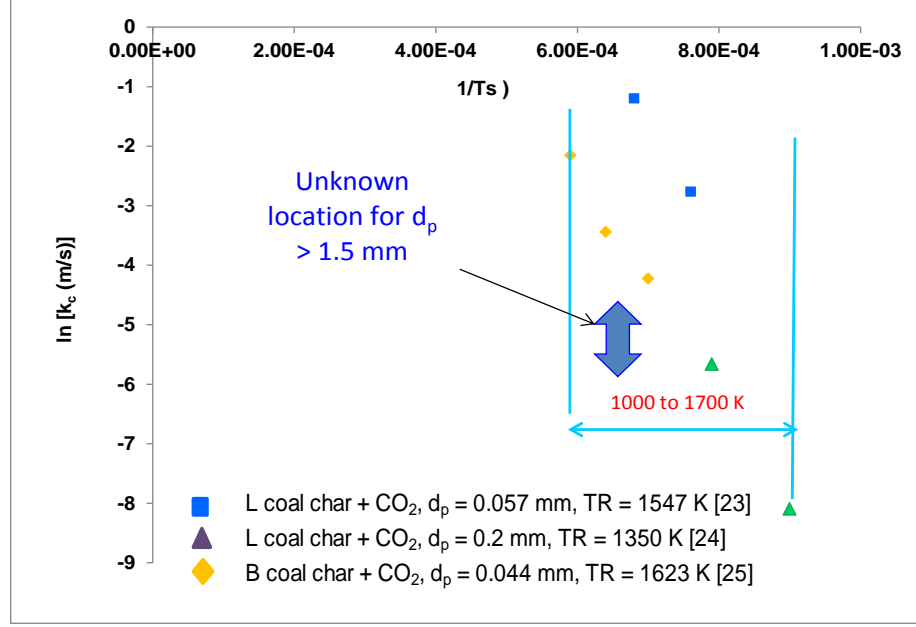


Figure 2-2. Arrhenius plot of CO_2 gasified particles for $0.057 < d_p < 0.2 \text{ mm}$

Although there is a plethora of experimental data on char reduction, very few were analyzed with Arrhenius plot representation; especially for large particles greater than 1 mm. As a result, most recent modeling studies on large char particle combustion under-predict particle surface temperatures and conversion times [26, 27]. Additionally, because tar (i.e., high molecular weight hydrocarbon gases) reduction investigations are still inadequate [28], thermal processing is also investigated in this work using steam and vitiated air as oxidizing agents.

2.1 Char Reduction Process

Air is commonly used as a char oxidizing agent because of its abundance and availability at relatively low cost as compared to other oxidants, such as O_2 or steam. However, oxygen in air is highly diluted with nitrogen, producing synthesis gases with generally low heating values at 5.6 MJ/m^3 as compared to 11.2 MJ/m^3 with pure O_2 gasification [29]. As a result, other oxidants are also considered in this study to

enhance syngas heating values such as steam and its combination with either O₂ or air. Because these types of oxidants have not been thoroughly investigated especially for particles greater than 1 mm in diameter under isothermal and non-isothermal conditions, these are investigated in this work.

Typically, real-world fluidized bed reactors are operated under non-isothermal conditions. Although isothermal experimental conditions can be maintained during char reduction, surface particle temperature values are expected to change and can achieve higher values than reactor temperatures, especially during combustion of particles (see Table 2-1). Additionally, the investigation of the time dependent kinetic parameters and diffusional effects of char particles greater than 0.2 mm are still few and further research should be conducted to enhance the understanding of char reactivity as well as the relative effects of kinetics and diffusion during reduction. A greater understanding of these processes will increase the development and deployment of efficient fluidized and packed beds gasifiers as well as combustors for compact and small scale processing capacities (i.e., less than 3000 kg/day), which are ideal in remote and portable applications.

Table 2-1. Reactor and surface particle temperatures of char

Thickness (mm)	Char source	d _p (mm)	Oxidizer	TR (K)	T _s (K) (Calculated)	Reference
	Coal char	0.1	Air	1600	2300	[15]
	H coal char	0.1	6 to 36 % O ₂	1560	2055	[17]
1.23	Carbon		Air	923	NP	[30]
	Coal char	0.038	5 to 10 % O ₂	1460	1600	[16]
	B coal char	0.044	CO ₂	1623	1500	[22]
	L coal char	0.057	CO ₂	1547	1470	[23]
	L coal char	0.2	CO ₂	1350	1200	[24]
Legend: NP - Not provided, d _p - particle diameter, H -Highvale, B - Bituminous, L - Lignite, TR - Reactor temperature and T _s - Surface temperature						

2.1.1 Char reduction conversion curves

Figure 2-3 shows experimental results for a typical char conversion, revealing some of the general characteristics of solid-gas reactions. The “X” represents the conversion and “T” represents the measured reactor temperatures. Region “1” indicates rapid adsorption of gases at the beginning of the induction period which also results in a small mass loss. According to House [31], many solids have an attraction for certain gases and this observed feature is very common. It is considered that region “1” depicts the end of pyrolysis stage as a result of volatile matter release after drying stage is completed. Region “2” represents the completion of the gas induction period, which is also the region wherein the reaction is about to accelerate. Region “3” represents the reaction when it is progressively accelerating at a maximum rate. Region “4” is usually called the decay period, representing a stage when the reaction reaches completion.

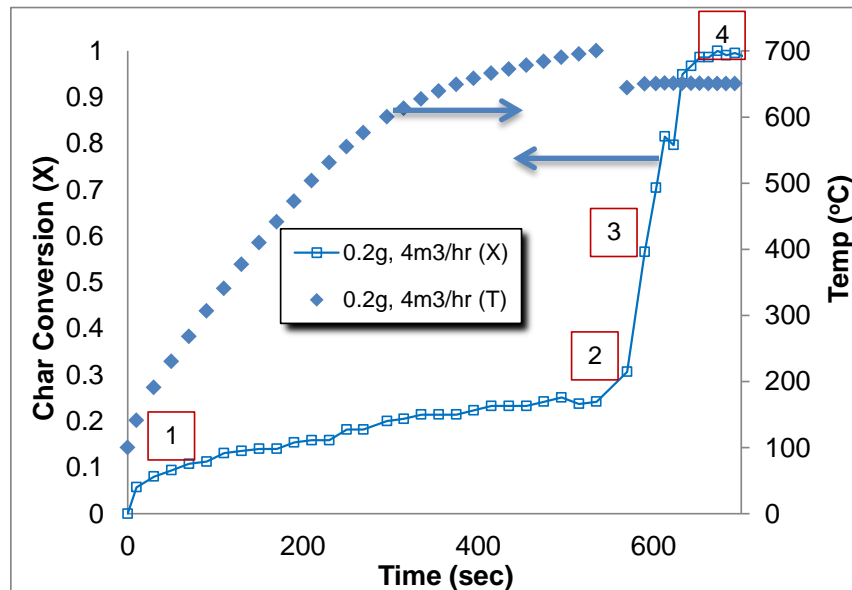


Figure 2-3. Typical char conversion, of solid-gas reactions.

2.1.2 Uncertainties on calculated kinetic parameters

Kinetic parameters of homogeneous and heterogeneous chemical reactions consist of the activation energy, frequency factors and the order of reaction. The activation energy was first introduced by the Swedish scientist Svante Arrhenius which he defined as the minimum energy input into chemical reactants for a chemical reaction to occur either in an exothermic or endothermic process. Activation energy of a reaction is designated as E_a with kilojoules per mole (kJ/mol) as its unit. Because Arrhenius was the first to introduce the Boltzman factor, i.e. $\exp(-E_a/RT)$ to calculate chemical reaction rates, the nonlinear equation $k_c = A \times \exp(-E_a/RT)$ is called the Arrhenius law or equation. The frequency factor, A includes the effects of collision terms, steric factor associated with the orientation of colliding molecules and temperature dependency [32]. Murphy et al. [17] suggested that the frequency factor can also represent the reactivity, which they claimed to be consistent with char kinetic rates of coals [33]. Additional discussions on the Arrhenius equation is provided in section 2.4.

Generally, the value of the Arrhenius equation is not the same during the combustion or gasification process over a wide temperature range. Hence, the kinetic parameters at low temperatures are not identical at high temperatures as illustrated in Figure 2-4. In Figure 2-3, the combustion or gasification rates of char particles tend to decrease with increasing conversion after these have achieved their maximum rates. This was also observed in an earlier work for the combustion of carbon particles when reduction rates decreases near complete conversion [34]. As a result, a linear fit approach for the entire gasification or combustion data will have some challenges

when obtaining the kinetic parameters. One way to get around this difficulty is to use a discrete time linear fit approach on the experimental data to obtain kinetic parameters. For example, in Figure 2-4, the activation energy of the high temperature and low temperature data are 92.5 and 20.7 kJ/mol, respectively. Subsequently, the frequency factors for the high temperature and low temperature data are $2.0\text{E}+05$ and 30.4 m/sec, respectively. These kinetic parameters are based on a unity order of reaction as these are applied using a one film ash segregated core gasification or combustion model for the external reduction of char particles. The use of discrete time linear fit approach have not been used in literature before which will be pursued in this study when dealing with the complete oxidation of disk-shaped and spherical-shaped char particles that are combusted or gasified at low and high temperatures. However, one caveat about kinetic data obtained from Arrhenius law is the presence of free radical reactions, which are expected to be present especially in some carbonaceous feedstocks where hydrogen element is present such as biomass and coal chars. Also, the ash content of char particles can significantly influence char reactivity. Although many reactions follow the Arrhenius law, low-activation-energy free radical reactions and reactions due to the recombination of simple radicals during combustion are the exceptions [3].

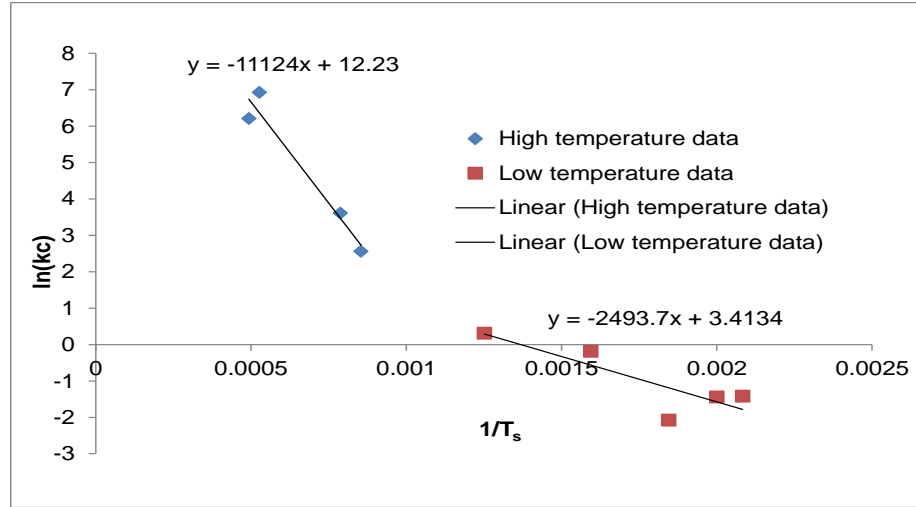


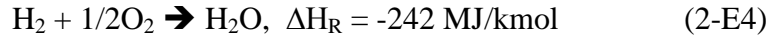
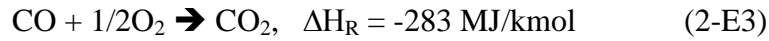
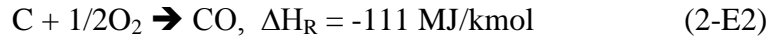
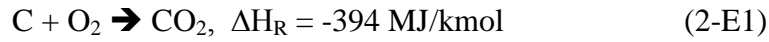
Figure 2-4. Typical low and high temperature Arrhenius plot

Majority of previous studies on high-temperature char combustion kinetics starts with an assumed char kinetic expression and then a linear fit is performed for the entire data set. However, this technique is complicated by Zone II particle reduction, where both kinetic and diffusion controls are important, as would be expected to be the case for large particles [17]. It will be shown later (see chapter 4) that the derived kinetic parameters for a generalized kinetic model undergoing near Zone II char combustion and CO₂ gasification regimes have inconsistencies using random pore model. Therefore, a discrete time nonlinear fit procedure is also investigated in this work. This is a novel procedure that has been investigated by Murphy et al. [17]. The results of linear and non-linear regression fits will be provided later in chapter 4 for the combustion and gasification of the different particle shapes being investigated.

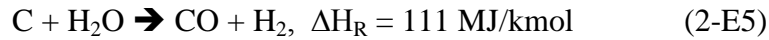
2.2 Char Reactions

As stated previously, gasification and combustion of char is a complex system comprising of many competing intermediate reactions both at the solid and gas phases within the particles. These reactions depend strongly on temperature, pressure, particle structure, size, porosity, carbon source, and thermal history. Char and steam reactions are typically coupled with exothermic partial oxygen combustion and endothermic reactions to produce synthesis gases. The principal reactions include these reactions [3]:

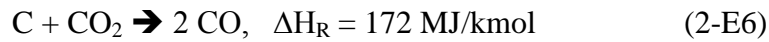
For combustion reaction,



For water gas reaction,



For Boudouard reaction,



For methanation reaction,



For water gas shift reaction,



Combustion or exothermic reaction equations (2-E1) through (2-E4) are often used to provide heat in a combustor or gasifier to break up chemical bonds and drive

reaction equations (2-E5) and (2-E6). The rate of reaction of the water gas reaction is faster than the Boudouard reaction because it is less endothermic. However, the Boudouard reaction is much easier to investigate as compared to the water gas reaction because the product gas component consists of only CO_2 and CO . Water gas reaction studies are more complex because of the competing reactions that can occur when hydrogen gas reacts with other species such as CO , CO_2 through equations (2-E5), (2-E7) and (2-E8). The Boudouard reaction is important in downstream systems due to heat transfer in steel surfaces which can promote its reverse reaction, forming soot particles [29]. Another consideration is the fact that partial combustion reactions as depicted by (2-E2) produce CO , which can promote the water gas shift reaction when steam is used as an oxidizing agent. The water gas shift reaction is considered to occur due to heterogeneous catalysis by the carbon surface especially at temperatures below 1100°C [29]. And the methanation reaction is typically important for two reasons: (1) the energy content of the syngas is increased and (2) the oxygen required is reduced because of the additional heat released in methane generation.

The gasification and combustion of solid fuels are considered heterogeneous reactions where the reactants exist both in solid and gaseous states. Generally, these reactions are subdivided into the following processes [35]:

1. Transport of the reactant molecule (e.g. O_2 , air, H_2O or CO_2) to the solid surface either by convection and/or diffusion
2. Adsorption of the reactant molecule on the solid surface

3. Elementary reaction steps, involving various combinations of adsorbed molecules on solid surface
4. Desorption of product molecules from the solid surface
5. Transport of the product molecules away from solid surface by convection and/or diffusion.

Amongst these processes, (a) and (e) can be analyzed using mass transfer concepts. The intervening steps are more complicated, especially steps (c). Step process (b) can be analyzed depending on how strongly or weakly the reactant gas molecules are adsorbed to the solid surface. For a single gas molecule reactant (oxygen), the global reaction rate (R_c) with a unity order of reaction for an oxygen molecule that is weakly adsorbed to the surface can be expressed as follows in equation (2-E9) [8]:

$$R_c = \dot{m}_{c,s}'' = k_c MW_c [O_{2,s}] \quad (2E-9)$$

where $[O_{2,s}]$ is the molar concentration of O_2 at the surface and k_c is the rate coefficient of reaction, which is expressed in Arrhenius form. When the oxygen molecule is strongly adsorbed at the solid surface, the reaction rate becomes independent of the gas-phase concentration of oxygen as follows in equation (2-E10) [8]:

$$R_c = \dot{m}_{c,s}'' = k_c MW_c \quad (2E-10)$$

Both equations (2E-9) and (2E-10) assume a global reaction rates at the solid surfaces with a unity order of reaction, which can be further classified into three reduction scenarios; (a) one-film, (b) two-film model and (c) continuous-film [8]. The one-film model assumes that there is no flame in the gas phase (no combustion is

taking place at the boundary layer) and the maximum temperature occurs at the solid surfaces. For the two-film model, a flame exist in the gas phase at some distance from the solid surfaces where intermediate species (e.g., CO) reacts with the incoming reactants (e.g. O₂). A continuous-film model assumes a distributed flame zone within the boundary layer [8].

Amongst these three models, the one-film provides the simplest model and it will be pursued further in this study to characterize the kinetic parameters, evolution of char surface temperatures using simple energy equation, contribution of diffusional effects and energy parameters.

2.3 Heterogeneous Char Reductions

In order to determine which regime is dominant during internal reactions within a solid particle, Thiele [9] developed the concept of effectiveness factor and he introduced a dimensionless number, called the Thiele modulus to calculate the factor. Equation (2-E11) provides the formulation of Thiele modulus (ϕ) as a dimensionless number. This provides the ratio of the external reaction rate to pore diffusion rate such that when $\phi \ll 1$, the surface chemical reaction rate is slow as compared to pore diffusion rate and conversely, when $\phi \gg 1$ the surface chemical reaction rate is much faster than the pore diffusion rate. In a first order reaction for a spherical char, Thiele modulus is defined by using an arbitrary oxidant as follows [9]:

$$\phi = r \sqrt{\frac{\frac{d}{dt}[O_{ox,s}]}{D_{eff}[O_{ox,s}]}} \quad (2-E11)$$

where r , $\frac{d}{dt}[O_{ox,s}]$, D_{eff} and $[O_{ox,s}]$ are the radius of the char, conversion rate of the oxidant at surface conditions, effective diffusion of the oxidant and the concentration of the oxidant at the outer surface of the char, respectively. By this definition, for a $C + O_2 \rightarrow CO_2$ or $C + CO_2 \rightarrow 2CO$, equation (2-E11) is modified for a spherical char particle in terms of mass burning rate with a unity order of reaction in equation (2-E12) as follows:

$$\phi = r \sqrt{\frac{v\dot{m}_c \rho_c S_{gc}}{D_{eff} [O_{ox,s}] MW_{ox}}} \quad (2-E12)$$

Another factor, the effectiveness factor, η as provided in equation (2-E13) represents the extent to which chemical reaction rates are affected by internal diffusion through char pores [9]. As the diffusion rate decreases, Thiele modulus increases which will result to a decrease in the effectiveness factor. Effectiveness factor is the ratio of the observed or actual chemical reaction rate to the maximum possible chemical reaction rate without internal diffusion control. This also means that the effectiveness factor provides an insight how far the oxidant diffuses into the porous char before reaction takes place. When the value of effectiveness factor is nearly equal to one, the observed chemical reaction rate and the maximum possible chemical reaction rate are nearly identical.

$$\eta = \frac{3}{\phi} \left(\frac{1}{\tanh(\phi)} - \frac{1}{\phi} \right) \quad (2-E13)$$

The calculations of these parameters are based on pure carbon density of 1950 kg/m³[36] and the initial ash content of the char as provided. Based on a one (1) kilogram of char basis, two possible mechanisms can occur with O₂ as an oxidant. Therefore, the stoichiometric coefficients in (2-E12) can be either 2.667 for char plus O₂ oxidation and 3.667 for char plus CO₂ gasification.

2.3.1 Initial specific surface areas of char particles

In the absence of experimental data, the initial specific surface area of char is based on oakwood char is taken at 400 m²/g [37]. Presently, majority of experimental studies to measure char specific surface areas are based on the Brunauer-Emmett-Teller (BET) method via the physical adsorption of gas molecules on the surfaces [38]. The specific surface area of eucalyptus wood charcoals measured using BET method (N₂ at 77 K) was 387 m²/g [39]. Values between 69 and 110 m²/g are also obtained for charcoals prepared by rockrose treatment and extracted rockrose in the atmosphere when temperature is increased [40]. The BET method is still an area of active research area in order to accurately account the inherent randomness and complexity of porous char structure which is also very likely to fragment during conversion, depending on char chemical composition as well as gasification or combustion operating conditions.

Specific surface areas for coal chars vary widely between 1 and 1000 m²/g [14]. For 25 % porous synthetic coal char particles, the specific area is 247 m²/g for a 3.0 structural parameter [41]. Although the coal char particles are less porous than 25 % in this study, the specific surface area is expected to be greater than 247 m²/g because the experiments are conducted as multi-particle system varying between 2 to

9 particles. Additionally, the combustion and gasification regimes at the char surface are anticipated to have $\text{Ø} \gg 1$, a condition when external reaction rates are much faster than pre diffusion rates. As a result, the coal char structural parameter is expected to be lower than 3.0, a condition that is typical for Zone I (reaction controlled) and Zone II (reaction-diffusion controlled) regimes [41]. Therefore, a structural parameter of 2.5 is considered in this study. In the absence of the actual measurement of coal char particles as used in this study, a specific surface area of 416 m²/g is also considered. This was the average specific surface area of coal char particles from literature [14, 41].

In the absence of a reliable model to estimate how the initial surface area changes with extent of reaction, the initial specific surface area ($S_{gc,0}$) per unit mass is postulated to change with the degree of char conversion as shown below using “k” and “0” as subscripts for time marching from initial conditions, respectively. This formulation [42] is provided in equation (2-E14) below:

$$S_{gc,k} = S_{gc,0} \sqrt{1 - \phi \ln(1 - X_k)} \quad (2-E14)$$

The initial char particle specific surface area ($S_{gc,0}$) is dependent on the conversion, char preparation, governing reaction conditions, chemical kinetics of reaction and presence of fragmentation during reduction. For macropore (pores with internal width greater than 50 nm) with wood char particles, $S_{gc,0}$ do not exhibit a significant increase as conversion progresses under Zone II burning regime, a condition when external diffusion and chemical reaction rates are nearly identical [37,

43]. As a result, a constant structural parameter value equal to 2 is selected to provide a moderate increase in specific surface area per unit mass. This value is 5 orders of magnitude less than 10, a structural parameter that is obtained for wood char when it is pyrolyzed at 800 °C in 15 minutes [44]. A structural parameter value of 2 is considered a good value because char pore sizes are assumed to be mostly in the macropore range, where there is no significant change in specific surface area as reaction progresses. Additionally, as will be shown later, the activation energies calculated are very close to within + 0 to – 30 kJ/mol based on published literature for $C + O_2 \rightarrow CO_2$ reactions, which are generalized to be around 181 kJ/mol [10, 34, 45, 46].

2.3.2 Effective and bulk diffusion

When dealing with the effective diffusion of the oxidant, the bulk and Knudsen diffusion contributions on the mass transport rate of the oxidants within the porous structure of a burning char particle is considered [47]. The combined effects of these two diffusion mechanisms are described by an effective diffusion coefficient (D_{eff}), which is calculated using equation (2-E15):

$$\frac{1}{D_{eff}} = \frac{1}{D_{K,eff}} + \frac{1}{D_{A/B}} \quad (2-E15)$$

where, $D_{K,eff}$ is the effective Knudsen diffusion coefficient for the oxidant (O_2 or CO_2), which embodies transport through pores having diameters less than the oxygen mean free path. The bulk diffusion coefficient of binary gas phase system ($D_{A/B}$) is calculated using equation (2-E16) [48]:

$$D_{AB} = \frac{1.8583 \times 10^{-7} \sqrt{T_s^3 (1/MW_A + 1/MW_B)}}{P \sigma_{AB}^2 \Omega_{DAB}} \quad (2-E16)$$

where, gas A and B are the gas species (e.g., O₂, CO₂, CO and air) and σ_{AB} and Ω_{DAB} are the combined hard sphere collision diameters and dimensionless collision integral, respectively. Thomson [49] provides a methodology to calculate combined Lennard-Jones parameters such as σ_{AB} and Ω_{DAB} . The Knudsen diffusion coefficient (D_K) accounts for the collisions of the molecules on the pore walls which becomes important when the mean free path of colliding oxidant molecules is equal to or greater than the geometric characteristics of char pore structure [48]. Hence, D_K depends on pore radius and mean velocity of the gases and is calculated using equation (2-E17) as follows [49]:

$$D_K = \frac{2r_p}{3} \sqrt{\frac{8k_B N_{av} T}{\pi MW_{ox}}} \quad (2-E17)$$

The effective Knudsen diffusion ($D_{K,eff}$) is calculated using equation (2-E18):

$$D_{K,eff} = D_K \frac{\theta}{\tau} \quad (2-E18)$$

where, θ/τ (porosity/tortuosity) is a correction for a porous char and the tortuous path through which the gas molecules diffuse inside the individual pores of the char. A value of three (3) is taken for tortuosity for porous char [47]. The accounting of wall roughness and interconnections of the pores is estimated with the following equation

(2-E19) by Wheeler wherein “ r_f ” is the roughness factor, which is equal to 2 for carbon surfaces [50]:

$$r_p = \frac{2V_g}{S_{gc}} r_f (1 - \theta) \quad (2-E19)$$

The resulting calculated results for the kinetic parameters, porosities, Thiele modulus, effectiveness factors are provided in Chapter 4.

2.3.2 Char reactivity and pore structure

Char reactivity is highly influenced by pore structure and porosity. During coal or biomass pyrolysis, volatile matter is released which leads to an increase in porosity. Due to the inherent porous structure, the diffusion of reactant and product gases within the particle is enhanced. Additionally, during char combustion or gasification processes, the pore structure also fragments and collapses. For large particles, this leads to the formation of smaller particle sizes, which will increase conversion. At higher temperatures, ash fumes may volatilize and escape the surface depending on the type of ash and its properties. The rate of change of specific char reactivity during oxidation is calculated as follows in equation (2-E20) [41]:

$$R_k = \frac{1}{1 - x_k} \frac{dx_k}{dt} = R_{i,k} S_{gc,k} \quad (2-E20)$$

where, R_k is the rate of change of specific reactivity, x_k is the conversion (ash free) at time k and $R_{i,k}$ is the intrinsic reactivity per unit of internal surface area. Knowing the

value of S_{gk} from equation (2-E14), an expression $R_{i,k}$ can be rewritten for equation (2-E20) as follows:

$$R_{i,k} = \frac{R_k}{S_{gc,k}} = \frac{dx_k/dt}{S_{gc,0}(1-x_k)\sqrt{1-\phi\ln(1-x_k)}} \quad (2-E21)$$

Equation (2-E18) provides a method to calculate intrinsic reactivity, which is the reaction rate per unit area of pore surface in the absence of diffusion control [14].

2.4 Char Reduction Models

Char gasification and combustion processes can be analyzed with equilibrium, homogeneous, random pore, Langmuir-Hinshelwood (LH), Four Pairs Coats-Redfern (FPCR) and Reich-Stivala (RS) models. Details of some of these models are provided in Appendix VII. These models are generally very useful for small particles less than 0.2 mm in diameter. The LH model uses the product concentration gases to calculate the kinetic parameters (KPs). Usually, based on magnitude values, the product concentration gases are more prone to larger uncertainties than weight measurements [31]. For this reason, kinetic parameters and other properties are mainly calculated in based on weight losses with temperature and time measurements. For spherical biomass particles, the changes in the diameter with reaction time are also observed with a video recorder via the optical quartz lens in the experimental reactor.

Char kinetic modeling analyses are generally performed depending on whether the reaction is considered isothermal or non-isothermal. Isothermal reactions are normally analyzed with the homogeneous and random pore models using temperature programmed reaction technique (TPR). TPR is a method wherein the

weight loss is measured during the heating of a solid sample in a reactive gas medium to a desired pre-determined temperature at constant heating rate [51]. Although isothermal conditions simplify greatly the analysis of data via determination of kinetic parameters, these are very ideal conditions and actual particle surface temperatures are normally higher than reactor temperatures especially during combustion processes. Therefore, as performed by previous investigators [16, 17, 23, 24, 25], the surface temperatures are considered in data analysis using the governing energy conservation models which are discussed in section 2.4.4.

2.4.1 Random pore model for spherical shaped chars

The RPM was used in the analysis of experimental data with temperature programmed reaction (TPR) technique to determine the kinetic parameters of gasification using air at atmospheric pressure [51]. Miura et al. [51] and Kajitani et al. [22] determined that kinetic parameters obtained from the random pore model provide good agreement with the experimental data. As shown in equations (2-E22) and (2-E23), the RPM considers the physical structural changes of gas reacted internal surfaces during reduction. Bhatia et al [42] showed that RPM can be applied to coal gasification reaction. This model assumes pore growth and the overlapping random of pore surfaces which could either increase or decrease the available area for reaction simultaneously. This model is first applied to the TPR data of char gasification by Miura and company [51]. Miura et al. suggested that kinetic parameters must be estimated from the experimental data by curve fitting between X and T . Interestingly, the relationship between the apparent rate and temperature is a unique kind of Arrhenius plot and the activation energy can be estimated from its

slope.

RPM also allows direct calculation of the activation energy and frequency factor in terms of conversion for a given structural parameter that is prevalent during the reaction inside randomly growing and overlapping pore surfaces of reacted particles. This model has been used in analyzing oxidation data for micrometer sized particles [51]. Bhatia et al. are credited for the RPM which is extensively used to describe the kinetics of internal reactions of porous structures and this is expressed as follows in equation (2-E22) [42]:

$$\frac{dX}{dt} = k_o \exp\left(\frac{-E_a}{R_u T_s}\right) (1 - X) [1 - \phi \ln(1 - X)]^{\frac{1}{2}} \quad (2-E22)$$

where, X , k_o , T_s and ϕ are the conversion, pre-exponential factor, char surface temperature and the structural parameter, respectively. With the use of scanning microscope and the Brunauer-Emmett-Teller (BET), the structural parameter (ϕ) is calculated with equation (2-E23) in terms of the untreated pore structure when the conversion X equals zero (0) as follows:

$$\phi = \frac{4\pi L_o (1 - \theta_o)}{(\rho_o S_{gc,0})^2} \quad (2-E23)$$

where, L_o , θ_o , ρ_o and $S_{gc,0}$ are the equivalent length of overlapping pores per unit volume, porosity, density and specific surface area per unit mass under initial conditions. For a given initial internal specific surface area per unit mass, the internal activation energy of these considered spherically-shaped particles are calculated using the above equations based on surface temperatures and degree of conversions with

respect to time. Although porosity model calculations are still under development, the internal specific surface area is assumed to be influenced by the extent of conversion and the pore structural parameter [42]. The following are the assumptions used when considering the random pore model for char reductions:

1. The pores are considered overlapping and randomly growing during the reactions, which can either increase or decrease the area available for reaction.
2. The effects of oxidant convection into the particle pores are ignored.
3. Internal diffusion rate is considered to be infinitely fast.
4. Because the experiment is conducted at very high air-to-fuel oxidation, carbon char reacts kinetically with O_2 in air and CO_2 is produced.
5. O_2 and CO_2 are weakly adsorbed on the internal surfaces, which means $d[Char]/dt = k(T)[O_2]$ and $d[Char]/dt = k(T)[CO_2]$ for O_2 or air combustion and CO_2 gasification, respectively.
6. The gas phase consists only of O_2 , CO_2 and inert gas (N_2). The O_2 and CO_2 diffuse inward and react with the internal surface to form CO_2 , which diffuses outward.
7. The spherically-shaped internal surface is porous and the oxidants react with the internal surfaces.
8. The spherically-shaped surface temperatures are calculated based a blackbody particle and heat conduction into the particle interior is neglected.
9. Convective heat transfer is considered during gasification
10. Reactions of gas-phase products at the external boundary layer are neglected.

2.4.2 One-film ASCM for disk-shaped char particles

As shown below in equation (2-E24), a one dimension (1D) one-film kinetic-diffusion equation for an exposed disk-shaped particle is presented to couple the external diffusion effects and kinetics. This model is developed and derived to capture the physical characteristics of the experiments performed for thin layers with some idealizations to enable one dimensional reduction analysis, see Figure 2-5. A disk-shaped char particle is considered for this study and the following are the assumptions used while considering a one-film ash segregated core model [8]:

1. The solid carbon surface burns in quiescent medium such that the effects of convection are ignored. This can be assumed because the velocity (i.e., 0.1 m/s) at the solid surface is very small.
2. At the particle surface, carbon char reacts kinetically with reactant molecule (O_2 or CO_2).
3. The reactant molecules (O_2 or CO_2) are weakly adsorbed on the char surface, which means that the $d[Char]/dt = k(T)[O_2]$ and $[Char]/dt = k(T)[CO_2]$ during combustion and gasification governs, respectively.
4. The gas phase consists of only O_2 and CO_2 for combustion conditions. The O_2 diffuses inward and reacts with the carbon surface to form CO_2 gas which diffuses outward.
5. The gas phase consists of only CO_2 and CO for gasification conditions. The CO_2 diffuses inward and reacts with the carbon surface to form CO gas which diffuses outward.

6. The carbon internal surface is impervious to gas-species and intra-particle gas diffusion is ignored. This is made possible by using disk-shaped particles.
7. The surface temperatures are calculated based on blackbody particle, steady-state process and no heat conduction into the particle interior.

Although the measured or observed weights and particle diameters changes sometimes erratically due to experimental noises, these are optimized with nonlinear regression to enable a stable calculation of surface temperatures, which are used as the basis in calculating kinetic parameters.

The derivation of a one-film model for disk-shaped char is provided in Appendix I. This model provides the rate of mass loss due to diffusion and kinetic reactions for thin disk-shaped char particles by considering constant values of stagnant layer (H) and thickness (h). Kinetic calculation procedure is initiated by solving first the rate coefficient (k_c) in equation (2-E27). Then the activation energies and frequency factors are calculated by fitting observed and experimental values in equation (2-E24) until the weight curve model approximates the experimental values at various times during reduction. The changes in apparent activation energies, surface char temperatures and resistances of the governing external chemical reaction and diffusion rates are calculated with Euler Explicit Method for each case, i.e., between every 5 to 20 seconds. This numerical method allows one to iteratively calculate the rate coefficients with respect to the variations of conversion with time. When the mass conversion rate model is finally established to follow the experimental data curve, discrete time linear method is used for the Arrhenius equation to estimate the activation energy and frequency factor at suitable time

intervals (during pre-heating and combustion periods). A discrete time nonlinear fit is also applied to calculate the activation energies using the average estimated frequency factors as initially determined with the discrete time linear approach. Suitable discrete time intervals are determined by the characteristics of the natural logarithmic plot of reaction rate coefficients as a function of the reciprocal of temperatures. For disk-shaped particles, the one-film ash segregated core model is as follows:

$$\frac{dm}{dt} = \frac{Y_{ox,\infty}}{\frac{H(v_I + Y_{ox,s})}{\rho_{ox} D \pi r^2} + \frac{MW_{ox} \times R_u T_s}{\pi r^2 k_c MW_c \times P \times MW_{ox}}} \quad (2-E24)$$

where dm/dt is the derivative of mass loss with respect to t , r is the instantaneous equivalent char radius in the container, $Y_{ox,s}$ is the mass fraction of oxidant (i.e., O_2 or CO_2) at the surface of the char, $Y_{ox,\infty}$ is the mass fraction of oxidant at the far field, D is the mass diffusivity of reactant and product gases in the reaction, H is the height of the stagnant layer, v_I is the stoichiometric coefficient (2.667 for combustion and 1.333 for gasification), k_c is the rate coefficient, n is the order of reaction ($n=1$) and MW are the molecular weights of species (i.e., oxidant or carbon) of interest. Using electrical current flow analogy, the expressions in the denominators of equation (2-E24) can be categorized explicitly as two rate resistances with equations (2-E25) and (2-E26) as follows for R_{diff} (diffusion rate resistance) and R_{kin} (kinetic or reaction rate resistance), respectively:

$$R_{diff} = \frac{H(v_I + Y_{ox,s})}{\rho_{ox} D \pi r^2} \quad (2-E25)$$

$$R_{kin} = \frac{MW_{ox} \times R_u T_s}{\pi r^2 k_c MW_c \times P \times MW_{ox}} \quad (2-E26)$$

As introduced earlier in the previous section, the reaction rate coefficient is shown in equation (2-E27) as follows:

$$k_c = A \times \exp\left(-\frac{E_a}{RT_s}\right) \quad (2-E27)$$

The reaction rate coefficient (k_c) is calculated by fitting the experimental data into equations (2-E28). In this model, a unity order of reaction is used to simplify the analysis and with the use natural logarithms in equation (2-E27), the values of E_a and A can be directly calculated. A pure diffusion-controlled condition exists when $R_{kin} = 0$ and conversely, a pure (intrinsic) kinetic-controlled condition exists when $R_{diff} \rightarrow 0$. The ratio of R_{kin} to R_{diff} provides a convenient way of indicating when the reduction is considered externally diffusion-controlled or externally kinetically-controlled, i.e., $R_{kin}/R_{diff} \ll 1$ or $R_{kin}/R_{diff} \gg 1$, respectively [8]. The calculated KPs are presented later along with the analysis of the results in chapter 4.

Under pure kinetic conditions, when the diffusion rate resistance is insignificant or negligible, equation (2-E24) can be re-written as (2-E28) with O_2 as an oxidant:

$$\frac{dm}{dt} = \pi r^2 k_c \frac{MW_c \times MW_{tot} \times P \times Y_{O_2,s}}{MW_{O_2} R_u T_s} \quad (2-E28)$$

Alternatively, when pure diffusion reduction or no chemical reactions is taking place, equation (2-E32) can also be re-written in equation (2-E29) as:

$$\frac{dm}{dt} = \pi r^2 \rho_{O_2} D \frac{Y_{O_2, \infty}}{H(v_l + Y_{O_2, s})} \quad (2-E29)$$

Because there is a need to know the contributions of the different parameters that can affect the activation energy under pure kinetic or reaction conditions, equation (2-E28) is expressed in equation (2-E30) below for this condition:

$$E_a = RT_s \times \ln \left[\frac{\pi r^2 \times A \times MW_c \times MW_{tot} \times P \times Y_{O_2, s}}{\frac{dm}{dt} \times (MW_{O_2} R_u T_s)} \right] \quad (2-E30)$$

However, under coupled conditions, the activation energy expression is expressed in equation (2-E31) as:

$$E_a = R_u T_s \times \ln \left\{ \frac{A \times \rho D \times MW_{O_2} R_u T_s \frac{dm}{dt}}{MW_c \times P \times MW_{tot} \times \left[H \frac{dm}{dt} (v_l + Y_{O_2, s}) - \rho D \pi r^2 Y_{O_2, \infty} \right]} \right\} \quad (2-E31)$$

To enable the use of equation (2-E24) at specific times, the radius with respect to time is also considered during reduction. In most of the experiments, it is observed that as the reaction progresses, the particles decrease or shrink. The radius does not directly represent the actual radius of the disk-shaped arranged particles but rather the equivalent size reduction as the char shrinks due to oxidation. Figure 2-5 illustrates this as shown by assuming that the thickness of the char (h) is constant. With this consideration, starting with the basic formula for mass with respect to density and volume, the char mass can be expressed as follows in equation (2-E32):

$$m = \rho_c \times v \quad (2-E32)$$

Substituting the volume with respect to char radius and depth, the mass can be expressed in equation (2-E33) as:

$$m = \rho_c \times \pi r^2 h \quad (2-E33)$$

Differentiating equation (2-E41) with respect to time yields to equation (2-E34):

$$\frac{dm}{dt} = \rho_c \times 2\pi r h \frac{dr}{dt} \quad (2-E34)$$

Knowing the values of dm/dt , the changes in radius with respect to time can now be calculated with equation (2-E35):

$$\frac{dr}{dt} = \frac{1}{2\pi r \rho_c h} \times \frac{dm}{dt} \quad (2-E35)$$

where, dr/dt is the instantaneous rate of change of radius, r is the char radius at time t , ρ_c is the char's bulk density as measured, and dm/dt is the instantaneous experimental rate of mass. Depending on the region of the reactions, dm/dt and r are constantly changing and these are expected to change significantly when reactions are fast. The experimental values of dm/dt are fitted into equation (2-E45) to calculate dr/dt .

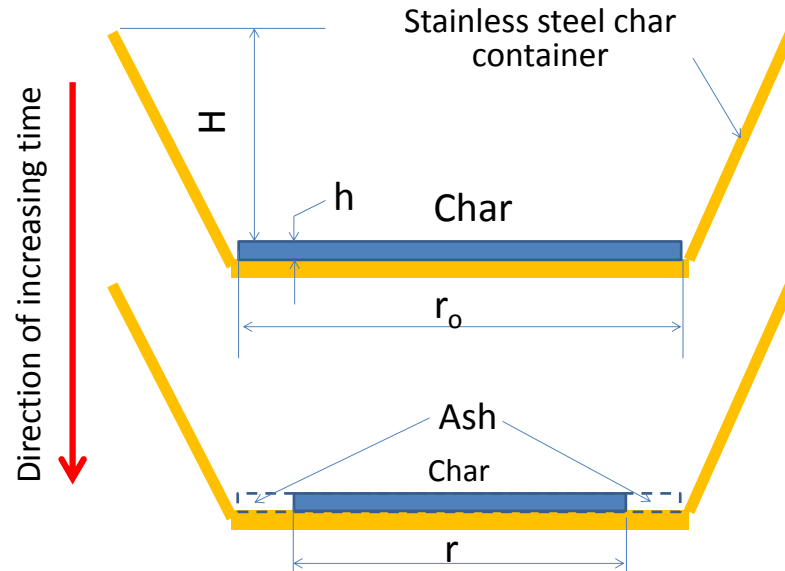


Figure 2-5. Expose thin disk-shaped disk model

2.4.3 One-film ASCM for spherically shaped chars

Characterizing and estimating the kinetic parameters for the reduction of large particles greater than 1 mm is not trivial, much more for multi-particle systems. Central to this issue is that the methods to calculate the kinetic parameters parameters have not yet been fully explored or established for Zone II reduction [15, 52] as well as Zone III regimes. Estimated kinetic parameters can vary substantially because of the differences in experimental temperature reactor conditions, experimental particle arrangements and variations of physical and chemical properties of experimental samples as used by many previous investigators [19, 30]. A one-film kinetic-diffusion equation ash segregated core model (ASCM) is used to estimate the external kinetic parameters such as activation energies and frequency factors a unity order of reaction. Figure 2-6 provides the concept of the ASCM for a char undergoing a combustion or reduction process. ASCM assumes that the ash particles are removed from the

particle external surfaces and is always exposed for combustion or gasification. This can actually occur on fluidized beds or when the particles are constantly moving and colliding with other particles and against reactor walls.

One-film Ash Segregated Model

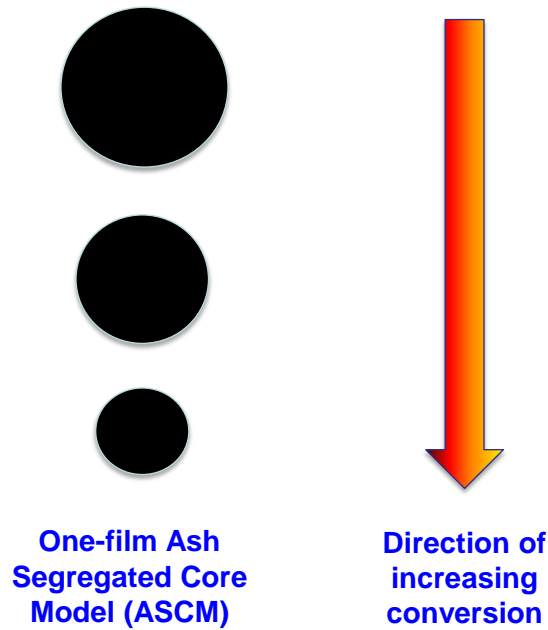


Figure 2-6. ASCM for a char undergoing a reduction process

For spherical particles, the ASCM already exists as model and its derivation was presented by Turns [8]. In this model, the effects of external diffusions are included and it can be used to analyze large particles (as will be shown later), ranging from 4 to 7 mm in equivalent diameters, which are ideal feedstock sizes for fluidized bed and packed-bed gasifiers. Generally, large particles are expected to be dominated by external reaction and internal diffusion rates, which is shown later in section 4. The changes in apparent activation energies, surface char temperatures and reduction rate resistances of the governing external chemical reaction and diffusion rates are

calculated by applying Euler Explicit Method on each particle at each time interval of interest. This numerical method allow one to iteratively calculate the reaction rate coefficients with respect to the variations of conversion with time. After the model is established to follow the experimental data curve, discrete linear fits are used on the Arrhenius equation to estimate the activation energies and frequency factors. The discrete linear is a novel method being considered in this study to analyze the changes as well as estimate the intrinsic (no diffusional influence) or apparent (with diffusional influence) kinetic parameters as reduction progresses. The assumption behind this approach is that the kinetic parameters such as activation energies and frequency factors can vary during char reduction due to changes in char surface temperatures and other factors such as the catalytic effect of ash particles. This is further discussed in chapter 4. During the injection of oxidants, calculated surface temperatures as well as reactor temperatures are considered to estimate the activation energies and frequency factors. This approach is expected to provide kinetic parameters for large particles, which are also anticipated to be strongly influenced by the inherent effects of non-isothermal reactor temperature conditions and diffusion.

The following are the assumptions used while considering a one-film and ash segregated core model (ASCM) [8]:

1. Spherically-shaped carbon surface burns in quiescent medium.
2. At the particle surface, carbon char reacts kinetically with O_2 in air and CO_2 to produce CO_2 and CO , respectively. This means that the prevailing reactions are $C + O_2 \rightarrow CO_2$ and $C + CO_2 \rightarrow 2CO$ for combustion and gasification, respectively.

3. O_2 and CO_2 are weakly adsorbed on the char surface, which means that the reduction rates $[Char]/dt = k(T)[O_2]$ and $d[Char]/dt = k(T)[CO_2]$ are considered for combustion and gasification, respectively.
4. The gas phase consists only of O_2 , CO, CO_2 and inert gas (N_2). The O_2 and CO_2 diffuses inward and reacts with the carbon surface to form CO_2 and CO, which diffuse outward.
5. The spherically-shaped carbon internal surface is impervious to gas-species and inter-particle gas diffusion is ignored.
6. The spherically-shaped surface temperatures are calculated based a blackbody particle, steady-state process and no heat conduction into the particle interior.
7. Although the measured or observed weights and particle diameters changes sometimes erratically due no experimental noises, these are optimized with nonlinear regression curves (exponential or power curves) on the experimental data to enable a stable calculation of surface temperatures, which are also used as the basis in obtaining the apparent kinetic parameters.

The effects of convection during combustion is ignored for mathematical expediency. However, under gasification conditions, convective heat transfer is considered. The gas phase thermal conductivities and specific heats of air, CO_2 and CO are varied based on the calculated surface temperatures. Varying Lennard-Jones parameters as published in literatures are used to calculate the diffusion coefficients of gases for these reactions [8, 48]. The Thiele modulus, effectiveness factors and porosities of spherically-shaped modeled multi-particles are also varied based on char surface temperatures and degree of conversions. Therefore, under these assumptions,

equation (2-E36) is used to estimate the external apparent kinetic parameters, which are represented as E_a (activation energy) and A (frequency factor) for spherical shaped particles [8]:

$$\frac{dm}{dt} = \frac{Y_{Ox,\infty}}{\frac{v_I + Y_{Ox,s}}{\rho_{ox} D 4\pi r} + \frac{v_I \times R_u T_s \times \exp\left[\frac{E_a}{R_u T_s}\right]}{4\pi r^2 \times A \times P \times MW_{ox}}} \quad (2-E36)$$

Equation (2-E36) assumes that the overall burning rate follows an electrical current flow for series circuits. Hence, if two resistances or resistors are considered to be connected in series, two char burning rate resistances, equations (2-E37) and (2-E38) is introduced as follows:

$$R_{diff} = \frac{v_I + Y_{Ox,s}}{\rho_{ox} D 4\pi r} \quad (2-E37)$$

$$R_{kin} = \frac{v_I \times R_u T_s \times \exp\left[\frac{E_a}{R_u T_s}\right]}{4\pi r^2 \times A \times P \times MW_{ox}} \quad (2-E38)$$

where, R_{diff} is the resistance due to external diffusion and R_{kin} is the resistance due to chemical or kinetic reactions. The ratio of the kinetic and diffusion rate resistances is provided in equation (2-E39) for a one-film model [8]:

$$\frac{R_{kin}}{R_{diff}} = \left[\frac{v_I}{v_I + Y_{Ox,s}} \right] \left[\frac{R_u T_s}{P \times MW_{ox}} \right] \left[\frac{\rho_{ox} D}{k_c} \right] \left[\frac{1}{r} \right] \quad (2-E39)$$

The one-film ash segregated core model provides a convenient method to calculate the external kinetic parameters and it allows a straightforward determination

of the reduction regimes, i.e., whether the reaction is either purely kinetic controlled or purely diffusion controlled or a combination of both. However, it only accounts for external surface reactions as char conversion progresses under time dependent conditions.

2.4.4 Energy conservation models

The char surface temperature (T_s) is calculated iteratively by considering a blackbody particle (emissivity = 1), a steady-state process and a negligible heat conduction into the particle interior. Char surface temperatures are calculated based on + or – 1 % of the total energy released and absorbed both for the combustion and gasification conditions, respectively. Distributed energy loss during combustion is mainly due to radiation and the energy loss due to conduction is very small as discussed later in chapters 4 and 5 as well as appendix V. With this consideration, the energy flows at the particle surface and mass transfer effects on energy are coupled to allow a derivation of the governing equations both for disk and spherically shaped particles. The resulting equations incorporate the energies that are released from the surface to generate the heat of radiation. The gas phase thermal conductivities and specific heats of air, O_2 and CO_2 are varied based on the calculated surface temperatures. Varying Lennard-Jones parameters with changes in temperature as published in literatures are also used to calculate the bulk and effective diffusion coefficients of prevailing gases produced from these reactions [8, 45]. It is critical to point out here that gas phase reactions taking place at the particle boundary layer is neglected for mathematical expediency. Also, for large particles, most of the CO produced are combusted at the particle surface where actual combustion is assumed to

be taking place. Based on this simplification, equation (2-E40) is derived and can be used to calculate spherically shaped char surface temperatures as follows [8]:

$$\dot{m}_c \Delta h_c = \dot{m}_c c_{pg} \left[\frac{\exp\left(-\frac{\dot{m}_c c_{pg}}{4\pi k_g r}\right)}{1 - \exp\left(-\frac{\dot{m}_c c_{pg}}{4\pi k_g r}\right)} \right] (T_s - T_\infty) + \varepsilon_s 4\pi r^2 \sigma (T_s^4 - T_\infty^4) \quad (2-E40)$$

where, \dot{m} , Δh_c , c_{pg} , k_g , T_s , T_∞ , r , σ and ε_s are the char mass burning rates, heat of combustion, gas specific heat, gas thermal conductivity, particle surface temperature, reactor temperature, particle radius, Stefan-Boltzman constant and the surface emissivity, respectively. In equation (2-E40), all the thermodynamic values such as specific heats and thermal conductivities are evaluated based on time evolution of surface temperatures during conversion. The first and second terms of the right hand side of equation (2-E40) are the energy losses due to diffused gases and radiation into the surrounding or oxidizing medium, respectively.

For disk-shaped char particles, the first term on the right hand side of equation (2-E40) which provides the energy loss due to mass transfer of the diffused product gases during combustion is expressed in equation (2-E41) as:

$$\dot{Q}_{s-f} = H \rho c_p D (T_s - T_\infty) \quad (2-E41)$$

where:

H = Height of the stagnant layer from the surface to the freestream location

c_p = constant pressure specific heat of diffused gases

ρ = density of diffused gases

D = mass diffusivity of gases

\dot{Q}_{s-f} = energy loss due to diffused gases into the oxidizing medium

A derivation of equation (2-E41) is presented in Appendix II. For combustion conditions, these energy equations assume that the energy loss due to transport by convection is negligible and no energy is released due to chemical reaction in the gas phase under steady state conditions. This implies that the desorbed CO gas is instantaneously converted to CO₂ gas at the external surfaces being modeled. Therefore, with the addition of energy loss due to radiation, a simplified total energy equation model for disk-shaped particles is expressed in equation (2-E42) as:

$$\dot{m}_C \Delta h_C = H \times \rho C_p D (T_S - T_\infty) + \varepsilon_S \pi r^2 \sigma (T_S^4 - T_\infty^4) \quad (2-E42)$$

For the gasification of disk-shaped particles, the first term on the right hand side of equation (2-E42) is neglected because convection due to diffused gases is very small, leaving behind the radiation equation and convected energy from the surroundings. However, the temperature terms (T_s and T_∞) are switched because the reactor radiates to the char surface.

A derivation of the relevant energy equations is also presented for CO₂ gasification of spherical particles in Appendix IV. This equation is expressed as follows in equation (2-E43):

$$\dot{m}_C \Delta h_C = h \times 4\pi r^2 (T_\infty - T_S) + \varepsilon_S 4\pi r^2 \sigma (T_\infty^4 - T_S^4) \quad (2-E43)$$

where, \dot{m} , Δh_C , h , r , T_∞ , T_S , ε_S , and σ are the char mass gasification rates, heat of gasification reaction, convection heat transfer coefficient, particle radius, measured reactor temperature, particle surface temperature, emissivity and Stefan-Boltzman

constant, respectively. Equation (2-E43), provides a steady-state process and it is evaluated at each time step to estimate surface temperatures.

2.4 Tar Reduction Process

Tars are either condensable or non-condensable organic substances and tars that condense between 200 to 600 °C can generate coke when thermally processed [53]. Elliot [53] has categorized tars into three types, see Table 2-2.

Table 2-2. Categories of Tar [53]

Category	Formation Temperature	Constituents
Primary	400 to 600 °C	Mixed Oxygenates, Phenolic Ethers
Secondary	600 to 800 °C	Alkyl Phenolics, Heterocyclic Ethers
Tertiary	800 to 1000 °C	Polynucleic Aromatic Hydrocarbons

As shown in Table 2-2, at higher temperatures, primary tars are cracked to produce secondary and tertiary components. With good mixing and effective reduction processes, primary and tertiary products would not exist together. The formation of tertiary tars is the result of both lignin and cellulose in the feedstock, but lignin has shown to form heavier aromatics rapidly than those from cellulose [53].

In Table 2-3, Elliot [53] classified chemical product components of tars from different processes in each temperature regime based on gas chromatograph and mass spectrometer measurements. As indicated in Table 2-3, phenols (o-cresols) is one of the major components of pyrolysis and steam gasification processes between 600 and 800 °C. Phenols are aromatic organic compounds and these could be solid or liquid at room temperatures because their melting points (29.8 °C) are very close at these

conditions. Because of their existence especially at normal pyrolysis and gasification temperature conditions, the thermal destruction of o-cresol modeled as phenol is the focus of this work.

Table 2-3. Chemical Components of Gasifier Tars [53]

Conventional Flash Pyrolysis (450 – 500 °C)	High-Temperature Flash Pyrolysis (600 – 650 °C)	Steam Gasification (700 – 800 °C)	High-Temperature Steam Gasification (900 – 1000 °C)
Acids, Aldehydes, Ketones, Furans, Alcohols, Complex Oxygenates, Phenols, Guaiacols, Syringols, Complex Phenols	Benzenes, Phenols, Catechols, Naphthalenes, Biphenyls, Phenanthrenes, Benzofurans, Benzaldehydes	Naphthalenes, Acenaphthalenes, Fluorenes, Phenanthrenes, Benzaldehydes, Phenols, Naphthofurans, Benzanthracenes	Naphthalene*, Acenaphthylene, Phenanthrene, Fluoranthene, Pyrene, Acephenanthrylene, Benzanthracenes, Benzopyrenes, 226 MW PAHs, 276 MW PAHs
*At the highest severity, naphthalenes such as methyl naphthalene are stripped to simple naphthalene			

A syngas quality requirement for gas engines and turbines is provided by Hasler et al. [54] in Table 2-4. Presently, because most proven energy conversion devices use internal combustion engines and gas turbines, the goal is to reduce tar content in the syngas between 0 to 100 mg/m³ and not detectable levels for these systems, respectively. With regards to the tar concentrations, these are estimated based on the volume of syngas measured at 0 °C and 1 atm.

Table 2-4. Syngas Quality Requirements for Energy Generation [54]

Contaminants	Units	IC Engines	Gas Turbines
Particles	mg/m ³	< 50	< 30
Particle Size	µm	< 10	< 5
Tar	mg/m ³	< 100	n.d.*
Alkali Metals	mg/m ³	n.d.*	< 0.24
Notes: m ³ - cubic meters of gas measured at 0 °C and 1 atm n.d.* - Not detectable			

Tar formations are inherently dependent on the type of solid waste material, as

well as operating conditions of gasification processes. Tar is a mixture of organic components ranging from low molecular weight molecules (e.g., C_7H_8O , o-cresol) to heavy polycyclic aromatic hydrocarbons (PAHs, e.g., naphthalenes) [55]. Gasification reactor operating conditions, such as, the amount and types of gasifying agents, physical and chemical properties of feedstock, residence time, heating rates, temperatures, pressures, and geometry all play a key role in tar formation and reduction. Van Paasen and Kiel [55] have defined harmful tars are those that cannot be detected with a gas chromatograph (GC) or mass spectrometer (MS). Harmful tars can plug reforming catalysts, disable sulfur removal systems, corrode or damage off-gas systems, such as, heat recovery boilers, induced draft fans, pumps, compressors, heat exchangers, gas turbines and other off-gas downstream systems. Tars are considered cumbersome and challenging parameter for the successful commercialization of gasification systems [56]. Beside the known harmful effects of tars in energy conversion systems, the thermal efficiency of gasification systems could be reduced when residual tars are not effectively destructed thermally.

Tar cracking investigations have been undertaken extensively using air as an oxidizing agent [57, 58] in a batch mode. One example of this work is cracking pyrolysis tars [59]. With this system, Rath et al. [59] used a thermogravimetric analyzer (TGA) operated between 105 to 1050 °C to generate tars that were processed with a consecutive tubular reactor operating between 600 to 800 °C. The purpose of their research was to determine the kinetic parameters of tar cracking and distribution of the formed products by considering non-isothermal conditions and axial dispersion of product gas. This consideration was made because the tubular reactor inside

temperature is not constant in the axial direction and the kinetic constant dependence on temperature for the Arrhenius law is not linear. The results showed that different types of tar are produced and one of these tar types does not crack.

Chen [60] and Di Blasi [61] also performed one dimensional (1D) numerical tar reducing investigations. However, in most of their models, turbulence which is known to play a significant role in the tar partial oxidation was neglected because of the complexity of the system. In an attempt to perform a more comprehensive analysis of turbulent tar cracking system, Gerun et al. [62] used a 2D numerical model to investigate the effect of turbulence while coupling this with a tar cracking model. Their 2D numerical model also included thirteen (13) global tar cracking kinetic models while also incorporated heat transfer radiation and turbulent flow. However, swirl and air recirculation effects during injection were neglected in their numerical study to simplify their analysis. Heterogeneous reactions were also neglected based on an assumption that char particles fall fast in a fixed bed reactor with a residence time of less than 0.1 second in the oxidation zone where oxygen reacts with the tar. Based on their study, Gerun et al. [62] elucidated the fact that tertiary tars are destructible with combustion and also tar pyrolysis gas composition significantly influences thermal cracking rates. However, their thermal tar cracking kinetic data generated uncertainties in their models. Houben et al. [63] have demonstrated that using an internal pyrolysis recycle loop in a fixed bed gasifier for biomass could produce very low tar content modeled as naphthalene. As shown in Figure 2-7, their system uses an air ejector with several nozzles to induce in the syngas evolved from the gasifier so that gases are partially cracked with air, causing

an increase in temperature in the recycle loop. In their study, the effect of partial combustion of the fuel gas mixture on naphthalene (used as a tar model) was examined for different air fuel ratios for varying amounts of H₂ and CH₄ concentrations. For low air fuel ratios and higher hydrogen concentrations, they found that the tar was reduced very effectively, reaching conversions of up to about 90 %. From this result, it might be possible to enhance tar cracking using steam as an oxidizing agent. With this arrangement, H₂ production during cracking of heavy hydrocarbons or tar via the water-gas shift reaction, $\text{CO} + \text{H}_2\text{O} \rightleftharpoons \text{H}_2 + \text{CO}_2$ could be enhanced. Also, steam gasification of solid carbon materials has been characterized by the existence of very reactive conditions resulting to an increase in hydrogen gas production at temperatures as low as 630 °C [64]. These very reactive conditions have been assumed to be caused by localized exothermic reactions between (O₂) gas, solid carbon and H₂ (hydrogen), producing highly reactive radicals such as hydrogen atoms, oxygen atoms, hydroxide (OH) and hydroperoxyl (HO₂). For this reason, it may be possible to exploit these reactive reactions to enhance tar cracking and minimize the need of elaborate feedstock and gas conditioning requirements. Additionally, the intrinsic chemical kinetic parameters for the thermo-chemical cracking of tars with steam as a major oxidizing agent are still unknown especially for practical gasifiers operating under non-isothermal conditions.

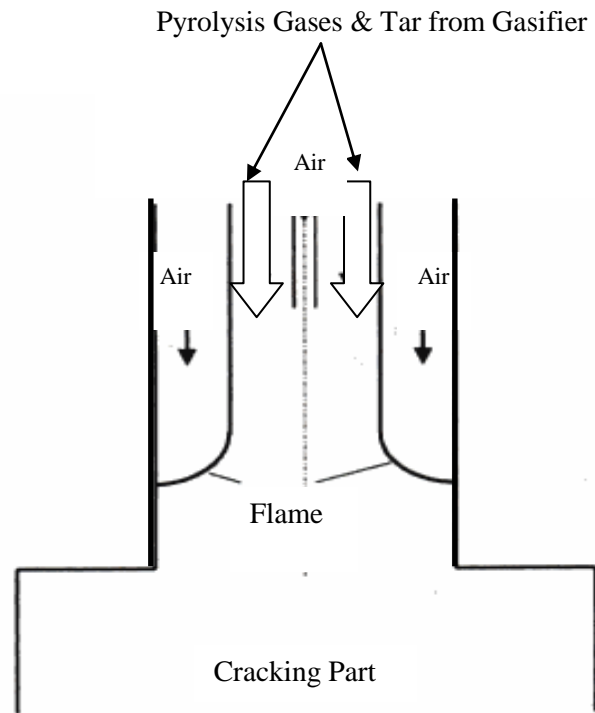


Figure 2-7. Air-ejector and tar cracking device [63]

Chapter 3: Experimental Setup and Conditions

This chapter describes the experimental setup and test conditions for the three char and tar materials being investigated. The three large particle shapes investigated here are disk-shaped carbon particles, near spherical oakwood and irregular-shaped coal char particles. For tar reduction experiments, o-cresol is used as a model for phenol tars.

3.1 Disk-shaped Large Particles

Commercial lamp black (also called oil black; Fisher, CAS 1333-86-4, catalog no. C198-500) particles are arranged to form large disk-shaped particles with thicknesses between 1.52 mm to 5.5 mm. This carbon black material is manufactured from oil with extreme heat without using any solvent. This material is chosen because of its relatively well defined characteristics with less than 0.1% tar content with total polycyclic aromatic hydrocarbons (PAHs) concentration of about 700 ppm. Properties of Fisher lamp or carbon black are given in Table 3-1 [65]:

Table 3-1. Physical properties of commercial carbon black

BET Surface Area (m ² /g)	Total Pore Volume (ml/g)	Percentage of Mesopores by Weight (2 nm < pore dia. 50 nm)	Percentage of Macropores by Weight (pore dia. > 50 nm)	Percentage of Micropores by Weight (pore dia. < 2 nm)	Particle Size per SEM	Density g/cm ³
29.8	0.047	77.6	22.1	1.3	~ 6 μ m	1.3 to 1.7

The specific density is between 1.3 to 1.7 g/cm³ and BET particle surface areas (measured by N₂ adsorption) vary between 1.3 to 4.9 m²/g [66]. However, the specific surface areas could be less when these are put together due to Van Der Waal molecular forces. A single group of carbon particles as used in the experiments has a

bulk density of about 0.335 g/cm³. This represents an 82.8 % porosity based on the density of pure carbon at 1950 g/cm³ [36]. Figure 3-1 shows that these particles tend to approximate a spherical shape. Carbon black structure is compact so that the pores are too small for reactant gases to penetrate at atmospheric conditions. However, if these were arranged in thin disk -shaped configurations, the regime of reduction or conversion rates can be kinetic controlled with diffusion rates being extremely fast. For thicker shapes, it could be under kinetic-diffusion controlled.

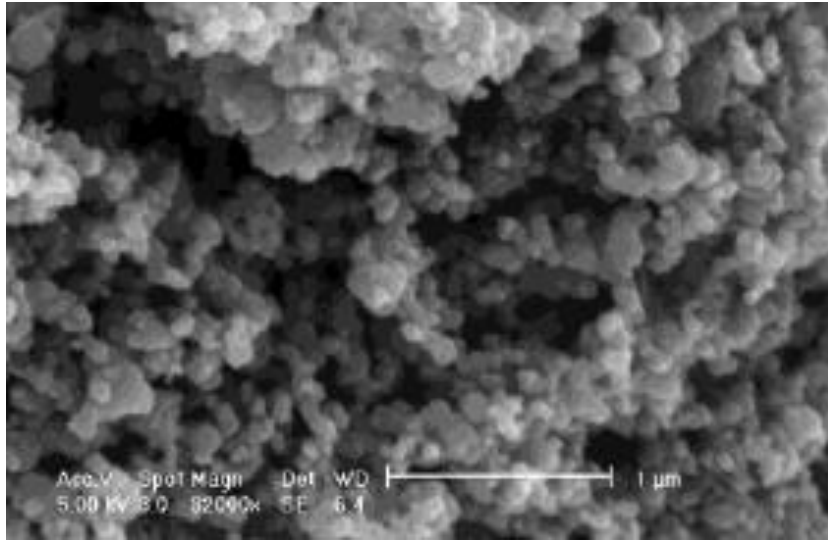


Figure 3-1. SEM images of fisher lampblack [66]

Figure 3-2A depicts a typical single 0.06 micrometer diameter particle resting on a surface. Particles in this configuration experience a lifting force perpendicular to direction flow of oxidants and as shown. This lifting force can be calculated with equation (3-E1) assuming that the particles are nearly spherical in shape [67]:

$$F_L = \frac{0.58\rho_g u^4 (d_p)^4}{v^2} \quad (3-E1)$$

where F_L , ρ_g , u , d_p and ν are the lifting force, oxidant density, oxidant velocity, particle diameter and oxidant kinematic viscosity, respectively. The Reynolds number of a single particle is 5.83E-05 and for a very low Re, the drag force for a spherical particle is estimated with the following equation [68]:

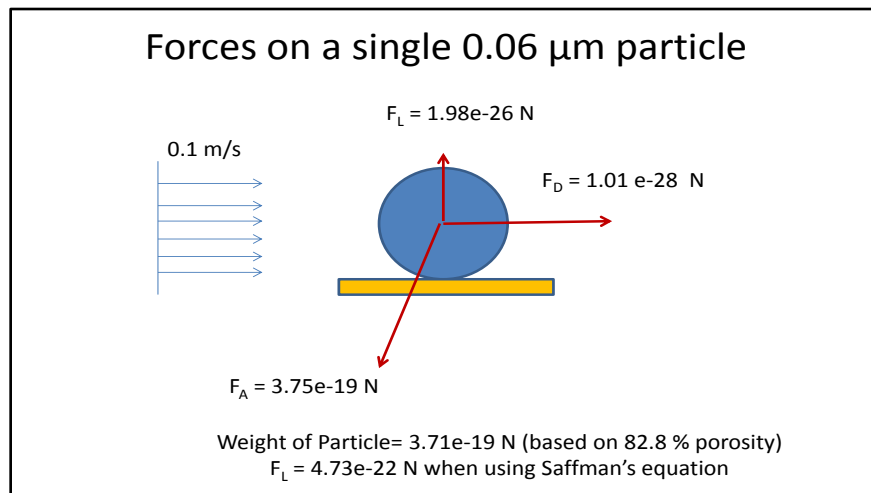
$$F_D = 8 \frac{(\rho d_p u)^2}{\rho \left\{ 1 + K_n \left[1.257 + 0.4 \exp \left(\frac{-1.1}{K_n} \right) \right] \right\}} \quad (3-E2)$$

where F_D , u , d_p , ρ and K_n are the drag force, oxidant velocity, particle diameter, density and Knudsen number, respectively. The required anchoring force is estimated with the following equation for a coefficient of friction of 0.14 between carbon and steel surfaces [68]:

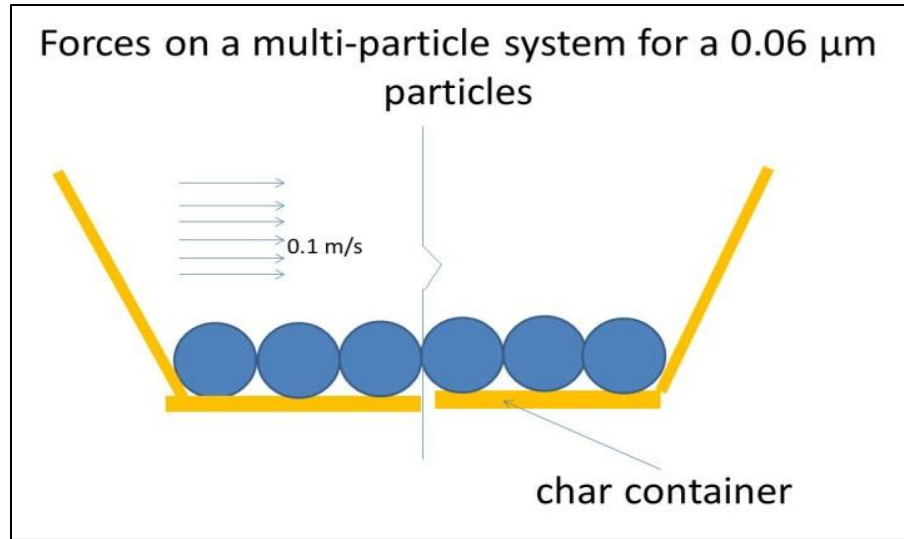
$$F_A = \sqrt{W_p^2 + [0.14(W_p - F_L)]^2} \quad (3-E2)$$

where F_A , F_D and W_p are the anchoring, drag and particle weight forces, respectively. The normal force is the difference between the particle weight and the lifting force, F_L . When these equations are evaluated based on particle diameter of 0.06 μm , these provide lifting and drag forces equal to 1.98×10^{-26} (Saffman's equation provides $F_L = 4.73 \times 10^{-22}$ N when particle is in suspension) and 1.01×10^{-28} newton, respectively (see Figure 3-2A). Because the particle weight at 3.71×10^{-19} newton (based on 82.8 % porosity) is greater than the lifting force, it is expected that the particle cannot be lifted up. The drag force at 1.01×10^{-28} newton is also lower than the maximum possible anchoring force (F_A) at 3.75×10^{-19} newton for the single particle, which implies that the particle cannot roll out or get entrained in the oxidant gas stream.

Nonetheless, for a multi-particle system as shown in Figure 3-2B, the resulting drag and lifting forces are also further firmly constrained at the contact points between the particles via Van der Waal electrostatic forces and the container surfaces at the extreme locations. The experiments also indicate that the changes in char weight after conversion during any of the experiments did not indicate any substantial loss in weight even when oxidant flow is maintained for a long period of time as shown in Figure 4-1 in section 4. Based on the numerical analyses presented above as also verified with experimental results, it is very likely that nearly no particles can escape the char particle container during reduction experiments.



(A)



(B)

Figure 3-2. (A) Forces on a single particle char and (B) Forces acting on multiple particles

To maintain equilibrium on the particle, the resultant forces required are $1.98\text{e-}26$ N and $4.73\text{e-}22$ N when using 3-E1 and Saffman's equations, respectively. However, the calculated anchoring force ($3.75\text{e-}19$ N) is much greater than these forces. Therefore, most of the weight losses measured in the experiments is mostly attributed to the conversion of char either to CO or CO₂. A photo of a leftover ash after an experiment for the reduction of 1 g sample is provided in Figure 3-3. As shown, most of the ash particles remain inside the container and these are not entrained.



Figure 3-3. Typical char conversion in thin disk-shaped chars

Figure 3-4 shows the experimental char reduction system that is used to perform experiments using oxygen (O_2), steam, air and combination of these as oxidizing agents. Hot vitiated air is used to preheat the reactor section at desired injection temperatures. The reactor is operated slightly above atmospheric pressure (i.e. 0.5 to 1 psig) to reduce air infiltration into the system. The 0.2 gram samples are lowered into the reaction zone when the temperature reaches $100\text{ }^{\circ}\text{C}$ to ensure that the experiments are started at dry state conditions. The hot gas stream produced from the combustion of propane (C_3H_8) is used to preheat and provide the gasifying agents of the reactor until temperatures reach 504 , 584 and $644\text{ }^{\circ}\text{C}$ when O_2 is injected into the reactor. All sample char particles are contained in stainless steel pan as shown with one-half of the char particle surface area receiving direct interaction with the surrounding oxidant via diffusion through the stagnant layer. These injection temperatures are within the starting point of previous combustion and gasification experiments [30, 69, 70]. The sample char particles are very fine and evenly spread out inside the reaction container to form a nearly uniform very thin layer of about 1.52 mm to accelerate diffusion rates at the surface. The applied heating rates during

the pre-heating stage of char oxidation experiments are nearly identical for all three (3) test cases to ensure that the calculated kinetic parameters can be meaningfully compared under various reactor injection temperatures. The pre-heating stage is between room temperature and the predetermined injection temperatures for the three temperature cases examined here. Equilibrium calculations for the stoichiometric combustion of propane indicate that the gases used to heat up the reactor zone contain 0.9 % argon, 0.1 % CO, 8.4 % CO₂, 11.3 % H₂O, 5.4 % O₂ and 73.4 % N₂ by moles. GC analysis also indicates that these equilibrium values are about the same. The preheating rates for all the experiments are maintained between 118 and 120 °C/min by using the same amount of combusted propane and air in all the experiments.

The experiments are performed under identical conditions except for the injection temperatures, which are pre-selected from several previous tests, enabling complete conversion of sample particles for each test. This allowed the measurement of the lowest possible temperatures required to completely consume the samples using pure oxygen as an oxidant. Low or moderate temperature conditions are especially considered advantageous to ensure that the least amount of energy is expended for 100 % conversion of char. Two sample sizes (i.e., 0.2 g and 0.9 g) are performed separately. The 0.2 g sample has the following conditions using 4 m³/h (cmph) of O₂ at 1 atm:

1. Injection temperatures: 504, 584 and 644 °C
2. Average particle thickness: 1.52 mm

The test conditions for ~ 0.9 g sample are shown in Table 3-2 for sample thicknesses varying between 5 to 6 mm.

Table 3-2. Carbon particles with steam and its combination with air and O₂

Weight (g)	Average Steam Flow (g/s)	Air Flow (m ³ /h)	O ₂ Flow (m ³ /h)	Average Temperature (°C)
0.9	0.1			775
0.9	0.1	2		775
0.9	0.1		2	775

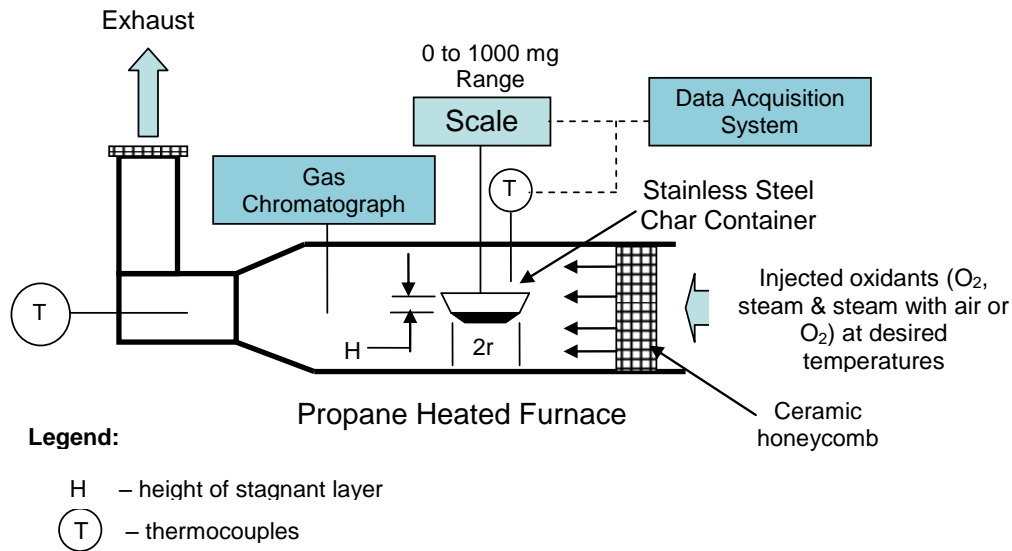
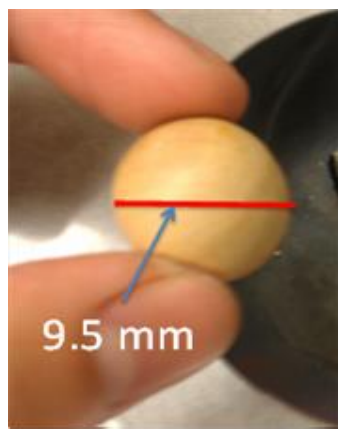


Figure 3-4. Experimental schematic diagram

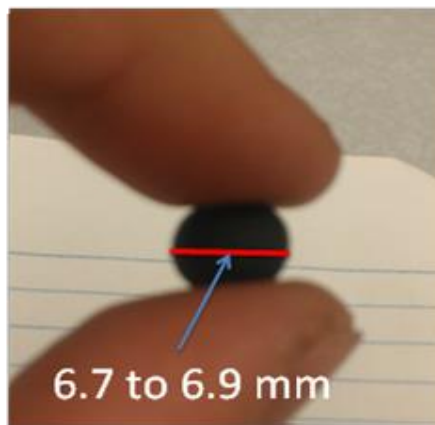
3.2 Spherical Wood Char Particles

A number of fresh and identical spherical oakwood particles (see Figure 3-5A) are pyrolyzed and the resulting particles shown in Figure 3-5B are used as samples for reduction experiments. The resulting porosity is about 82 % based on pure carbon density of 1950 kg/m³ [36]. The total amount of ash as measured in this study is about 5.2 % based on a 0.48 gram of fresh oakwood char, which is very close to those published in literature [39]. Published ultimate analysis of oakwood particles

consists of 6.2 % H₂, 50.2 % C, 43.5 % O₂ and 0.1% N₂ [40]. The spherical oakwood char particles are prepared using an electric furnace operated isothermally at 230 °C for 24 hours under atmospheric conditions. Char sample preparations and degrees of pyrolysis conditions are all identical. Therefore, the sample particles and their inherent porous structure should be nearly consistent for this study. These char particles are depicted in Figure 3-5B [39] for an average weight of 0.078 g sample. Figure 3-6 provides the char porous structure of oakwood chars that were investigated by Pastor-Villegas et al. with the use of scanning electron microscope (SEM). The pore diameters were variable between 10 to 20 micrometers [39]. However, majority of the pore diameters were nearly about 10 micrometers, which is much larger than 50 nm [39] and hence, these char particles have macroporous structure.



(A)



(B)

Figure 3-5. (A) Raw spherical oakwood and (B) 0.076 g spherical oakwood char

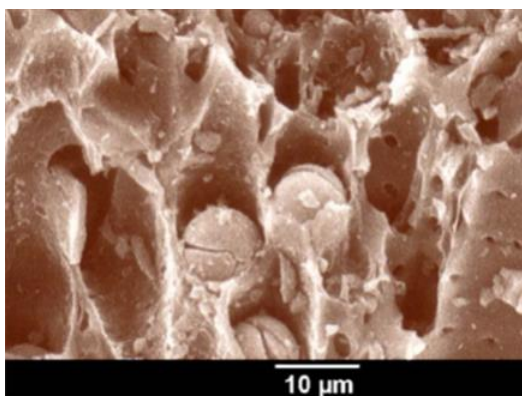


Figure 3-6. SEM micrographs of oakwood char particles

The experimental system is shown in Figure 3-7, which consists of a precision weighing scale, a propane fired reactor, lenses to perform imaging, a light source and a high speed camera. The reactor is operated slightly above atmospheric pressure to reduce air infiltration into the system. The weighing scale shown is mounted on a nearly rigid aluminum structure. This structure is mounted on a resilient table to mitigate and absorb external effects of weight disturbances around the vicinity of experimental facility. Data acquisition computer is used to obtain all the relevant experimental data such as reactor temperatures near particle surface and weight measurements. The diameters of the spherical shaped particles are monitored and measured using imaging software with the use of a high speed camera.

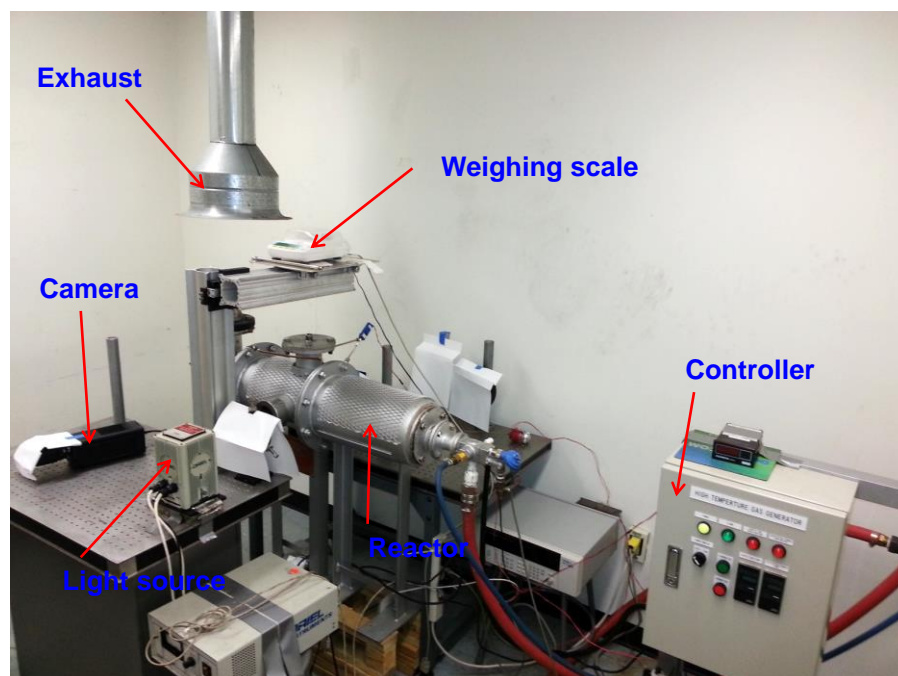


Figure 3-7. Experimental system

The experiment is performed by first measuring and recording the initial weight and diameter of particles. The particles are then tethered to a stainless steel wire connected to the weighing scale. After centering these samples inside the reactor, these are removed to allow the preheating of the reactor under specified conditions and to prevent any premature reactions. A temperature logger is used to record temperatures every 5 seconds. When the reactor reaches the required oxidant injection temperature, the desired amount of oxidant (O_2 or air or their combinations) in terms of m^3/h (cmph) is introduced into the reactor for the specified flow rates as measured under room temperature conditions (see Table 3-3). When the required oxidizing agent flow rate is established, the test particle is lowered into the reactor as quickly as possible. When the reaction reaches 40 seconds, testing is halted. Table 3-3 details the test matrix for spherically shaped char particles used in this study. The

weights given are the initial weights of single particles. The Reynolds numbers are calculated based on bulk gas temperatures used in these experiments.

Table 3-3. Test matrix used for wood char particles

Test No.	Weight (g)	Temp (°C)	Diameter (mm)	Air Flow (m ³ /h)	O ₂ flow (m ³ /h)	Re
1	0.075	800	6.7	6		51
2	0.075	850	6.7	6		50
3	0.076	800	6.8	6	2	38
4	0.078	850	6.8	6	2	37

3.3 Irregular Shaped Coal Char Particles

Irregular shaped coal char particles are used in this experimental study. The porosity of these particles is estimated to be around 14.3 % based on 1950 kg/m³ [36]. Table 3-4 provides the as received proximate and ultimate analyses of coal char particles, which have 11.48 % ash and 3.81 % volatile matter. The char container system used for irregular shaped coal char particles is shown in Figure 3-8. This contains the irregular particles ranging from 2 to 9 pieces with average weight of 0.079 g as shown in Figure 3-9. A minimum of 2 particles are used to get an equivalent single particle diameter of 4 mm. The mesh screen that contains the particles are suspended from the weighing scale, allowing continuous weight and temperature measurements during the experiment with respect to time. The mesh screen is designed to keep the reacted pieces together during experiments. The experiments are halted when the weights reached a constant value, which indicates that no additional reduction is taking place.

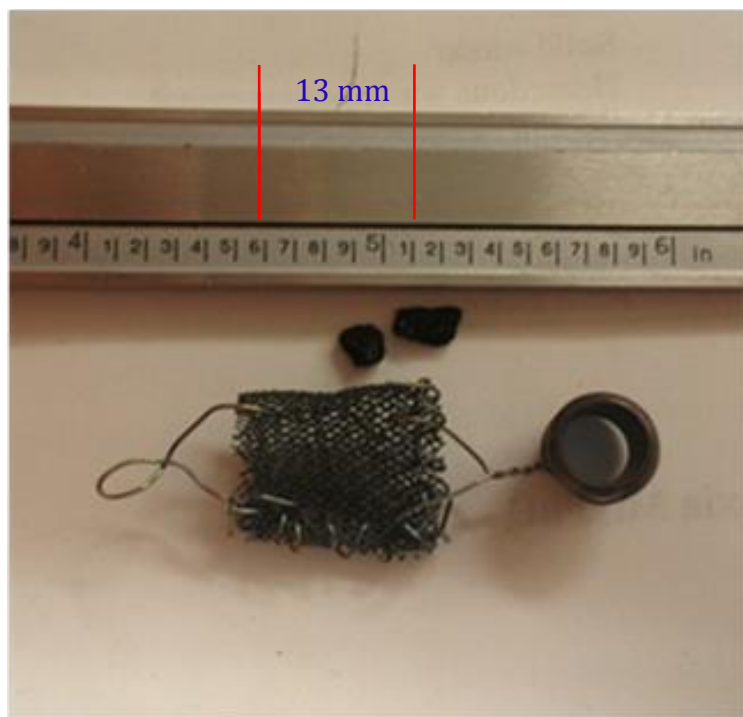


Figure 3-8. Particle mesh screen container

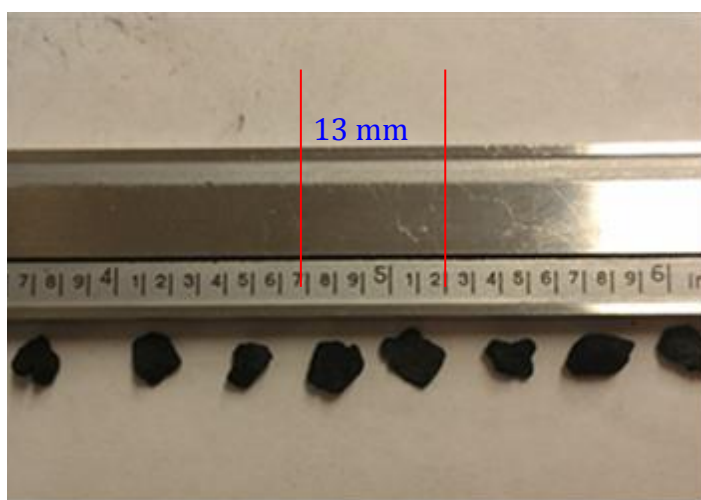


Figure 3-9. Irregular shaped char samples

The experimental system is identical to the setup used for spherical char particles (see Figure 3-7). The experiments are started by first measuring and recording the initial weight of char particles to be thermally oxidized. Subsequently,

the irregular shaped char particles are placed in a mesh screen container, which is attached to a stainless steel wire as shown in Figure 3-8. After centering these samples inside the reactor, the samples are removed to preheat the test section. The reactor is operated slightly above atmospheric pressure to reduce air infiltration into the system. Data logger is used to record temperatures and weights every 5 seconds. When the reactor reaches the required temperature, the desired oxidant (CO₂ or air) is injected into the reactor between 3 to 8 m³/h. When the oxidizing agent flow rate is established, the sample char particle is lowered into the reactor as quickly as possible. Upon inserting the samples into the reactor, the particle container weight is measured continuously with the weighing scale. When the weight measurements reached a steady condition, this indicates that the char has reached the greatest conversion possible and the experiment is halted. The test matrix for the irregular shaped char particles is shown in Table 3-5. The weight given is the initial total weight of the samples based on the total number of particles examined. The estimated Reynolds number provided for each test number below is based on the equivalent diameters of the multi-particle systems. Reynolds numbers shown in Table 3-5 are calculated based on the bulk gas temperatures as used in the experiments.

Table 3-4. Proximate and ultimate analysis of coal chars particles

Proximate Analysis	
Ash	11.48
Volatile	3.81
C fix	84.71
Sum	100.00
Ultimate Analysis	
Ash	11.477
C	87.710
H	0.402
N	0.332
S Comb.	0.075
O	0.004
Sum	100.000

Table 3-5. Experimental test matrix used in the investigation for coal char particles

Test No.	No. of Pieces	Temp (°C)	Total Weight (g)	Equivalent Diameter (mm)	Void Fraction	Oxidant Density (kg/m ³)	Re	Air Flow (m ³ /hr)	CO ₂ Flow (m ³ /hr)
1	2	900	0.052	4.14	0.37	0.30	40	8	
2	2	900	0.05	4.09	0.37	0.46	24		3
3	3	900	0.052	4.14	0.37	0.30	22	4.5	
4	2	900	0.055	4.22	0.37	0.46	49		6
5	3	930	0.06	4.34	0.37	0.45	25		3
6	3	800	0.05	4.09	0.37	0.50	25		3
7	9	800	0.167	6.11	0.37	0.50	38		3
8	9	900	0.172	6.17	0.37	0.46	36		3
9	5	900	0.112	5.35	0.37	0.46	31		3
10	2	850	0.05	4.09	0.37	0.48	24		3
11	2	1000	0.048	4.03	0.37	0.42	22		3

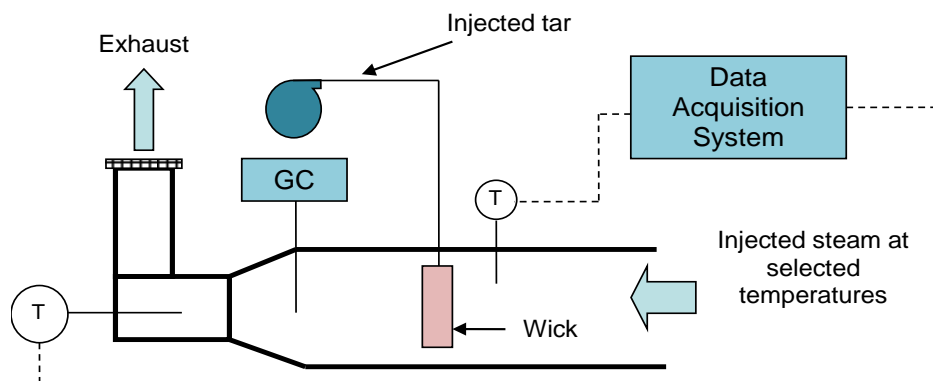
3.4 Tar Reduction

O-cresol black (Fisher Scientific, CAS 95-48-7) is used as a model material for phenol-based tar. Physical and chemical properties are given in Table 3-6 (O-cresol MSDS from Fisher Scientific):

Table 3-6. Physical and Chemical Properties of Examined O-cresol

Boiling Point at 1 atm (°C)	Molecular Formula	Density (g/cm ³)	Viscosity at 35 °C (cP)	Molecular Weight	Autoignition Temperature (°C)	Flash Point (°C)
191	C ₇ H ₈ O	1.04	4.75	108.14	555	81

Experimental tar reduction setup shown in Figure 3-10 is used to perform experiments using steam with vitiated air to maintain desired temperatures. It is anticipated that this experimental work will provide a baseline experimental data in understanding non-catalytic tar cracking kinetics using steam as an oxidizing agent for a non-swirling continuously fed bench-scale reactor that is operated non-isothermally. The hot gas stream produced from the combustion of propane (C₃H₈) with air is used to preheat the test section of the reactor to the desired temperatures. At desired temperatures between 800 to 900 °C, o-cresol tars are injected between 4 and 8 cc/min, simulating initial updraft fixed-bed tar concentrations between 20000 to 40000 mg/m³ at standard conditions. These concentrations represent 1.7 and 0.87 steam-to-mass ratios for 20,000 and 40,000 mg/m³, respectively. Reactor temperatures are within the suggested starting point of steam gasification [69]. The experiments are performed in the temperature range between 800 to 900 °C.



Legend:

Propane Heated Furnace




-  – Thermocouples
-  – Gas Chromatograph
-  – Injection Pump

Figure 3-10. Bench Scale Experimental Setup used for Tar Reduction

Chapter 4: Results and Discussion

This chapter discusses the experimental and modeling analyses results for the gasification and combustion of the three major large char particles and tar.

4.1 Reduction of Disk-shaped Carbon Particles with O₂

The objective of this investigation is to determine the effects of O₂ flow rate at 4 m³/h (cpmh) for the combustion of nearly identical sample weights (0.2 g) of carbon black particles for the following:

1. Conversion time with three injection temperatures
2. Estimated char surface temperatures via modeling
3. Air and partial CO₂ gasification modeling of the preheating stages prior to O₂ injection
4. Char surface and reactor temperatures as the basis of calculating the kinetic parameters

4.1.1 Effect of different injection temperatures on conversion

Figure 4-1 provides the results obtained on the complete combustion of 0.2 gram sample, using pure oxygen at a constant flow rate of 4m³/hr and injection temperatures at 504 °C, 584 °C and 644 °C.

All these three (3) cases reached 100 % with the subsequent release of energy resulting from exothermic reactions. It took a total of 640, 140, and 113 seconds to reach 100 % conversion with O₂ injections at 504, 584, and 644 °C, respectively. A long induction period (560 sec) is noticeable for the lowest injection temperature at 504 °C. As discussed earlier in section 2.1.1, the induction period is associated with

the non-accelerated reduction condition from the time of injection up to the start time of accelerated reduction. The other higher injection temperatures exhibited no induction period, because the adsorption of O_2 gas within the particles happened almost instantly when O_2 is injected. This indicates that reactions for injection temperatures at 584 and 644 °C occur quickly as indicated by the estimated surface temperatures at 1600 and 1800 K, respectively as O_2 is injected. Based on the lowest injection temperature at 504 °C, the lowest reactor temperature at which accelerated reduction starts to occur is at 584 °C. All accelerated reductions occur as a pure reaction regime based on the one-film ASCM equation.

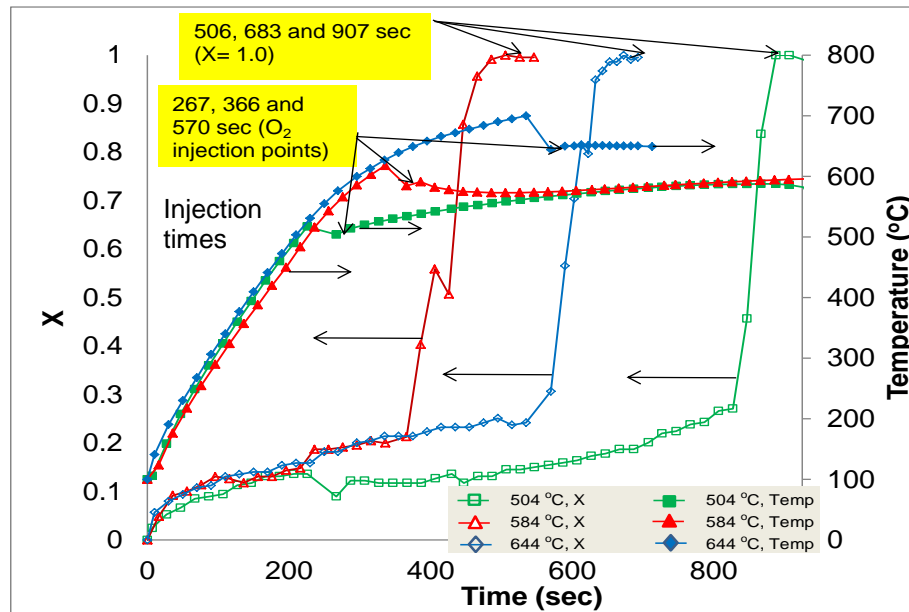


Figure 4-1. Char conversion of 0.2 g sample with 4 cmph O_2

When the reactor furnace is turned off to inject pure oxygen, the furnace temperatures drop for some period of time and then rises again due to exothermic reactions for all cases until most of the char particles are consumed. Interestingly, the reactor temperature operates nearly isothermally at the beginning of the accelerated

conversion at 644 °C. This condition continues up to the time that the particles are fully combusted. This also implies that the heat release during char combustion is about equal to the heat loss by the furnace to its surroundings plus the heat loss due to convection of gas products and heat to the exhaust system. However, for the injection temperatures at 584 °C, reactor temperatures drop some time (i.e., 60 sec) when the furnace is turned off and the reactor temperatures rise again after this period. All char reductions are exothermic reactions, either due to $C + 1/2O_2 \rightarrow CO$ or $C + O_2 \rightarrow CO_2$ reaction. These reactions are observed by the slight increase in conversion for the $T=504$ °C from 10 % at the beginning of injection up to 27 %.

4.1.2 Effect of injection temperatures on char surface temperatures

Figures 4-2, 4-3 and 4-4 provide char surface temperature profiles (via energy equation described earlier in section 2.4.4 for thin disk-shaped particles) for each case as a function of reaction time. The char surface (T_s) and reactor (T_{inf}) temperatures are plotted with time. Reactor temperatures are measured with a thermocouple downstream of sample location. Based on energy calculations, the energies being released during accelerated reactions are more likely due to $C + O_2 \rightarrow CO_2$ reactions. This is established with the fact that the $C + O_2 \rightarrow CO_2$ reactions provide a better fit as compared to the $C + 1/2 O_2 \rightarrow CO$ reactions for all modeling cases. The estimated maximum char surface temperatures during the accelerated periods are 2333 K ($t=80$ sec) and 1802 K ($t=0$ sec) for injection temperatures at 584 and 644 °C, respectively.

At the lowest injection temperature of 504 °C, the estimated char surface temperature is 2235 K at 600 sec at the end of the accelerated reduction period. This period corresponds to reactor temperature at 587 °C, which is very close to the other

case with injection temperature at 584 °C. This implies that the lowest operating reactor temperature condition for $C + O_2 \rightarrow CO_2$ will occur for reactor temperatures as low as 584 °C.

For injection temperatures at 584 and 644 °C, surface temperatures are significantly higher than reactor temperatures when char conversion begins to accelerate. However, at 504 °C, this condition occurs only when some reduction has taken place. Nonetheless, the highest char surface temperature during accelerated reduction is provided by the lowest injection temperature at 504 °C. This condition is probably due to the effect of the induction period wherein O_2 is fully adsorbed before onset of reaction. It is possible that an induction period existed for higher temperature cases; however, these could be apparent because their durations are very short. Another potential reason that may cause high surface temperatures at the lowest injection temperature ($T=504$ °C) is the large amount of ash formed, which acts as a catalyst during accelerated reduction period. Interestingly, the char surface temperature with the highest injection temperature case at 644 °C begins with maximum char surface temperature at 1802 K and then decreases with conversion. The char surface temperature for the second case at 584 °C increases from a minimum of 1600 K, reaching a maximum value of 2333 K. For the 504 °C case, char surface temperature gradually increases and then rapidly rises when the reactor temperature reaches 587 °C. The highest peak temperature for this case is 2235 K, which also matches greatest char conversion rate ($4.1E-03$ g/sec) when compared to the other injection temperatures at 584 ($6E-03$ g/sec) and 644 °C ($3.5E-03$ g/sec). The estimated maximum temperatures are lower between 100 to 400 °C as compared to

measured temperatures for the combustion of coal char particles under enriched oxygen environments. Specifically, these are between 2300 and 2400 K for very small coal particles between 106 to 125 μm [17]. This is expected because the coals chars that are used by Murphy et al. [17] have high volatile matter between 34 to 37 % as compared to only about 0.1 % (tar content) for the carbon black particles as used in these experiments.

The trend for the weight losses are also shown in these figures. For the injection temperatures at 644 and 584 $^{\circ}\text{C}$, weights decrease immediately and rapidly at the beginning at $3.5\text{E-}03$ and $2.6\text{E-}03$ g/sec, respectively. The rates of weight loss decrease with increasing reaction time for all cases. However, for the temperature injection at 504 $^{\circ}\text{C}$, the highest weight loss rate occurs only towards the end of conversion at $4.1\text{E-}03$ g/sec (see Figure 4-4).

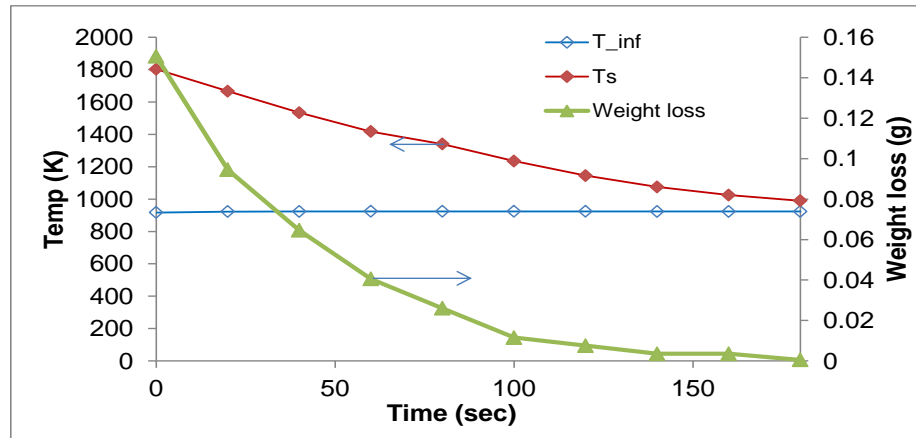


Figure 4-2. Char surface temperature profile for injection temperature at 644 $^{\circ}\text{C}$

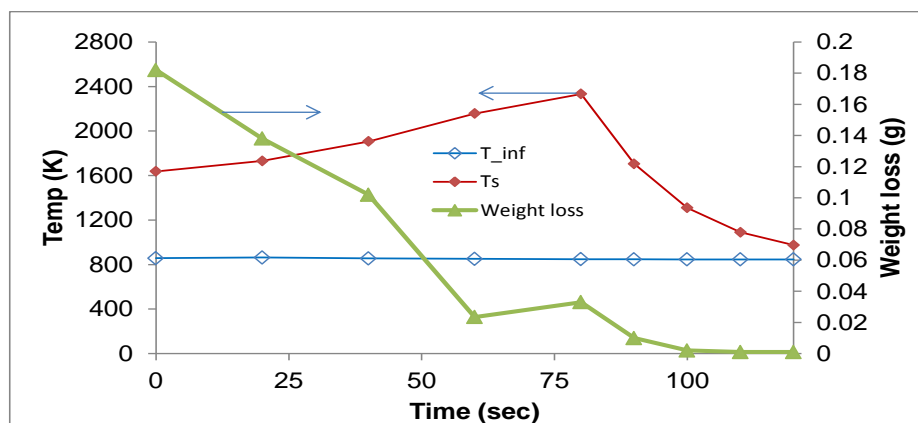


Figure 4-3. Char surface temperature profile for injection temperature at 584 °C

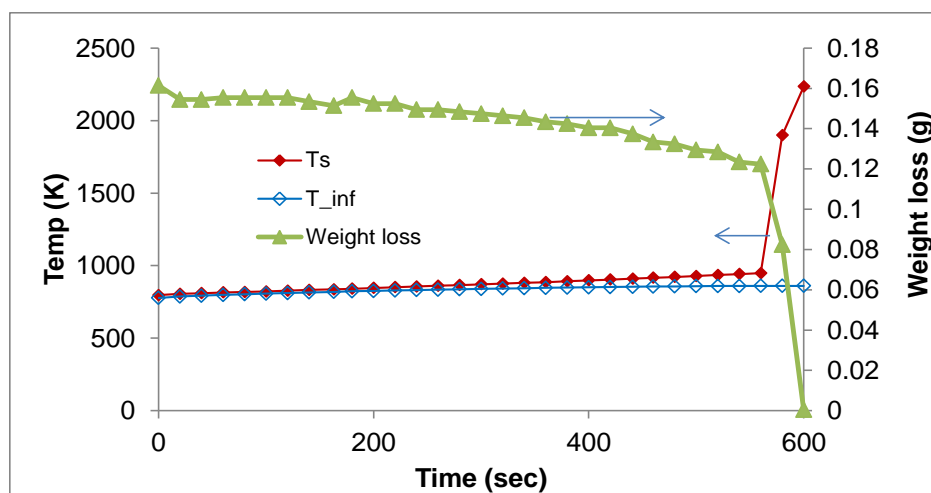


Figure 4-4. Char surface temperature profile for injection temperature at 504 °C

From a pragmatic perspective, lowest injection temperature at 504 °C requires least amount of input energy to eliminate the same amount of char. However, the least amount of oxygen used for these cases is provided by the injection temperature at 584 °C. Pre-heating the reactor with vitiated air serves as a good practice to reduce input energy before injecting costly oxidants into the reactor.

4.1.3 Effect of air and partial CO₂ gasification models during preheating

Two approaches are used to model and analyze char reduction data during the initial preheating stages before O₂ injection is performed with these cases. These two preheating models are air gasification and CO₂ gasification which are used to determine the following:

1. Compare the accuracy of these two models when reduction data are fitted into the model equation
2. Existence of apparent kinetic parameters
3. Determine and compare predicted regimes for these two approaches

In the first approach, the process is modeled using pure air as gasifying agent. Stoichiometric coefficient values at 1.33 and 2.66 are first used in the ASCM equation to verify which of these two values better fit the experimental values. Based on this numerical test, it is determined that a stoichiometric coefficient (ν_I or ν) value of 1.33 fits experimental data better as compared to ν equals 2.66. This suggests that char reductions at preheating stages are mainly caused by air gasification. This model is first applied to determine the relative effects of external chemical reactions and diffusion. However, via the reduction model, it is determined that no external chemical reactions exist and reduction is purely operating under diffusion controlled.

Because the model for char reduction behavior during the preheating period is not a robust fit in the first modeling case, a second model test is also investigated by using partial CO₂ gasification. This model couples the diffusion and kinetic effects during preheating stages up to the time when O₂ is injected at predetermined injection temperatures of interest. This model assumes that both diffusion and kinetic effects

are important during preheating stages. Because CO_2 component has the largest mass fraction ($\sim 16\%$ based on equilibrium calculations) for vitiated air, the preheating stage is modeled as a partial CO_2 gasification condition. This is accomplished by treating the mass fractions of H_2O ($\sim 9\%$ based on equilibrium calculations) and O_2 ($\sim 2.6\%$ based on equilibrium calculations) as CO_2 to account for gasifying effects of H_2O and O_2 . Although this is not the actual case, this model reduces mathematical complexity associated with multi-component diffusion coefficients and reactions.

Figures 4-5, 4-7 and 4-8 provide a plot of air gasification model (First Modeling Case labeled in the plots as “diffusion controlled”) for these three (3) temperatures cases. Subsequently, Figures 4-9, 4-10 and 4-11 provide the effect of partial CO_2 gasification model (Second Modeling Case, labeled in the plots as “simulated CO_2 gasification”) for the three (3) temperatures cases examined. These results clearly reveal that simulated partial CO_2 gasification model provides a better fit as compared to air gasification for preheating stages using vitiated air. An evaluation of the standard deviations on reduction data for these two models is provided in appendix VI. The calculated KPs for these two models are presented subsequently in section 4.1.4.

4.1.4 Effect of temperatures in calculating the kinetic parameters

During O_2 injection or combustion period, two modeling approaches are also used in modeling char reduction via the one-film ASCM. One approach is the use of reactor temperatures to calculate KPs. The other approach is to use estimated surface temperatures to estimate KPs. The objective of this analysis is to determine the following:

1. Calculate intrinsic kinetic parameters and characterize the regimes for all cases
2. Effects of using discrete time linear and non-linear fits to Arrhenius equation to calculation of KPs

The second portion of the reduction process ($C + O_2 \rightarrow CO_2$) is modeled to be purely a kinetic-controlled process because this provides a good fit with experimental data (see Figures 4-5, 4-6 and 4-7). For the lowest temperature case at 504 °C, non-accelerated region (from $t = 267$ to $t = 827$ sec, of Figure 4-7) is also modeled as pure kinetic control (no diffusion effects) because the ASCM fits well the experimental data. To determine the regime of reduction, the mass fraction of oxygen ($Y_{O_2,s}$) at char surface is assigned as 100 % at the beginning of the injection period and the diffusional effects (see equation 2-E25) are tested by either removing it or not from the ASCM equation per equation (2-E24). This approach is performed to check which fits better under the different reduction temperatures. When the diffusional effects are removed, the model fits the experimental data, implying a pure kinetic controlled condition when pure O_2 is injected. During this condition, a stoichiometric coefficient with a value equal to 2.66 also is determined to provide a better fit for all test cases as compared to 1.33. This suggests that second portion of the reduction periods are all dominated by $C + O_2 \rightarrow CO_2$ reactions. This condition is determined to be a major reaction pathway during the non-accelerated, accelerated and decelerated reduction conditions for all combustion cases. There are no decelerated conditions for lowest injection temperature at 504 °C (see Figure 4-11). Nonetheless, this confirms the claims of some authors that large particles tend to be dominated more by $C + O_2 \rightarrow$

CO_2 versus $\text{C} + \frac{1}{2} \text{O}_2 \rightarrow \text{CO}$, which occur very close to external surface of spherical particles [11]. When oxygen is injected, it is assumed that vitiated air is quickly purged out with pure oxygen and numerical analysis shows that a pure kinetic-controlled regime takes place at the char surface. Mathematically, this is applied by assigning oxygen mass fraction at the char surface as unity, and the diffusion term contribution in equation (2-E25) is treated as zero because this is occurring infinitely fast. Because char surface temperatures are not known, observed reactor temperatures are used as the basis in calculating the KPs. After O_2 injections, the surface oxygen mass fractions are modeled as unity or 100 %.

To further explore an alternative model for the first modeling case described earlier, a second case but more rigorous approach is also considered. This second modeling case explores both the effects of diffusion and kinetics for the entire char reduction, starting at preheating stages with vitiated air up to the time of pure O_2 injections. This procedure is also expected to provide unique values of activation energies and frequency factors when using a discrete linear fit approach to calculate Arrhenius equation at the preheating stages, non-accelerated regions, accelerated regions and decelerated regions.

4.1.4.1 DNLFF modeling results using T_∞ and ASCM

For discrete nonlinear fit (DNLFF), calculated activation energy for the accelerated region is 126 kJ/mol with a trial frequency factor of $1.0\text{E}+06$ m/sec at 644 °C. This trial frequency factor is also applied to all other cases. Ultimately, the values of frequency factors will be refined using discrete linear fit method on the Arrhenius equation. Under the decelerated regions, nonlinear fit is used to calculate activation

energies and these are found to vary between 138 and 140 kJ/mol, which is an indication of a decreased reactive condition from the accelerated activation energy at 126 kJ/mol. This could be the result of an ash layer blocking the penetration of O_2 gas into the surface (see Figure 4-6). As stated earlier, the reactor temperatures are nearly under isothermal condition which is around 650 °C (see Figure 4-5).

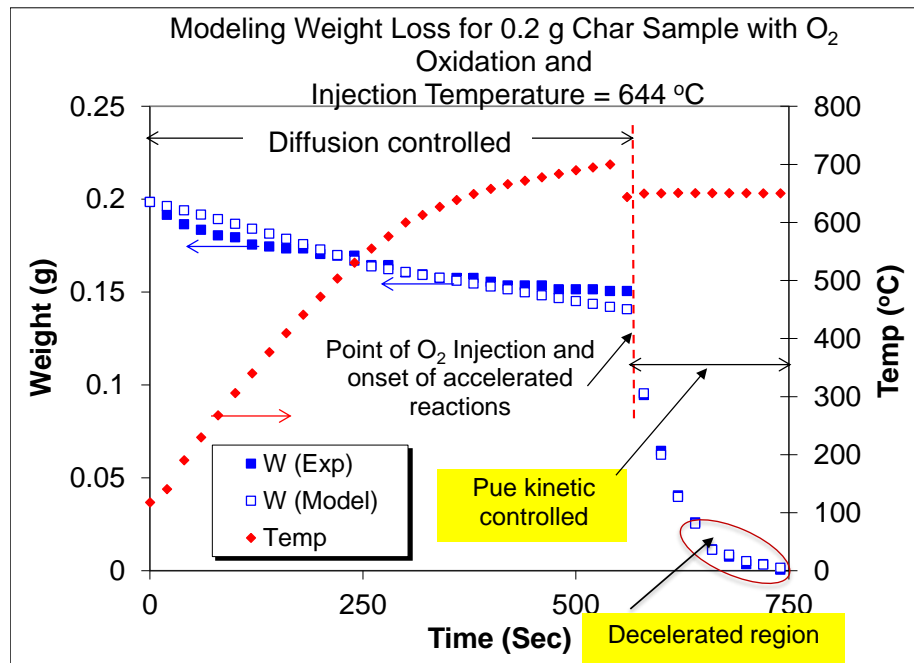


Figure 4-5. Modeling weight loss for 0.2 g char at IT= 644 °C with DNLR



Figure 4-6. Ash formation at the top layer of char particles

With the same modeling approach for the second sample test case, i.e., $T = 584\text{ }^{\circ}\text{C}$ (see Figure 4-7), diffusion controlled air gasification is used at the preheating stage and pure kinetic controlled zone is used during rapid reaction. For nonlinear fit method, the calculated activation energy varies between 117 to 120 kJ/mol and 119 to 137 kJ/mol with a frequency factor of $1.00\text{E}+06\text{ m/sec}$ during accelerated and decelerated periods, respectively. As observed earlier with the first test case at an injection temperature of $644\text{ }^{\circ}\text{C}$, activation energy increases during deceleration period with an average value of 9.5 kJ/mol, which is an indication of a decreased reactive surface which could be due to the inhibiting effects of ash formations.

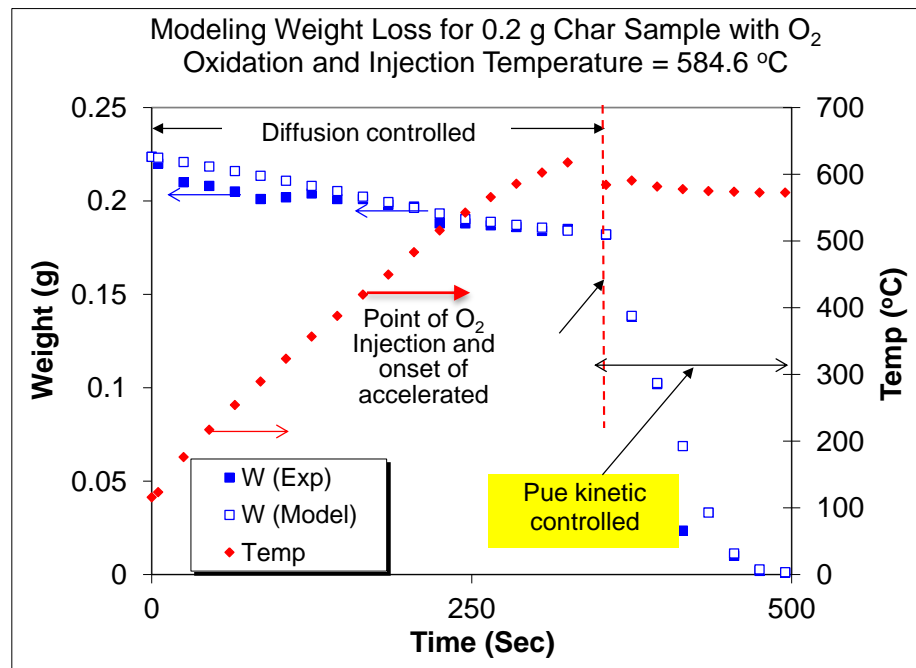


Figure 4-7. Modeling weight loss for 0.2 g char at IT= 584.6 °C with DNLR

Unlike the previous two cases, the third sample test case ($T = 504\text{ }^{\circ}\text{C}$ temperature injection) has a non-accelerated period after injection of pure O₂. This period occurred for 560 seconds before the weight loss rate accelerated (see Figure 4-8). The estimated activation energies at discrete period for non-accelerated region is

144 kJ/mol. However, for the accelerated region, activation energies vary between 110 to 141 kJ/mol. Similarly, like the previous two cases, this indicates that non-accelerated period is less reactive because activation energy is greater.

Figure 4-8 provides the modeling results with the lowest injection temperature of 504 °C using the same mass of char (0.2 gram) and O₂ flow rate. As compared to the reactions with injection temperatures at 644 and 584.6 °C, the reaction at 504 °C takes considerably long time (640 seconds) to completely eliminate char.

The two regions could indicate two possible types of reactions that are dominant. The first part, which is called the non-accelerated region, seems to be dominated by $C + 1/2O_2 \rightarrow CO$ mechanism. However, when this is tested and verified using equation (2-E24) by checking the governing stoichiometric coefficients, $C + O_2 \rightarrow CO_2$ model provides a better fit as compared to gasification reaction. Similarly, the accelerated region is dominated by $C + O_2 \rightarrow CO_2$ because this also fits well the experimental data. Mathematically, as provided by equation (2-E24), this suggests that the accelerated region is purely combustion and purely kinetically controlled.

All these calculations are based on a constant frequency factor using a non-linear approach and based on reactor temperatures. As discussed earlier Chapter 2, because of the variability of activation energies with respect to the order of reactions, kinetic parameter calculations are not unique and highly likely not a good representation of actual values. Although it is not shown here, it is found that increasing the frequency factors also causes an increase in calculated activation energies. Therefore, the kinetic parameter calculations could vary and it is

recommended that further investigations should be performed using discrete linear fit approach while also using estimated surface temperatures as the basis of kinetic calculations instead of reactor temperatures as performed earlier in this section.

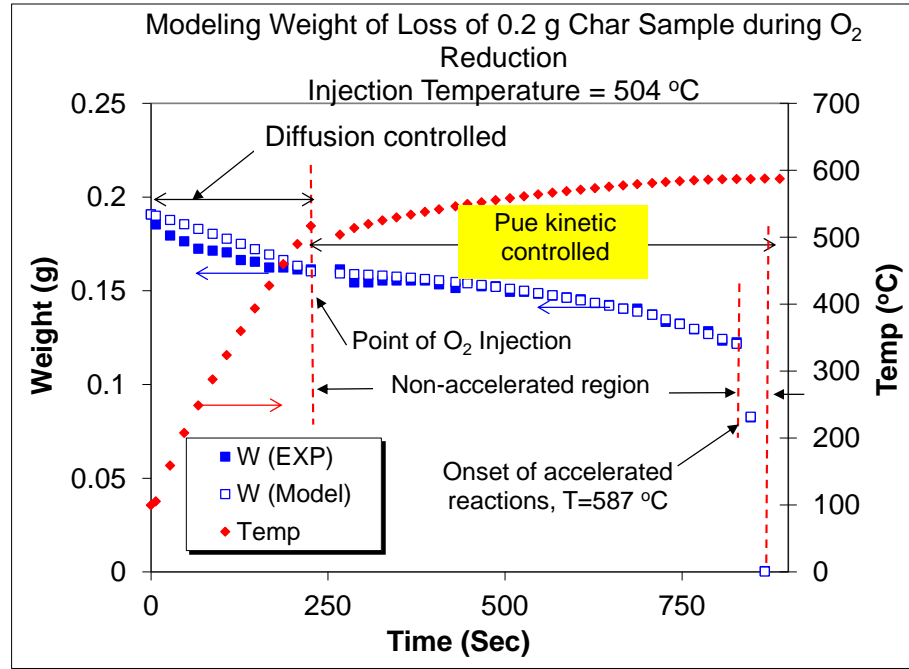


Figure 4-8. Modeling weight loss for 0.2 g char at IT = 504 °C with DNLR

4.1.4.2 DLF via T_s and CO₂ gasification model

As discussed earlier at the beginning of section 4.1.3, CO₂ gasification model is applied for the preheating stages to determine if model fidelity can be improved from air gasification model. Also, instead of using the reactor temperatures (First Model Case) via DNLF, char surface temperature (Second Model Case) is used to calculate kinetic parameters with discrete linear fit (DLF) on the Arrhenius equation during oxidation stages for all cases. As a result of the CO₂ gasification model, it is shown earlier that this fits better the experimental data when compared to the air gasification model (see Figures 4-5, 4-7 and 4-8).

For the first sample test case ($T=644\text{ }^{\circ}\text{C}$ injection temperature), the DLF provides a pure diffusion-controlled regime for the first 60 seconds during the preheating stage (see Figure 4-9). As the temperature continues to rise beyond 60 sec, the regime is characterized near Zone II (i.e. $R_{\text{kin}}/R_{\text{diff}} = 13$). Diffusional rate effects are observed numerically to be important during this heating period. Subsequently, when pure O_2 is injected at $644\text{ }^{\circ}\text{C}$, a pure or intrinsic kinetic-controlled model is observed during the entire period, showing two trends; an accelerated reduction process for the first 100 seconds (after O_2 injection) and a deceleration reduction process lasting for about 80 sec towards the end (see Figure 4-9). Overall, it is also observed that a pure or intrinsic kinetic controlled process exist for accelerated and decelerated regions in this case.

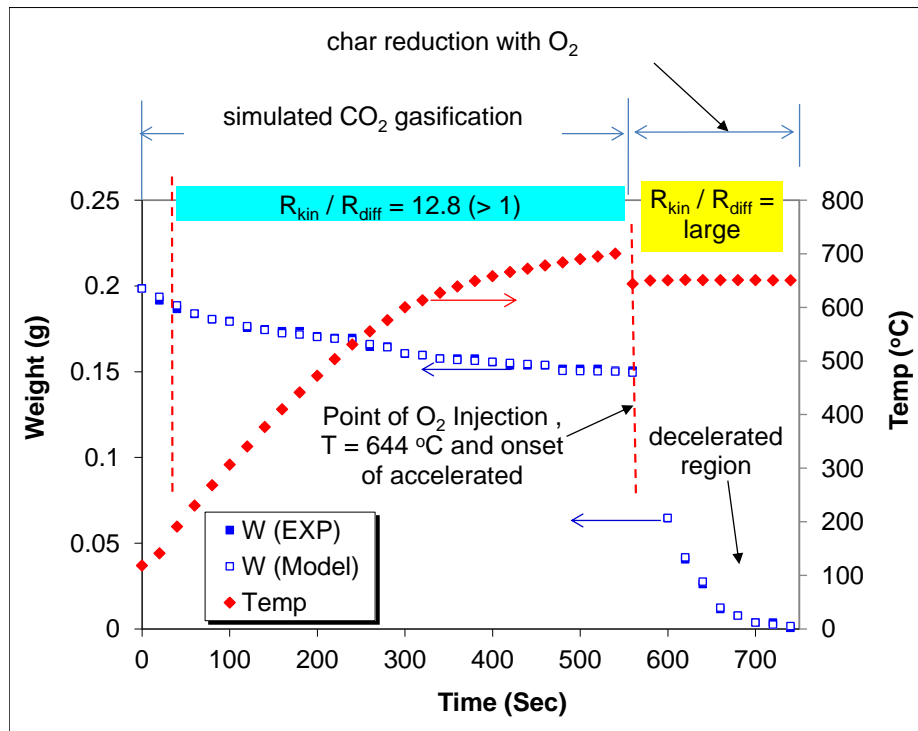


Figure 4-9. Modeling weight loss for 0.2 g char at IT = 644 °C with DLR

For the second modeling approach, it is also observed that CO₂ gasification model fits better the data when compared to air gasification model during preheating stage (see Figure 4-10). Similarly as in the first case, this second model test case (i.e., T=584 °C injection temperature) provides pure diffusion-controlled regime for the first 60 seconds during preheating stage. Beyond the first 60 sec, as the temperatures continue to rise until it reaches injection temperature, the regime is characterized to be near Zone II (i.e., $R_{kin}/R_{diff}=12.5$). Obviously, diffusion effects are also observed to be important during heating periods. However, when pure O₂ is injected at 584 °C, a pure or intrinsic kinetic-controlled condition exists during the entire char reduction period, showing also two trends; an accelerated reaction process for the first 60 seconds from the point of O₂ injection and a deceleration reaction process lasting about 60 sec towards the end. This further validates a fact that char thickness at 1.52 mm has intrinsic kinetic parameters that can be estimated.

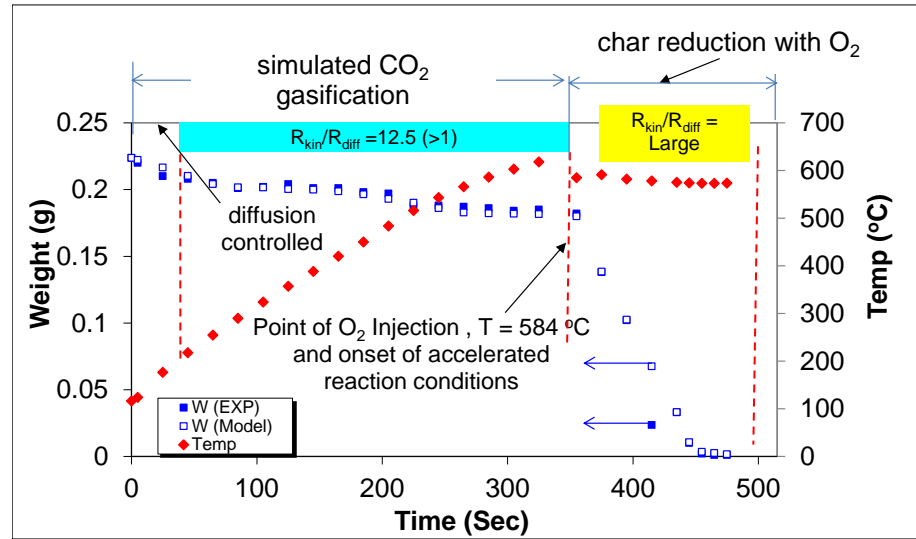


Figure 4-10. Modeling weight loss for 0.2 g char at IT = 584 °C with DLR

For the lowest injection temperature case at 504 °C, it is further observed that CO₂ gasification model fits better when compared to air gasification model during preheating stage (see Figure 4-11). Similarly in the previous two test cases, this test model provides pure diffusion-controlled regime for the first 60 seconds. Beyond the first 60 sec, as temperature continues to rise until it reached injection temperature, the regime is characterized near Zone II (i.e. $R_{kin}/R_{diff} = 22$). As a result, diffusional effects are also observed to be important during this preheating period. When pure O₂ is injected at 504 °C, a regime near Zone II (i.e. $R_{kin}/R_{diff} = 34$) is likewise observed during the reduction period before accelerated reaction conditions. Overall, the combustion reduction process show two trends; a near Zone II process and an accelerated pure (intrinsic) kinetic controlled (i.e. $R_{kin}/R_{diff} = \text{large}$) process occurs, lasting about 40 sec towards the end. Interestingly, the kinetic controlled process at non-accelerated region appears to be controlled by chemical reactions, especially at the beginning for at least the first 180 seconds (see Figure 4-12). Overall, it is also observed that a pure kinetic controlled process exists for this sample case but only during accelerated region. This indicates that a layer of char with thickness up to 1.52 mm has intrinsic kinetic parameters at accelerated regions.

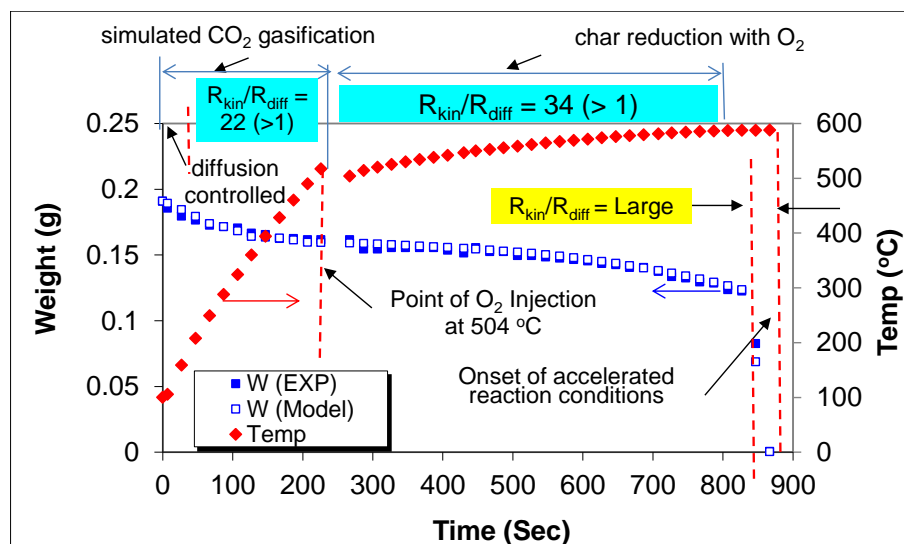


Figure 4-11. Modeling 0.2 g char reduction (IT = 504 °C) with DLR °C

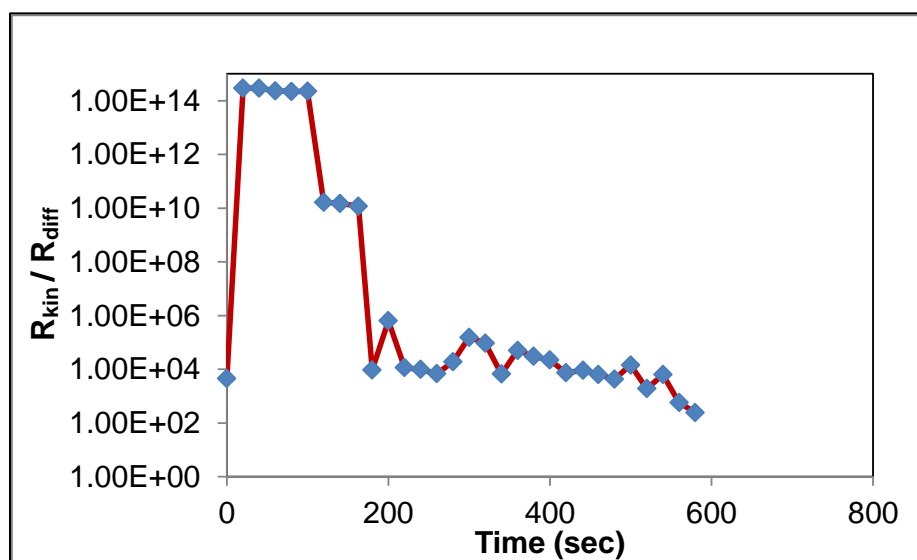


Figure 4-12. R_{kin}/R_{diff} ratios during non-accelerated region for IT = 504 °C

4.1.4.3 Estimated kinetic parameters

Table 4-1 provides the summary of all modeling results for the kinetic parameters at discrete time regions, which include heating periods, non-accelerated, accelerated and decelerated conditions. The heating periods are endothermic processes and the remaining conditions are exothermic processes. The char surface

temperatures are calculated based on the steady-state energy equations presented earlier in section 2.4.4. Discrete time non-linear fit method is used to solve the Arrhenius equation at various regions for the first model case. Pure air gasification reductions are also applied for the first model case, which provides pure diffusion (no kinetic reduction effects) during the preheating stages. This first model case is also used to calculate the kinetic parameters based on reactor temperatures and it shows that during char combustion (i.e., non-accelerated linear region, accelerated region and decelerated region), there is a rise in activation energies from accelerated regions to decelerated regions. A decrease in activation energy is estimated from the non-accelerated region to the accelerated region for the 504 °C injection temperature from 144 to 124 kJ/mol. A constant frequency factor of 1.0 E+06 m/s is used for the first model case.

Discrete linear fit on the Arrhenius equation is used for the second model case, starting at the preheating stage, which is modeled also as CO₂ partial gasification. The rise in the activation energies is observed with the second model case at 644 °C from 37.3 to 69.5 kJ/mol from accelerated region to decelerated region. Based on the first and second model cases, the activation energies are strongly influenced by estimated char surface temperatures. For the IT= 644 °C, the activation energy decreases from 126 kJ/mol (first model case) to 37.3 kJ/mol (second model case) during accelerated region. During the decelerated reaction period, this case also provides lower activation energy and frequency factor of 69.5 kJ/mol and 2.2 E+04 m/sec, respectively for the second model case as compared to the first model case values with 139 kJ/mol and 1.0 E+06 m/sec.

During the preheating period (see Table 4-2), an attempt is made to calculate the activation energy and frequency factor for a partial CO₂ gasification model, however, this did not yield any results. One possible reason for this is that the final char conversions at the end of the preheating period are not sufficient, i.e., < 25 %. Nonetheless, the higher reactor or injection temperatures provide higher values of R_{kin}/R_{diff} ratios, indicating that these are more controlled kinetically than those at lower temperatures. However, these conditions indicate that average conversion rate is faster for IT = 504 °C as compared to IT = 584 °C at 1.75 E-04 g/s and 1.0 E-04 g/s, respectively but only during preheating. The average weight ratio of ash content to unconverted char is also greater for higher injection temperature at 0.0274 as compared to the lower injection temperature at 0.0271. This behavior is assumed to be caused by the inhibiting effect of increased average ash content by restricting the oxidants in reacting with the carbon particles at higher injection temperatures.

Table 4-1. Modeling results for KPs at various injection temperatures (IT)

IT (°C)	IT (K)	TR_min (K)	TR_max (K)	Ts_min (K)	Ts_ave (K)	Ts_max (K)	First Model Case		Second Model Case	
							Ea (kJ/mol)	A (m/s)	Ea (kJ/mol)	A (m/s)
Heating Period (Modeled as Air and CO ₂ Gasification for 1st and 2nd case models, respectively)										
644	917	391	968	298	723	952	NC	NC	NC	NC
584	857	389	876	298	574	845	NC	NC	NC	NC
504	777	373	790	298	495	743	NC	NC	NC	NC
Non-Accelerated (Linear) Region with O ₂										
504	777	777	860.2	796	869	942	144	1.00E+06	108.8	3.62E+06
Accelerated Region with O ₂										
644	917	917	923	1235	1552	1802	126	1.00E+06	37.3	1.86E+03
584	857	850	860	1637	1953	2333	119	1.00E+06	94.9	5.53E+04
504	777	777	860.2	949	2067	2235	124	1.00E+06	NC	NC
Decelerated Region with O ₂										
644	917	920	920	990	1093.6	1145	139	1.00E+06	69.5	2.20E+04
584	857	850	850	973	1270.6	1705	128	1.00E+06	52.6	5.40E+03
504	777	860	860	NC	NC	NC	NC	NC	NC	NC
Legend: NC - Not Calculated, IT - Injection Temperature, TR- Temperature of Reactor and Ts - Surface Temperature										

Table 4-2. Overall modeling results during preheating

IT (°C)	Ea (kJ/mol)	A (m/s)	T _{s,ave} (K)	R _{kin} /R _{diff}	\dot{m}_{ave} (g/s)	W _{Ash} /W _{Carbon}
504	NC	NC	495	6	1.75E-04	0.0271
584	NC	NC	574	10	1.00E-04	0.0274
644	NC	NC	723	12	8.33E-05	0.0307
Legend: IT - injection temperature, T _{s,ave} - average surface temperature, W - weight and NC - not calculated						

Kinetic parameters, char surface temperatures, char burning rates (\dot{m}) and ash contents are provided in Table 4-3 for the overall combustion (non-accelerated, accelerated and decelerated regions) of disk-shaped shaped char particles. These data are obtained with the use of the second model case. Evidently, higher average values of char surface temperatures, char burning rates and the estimated ash-to-carbon weight ratios (average) result to lower activation energies and frequency factors. These calculations indicate that combustion of these particles are purely (intrinsic) kinetic controlled (i.e. $R_{kin}/R_{diff} \gg 1$ or very large) as also indicated by the one-film ASCM for disk-shaped particle equation when data is fitted.

Table 4-3. Overall modeling results during combustion

Ea (kJ/mol)	IT (°C)	A (m/s)	T _{s,ave} (K)	\dot{m}_{ave} (g/s)	W _{Ash} /W _{Carbon}
50.2	584	3.72E+03	1649.7	1.51E-06	2.9
67.5	644	1.87E+04	1322.9	9.3E-07	2.4
74.9	504	3.50E+04	946.1	3.3E-07	0.7
Legend: IT - injection temperature, T _{s,ave} - average surface temperature and W - weight					

4.1.5 Summary of experimental and modeling

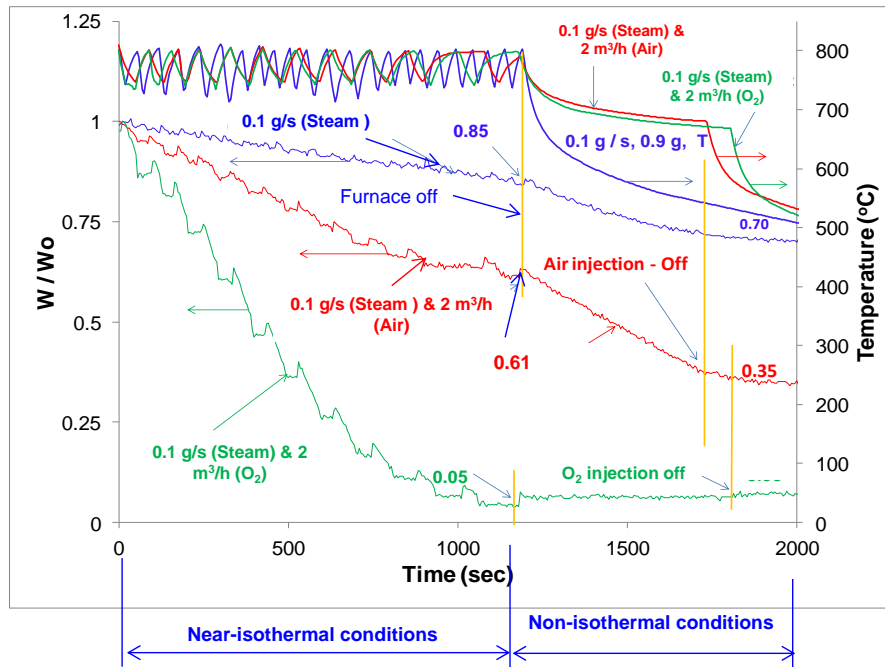
Disk-shaped char with maximum thickness up to 1.52 mm has been rigorously examined as it reacts with 100 % O_2 . Char and O_2 reactions show that these are mostly intrinsic kinetic controlled conditions during combustion. Also, the one-film model has been demonstrated here that apparent kinetic parameters can be characterized via discrete time nonlinear and linear fits to the Arrhenius equation. However, discrete time nonlinear method can only be applied when the frequency factors are known. Nevertheless, this method can provide relative measure of reactivity of char reductions [17]. It also took 140 sec to completely eliminate the char sample at $IT = 584^\circ C$ as compared to 113 and 640 sec for injection temperatures at $644^\circ C$ and $504^\circ C$, respectively. Longer induction period is noticeable for lowest injection temperature at $504^\circ C$, which is associated with a non-accelerated reduction condition during O_2 injection. However, the other higher injection temperatures exhibited no induction period, indicating full adsorption of O_2 gas within the particles almost instantly during combustion. This also indicates that reactions for injection temperatures at 584 and $644^\circ C$ occurred quickly as indicated by the estimated maximum char surface temperatures at 2333 and 1802 K, respectively. At the lowest injection temperature at $504^\circ C$, estimated maximum char surface temperature is 2235 K during accelerated combustion period. This period corresponds to the measured reactor temperature of $587^\circ C$, which is very close to the other case at $IT = 584^\circ C$. This means that the lowest operating reactor temperature for char and O_2 reactions can occur at reactor temperatures as low as $584^\circ C$.

On modeling results, fitting the data allows one to determine the regime of char reduction and kinetic parameters. The accuracy of this procedure depends strongly on how well the model equations capture the actual physics of heterogeneous reduction problem. When the data are applied into the ASCM for disk-shaped particles, there are obvious situations that these do not fit well. However, when diffusion contribution is not considered, a good fit is obtained, allowing one to determine that a pure kinetic controlled or Zone I combustion exists. This means that the estimated kinetic parameters are intrinsic. Conversely, during the preheating periods with the use of vitiated air model wherein partial oxidation or gasification is expected, there is also a situation when the data cannot be fitted properly with ASCM. However, if the kinetic contribution is also removed, the data fit well. This means that the regime is operating purely under diffusion conditions (pure Zone III), i.e., R_{kin}/R_{diff} equals zero.

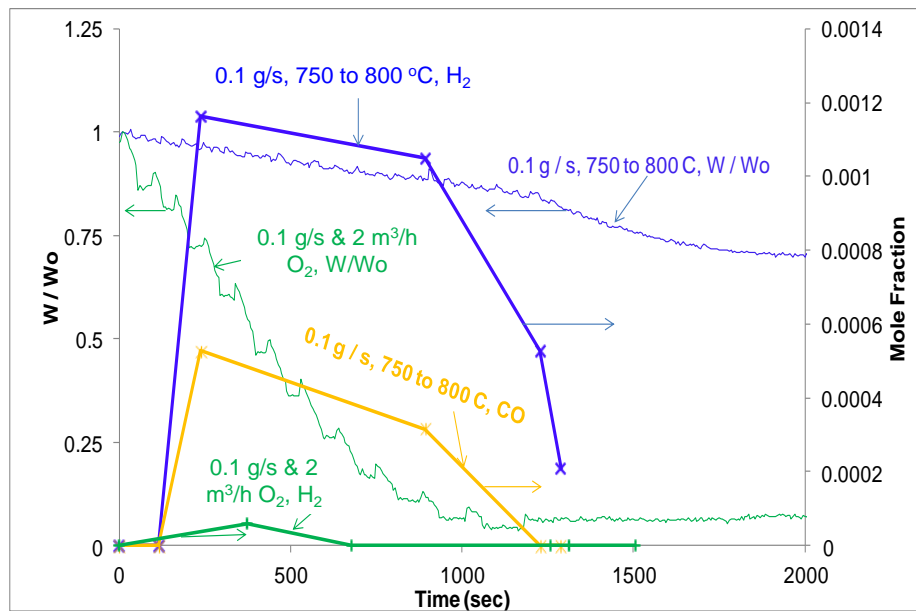
4.2 Reduction of Disk-shaped Carbon Particles with Steam, Air and O₂

The objective of this investigation is to determine the effects of steam, steam plus air and steam plus O₂ for the reduction of char initially at 0.9 g. As shown in Figure 4-13A, three experiments are conducted for 0.9 gram samples using 0.1 g/s of steam and its combination with air and pure oxygen. A baseline test is performed first with pure steam as a gasifying agent without air or O₂. Then two additional tests are conducted separately for the same steam mass flow rate (0.1 g/sec) with air or pure oxygen each at 2 m³/h. The first stage of the experiments are near isothermal conditions maintained between 750 to 800 °C for 1140 sec, resulting to 85 %, 61 % and 5 % of unreacted char for steam-only, steam-plus-air and steam-plus-oxygen,

respectively. The steam-plus-oxygen reaction provided the best reduction performance. After 1140 sec, the furnace is turned off, allowing reduction temperature to cool down while maintaining gas reactants (steam, steam plus air and steam plus O₂) flow and investigate non-isothermal reaction conditions from 800 to 500 °C. Interestingly, the steam-only and steam-plus-air reactions improved the reduction, leaving 70 and 35 %, respectively of unreacted char. Because the char is nearly completed for the steam-plus-oxygen reaction during the first stage (near-isothermal conditions) of the experiment, the amount of unreacted char remained nearly the same after 1140 sec during non-isothermal stage. Although the reactor temperatures are much higher in the first stage as compared to the second stage (non-isothermal), the latter provided a faster reduction rates for steam-plus-air and steam-only conditions. This could be attributed mainly by the high dilution of N₂ in the vitiated air (products of combustion of propane) to maintain near isothermal reactions on the first stage. Figure 4-13B provides a gas sampling analysis of these experiments which indicates a sudden spike in hydrogen and CO production at the beginning of near isothermal reactions for the char-steam only conditions. The steam-plus-pure oxygen reduction also produced H₂ gases but with significantly less amount. The gas analysis for steam-plus-air reactions is also measured but the values of H₂ and CO are not within detectable limits. Nonetheless, these observations imply that steam gas (C+H₂O → CO +H₂) and Boudouard (C + CO₂ → CO) reactions are more active between 750 to 800 °C for steam-only reactions as compared to steam-plus-oxygen and steam-plus-air conditions for near isothermal reactions.



(A) Near and Non-Isothermal Plots



(B) Hydrogen and CO Production Plot

Figure 4-13. Oxygen enrichment of steam char gasification

4.2.1 Summary of experimental results

Disk-shaped chars with maximum thickness up to 5.5 mm are examined as it reacts with steam, steam plus air and steam plus O₂. Effect of steam mass flow at 0.1 g/s for a 0.9 g char sample for TR between 500 to 800 °C provides 15 % at the end of near-isothermal process. Under non-isothermal reactor conditions (from 800 to 525 °C), char conversion reaches 30 % or 70% unreacted char. Although the reactor temperatures are much higher in near-isothermal stage as compared to the non-isothermal stage, the latter provided a faster reaction due to N₂ dilution at the earlier stage where near isothermal condition is maintained. The effect of air at 2 m³/h enrichment with steam mass flow at 0.1 g/s and for 0.9 g char sample from 800 to 670 °C provides 39 % conversion (61 % unreacted char). Steam-plus-air also provides additional conversion reaching up to 65 % (35 % unreacted char) during the non-isothermal process. It is also observe here that air mixed with steam gasification is favorable by as much as 24 % conversion as compared to pure steam gasification. Although the reactor temperatures are much higher in near-isothermal stage as compared to non-isothermal stage, the latter provided a faster reaction due to N₂ dilution at the first stage and near isothermal conditions. Overall, the conversion rates are 7 and 3 times faster with O₂ enrichment and air on steam gasification, respectively as compared to pure steam gasification for 5.5 mm thick carbon particles.

4.3 Reduction of Spherical Oak Wood Char Particles

This section provides the results and conclusions about the combustion of large near spherical oakwood char particles. As indicated earlier for disk-shaped particles, linear and nonlinear fit approaches for solving the Arrhenius equation are

used in estimating the kinetic parameters. Similarly, nonlinear fit is also used to optimize mass loss curves and particle diameter data points to stabilize the energy equation while estimating char surface temperatures. The kinetic parameters and other operating conditions are obtained using RPM and ASCM which are presented earlier in sections 2.4.1 and 2.4.3, respectively.

4.3.1 Effect of ash on char reduction

Figure 4-14 A provides the condition when a particle is inside the reactor during combustion with air at 800 °C, using test matrix Test No.1 Figure 4-14 B depicts a final ash formation for the particle, indicating that the leftover ash is still intact. Table 4-2 provides the melting and boiling points of major ash constituents of oakwood char based on literature [18]. The total amount of ash as measured in this study is about 5.2 % based on a 0.48 gram of fresh oakwood char, which is very close to those published in literature [37]. White oakwood ash is composed primarily of calcium at 31.5 % when measured at 600 °C [18] (see Table 4-4). It is evident from this photo that most of leftover ash is still intact with the structure still well maintained. The remaining ash does not volatilize or soften (see Figure 4-14). However, unreacted char still remains inside the ash surface layer because only about 36 % is converted during experiments. Based on the conservation of energy equation that is used to calculate the char surface temperature in equation (2-E40), the estimated maximum surface temperature for this particular case is 1370 K. This temperature falls in between 1112 K and 1484 K, the melting and boiling point, respectively of calcium, which is a dominant ash constituent. However, at 1370 K, potassium volatilizes because its boiling point is low (1047 K). Therefore, it is possible

that most of the potassium ash constituents are vaporized for all cases because the minimum and maximum calculated surface temperatures are between 1310 and 1755 K, respectively. For Test No. 1 (800 °C with 6 cmph Air), the ash structure is still intact and does not fragment under oxidant flow conditions for $Re = 51$. Assuming that most potassium has vaporized, it is possible that leftover ash is mostly calcium with some traces of other constituents identified in Table 4-4. Also, as reaction progresses, the char outer layer is oxidized and the internal structure is collapsing internally which is indicated by the observable reduction in the diameters (see Figure 4-15).

Table 4-4. Percent weight [18], melting points and boiling points of oakwood

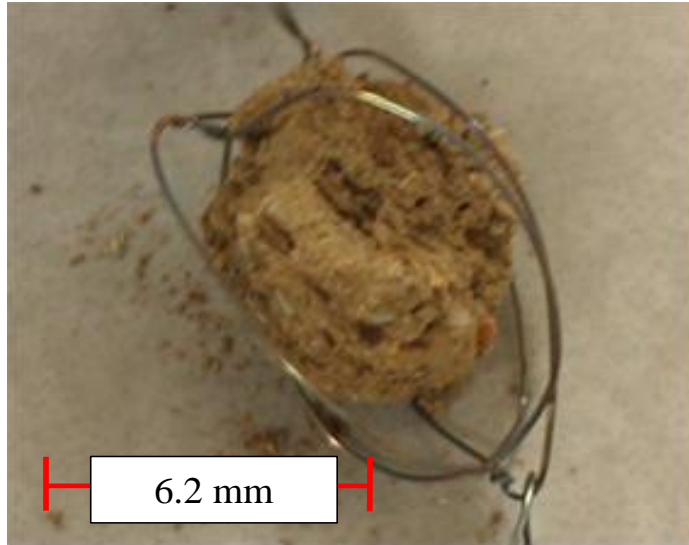
Elements	Percent by Weight	Melting Pt. (K)	Boiling Pt. (K)
Calcium	31.53	1112	1484
Potassium	10.25	337	1047
Magnesium	7.57	923	1107
Sulfur	1.21	386	718
Phosphorus	0.56	317	553
Manganese	0.14	1519	2334
Silicon	0.13	1683	2628
Zinc	0.08	693	1180
Iron	0.09	1808	3023
Aluminum	< 0.03	933	2740
Sodium	< 0.06	371	1156
Boron	< 0.04	2573	2823
Copper	< 0.02	1356	2840

Figure 4-15 (A) provides the images of oakwood spherical char particle initially at 0.076 g for a reactor temperature of 800 °C. Air and oxygen with flow rates at 6 m³/h and 2 m³/h, respectively are used in this experiment. As reaction progresses, particle external surface is reacted first. Because char is highly porous, the oxidants also reacted with the internal pore areas as indicated in Figure 4-14B.

Combined oxidant flow rates correspond to Reynolds number equal to 37 based on the original diameter of oakwood char at 6.8 mm. The porosity of oakwood char particle is estimated at 0.83 based on a density of 0.325 g/cm³ and a solid char density of 1.95 g/cm³ [36]. As shown in Figure 4-15A, the spherical images decrease in diameter with respect to time from the start of the reaction (See Frame 540) towards the end of the reaction (see frame 1590). It is observed that the leftover char and ash slowly drop to the bottom of the stainless steel wire tethering device (see Frames 540 to 1590) as combustion takes place. Figure 4-15 (B) provides the images



(A)

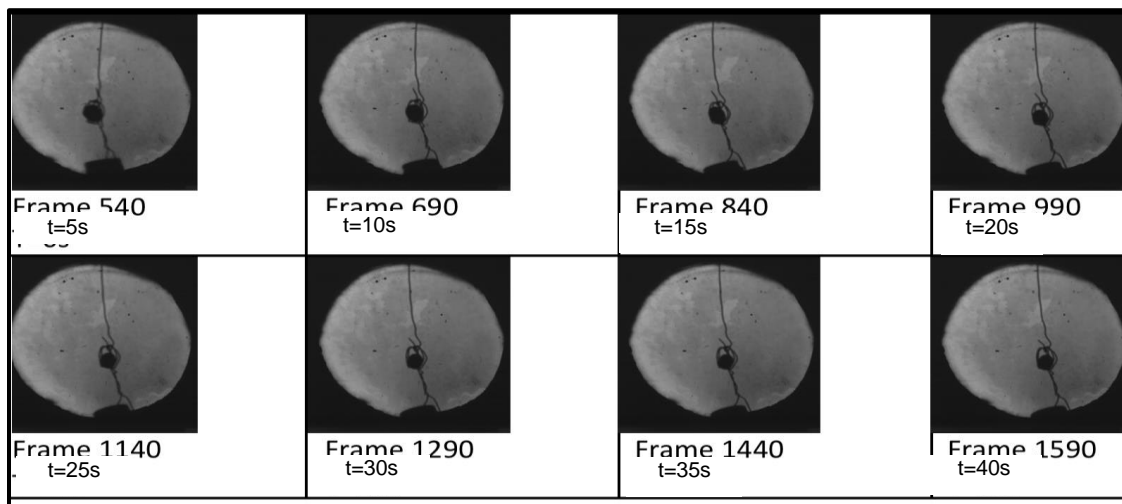


(B)

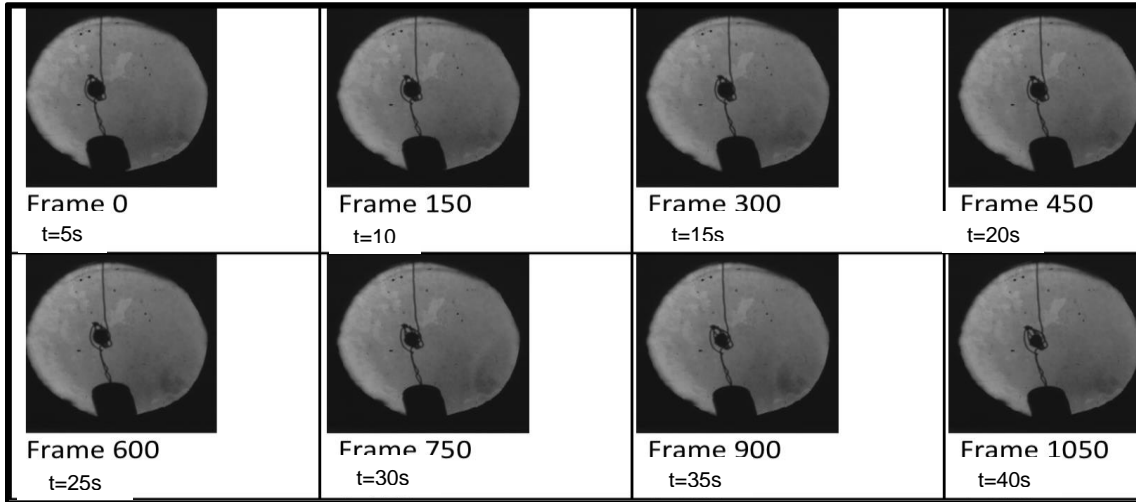
Figure 4-14. (A) Char inside reactor and (B) Ash leftover for Test No. 1

of oakwood spherical char particle initially at 0.078 g for a reactor temperature of 850 °C with 6 cmph air and 2 cmph O₂.

In general, these images show that decrease in diameters is almost exponential. Therefore, nonlinear regression is used to model the decrease in diameters and also the weight changes.



(A) Test No. 3



(B) Test No. 4

Figure 4-15. Five second images of spherical char particles (Test Nos. 3 & 4)

4.3.2 Effect of different temperatures and oxidizing agents on reduction regimes

The effect of kinetics (chemical reaction) and external diffusions are characterized by comparing evolution of the relative rate resistance ratios as calculated using equations (2-E37) and (2-E38). Figure 4-16 provides how these ratios change with respect to time with the directional arrows, showing the direction of increasing kinetic (reaction) and diffusion rates. As indicated, the external diffusion rates are generally fastest at 800 °C with 6 cmph air and 2 m³/h (cmph) O₂ which is followed by higher temperature condition at 850 °C with 6 cmph air and 2 cmph O₂. This also means that the diffusion rates of O₂ enriched cases are faster as compared to pure air combustion of spherical char particles. Under these conditions, external diffusion rates also tend to favor lower temperature conditions in both oxidant type cases (i.e. air alone and O₂ enriched conditions).

For all conditions, the external diffusion rates are becoming faster while the external kinetic rates are becoming slower with reaction time.

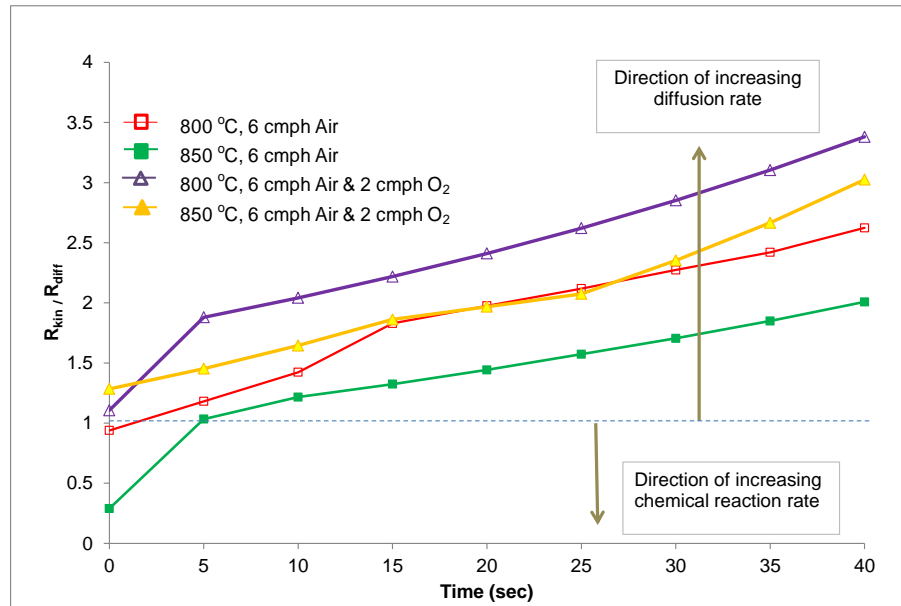


Figure 4-16. Resistance ratios of kinetic and diffusion rates

4.3.3 Effect of reactor temperatures on weight and other variables

Figures 4-17 A and 4-17 B provide the experimental data for changes in weights and diameters for all test cases.

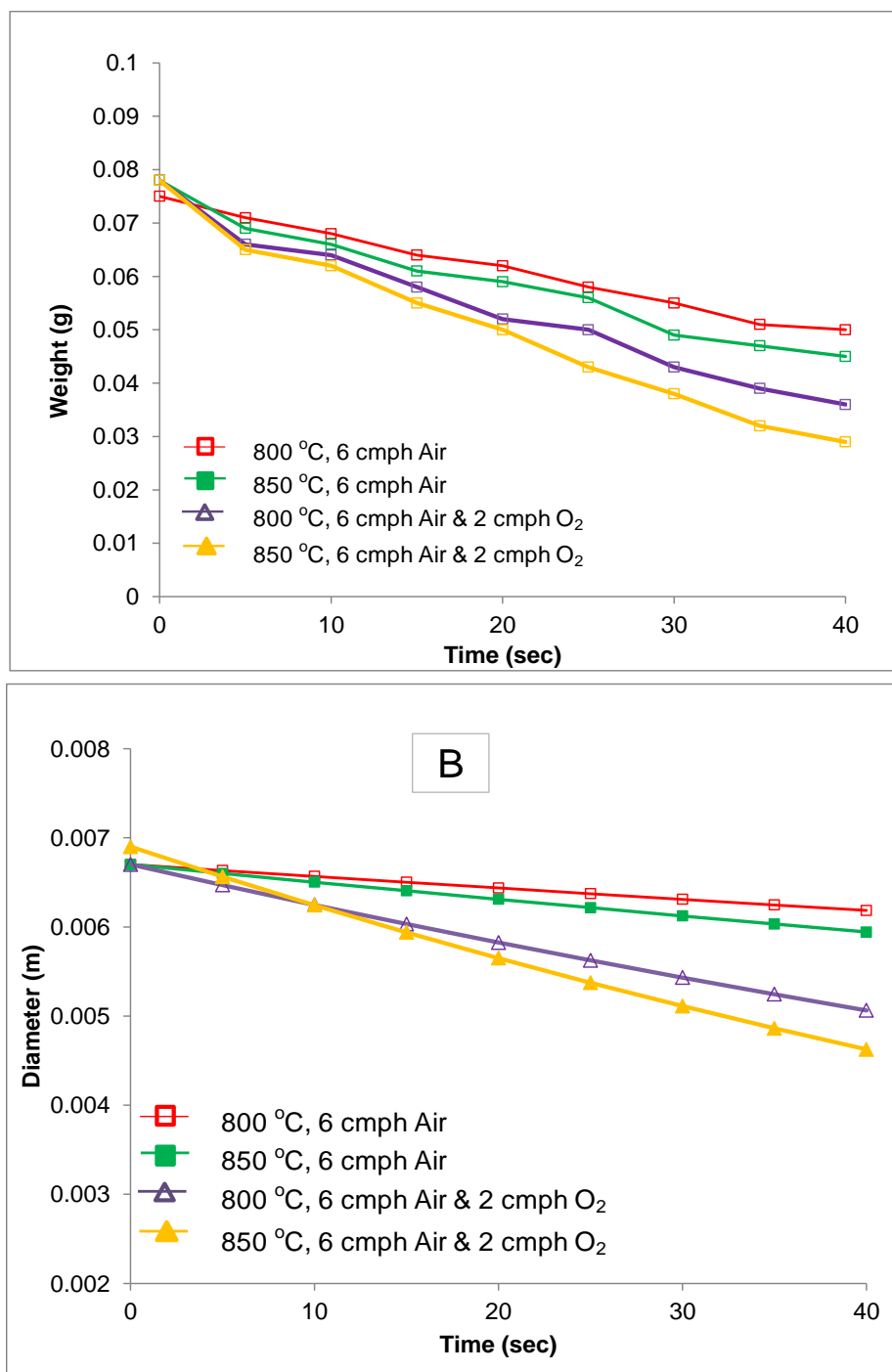


Figure 4-17. Raw data for weight (A) and diameters (B) versus reaction time

As it is done in previous analysis for disk-shaped arranged carbon particles, char surface temperatures and kinetic parameters are calculated using optimized raw data using nonlinear regression for changes in weights, conversions and diameters.

These results are provided in Figures 4-18 and 4-19. The greatest char conversion is obtained with Test No. 4 (850 °C with 6 cmph Air and 2 cmph O₂). As shown in Figure 4-18, for an identical reaction time of 40 sec, 62 % conversion is achieved with O₂ enrichment as compared to the same temperature and amount of air at 6 cmph without O₂ enrichment at 40 %. This is a significant increase in conversion. Similarly, for lower temperature case at 800 °C, conversion with O₂ enrichment reached 53 %, a 20 % greater than the case (Test No.1, 800 °C with 6 cmph Air) without O₂ enrichment which is at 33 %. Correspondingly, as depicted in Figures 4-19, for D/D₀ ratios (normalized diameters based on initial values), there is a significant decrease on these parameters as well at 37, 24.6, 11 and 8 % for 850 °C (6 cmph air and 2 cmph O₂), 800 °C (6 cmph air and 2 cmph O₂), 850 °C (6 cmph air) and 800 °C (6 cmph air), respectively. These results show that the effect of O₂ enrichment with as low as 25 % by volume have significant contribution on the conversion and reduction of oakwood char particles as compared to increased in reactor temperatures by 50 °C.

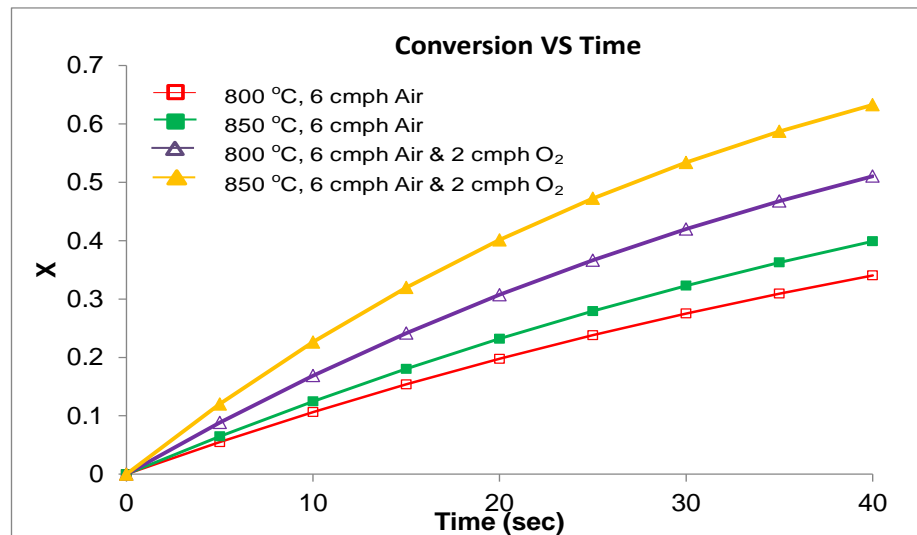


Figure 4-18. Conversion curves of spherical char particles

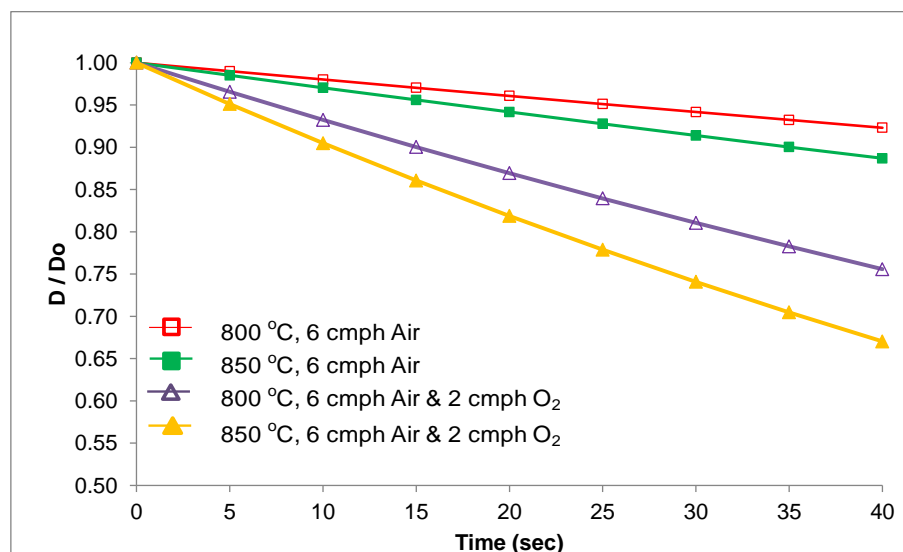


Figure 4-19. Normalized diameter reductions of spherical char particles

The O₂ enrichment provides the highest calculated particle surface temperatures per energy equation (2-E40). Also, as reactor temperatures are increased, surface particle temperatures also increase (see Figure 4-20). It is possible that the generation of ash is faster at the surface with higher particle surface temperatures than those at lower temperature conditions. This seems to be evident under these conditions such that, as conversion progresses, particle surface temperatures also decreases more moderately for 850 °C with O₂ enrichment as compared to the other three (3) cases. However, at higher char surface temperatures, this can also cause more ash constituents to vaporize.

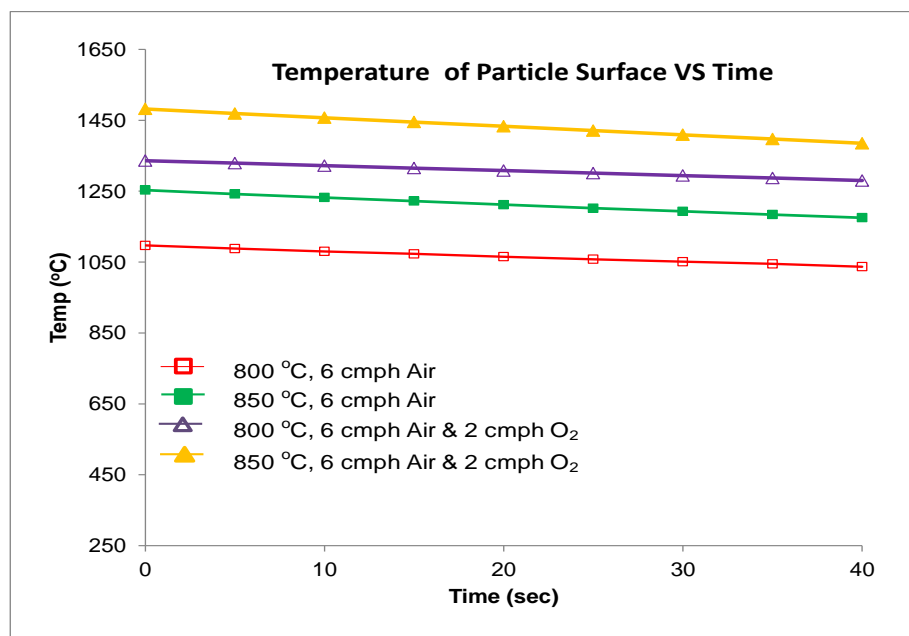


Figure 4-20. Estimated char surface temperatures

4.3.4 Kinetic Parameters via the ASCM and RPM

For ASCM, Figure 4-21 provides the resulting linear fit values of the estimated activation energies of the four (4) test cases investigated based on a unity order of reaction while considering external diffusion rates for a global reaction for $C + O_2 \rightarrow CO_2$. The highest activation energy (180 kJ/mol with ASCM method) for these four cases is obtained at 800 °C with 6 cmph air. This case also provides the highest activation energies per total weight converted (see Figure 4-22) with values at 6.9 kJ/mol-kg and 4.91 kJ/mol-kg for ASCM and RPM (see Table 4-5), respectively. Conversely, lowest activation energy (123 kJ/mol with ASCM) for these four cases is achieved with 850 °C plus 6 cmph air and 2 cmph O₂. This case also provides the lowest activation energy per total weight converted at 2.39 kJ/mol-kg (see Figure 4-22) based on ASCM method. The RPM method indicates that the third case (i.e., 800 °C, 6 cmph and 2 cmph O₂) has lowest ratio of activation energy to weight converted

(see Table 4-5). For ASCM method, activation energy drops from 180 to 163 kJ/mol for a 50 °C rise in reactor temperature (see Table 4-5). In the case of 800 and 850 °C both with O₂ enrichment, a 50 °C rise in temperature provides also a significant decrease in activation energy from 166 to 123 kJ/mol. This indicates that apparent activation energies will change less moderately with temperature conditions as compared to O₂ enriched conditions for large char particle combustion. Interestingly, ASCM provides apparent activation energies that agree with expectations that higher temperatures and O₂ enrichments result to lower activation energy values and frequency factors. For RPM, there is inconsistency of calculated kinetic parameters because higher reactor temperatures do not consistently provide lower activation energies as would be expected. Therefore, the apparent activation energy values obtained with ASCM method for spherically-shaped particles should be considered as a good starting point in characterizing large particle char reduction data.

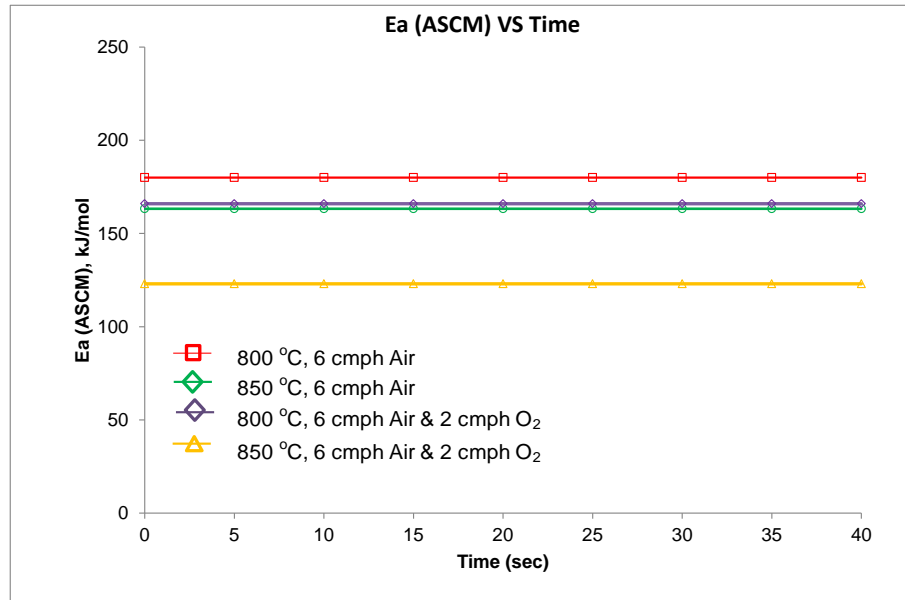


Figure 4-21. Activation energies using ASCM

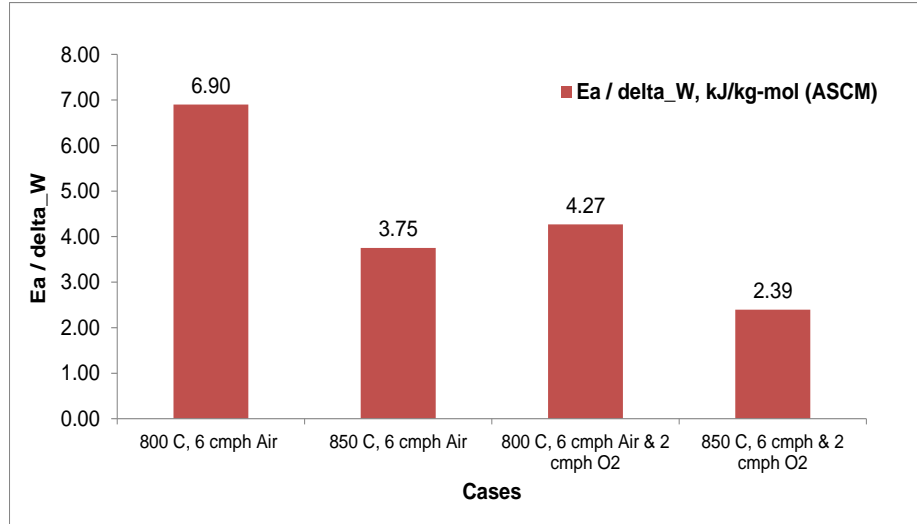


Figure 4-22. Ratio of activation energies (ASCM) to amount of char converted

Table 4-5 provides a summary of the linear fit derived kinetic parameters. As discussed earlier, higher temperatures and oxygen enriched conditions provide lower activation energies (E_a) and frequency factors (A and k_o). The ASCM method provides this expectation. However, this is not the case for RPM method except those with pure air oxidant conditions. The reason behind this is the fact that combustion regime is near kinetic-diffusion regimes (Zones II). According to Murphy et al., inter-particle variations in reactivity may scatter burning rates during diffusion controlled conditions [17]. However, this condition appears to be non-existent for single large particles during combustion because frequency factors (A) do not vary much for all cases. Generally, it is observed that ASCM is relatively stable in obtaining apparent kinetic parameters for large particles that are prone to operate near Zone II. The RPM assumes that 100 % of reduction is fully kinetic and diffusion is negligible, which is not the case. Also, RPM is developed in characterizing the internal char reductions of very small particles in the micrometer range in diameters. Conversely, values

obtained with ASCM provide a better picture of actual activation energies for large particles, as some researchers claim that external diffusion tends to be the mode of reduction for large particles greater than 1.5 mm in size [11]. This implies that during reduction period, heat generated during combustion at the particle's external surface cause more conversion at this location than inside the porous particle. This will be examined more in the next section via Thiele modulus.

Table 4-5. Summary of the linear fit derived kinetic parameters

Test No.	Temp (°C)	Air (cmph)	O ₂ (cmph)	Ea (ASCM), kJ/mol	A (ASCM), m/s	Ea (RPM), kJ/mol	ko (RPM), 1/s	Ea / delta_W, kJ/kg-mol (ASCM)	Ea / delta_W, kJ/kg-mol (RPM)
1	800	6		180	2.13E+06	128.0	8.34E+02	6.90	4.91
2	850	6		163	1.00E+05	114.2	1.11E+02	3.75	3.75
3	800	6	2	166	2.82E+05	97.6	2.58E+01	4.27	2.57
4	850	6	2	123	2.83E+03	142.8	4.24E+02	2.39	2.76

4.3.5 External reactions and pore diffusion rates

As depicted in Figure 4-23, for all of test cases, the values of Thiele modulus (\emptyset) range between 356 and 1093. This condition indicates that char reduction rates are mostly pore diffusion-controlled and external or surface chemical reaction rates are significantly faster than pore diffusion rates because majority of reduction conditions have Thiele modulus values well above 1.0. The 850 °C case with O₂ enrichment provides the highest Thiele modulus values during combustion. The \emptyset values are more favorable for higher reactor temperatures and O₂ enriched environments. This also implies that surface chemical reaction rates are faster for higher temperatures and enriched O₂ oxidant conditions. This observation agrees even with much smaller particles with sizes between 106 and 125 μm [17]. In addition, except for a few instances, \emptyset values tend to decrease monotonically, indicating that

ratio of external chemical reaction rates to pore diffusion rates are decreasing as conversion progresses.

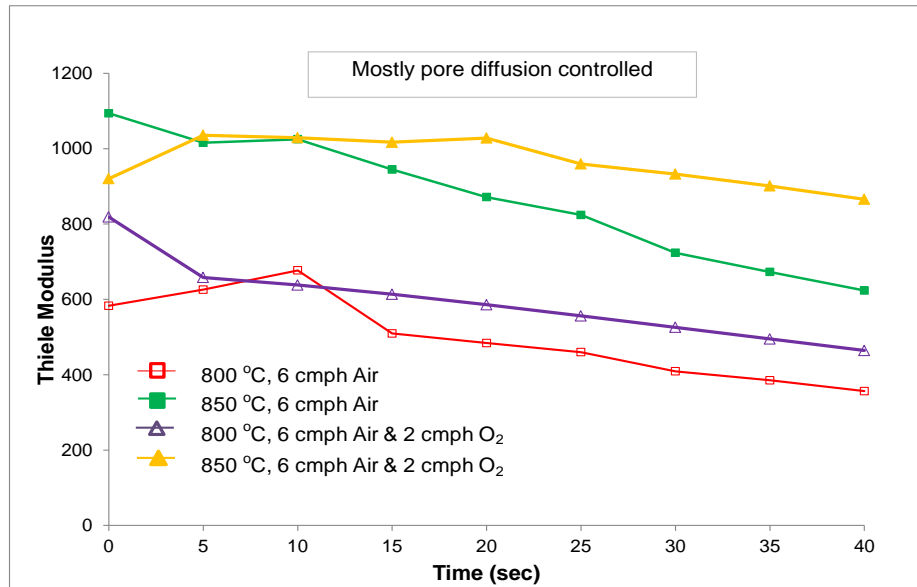


Figure 4-23. Thiele modulus versus reaction times

The values of effectiveness factor (EF) are significantly less than unity, indicating that oxidants do not diffuse well into the porous char because most oxidants are consumed at char particle surfaces (see Figure 4-24). Based on this figure, all of these cases have very low EF with values less than 0.008, especially at the beginning of reaction. This implies that oxygen has barely penetrated the pores to start internal reduction at the beginning of the process in all cases. However, as reduction progresses, EF values increase for all cases which shows that oxidant diffusion (influences reaction rates at the pores) into the pores is increasing with conversion. At the same temperatures, enriched conditions have lower EF factors because most oxygen is consumed at the particle surface. Regardless of type of oxidant (enriched or not) conditions, higher reactor temperatures also favor external reactions at particle surfaces.

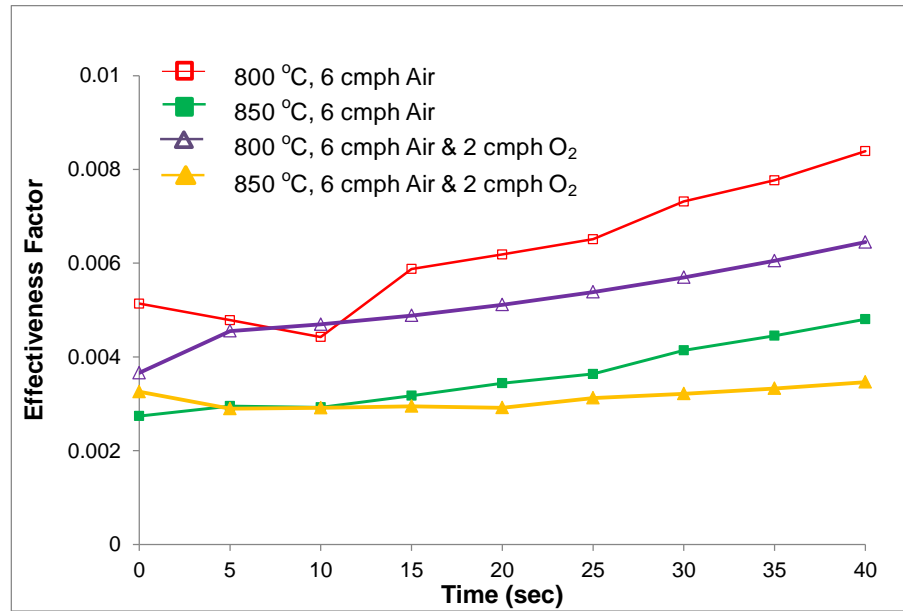


Figure 4-24. Effectiveness factors versus reaction times

For all cases investigated with large wood char particles, controlling or limiting factors that are active during char conversion under such specified conditions are discernable. As discussed earlier, effects and characteristics of reaction rates are observable based on EF values. Figure 4-25 provides the relationship between values of Thiele modulus and effectiveness factors for all cases during combustion of large wood char particles. Generally, all data points for these cases are pore diffusion controlled, which also means that rates of external chemical reactions are significantly faster than rates of pore diffusion (i.e. $\Phi \gg 1$). Additionally, this indicates that O₂ enriched conditions at 850 °C have the highest Thiele modulus values, which implies that external chemical reaction rates are fastest as compared to other cases. Also, with lowest EF values, it is clear that O₂ penetration into the pores are much more limited as compared to other cases, especially for those with 6 cmph air at 800 °C.

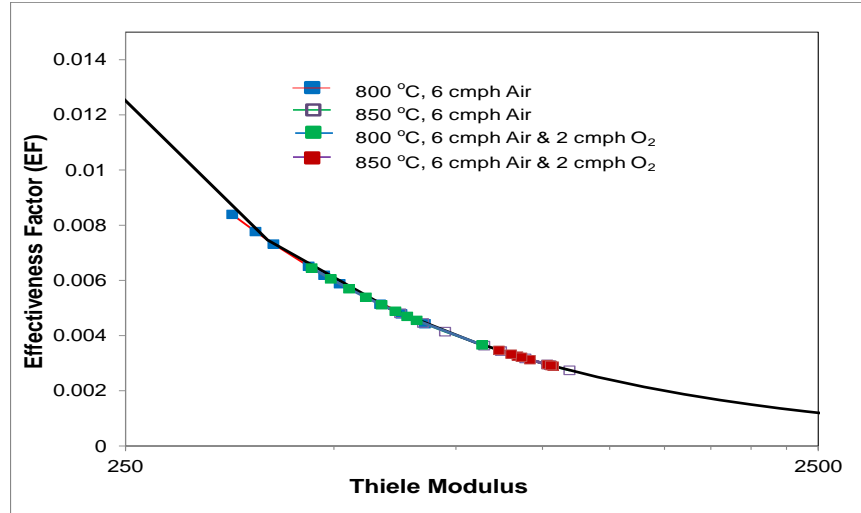


Figure 4-25. Thiele modulus versus effectiveness factors

Tables 4-6 and 4-7 provide the summary of controlling factors at every 5 seconds during combustion process as obtained with the ASCM and Thiele analysis. The analysis of char burnout using one-film ASCM provides direct insight on how these three regimes can overlap. At the char surface, chemical reaction rates are slower than external diffusion rates. Therefore, these cases are considered chemical reaction controlled (CRC) or kinetic controlled or Zone I regimes. When the process crosses the line where R_{kin} / R_{diff} is equal to unity, the regime is called Zone II or intermediate (I). At 800 and 850 °C with O₂ enrichment, all of these are increasingly external chemical reaction controlled (CRC) process during combustion, which also means that external diffusion rates are increasingly becoming faster than external chemical reaction rates (see Figure 4-16). At 800 and 850 °C without O₂ enrichment, regime shifts from intermediate and external diffusion regimes to kinetic controlled and intermediate regimes, respectively from $t=0$ sec to $t = 5$ sec. Thereafter, the regime becomes CRC or Zone I controlled just like all other cases.

For relationships of external reaction rates with pore (internal) diffusion rate conditions, Thiele modulus analysis approach is used. In Table 4-7, it is evident that all test cases are pore diffusion controlled, a condition where rates of external chemical reactions are significantly faster than internal diffusion rates for large particles.

Table 4-6. Chemical reaction rates with external diffusion rates

Temp	Air (m ³ /h)	O ₂ (m ³ /h)	t= 0sec	t= 5sec	t=10 sec	t=15 sec	t=20 sec	t=25 sec	t=30 sec	t= 35 sec	t=40 sec
800 °C	6		I	CRC	CRC	CRC	CRC	CRC	CRC	CRC	CRC
850 °C	6		EDC	I	CRC	CRC	CRC	CRC	CRC	CRC	CRC
800 °C	6	2	CRC	CRC	CRC	CRC	CRC	CRC	CRC	CRC	CRC
850 °C	6	2	CRC	CRC	CRC	CRC	CRC	CRC	CRC	CRC	CRC

Table 4-7. Chemical reaction rates with pore diffusion rates

Temp	Air (m ³ /h)	O ₂ (m ³ /h)	t= 0sec	t= 5sec	t=10 sec	t=15 sec	t=20 sec	t=25 sec	t=30 sec	t= 35 sec	t=40 sec
800 °C	6		PDC	PDC	PDC	PDC	PDC	PDC	PDC	PDC	PDC
850 °C	6		PDC	PDC	PDC	PDC	PDC	PDC	PDC	PDC	PDC
800 °C	6	2	PDC	PDC	PDC	PDC	PDC	PDC	PDC	PDC	PDC
850 °C	6	2	PDC	PDC	PDC	PDC	PDC	PDC	PDC	PDC	PDC

4.3.6 Effects of conversion parameters on activation energies

Table 4-8 provides the relationships of average ratios of resistances of kinetic-to-diffusion rate conditions, Thiele moduli and burning rates relative to activation energies. Based on the oxidant of two cases (air and O₂ enriched conditions) investigated, burning rates (\dot{m} , g/s), estimated char surface temperatures and Thiele modulus values are inversely proportional to activation energies. However, ratios of resistances of kinetic-to-diffusion rates are proportional to activation energies under the same types of oxidants (enriched or not).

Table 4-8. Relationships of activation energies with other reduction parameters

Cases	R_{kin}/R_{diff}	Thiele Modulus	Ea (kJ/mol), ASCM	\dot{m} (g/sec)	T_s (°C)
800 °C, 6 cmph Air	1.87	499	180	6.52E-04	1066.0
850 °C, 6 cmph Air	1.38	866	163.3	7.60E-04	1212.8
800 °C, 6 cmph Air & 2 cmph O ₂	2.4	595	166	9.73E-04	1308.0
850 °C, 6 cmph & 2 cmph O ₂	2	965	123	1.28E-03	1433.1

4.3.7 Summary of experimental and modeling results

The operating regimes of large particles between 6.7 to 6.8 mm at temperatures between 800 to 900 °C are investigated with O₂ enrichment at 800 and 850 °C under atmospheric conditions for up to 40 seconds of reaction time. With the use of the one-film ASCM and RPM, the following conclusions are made based on experimental results and numerical analyses provided:

1. Most of the loss in the particle diameter and weight during conversion are caused by consumption of char external surfaces (i.e. $\phi \gg 1$).
2. The effect of O₂ enrichment with as low as 25 % by mole fraction have more significant contribution on conversion and reduction of wood char particles as compared to a 50 °C rise in reactor temperatures.
3. For large char particles (i.e. between 6.7 to 6.8 mm), external chemical reaction rates favor higher temperature and O₂ enriched conditions. As reaction progresses further, reduction rates due to external diffusion rates increase with time for all cases.

4. The O_2 enrichment provides higher calculated particle surface temperatures than those without enrichment. Also, as reactor temperatures increase, surface particle temperatures also increase.
5. \emptyset values are more favorable for higher temperatures and richer O_2 oxidative environments, indicating that external chemical reaction rates are faster for higher temperatures and richer O_2 oxidant conditions.
6. The activation energies obtained with RPM have inconsistencies. This is due to the fact that RPM does not account for effects of diffusion and also assumes that conversion is purely kinetically controlled, particularly based on test nos. 2 and 4. The activation energy increases under O_2 enriched conditions for the same temperatures.
7. The activation energies decrease with increase in temperature and O_2 enrichment for ASCM.
8. Based on four cases (air and O_2 enriched conditions) investigated for large spherical particles, reduction rates (\dot{m} , g/s), char surface temperatures and Thiele modulus are inversely proportional to activation energies (based on ASCM). However, ratios of resistances of kinetic-to-diffusion rates and effectiveness factors are directly proportional to activation energies.
9. Overall, it is observed that a linear fit with ASCM is relatively stable in obtaining kinetic parameters for large particles that are prone to operate with $R_{kin}/R_{diff} > 3$ (near Zone II).

4.4 Reduction of Irregular Shaped Coal Char Particles

The results and conclusions about the investigation objectives of irregular shaped large coal char particles are discussed in this section. Different effects of char particles such as number of particles per container, amount of air or CO₂ flows, types of oxidants and temperatures are investigated. These effects are provided by plotting conversions and measured reactor temperatures throughout the process. Discrete linear fit technique on the Arrhenius equations is used in estimating the kinetic parameters, which are also provided. Discrete non-linear fit on Arrhenius equation is not investigated here because these do not provide a more accurate kinetic parameters and also the need to assume a frequency factor (A).

4.4.1 Effects of different amounts of air and number of particles at 900 °C

Figure 4-26 provides the effect of different amounts of air and number of particles when reactor temperatures and initial sample weights are nearly identical at 900 °C and 0.052 gram, respectively. The maximum conversions for these experiments are 87 % and 78 % (based on nonlinear regression) for air flows at 4.5 cmph with 3 pcs and 8 cmph with 2 pcs per sample, respectively. As indicated, conversion for lower air flow rate with 3 pcs per container exceeded the conversion of the other case by as much as 13 %. This seems to show that amount of air flow rate is not important as compared to number of particles or particle surface area for the same initial sample weight conditions, i.e., if air flow is not impeded and it is nearly uniform through each particle. Also, although other case has higher operating temperatures, this did not significantly influence conversion. For these cases, it is observed that overall conversion of greater number of particles is higher as compared

to conversion of less number of particles even if it has higher reactor temperature and air.

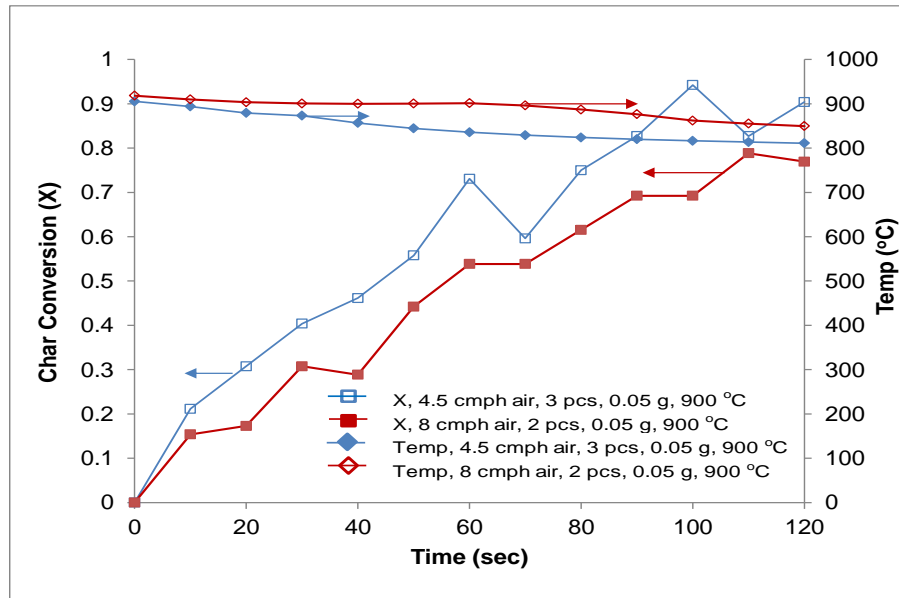


Figure 4-26. Effects of different amounts of air and number of particles at 900 °C

4.4.2 Effects of different number of particles on CO₂ gasification at 900 °C

Figure 4-27 provides the effect of different number of particles when reactor temperatures and initial sample weights are nearly identical at 900 °C. The maximum conversion for these experiments is also nearly identical at 44 % for CO₂ flow rate at 3 cmph with 2 and 3 pcs per container. This implies that under these specific conditions, greater number of particles or particle surface area for CO₂ gasification does not contribute much on conversion, unlike the combustion case as earlier discussed.

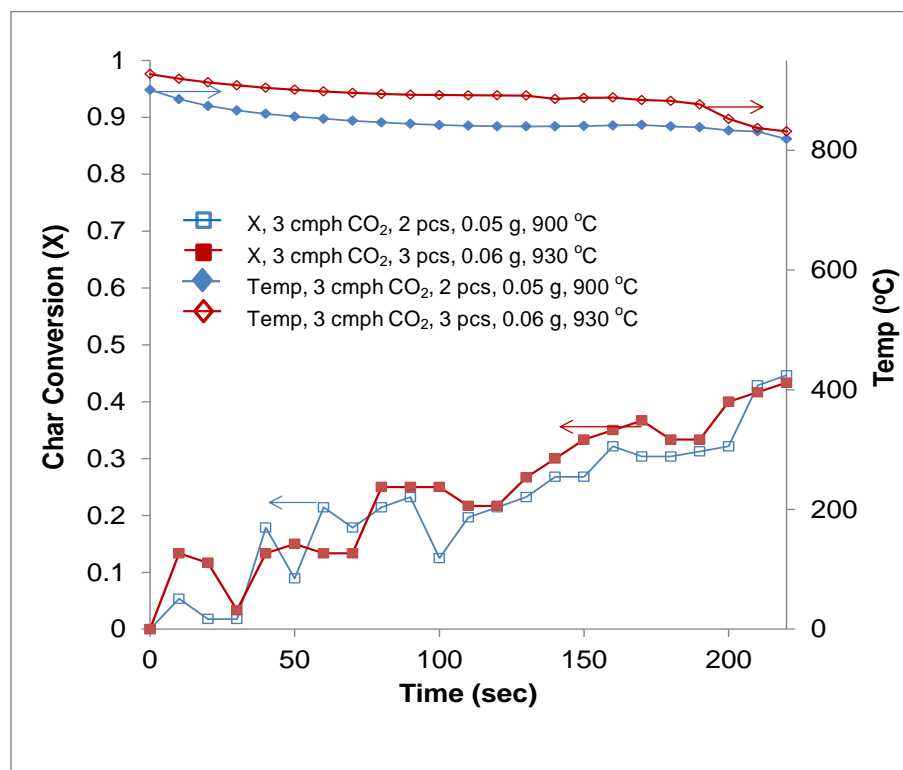


Figure 4-27. Effect of different no. of particles on 900 °C and 0.05 gram

The weight reductions agree well with leftover ash and unreacted char shown in Figures 4-28 A, 4-28 B and 4-28 C. More ash particles are generated with test case # 3 (4.5 cmph air) as compared to test case #s 1 (8 cmph air) and 2 (3 cmph CO₂). Test case # 2 (3 cmph CO₂) provides the least weight reduction as compared to other cases with air.

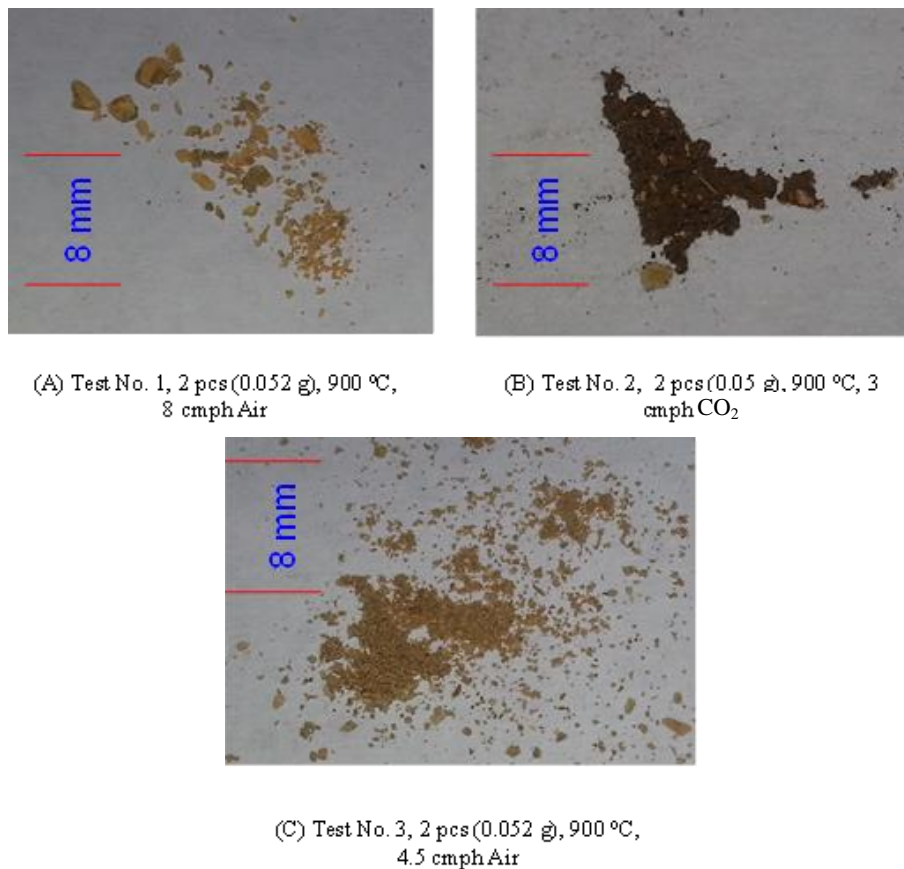


Figure 4-28. Leftover ash for test case nos. 1, 2 and 3

Increasing the number of particles further from 5 and 9 resulted in similar trend as in the previous case for nearly identical reactor temperatures (see Figure 4-29). After ~230 seconds, conversions for the 5 piece and 9 piece samples are 17 and 10 %, respectively. For these cases, higher operating reactor temperatures after 120 seconds did not cause any significant increase in conversion. Nonetheless, it is clear that greater number of particles under such conditions do not cause any significant improvement in conversion. The lower weight sample case (0.112 g) experienced a drop in temperature sooner than higher weight sample case (0.172 g). It is possible that tars released cooled the reacting zone. As shown in Figure 4-30, some larger

particles reacted better than some smaller particles as indicated by greater amount of ash formation on the surfaces (see Figure 4-30 A). In Figure 4-30 B, 5 piece sample provides more conversion as indicated by larger ash areas on sample particles. This shows that 5 particle configuration (test case # 9) allows more efficient oxidant flow than 9 particle configuration for the same volume space inside char reactor container. It is very possible that particle location relative to sample particle container will have a factor in the degree of conversion because this could influence the exposure of particle surfaces with oxidants. Hence, this might be worth considering when studying fixed-bed reactors that are designed to handle multiple large particles.

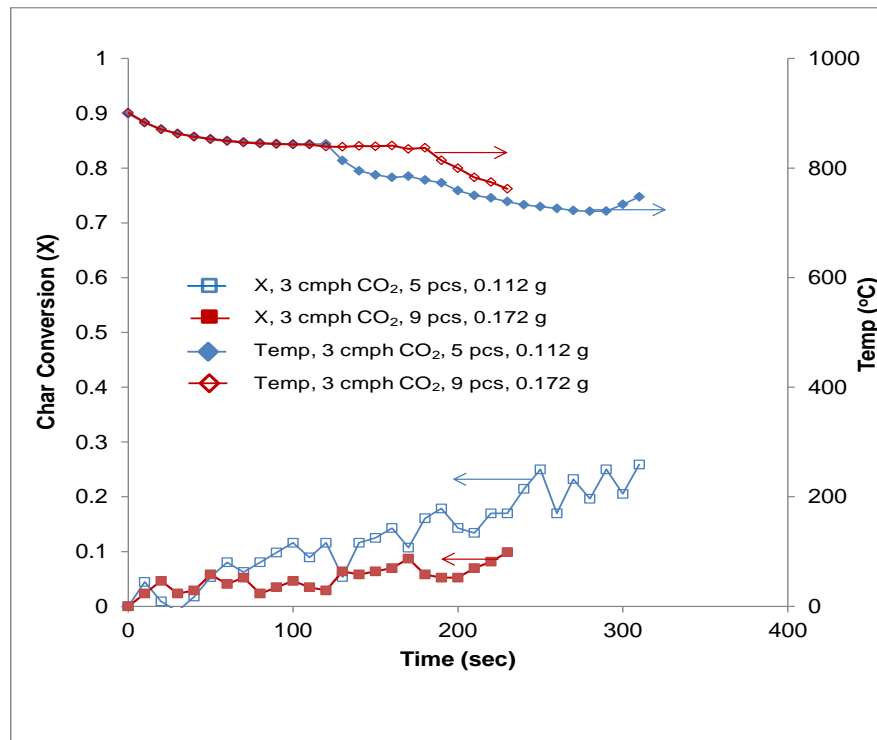
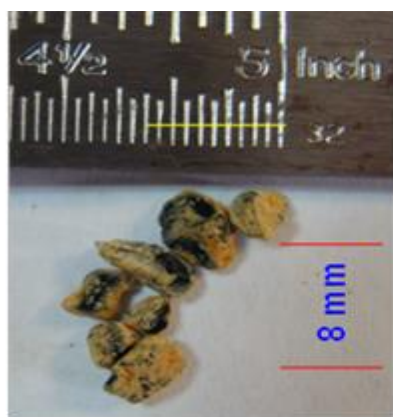
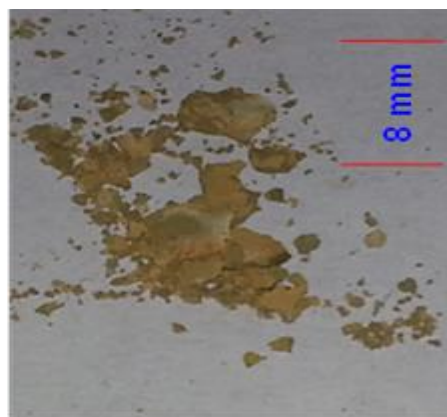


Figure 4-29. Effect of different no. of particles at 900 °C for 3 cmph of CO₂



(A) Test No. 8, 9 pcs (0.172 g), 900 °C,
3 cmph CO₂



(B) Test No. 9, 5 pcs (0.117 g), 900 °C,
3 cmph CO₂

Figure 4-30. Leftover ash for tests 8 and 9

4.4.3 Effects of different temperatures on CO₂ gasification

Figure 4-31 provides the effect of different temperatures for nearly identical initial sample weights, number of particles and CO₂ flow rates for 0.05 gram, 2 pieces and 3 m³/h, respectively. The maximum conversions for these experiments are 50 % at 1000 °C for a 120 seconds reaction time. Subsequently, maximum conversions at 850 and 900 °C are 10 and 34 %, respectively for 120 sec reaction time. These results show that reactor temperatures are important in CO₂ gasification, especially above 900 °C for large particles. For the first 10 seconds, the gasification conversions are nearly identical for all cases. One possibility of this phenomenon may imply that this period is the devolatilization or pyrolysis stage when some tars are released.

At the highest temperature with 1000 °C, conversion accelerates at the beginning and then again after 80 seconds. The first rapid increase in conversion is possibly caused by subsequent release of tar up to $t = 20$ sec. However, a second rapid carbon conversion increases after 80 seconds and after a 60 second during heating

process at the beginning of reaction. After 30 and 100 seconds, the same trend occurs at 900 °C and again possibly caused by tars being released at the beginning and carbon conversion after 100 sec. However, at 850 °C, conversion remains low, possibly because some tars are still present with particles. For the same reaction time, it is evident that reaction $C + CO_2 \rightarrow 2CO$ is faster at 1000 °C as compared to lower temperature cases. In the 850 °C case, it is possible that particles are still experiencing most tar releases and gasification reactions have not fully started yet. Nonetheless, it is observed that CO_2 coal char gasification at these temperatures is inadequate to effect a complete conversion. Therefore, it is recommended that higher temperatures should be further investigated.

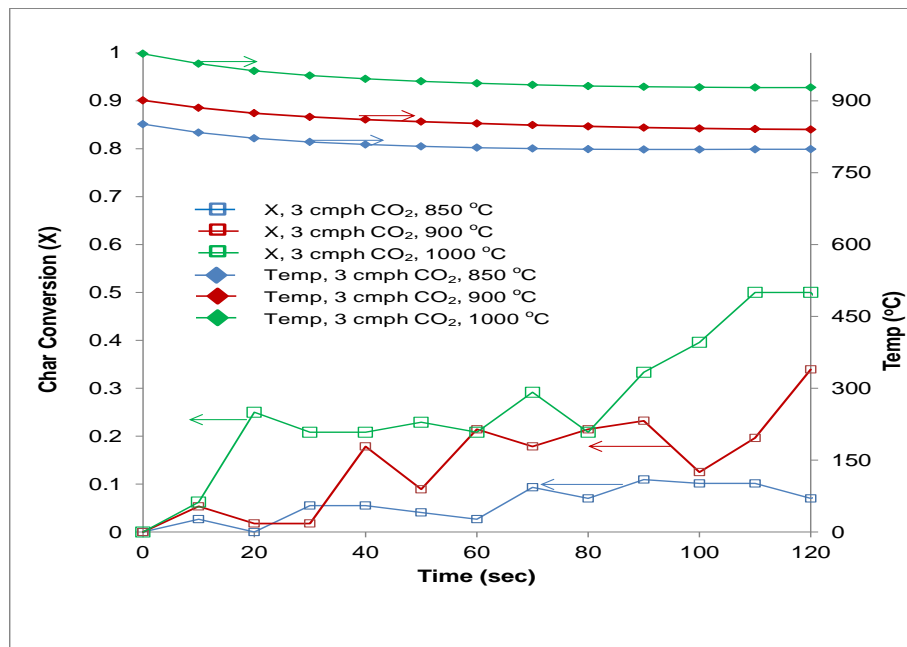


Figure 4-31. Effects of 850, 900 and 1000 °C on CO_2 gasification (2 pcs)

The leftover ash as shown in Figure 4-32 also agrees with the results presented in Figure 4-31 that more ash is formed for the higher reactor temperature as

compared to lower reactor temperature at 850 °C. The 900 °C is shown earlier in Figure 4-28 B.

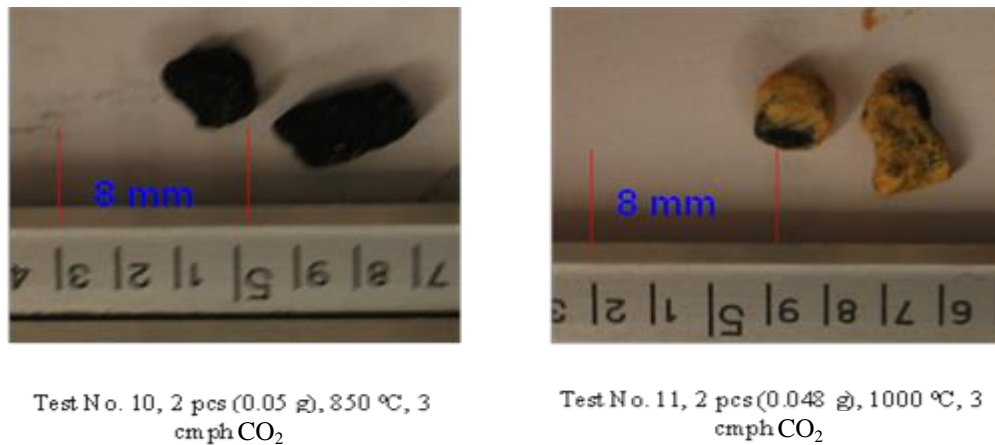


Figure 4-32. Leftover ash for tests nos. 10 and 11

Figure 4-33 provides the effect of different temperatures for nearly identical initial sample weights, number of particles and CO₂ flow rates with 0.05 gram (average), 3 pieces and 3 cmph, respectively. At 230 sec, maximum conversions at 800 and 930 °C are 30 and 38 %, respectively. These results also show that reactor temperature is important with CO₂ gasification. For the first 130 seconds, the gasification conversions are nearly identical even if temperature is higher in one case by as much as 130 °C. One possibility of this result may be the fact that this period is still at pyrolysis stage when some tars are still being released. This is also observed in previous cases as discussed earlier. However, identical conversions are only observed for the first 10 sec in the previous case. Nonetheless, after 110 seconds, conversion at higher temperature (i.e., at T= 930 °C) accelerates faster than at 800 °C.

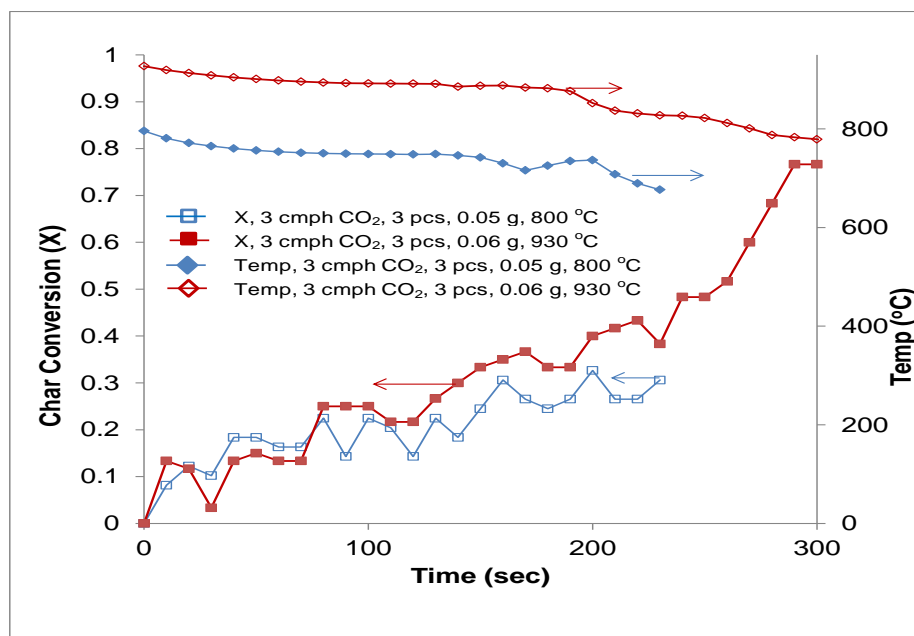


Figure 4-33. Effects of 800 and 930 °C on CO₂ gasification (3 pcs)

Figure 4-34 provides the leftover ash for two specified test conditions. Compared to test # 6, test # 5 results in more conversion because of the higher reaction temperature condition at 930 °C, with a final weight at 0.011 g after 314 seconds. The lower temperature condition at 800 °C has very low conversion as shown with the amount of ash formed after 230 seconds.

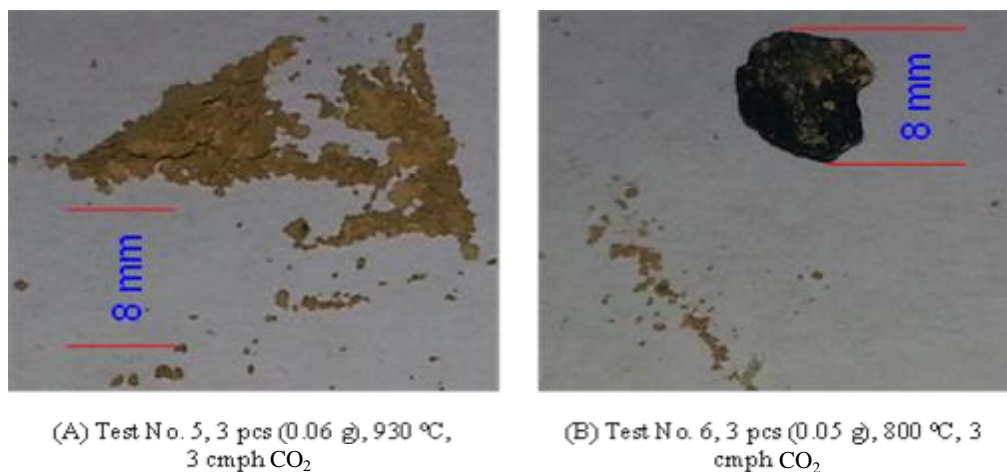


Figure 4-34. Leftover ash for tests 5 and 6

4.4.4 Effect of greater CO₂ flow rates at 900 °C

At nearly identical reactor temperatures starting at 900 °C and the same number of pieces, it appears that greater CO₂ flowrate is important (see Figure 4-35). In these cases, conversion at 6 cmph and 3 cmph are 29 % and 17.9 %, respectively after 70 seconds of reaction time. Interestingly, during initial reaction period from the start up to around 50 seconds, there is a rapid rise in conversion for higher flow rate condition. It is possible that some tars are released faster during reduction for greater flow rate (6 cmph of CO₂) versus at 3 cmph CO₂. And after 50 seconds beyond t= 70 sec, conversion with 3 cmph case is higher but not much different than at 6 cmph. Nonetheless, released tars could be more influence by the slightly higher temperatures at 6 cmph as compared to 3 cmph during the first 70 sec reduction time.

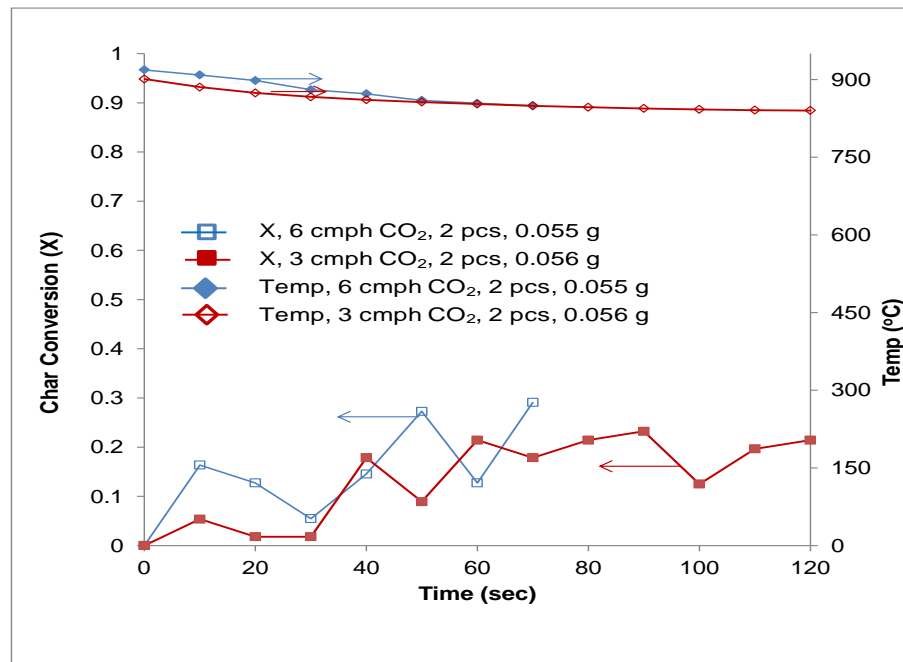


Figure 4-35. Effect of greater CO₂ flow rates at 900 °C

4.4.5 Effects of air and CO₂ on coal char reduction

Figure 4-36 provides the effect of nearly the same amounts of air and CO₂ of with nearly the same initial reactor at 900 °C. Nonetheless, it is obvious that CO₂ gasification provides higher overall operating reactor temperatures versus combustion during the entire reduction process. The total time needed for these experiments to reach 83 % conversion is 110 and 310 sec for air and CO₂, respectively. This result indicates that combustion is about 3 times faster than CO₂ gasification for these particles.

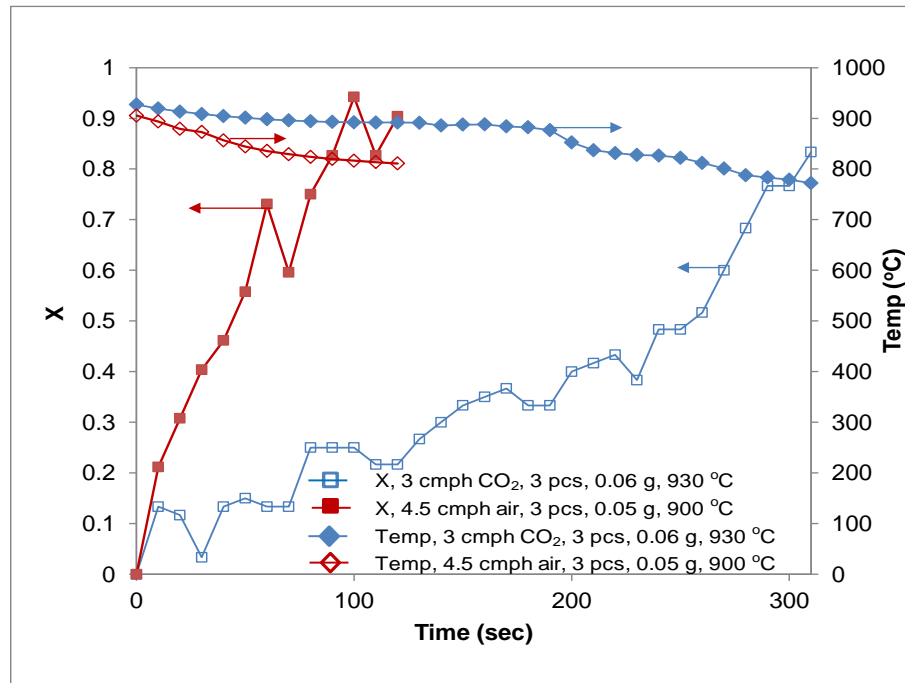


Figure 4-36. Effect of air and CO₂ on conversion at 900 °C

4.4.6 Calculated kinetic parameters

This section provides calculated KPs using linear fit on experimental data for combustion and gasification of irregular char particles (also modeled as spherical shapes) using both one film ASCM and RPM to analyze data. Nonlinear regression

analysis on weight and diameter changes is used here along with linear fits on the Arrhenius equation for kinetic parameter calculations. And similarly with the spherical wood char particles, nonlinear fit method on Arrhenius equation is not presented here because of the randomness of obtained kinetic parameters, in particular the need to assume frequency factors. Therefore, values of activation energies and frequency factors presented here are only those obtained with linear fit approach both via ASCM and RPM. Generally, activation energy values provided by RPM are higher than those from ASCM. Some values of kinetic parameters are not calculated (NC) due to lack of sufficient reduction data to properly obtain KPs. Two sections are discussed here for two types of reactions, $C + O_2 \rightarrow CO_2$ and $C + CO_2 \rightarrow 2CO$.

For $C + O_2 \rightarrow CO_2$ cases, Table 4-9 provides the KPs. As shown earlier in section 4.3, frequency factors decreased with increased in temperatures under O_2 enriched conditions using ASCM method but not for RPM method. Similarly, for irregular char particles, activation energies and frequency factors obtained with the ASCM also decrease with increase in surface temperatures (see Test Nos. 1 and 3), which is consistent with the expected increase in char reactivity during combustion. Calculation of the activation energy for Test # 3 produced no suitable values when RPM method is used even when conversion is high at 91 %. The decrease both in activation energy and frequency factor values at higher char surface temperature conditions are also observed for disk-shaped particles when linear fit is applied to calculate KPs. Additionally, it is observed that higher number of particles (3 pcs with Test No. 3) result to lower activation energy, lower frequency factor, higher surface

temperatures and higher conversion rate as compared to the 2 piece case (Test No.1). It is interesting to note that higher activation energy occurs when reaction time is increased, which also results in conversion increases (see Test Nos. 3 and 3). This observation indicates that activation energies should be based only on corresponding amount of conversion when these are evaluated.

For $C + CO_2 \rightarrow 2CO$ reactions (i.e., Test Nos. 2 and 11) under nearly similar conditions with respect to weight, no. of pieces and CO_2 flow rates, activation energies and frequency factors are observed to decrease as average reactor temperatures (T_∞) are increased via ASCM and RPM methods. The calculated KPs are observed to be strongly influenced by reactor temperatures (i.e., T_∞), which also strongly influences surface temperatures. Again, as observed earlier with the $C + O_2 \rightarrow CO_2$ reductions, activation energy occurs when reaction time is increased, which also results in conversion increase (see Test Nos. 5 and 5*). This observation indicates that activation energies should be based only on corresponding amount of conversion where these are evaluated.

As shown Table 4-9, some KPs are not calculated (NC) using ASCM and RPM due to lack of conversion (i.e. $X < 0.2$) under these conditions. This is also observed with disk-shaped particles when ASCM is applied during preheating process, which resulted to low conversions.

Table 4-9. DLF obtained kinetic parameters via ASCM and RPM

Test Nos.	No. of Pieces	IT	T _∞	T _s	Total Weight (g)	Equivalent Diameter (mm)	Air	CO ₂	Ea (ASCM), kJ/mol	A, m/s	X	Reaction Time (sec)	Ea (RPM), kJ/mol	k _o , 1/s
		°C					m ³ /hr							
1	2	900	889	1341	0.052	4.14	8		152.6	1.03E+05	0.77	120	157.4	1.58E+03
2	2	900	849	792	0.05	4.09		3	75.1	6.38E+01	0.26	120	114.8	9.55E+02
3	3	900	882	1346	0.052	4.14	4.5		78.0	3.58E+02	0.46	40	NC	NC
3*	3	900	846	1361	0.052	4.14	4.5		146.8	3.88E+04	0.91	120	NC	NC
4	2	920	880	774	0.055	4.22		6	114.1	7.60E+03	0.24	70	NC	NC
5	3	930	864	829	0.06	4.34		3	46.5	1.92E+00	0.34	150	73.2	2.92E+00
5*	3	930	882	817	0.06	4.34		3	112.0	2.32E+03	0.48	250	NC	NC
7	9	800	755	NC	0.167	6.11		3	NC	NC	0.10	190	NC	NC
8	9	900	838	NC	0.172	6.17		3	NC	NC	0.08	230	NC	NC
9	5	900	847	800	0.112	5.35		3	30.6	5.5	0.25	150	29.3	2.52E-02
10	2	850	806	730	0.05	4.09		3	NC	NC	0.10	150	NC	NC
11	2	1000	942	831	0.048	4.03		3	43.3	2.37E+00	0.47	120	71.2	7.92E+00
Legend: NC - Not Calculated, IT- Injection temperatures, T _∞ - Average reactot temperature, Ts - Average char surface temperatures, X - Weight conversion and * - greater reaction time and conversion														

4.4.7 Effects of diffusional parameters on X, Ea and \dot{m}

The resulting activation energies via ASCM and average ratios of resistances of kinetic-to-diffusion rates (R_{kin}/R_{diff}), Thiele modulus, char surface temperatures, effectiveness factors and reduction rates are provided in Table 4-10 for combustion reactions ($C + O_2 \rightarrow CO_2$) and CO_2 gasification reactions ($C + CO_2 \rightarrow 2CO$).

The average Thiele modulus values for $C + O_2 \rightarrow CO_2$ (see Test Nos. 1 and 3) indicate that surface chemical reaction rates are significantly faster as compared to internal or pore diffusion rates. Under the two cases, Test no. 3 indicates a higher Thiele modulus value, which is expected because of higher char surface temperatures during conversion. Based on this data, activation energy decreases when R_{kin}/R_{diff} , Thiele modulus, conversion, reduction rates (\dot{m}), surface temperature and X increases. With an average effectiveness factors significantly less than 0.1, this also means that oxygen consumption rates at the pores are very small, implying also that these reactions are controlled by pore diffusion.

Under ($C + CO_2 \rightarrow 2CO$) conditions, for identical initial weights processed and no. of pieces (see Test Nos. 2 and 11), a rise in temperature from 900 to 1000 °C, provides a decrease in activation energy but increase in R_{kin}/R_{diff} , Thiele modulus, conversion (X), reduction rates and surface temperature. Very low effectiveness factors further shows that CO_2 is mostly consumed at char particle surfaces and very little CO_2 diffuses inside the pores. Overall, it is observed that a linear fit with ASCM is relatively stable and consistent in obtaining KPs for large particles that are prone to operate with $R_{kin}/R_{diff} > 10$ (near Zone II).

Table 4-10. Effects of diffusional parameters on X, E_a and \dot{m}

Test Nos.	No. of Pieces	IT (°C)	E_a (kJ/mol): ASCM	R_{kin} / R_{diff}	Thiele Modulus	\dot{m} (g/sec)	Ts (°C)	EF	X
CO ₂ gasification (3 m ³ /h), Wo = 0.048 g < 0.05 g									
2	2	900	75.1	34.8	1390	8.42E-05	792	0.0038	0.26
11	2	1000	43.3	80.3	1460	1.36E-04	831	0.0036	0.47
5	3	930	46.5	36.2	1806	2.05E-04	829	0.0036	0.34
CO ₂ gasification (6 m ³ /h), Wo = 0.055 g									
4	2	920	114.1	27.6	889	1.41E-04	774	0.0039	0.24
CO ₂ gasification (3 m ³ /h), Wo = 0.112 g									
9	5	900	30.6	55.3	1576	9.40E-05	800	0.0037	0.25
Air combustion (Test No. 1 flowrate = 8 m ³ /h & Test No. 3 flowrate = 4.5 m ³ /h), Wo = 0.052 g									
1	2	900	152.6	37	6178	3.27E-04	1341	0.0022	0.77
3	3	900	146.8	40	14315	3.96E-04	1435	0.0021	0.91
Legend: IT- injection temperatures, \dot{m} - average conversion rates, EF - effectiveness factors and Ts - char surface temperatures									

4.4.8 Summary of experimental and modeling results

Combustion and CO_2 gasification of irregular coal char (3.8 % volatile matter and 11.5 % ash) particles between 4 to 6.2 mm at temperatures between 800 to 1000 °C are investigated under 1 atm for various reaction times. For both cases ($C + O_2 \rightarrow CO_2$ and $C + CO_2 \rightarrow 2CO$), higher activation energy occurs when reaction time is increased, which also results in conversion increases. This observation indicates that

activation energies should be based only on corresponding amount of conversion when these are evaluated.

Experimental and data modeling analysis results suggest the following conclusions under these conditions:

1. $C + O_2 \rightarrow CO_2$ cases – The maximum conversions for these experiments are between 77 and 91 % and exposed particle surface area significantly influences degree of conversion. The average values of Thiele modulus (i.e., much > 1) indicates that the surface or external chemical reaction rates are significantly faster as compared to particle's internal or pore diffusion rates. Also, with an average effectiveness factors less than 0.1, this also implies that oxygen consumption rates at the pores are extremely low and are pore diffusion controlled. However, external diffusion rates are faster as compared to external chemical reaction rates as indicated by high ratio values of R_{kin}/R_{diff} (i.e. 39). This also means that this is primarily chemical reaction or kinetic controlled. A decrease in activation energy results to an increase on the values of R_{kin}/R_{diff} , char surface temperatures, Thiele modulus and conversion rates.
2. $C + CO_2 \rightarrow 2CO$ cases – It seems that two series (primary and secondary) of tar releases are occurring at the early stages of reduction for reactor temperatures at 850, 900 and 1000 °C. However, at higher temperatures these releases tend to occur sooner as expected. For nearly identical reaction periods, number of particles and initial weight samples, the degree of conversion increases significantly (i.e., from 10 to 47 %) with increase in

temperature from 850 to 1000 °C. High reactor temperatures are important in CO₂ gasification, especially above 900 °C. Most of these conditions are pore diffusion controlled (i.e. $\Phi \gg 1$) and external or surface chemical reaction rates are significantly faster than pore diffusion rates. Lowest activation energies are observed for Test Nos. 5, 9 and 11, which are also accompanied with the highest values of Thiele modulus and $R_{\text{kin}}/R_{\text{diff}}$. The external diffusion rates are faster as compared to external chemical reaction rates as indicated by high ratio values of $R_{\text{kin}}/R_{\text{diff}}$ (i.e., average 57.5). This also means that this is primarily chemical reaction or kinetic controlled.

4.4 Thermal Reduction of Tar

The results obtained on tar (o-cresol) reduction as injected continuously between 4 and 8 cc/min are presented here. Steam mixed with vitiated is used as a reducing agent. Because the amounts of N₂ and CO₂ are nearly constant regardless of changes in residence time, concentrations of tar and steam injections during experiments. These gases are not included in analyses and plots. This essentially isolates N₂ and CO₂ gases, providing a clear determination of the effects of different processes being tested for the production of light gases. Therefore, only CO, H₂ and CnHm are analyzed. The O₂ content of syngas is also shown purposely because its values change remarkably, indicating partial oxidation of tar during reduction. The CnHm concentrations are generally composed of C₂H₂ with trace amounts of C₂H₄.

4.4.1 Effect of residence time on syngas produced

Figure 4-37 shows the experimental result on the effect of doubling residence

time when tar is injected continuously in the reactor at temperatures between 800 and 900 °C for a steam/tar mass ratio (S/T) of 1.7, which corresponds to a tar concentration of 20,000 mg/m³. As indicated, both CO and CnHm increase in value except H₂ gas. This indicates that carbon conversion increases with greater residence time. However, a small decrease in H₂ is observed, which may indicate that some H₂ gases are produced via CnHm production.

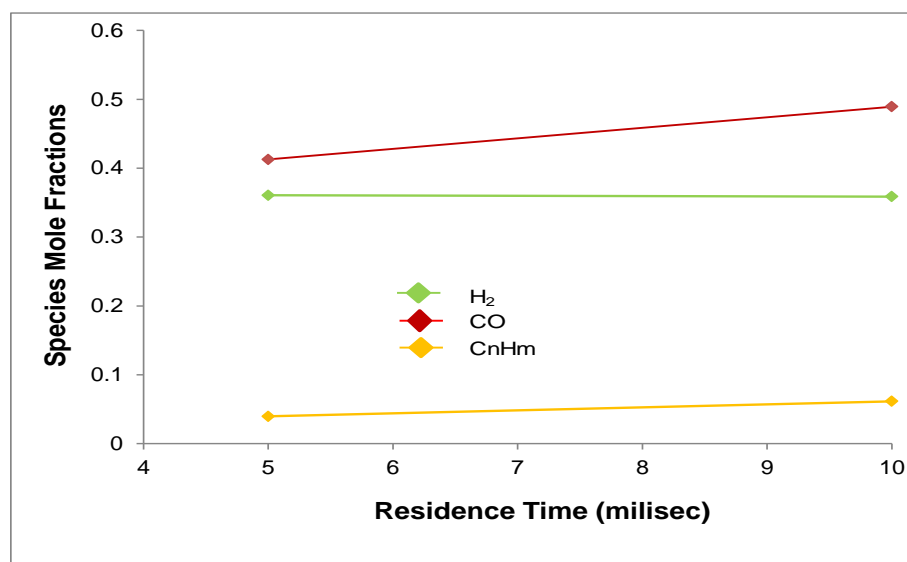


Figure 4-37. Syngas produced when doubling residence time

4.4.2 Effect of steam-to-tar mass ratio (S/T) on syngas evolution

The progress of syngas production increases as temperature is increased from 838 to around 859 °C, see Figure 4-38. For an increase in temperature above 840 °C, production of H₂, CO and CnHm (mostly C₂H₂ & C₂H₄) increase, especially for CO. This is also accompanied with a sharp decrease in O₂ which indicates an increase in tar conversion via O₂ consumption. CnHm production is also detected during this experiment and this may have to do with a high S/T at 1.7.

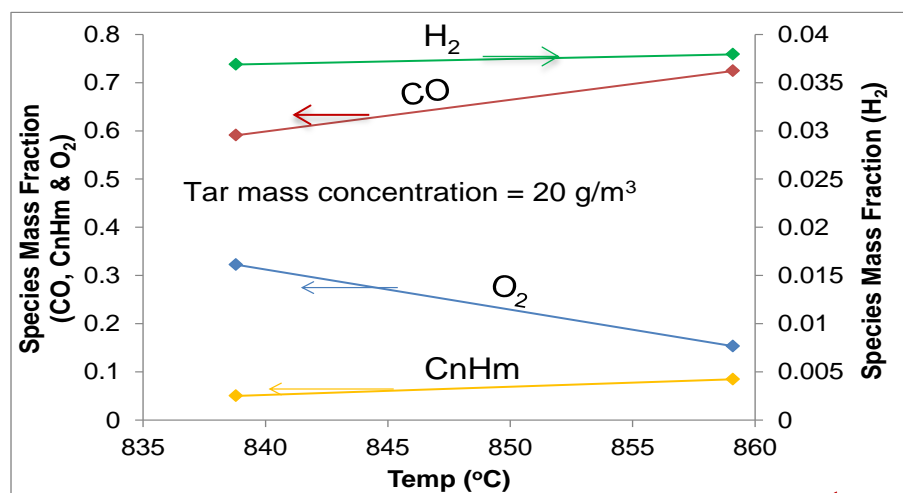


Figure 4-38. Evolution of syngas at $S/T = 1.7$.

At higher tar concentrations, gas production also increases between 820 to 873 °C, see Figure 4-39. As observed earlier for higher S/T , O_2 concentration also abruptly decreases in value, indicating that O_2 in the gas bulk mixture helps in tar conversion. Interestingly, $CnHm$ production cannot be detected and this could be due to low S/T value of 0.865.

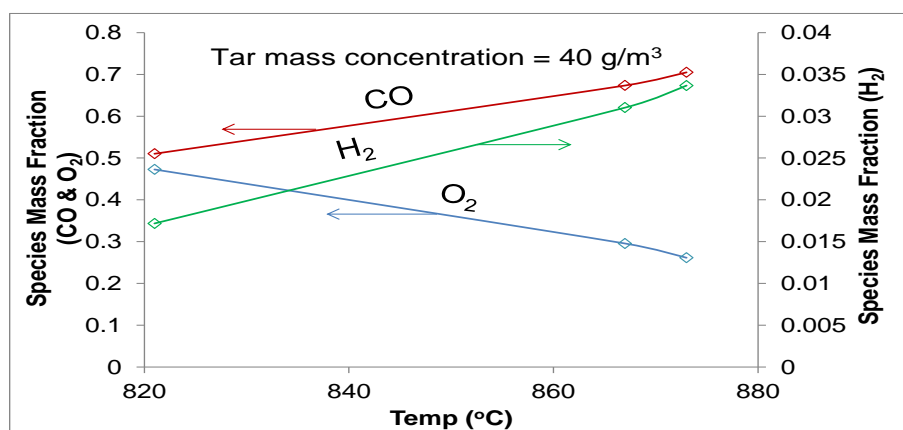


Figure 4-39. Evolution of syngas at $S/T = 0.865$

4.4.3 Effect of temperature on syngas production

Higher reactor temperatures results to higher syngas production, especially CO for both cases. The production of CO, H₂ and CnHm is higher for lower tar concentration (20 g/m³) and higher S/T as compared to higher tar concentration (40 g/m³) and lower S/T test condition (see Figure 4-40) for temperatures between 821 and 873 °C. As tar concentration increases to 40 g/m³, CnHm production becomes insignificant, indicating that tar conversion are mainly due to the production of CO and H₂ gas molecules for these temperatures. Nonetheless, production of H₂ increases more at higher tar concentration as compared to lower tar concentration condition as reactor temperature increases.

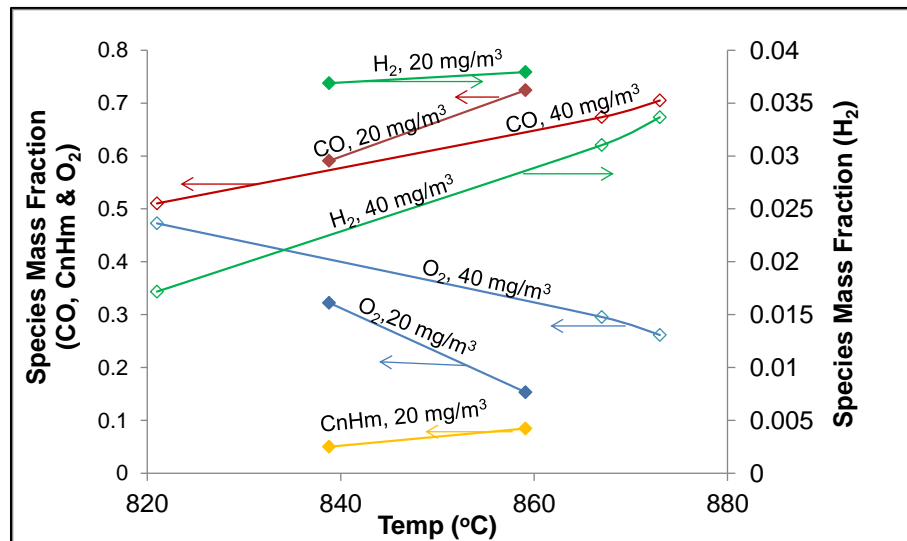


Figure 4-40. Temperature effect on syngas produced

4.4.4 Summary of experimental results

The following conclusions are made from this experimental study on tar reduction for a continuously fed reactor that is operated non-isothermally and non-catalytically using steam and vitiated as oxidizing agents:

1. Carbon conversion increases with greater residence times and temperatures.
2. The production of CO and CnHm (mainly C₂H₂ with trace amounts of C₂H₄) increases when residence time is increased for S/T at 1.7.
3. CnHm production is detected during this experiment for high S/T at 1.7. However, at lower S/T at 0.865, CnHm production is nonexistent. This implies that increasing the amount of steam during tar reduction can increase production of CnHm.
4. The production of CO and CnHm is higher for lower tar concentration (20 g/m³) and higher S/T as compared to higher tar concentration (40 g/m³) and lower S/T test condition for temperatures between 821 and 873 °C.
5. The production of H₂ increases more at higher tar concentration as compared to tar lower concentration condition as reactor temperature increases.

Chapter 5: Analysis of Results

This section provides relative comparisons of large and small particles via Arrhenius plot analysis, estimated kinetic parameters and calculated surface temperatures. A comparison on the Sherwood numbers of previously studied large particles is also presented. Investigated large char particle diffusional parameters (i.e. Sherwood, effectiveness factor, Θ and $R_{\text{kin}}/R_{\text{diff}}$) are also summarized and discussed here. Calculated energy released and absorbed both by combustion and gasification processes, respectively are also provided along with predicted reactor thermal efficiencies for various case studies investigated.

5.1 Comparison of Results with Literature Studies

5.1.1 Arrhenius plot of large particle reduction

The reaction rate coefficients for combustion of wood and coal char particles with diameters between 4 to 6.7 mm are shown in Figure 5-1 along with a collection of already analyzed experimental data from different kinds of porous coal chars with diameters less than 120 μm [16, 17]. Reaction rate coefficients of carbon particles are also provided in this Arrhenius plot for a thickness of 1.23 [30] and 1.52 mm [This Study]. These coefficients are based on a common oxygen pressure of 101.3 kPa at temperatures between 1270 and 2500 K. As indicated, the natural logarithm of reaction rate coefficients for combustion of large char particles (categorized near Zone II) lay below Zone I of small particles for identical T_s between 1390 and 1800 K. As shown in the composite plot, the data points can be group into various clusters

with different slopes. In section 5.1.4, kinetic parameters are also compared to elucidate further the effect of diffusion (external and internal) for these particles.

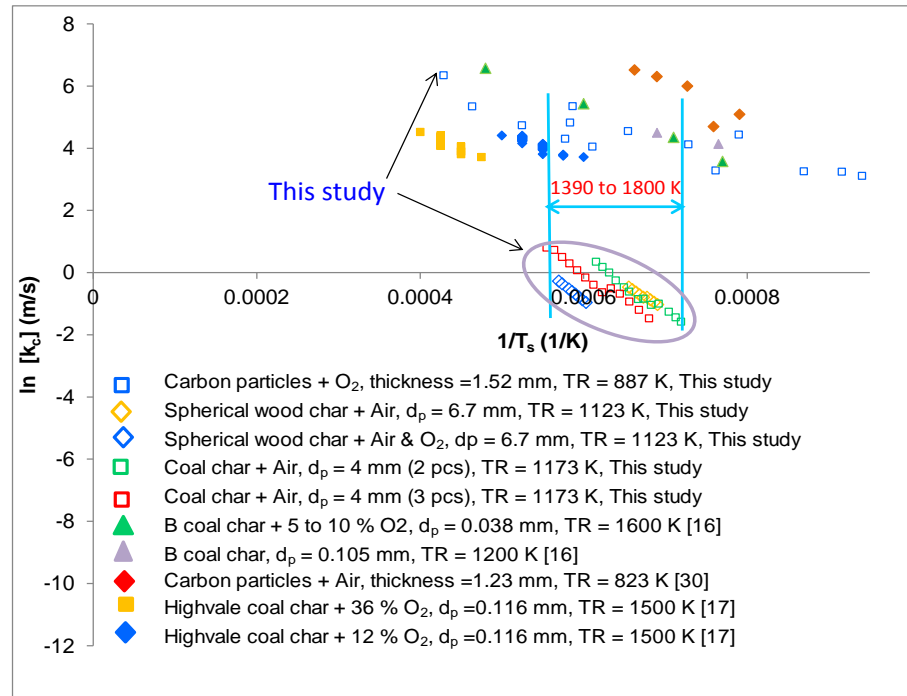


Figure 5-1. Arrhenius plot of large wood and coal char particles

The Arrhenius plot natural logarithm of reaction rate coefficients of CO₂ gasified large char particles (with $d_p = 4 \text{ mm}$) along with small particle diameters up to 0.2 mm from literature [23, 24, 25] is shown in Figure 5-2. These coefficients are based on a common CO₂ pressure of 101.3 kPa at temperatures between 1050 and 1270 K. As indicated, the CO₂ gasification of smaller particles has lower reaction rate coefficients as compared to larger particles for identical temperatures between 1050 and 1270 K.

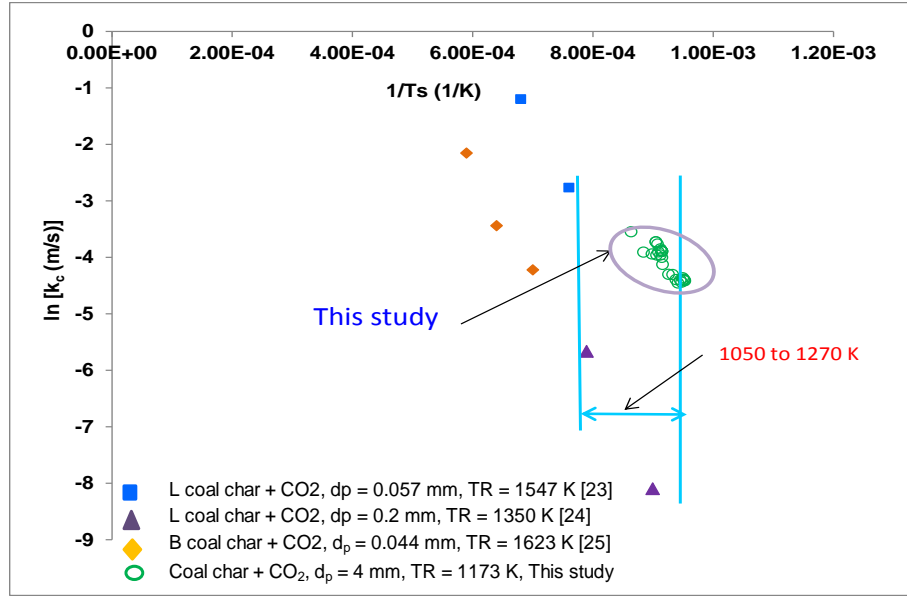


Figure 5-2. CO₂ gasification of large coal char particles

5.1.2 Sherwood number

Sherwood number (Sh) is the ratio of convective mass transfer coefficient to diffusive mass transfer coefficient. This parameter is useful in understanding how well oxidants are conveyed into the particles being gasified or combusted. For certain gasifiers and combustors like fluidized beds; Sherwood numbers should be characterized and examined. For spherical particles, Sherwood number is calculated per equation (5-E1) [11]:

$$Sh = 2 + 0.552 \times Re^{0.5} Sc^{\frac{1}{3}} \quad (5-E1)$$

And for flat particles, the Sherwood number is estimated per equation (5-E2) [11]:

$$Sh = 0.332 Re^{\frac{1}{2}} Sc^{\frac{1}{3}} \quad (5-E2)$$

where, Re and Sc are the Reynolds and the Schmidt (ratio of viscous diffusion rate to mass diffusion rate, $\mu/\rho D$) numbers, respectively.

The Sherwood numbers for CO_2 gasification of coal chars (4 to 6 mm) are presented below along with combustion of other large particles up to 7 mm in size in a composite plot (see Figure 5-3) [11]. As indicated, Sherwood numbers used in these experiments for coal char CO_2 gasification are very close with those in literature. This establishes the fact that particles investigated here as well as experimental oxidant flow conditions used are similar to previous studies. Also, it is evident that particle diameters are directly proportional to Sherwood numbers.

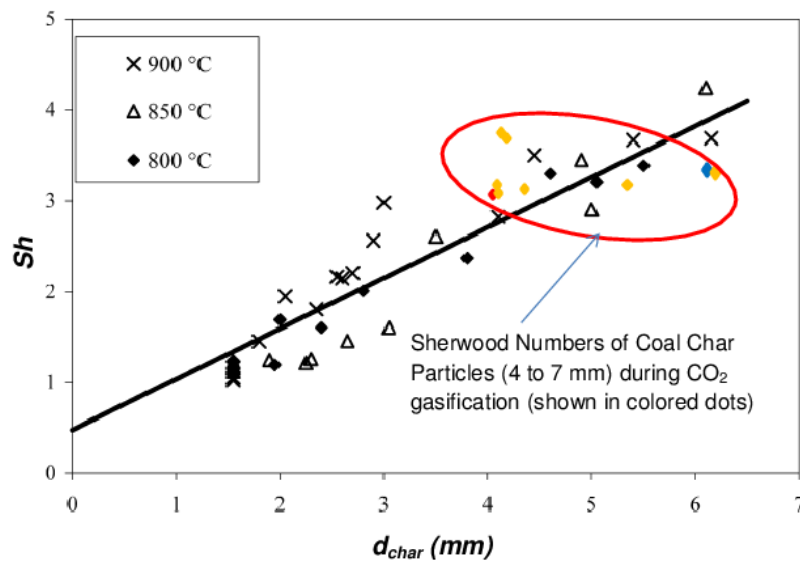


Figure 5-3. Sh for the CO_2 gasification of coal chars with literature data

For combustion of wood char particles, Sherwood numbers are a little bit higher than those performed by Dennis and company. However, these are still very close to those performed by La Nauze and Kung (see Figure 5-4) [71]. For gasified

coal char particles. these are a little lower than those investigated by La Nauze et al. [71].

From a pragmatic standpoint, experimental research modeling should aim to simulate real world applications. This includes proper selection of particle size, oxidant flow rates and other conditions. According to Smith [10], transfer of oxidants to burning particle needs to be characterized. One way to do this is to estimate the Sherwood numbers of these experimental conditions (see Figures 5-5, 5-6 and 5-7).

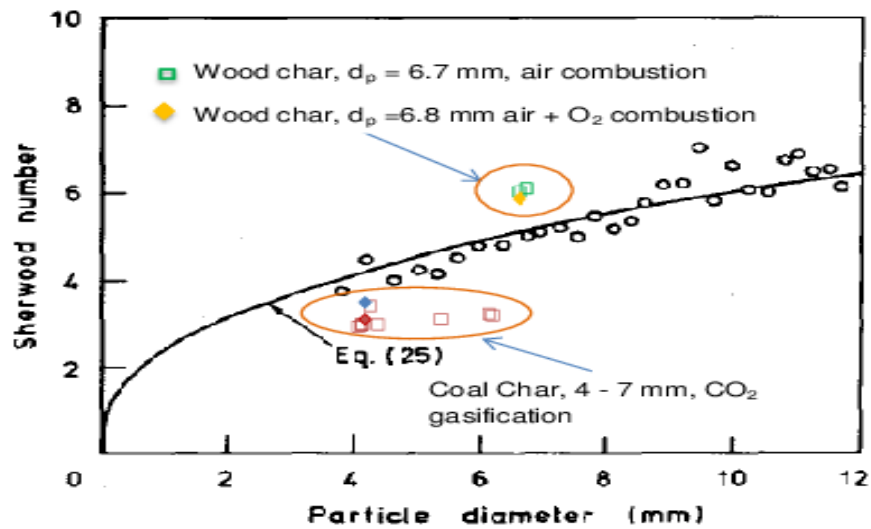


Figure 5-4. Sh for combusted wood char particles with petroleum coke spheres [71]

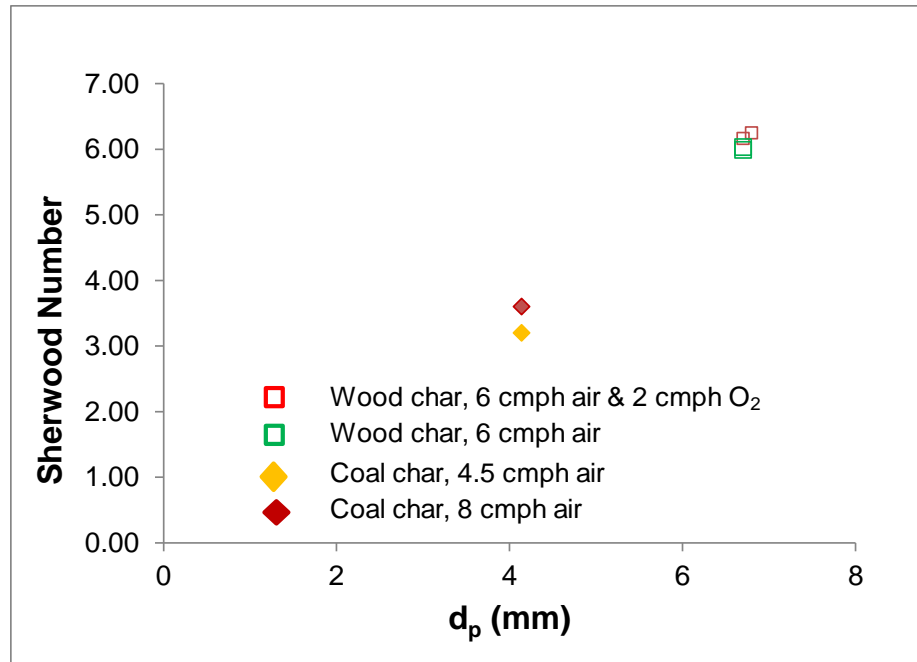


Figure 5-5. Sh of combusted wood and coal char particles

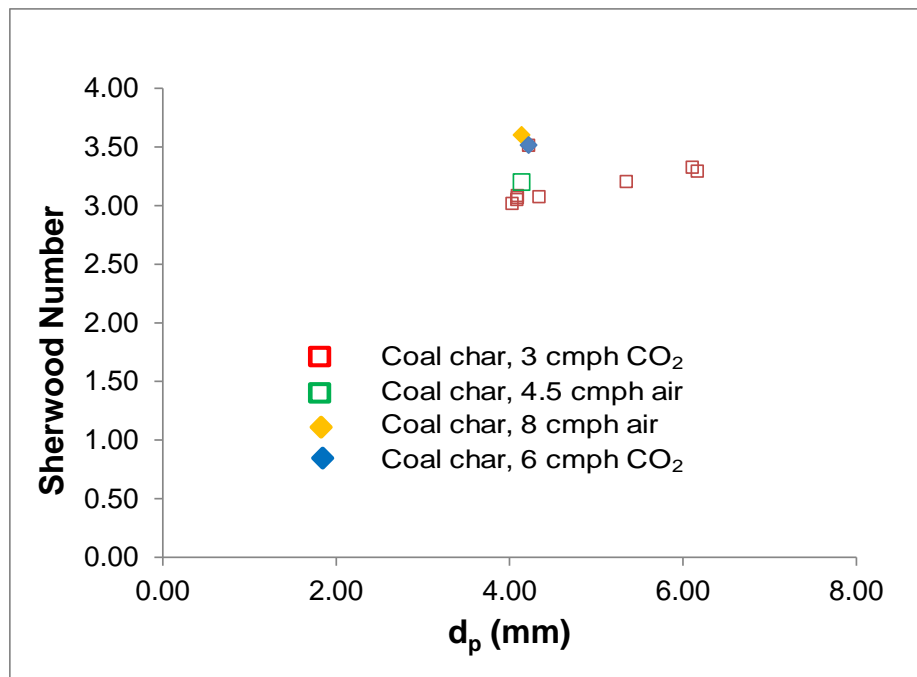


Figure 5-6. Sh. of combusted and gasified coal char particles

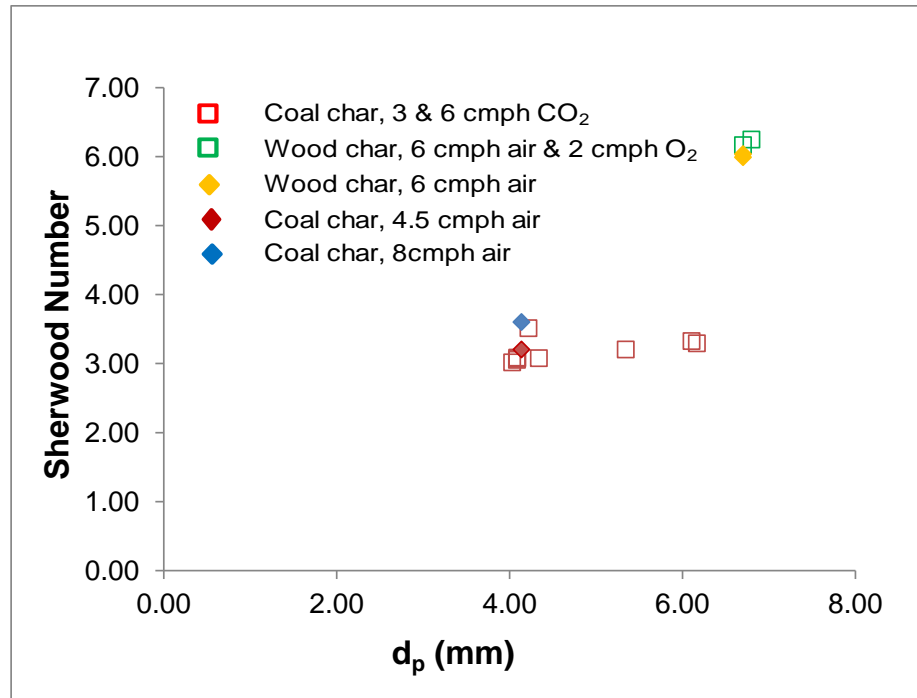


Figure 5-7. Sh of combusted and gasified coal char particles

5.1.3 Combustion and gasification surface temperatures

Table 5-1 provides a comparison of calculated combustion and gasification surface temperatures for large char particles and small char particles from literature. As expected, larger particles generally have significantly less surface temperatures as compared to small particles under combustion processes. Additionally, it is also observed that O_2 enriched conditions for large particles achieve higher surface temperatures than less enriched conditions for identical reactor temperatures and char particle materials.

Table 5-1. Average combustion and gasification surface temperatures

Thickness (mm)	Carbon & char sources	d _p (mm)	Oxidizer	TR (K)	Ts (K) (Calculated)	References
	Coal char	0.1	Air	1600	2300	[15]
	H coal char	0.1	6 to 36 % O ₂	1560	2055	[17]
1.23	Carbon		Air	923	NP	[28]
	Coal char	0.04	5 to 10 % O ₂	1460	1600	[16]
	B coal char	0.04	CO ₂	1623	1500	[22]
	L coal char	0.06	CO ₂	1547	1470	[23]
	L coal char	0.2	CO ₂	1350	1200	[24]
1.52	Carbon		100 % O ₂	887	1900	This Study
	Coal	4	Air	1073	1150	This Study
	Wood	6.7	Air	1098	1140	This Study
	Wood	6.8	Air + O ₂	1098	1371	This Study
	Coal char	4	CO ₂	1173	1084	This Study

Legend: Legend: NP - Not provided, d_p - particle diameter, H -Highvale, B - Bituminous, L - Lignite, TR - Reactor temperature and Ts - Surface temperature

5.1.4 Kinetic parameters

Comparison of calculated kinetic parameters is provided in this section for combustion and gasification of large and small particles. It is anticipated that kinetic parameters for large particles will not be the same as those for small particles because generally small particles operate under Zone I regime while larger particles tend to operate between Zones I and II. This difference is further discussed in the next two sections.

5.1.4.1 Combustion of various large particle shapes

Table 5-2 provides a data of obtained combustion kinetic parameters of two major model shapes studied in this work along with similar studies found in literature. Case item numbers 1 through 4 are for disk-shaped chars, which are mostly determined to be kinetic controlled or Zone I (R_{kin}/R_{diff} = very large). Case item numbers 5 and 8 are for combustion of very small spherically modeled particles,

which are determined to be under kinetic controlled regime. Case item numbers 6, 7 and 9 are for large spherical model shapes (i.e., wood char and irregular coal char particles), which are found to operate near kinetic-diffusion controlled regime or Zone II because $R_{kin}/R_{diff} > 1$. It is indicated that oakwood char particle (see item case numbers 6 and 7) and R_{kin}/R_{diff} values (1.6 and 2.2) are several orders of magnitude less than R_{kin}/R_{diff} value (39) of the coal char particle (see item case number 9). However, oakwood char particles (item nos. 6 and 7) operate near Zone II, that is $R_{kin}/R_{diff} = 1$. Nonetheless, for oakwood char particles, it is clear that as R_{kin}/R_{diff} and Thiele modulus values increase with oxygen enriched condition, activation energies decrease. For coal char particle, Thiele modulus value (i.e. 10246) is significantly greater than those of oakwood char (i.e. 682.5 and 780.2) even with a lesser Sherwood number. This indicates that destruction rate of coal char particle external surface as compared to destruction rate of its internal pores is several orders (13 to 15) magnitude greater as compared to oakwood char. This implies that the ratio of reaction rates to pore diffusion rates are also 13 to 15 times faster for large coal char particles as compared to large oakwood char particles. For higher S/V ratio (see item #s 7 & 9), R_{kin}/R_{diff} is also higher but with lower activation energy value, implying also faster diffusional rate condition.

As discussed earlier in section 4.1, disk-shaped char particles operate under pure kinetic controlled regime during accelerated reduction periods. The average activation energy value is 62.6 kJ/mol (see item no. 4), which is less as compared to those (124 kJ/mol) used by Jaramillo and company when using air as oxidant. This lower value indicates that char particle combustion with pure O_2 provides more

reactive conditions as indicated with much lower activation energies. Jaramillo et al. [30] estimated intrinsic activation energy of disk-shaped char particles at 124 kJ/mol when using an Arrhenius type model with reactor temperature conditions (between 848 and 923 K) (see Table 5-2 for $n=1$). However, when ASCM is used for this type of char, activation energy is 125 kJ/mol (see item # 2). This indicates that Arrhenius type model and derived ASCM as applied to disk-shaped particles agree well when both are used for reduction analysis and kinetic parameter characterization under Zone I. The activation energy estimated with numerical simulation is relatively higher as compared to activation energies of much larger oakwood chars (i.e., with diameters ranging from 6.7 to 6.8 mm, see items 6, 7 and 9). This is expected because larger particles are affected by diffusional effects, which cause these apparent kinetic parameters to be less than intrinsic values [17].

The apparent activation energies of irregular shaped coal char (modeled also as spherical shapes) particles is 150 kJ/mol (see item no. 9). For wood char particles, these vary between 144.5 and 171.5 kJ/mol (see item nos. 6 and 7). Based on these results, lower porosity char particles provide much higher Thiele modulus (see items 6, 7 and 9). This means that reaction rates at char particle surfaces are much faster as compared to reaction rates inside their pores. However, relative external diffusion rates at surface are faster, i.e. $R_{kin}/R_{diff} = 39$ (see item no. 9) versus 1.6 and 2.2 for case item numbers 6 and 7.

The overall combustion rates for the disk-shaped and irregular char particles are 3.3 (using O_2 as oxidant) and 1.3 (using air as oxidant) grams per hour, respectively. For spherical chars, processing rates are 2.5 (using air as oxidant) and

4.1 (using air and O₂ as oxidants) grams per hour for air and enriched conditions, respectively. This implies that oxygen as combustion oxidant significantly contributes to conversion rates.

Table 5-2. KPs and other parameters for the combustion of large char particles

Item Nos.	Model Shape	Char Basis	Oxidant	Thickness (mm) X db (mm) X H (mm)	Ts,ave (K)	Ea (kJ/mol)	A, ASCM (m ³)	A, Arrhenius Type (T ² Pa ²)	Method	X _{max}	S / V (1/mm)	m _{max} (g/sec)	Porosity (%)	R _{kin} /R _{diff}	Thiele Modulus	Effectiveness Factors	Shemwood Nos.	Processing rate (g/h)	Reference
1	Disk	Carbon black	Air	1.23 X 4 X 3	NP	*124		1.66E+06	Arrhenius-type	0.6	0.81	3.0E-06		very large				0.011	[30]
2	Disk	Carbon black	Air	1.23 X 4 X 3	NP	125.0	5.00E+09		ASCM	0.6	0.81	3.0E-06		very large				0.011	[30]
3	Disk	Carbon black	O ₂	1.52 X 22.5 X 25	1298 ^N	59.3		4.56E+00	Arrhenius-type	1	0.66	9.2E-04	83	very large				3.3	This Study
4	Disk	Carbon black	O ₂	1.52 X 22.5 X 25	1298 ^N	62.6	3.72E+03-3.50E+04		ASCM	1	0.66	9.2E-04	83	very large				3.3	This Study
5	Sphere	biomass	Air	<0.1 (d _p)	873	182.6			Num. Sim.(TGA)	1	NP	9.1E-06	NP	very large	NP	NP	NP	0.033	[72]
6	Sphere	biomass	Air	6.7 (d _p)	1140 ^N	171.5	1.12E+06		ASCM	0.4	0.9	7.1E-04	82	1.6	682.5	4.4E-03	6	2.5	This Study
7	Sphere	biomass	Air + O ₂	6.8 (d _p)	1371 ^N	144.5	1.42E+05		ASCM	0.63	0.9	1.1E-03	82	2.2	780.2	3.8E-03	6.2	4.1	This Study
8	Sphere	coal & graphites	Air	<0.1 (d _p)	1150 ^I	179.4	NP	NP	Global Reaction Rate	1	NP	NP	NP	very large	NP	NP	NP	NP	[10]
9	Sphere	coal	Air	4 (d _p)	1388 ^N	150.0	7.08E+04		ASCM	0.91	2	3.6E-04	14.3	39	10246	2.9E-04	3.4	1.3	This Study

Legend: NP=not provided, N/A= not applicable, t = thickness, d_p= diameter, H= height of stagnant layer, Ea = activation energy, A = frequency factors, X_{max}= maximum conversion, Ts, ave. = average char surface temperature (i.e. superscripts descriptions: I - isothermal, NI - nonisothermal), m_{max}= average burning rate, R_{kin}/R_{diff}= ratio of resistances of kinetic rates to diffusion rates, S= external particle surface area & V = external particle volume

5.1.4.2 CO₂ gasification of large particles

Table 5-3 provides the average obtained gasification activation energies of large irregular shaped char particles (modeled as spherical shapes) and small particles obtained from literature. Calculated frequency factors and activation energies based on RPM did not provide consistent results as discussed and presented earlier in section 4.4 with conditions operating mostly near Zone II. As a result, some kinetic parameters obtained with RPM are not included here. It is found that large particles have much lower activation energies (65.1 kJ/mol, see item no. 4) versus small particles (131 kJ/mol, see item no. 1) as found in literature for CO₂ coal gasification [15]. As pointed out earlier for combustion of large particles, lower activation energy values for these particles are affected by diffusion rates (i.e. R_{kin}/R_{diff} > 1 and Thiele modulus >> 1), which were determined to decrease activation energies [17]. One of

the factors for lower activation energy values is due to less conversion as discussed in previous sections. This observation is obviously the same for CO₂ gasification of char particles. However, calculated activation energies for each item as presented here is only valid for specific char source and maximum observed conversion. This means that kinetic parameters (i.e. activation energy and frequency factor) as shown in Table 5-3 are only valid for char source and up to the maximum conversion provided. Also, ASCM provides a little higher value on E_a as compared with the RPM method (see item #s 2 and 3) for biomass char [15, 73]. RPM and Arrhenius-type models do not provide suitable kinetic parameters (E_a & A) for larger particles (i.e., items 5 & 6). This is because RPM and Arrhenius-type model assume pure kinetic controlled condition and diffusional effects are neglected.

Table 5-3. KPs and other parameters for the gasification of large char particles

Item Nos.	Material	Oxidant	d _p (mm)	T _{s,ave} (K)	E _a (kJ/mol)	A, ASCM (ms) k _p , RPM (1/s)	Method	X _{max}	n	ṁ (g/sec)	R _{kin} /R _{diff}	Ø	η	Sherwood Nos.	Reference
1	Coal char	CO ₂	0.09	2000 ^{NI}	131	4.30E+06	Arrhenius-type	1	0.5	NP	Very large	NP		NP	[15]
2	Biomass char	CO ₂	0.25	1098 ^I	156	37	RPM	1	0.9	2.96E-06	Very large	0.6	0.9804	NP	[73]
3	Biomass char	CO ₂	0.25	1098 ^I	168	9.87E+04	ASCM	1	1	2.96E-06	Very large	0.6	0.9804	NP	This Study
4	Coal char	CO ₂	4	1068 ^{NI}	65.1	3.12E+02	ASCM	0.3	1	1.30E-04	48.2	1559	0.0019	3	This Study
5	Coal char	CO ₂	4	1068 ^{NI}	NS	NS	RPM	0.3	1	1.30E-04	48.2	1559	0.0019	3	This Study
6	Coal char	CO ₂	4	1068 ^{NI}	NS	NS	Arrhenius-type	0.3	1	1.30E-04	48.2	1559	0.0019	3	This Study

Legend: NP=not provided, NS = not suitable, d_p= diameter, E_a = activation energy, A = frequency factors, X_{max}= maximum conversion, T_{s,ave} = average char surface temperature (i.e. superscripts descriptions: I - isothermal, NI - nonisothermal), ṁ_{ave}= average burning rate, R_{kin}/R_{diff}= ratio of kinetic to diffusion rate resistances

5.2 Thiele modulus, effectiveness factor, Sh and R_{kin}/R_{diff}

This section provides the discussion of diffusional effects via the Thiele modulus (Ø), effectiveness factors (η) Sherwood numbers (Sh) and R_{kin}/R_{diff} ratios.

The Thiele modulus for combustion of large wood char particles vary between 683 and 780 with corresponding effectiveness factors varying between 0.0044 and 0.0038 (see Figures 5-8 and Table 5-4) for air and O₂ enriched conditions, respectively. This indicates that conversions of large wood char particles are mostly due to reaction rates at particle surface but pore diffusion also exists. A low effectiveness factors (η) indicates that pores are not well penetrated by oxidants.

For the combustion of coal char particles, average Thiele modulus values vary between 1,559 and 10,246 with corresponding effectiveness factors varying between 0.002 and 0.0003. The combustion of large coal char particles is also operating mostly as pore diffusion controlled and these are more severe as compared to combustion of large wood char particles. It is interesting to note that because wood char (82 % porous) is significantly more porous as compared to coal char particles (14.3 % porous), effectiveness factor values for wood char particles are significantly greater than those of coal particles.

In summary, reactivity and penetration of pores is preferable for high porous structure conditions and these also promote swelling and fragmentation of particles.

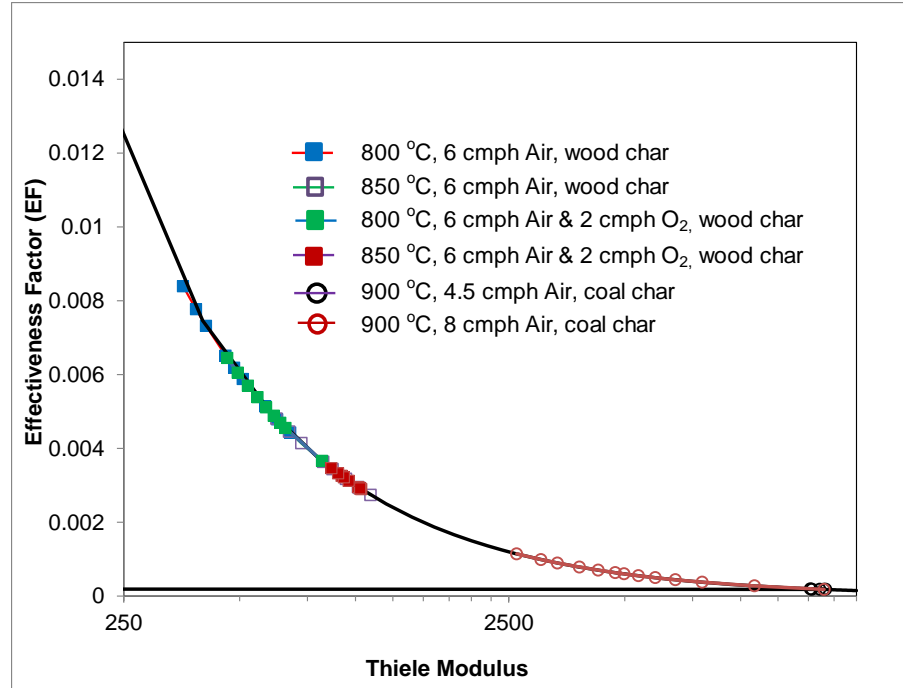


Figure 5-8. Average Thiele and EFs of wood and coal char

Table 5-4 provides the average extent of relative diffusional effects via R_{kin}/R_{diff} , ϕ and Sh in relation to other parameters (i.e., porosity, size, type of oxidants and conversion rates) for all large particle combustion studied here. Due to complexity and lack of suitable analytical tools for $C + H_2O \rightarrow CO + H_2$ reactions, these data have not been analyzed. For char particles between 4 to 6.8 mm, external reaction rates are much faster than pore diffusion rates (i.e., $\phi \gg 1$), more especially for less porous coal char particles when compared to oakwood char particles. It is further observed that oakwood char particles have the following diffusional characteristics and properties:

1. R_{kin}/R_{diff} values increase from 1.6 to 2.2 (38 % rise) with O_2 enrichment, promoting faster external diffusion rates

1. \emptyset values increase from 683 to 780 (14 % rise) with O_2 enrichment, promoting faster external reaction rate and
2. Effectiveness factor (η) or (EF) values decrease from 0.0044 to 0.0038 (14 % decrease) with O_2 enrichment, indicating less penetration of the pores because most of the O_2 is consumed at particle surface

On the other hand, coal char combustion has the following relative diffusional effects:

1. \emptyset values are much higher as compared to wood char particles and
2. External diffusion rates are faster than oakwood char (R_{kin}/R_{diff} of coal > R_{kin}/R_{diff} of oakwood char)

Table 5-4. Average diffusional properties of combusted large char particles

Materials	Oxidant	Porosity (%)	Size (mm)	R_{kin}/R_{diff}	\emptyset	η	Sh	\dot{m} (g/sec)
Carbon particles	H_2O	82.8	5.5	ND	ND	ND	ND	1.2E-04
Carbon particles	$H_2O + Air$	82.8	5.5	ND	ND	ND	ND	3.3E-04
Carbon particles	$H_2O + O_2$	82.8	5.5	ND	ND	ND	ND	8.5E-04
Spherical wood char	Air	82	6.7	1.6	683	4.40E-03	6.0	7.1E-04
Spherical wood char	Air + O_2	82	6.8	2.2	780	3.80E-03	6.2	1.1E-03
Coal char	Air	14.3	4	39	10,246	2.90E-04	3.4	3.6E-04
Coal char	CO_2	14.3	4	48.2	1559	1.92E-03	3	1.3E-04

For the CO_2 gasification of large coal char particles, the following properties are clear (see Table 5-5):

1. External reaction rates are much faster than internal diffusion rates because oxidants are mostly consumed externally
2. External diffusion rates are significantly faster than external reaction rates, i.e., $R_{kin}/R_{diff} > 1$

Table 5-5. Diffusional properties of gasified large char particles

Materials	Oxidant	Porosity (%)	Size (mm)	R_{kin}/R_{diff}	\emptyset	η	Sh	\dot{m} (g/sec)
Coal char	CO ₂	14.3	4	48.2	1559	1.92E-03	3	1.30E-04

5.3 Energy Analysis

In the design of combustors and gasifiers, it is important to be cognizant about highest peak energy and total energy released or absorbed during such processes. This information provides energy parameter design guidelines to size gasifier and combustor systems properly. Energy data also allow designers to evaluate process efficiency as well as required insulation and refractory materials that are needed to contain the thermo-chemical processes for combustion and gasification of large char particles.

5.3.1 Absorbed peak and total energy during gasification

Table 5-6 provides the peak and total energy absorbed during gasification. Test no. 11 provides the greatest total energy absorbed per unit weight because this receives greatest input thermal energy, i.e. IT=1000 °C. However, test no. 9 provides greatest total energy absorbed per unit weight converted at 14.3 kJ/g and this is attributed to its largest sample weight, which is a measure of the surface area of the particle. It is also observed that number of gasified sample pieces (see Test Nos. 5 and 9) influence the total energy absorbed. However, as discussed in section 4.4, up to a certain extent, total number sample pieces can adversely affect char conversion performance because of restricted oxidant exposure on other char samples. Figure 5-9 provides the relationship of the activation energy and total energy absorbed. A

$R^2=0.5316$ indicates that the total energy absorbed has a moderate influence on activation energy. Also, as the total energy absorbed increases, activation energy decreases, which indicates an increase in char reactivity.

Table 5-6. Peak and total energies absorbed

Test Nos.	IT (°C)	Peak Energy Input (J/s)	Total Energy Absorbed (kJ/g)	Total Energy Input (kJ/g)	Total Reaction Time (sec)	Ea (kJ/mol): ASCM
CO ₂ gasification (3 m ³ /h), Wo = 0.048 g < 0.05 g						
2	900	1.4	8.4	8.4	120.0	75.1
5	930	1.6	10.5	10.5	150.0	46.5
10	850	1.4	13.7	13.7	150.0	95.6
11	1000	2.6	10.7	10.7	120.0	43.3
CO ₂ gasification (6 m ³ /h), Wo = 0.055 g						
4	920	2.2	8.7	8.7	70.0	114.1
CO ₂ gasification (3 m ³ /h), Wo = 0.112 g						
9	900	1.4	14.3	14.3	150.0	30.6
Legend: IT - injection temperature						

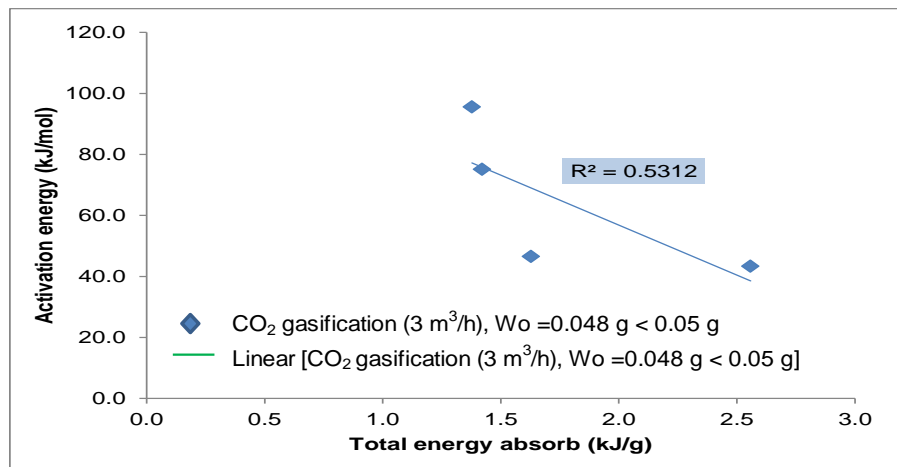


Figure 5-9. Relationship of the activation energy and the total energy absorbed

5.3.2 Peak and total energy releases during combustion

Table 5-7 provides peak and total energy releases for combustion test cases studied. As indicated, highest peak power released is obtained with the combustion of disk-shaped particles with values ranging from 85.3 to 134.5 J/s. The lowest power released is obtained with air combustion of spherical char particles at IT= 800 °C. The

highest total energy released per unit weight converted is at 40.6 kJ/g when combusting char with O₂ at 584 °C and this case also provides least peak power released for disk-shaped particles. This shows that injection temperatures play an important role for efficient combustion of disk-shaped particles.

For spherical char samples, higher injection temperatures and O₂ enriched conditions provide both higher values of peak power and total energies released. With irregular shaped particles, it is also observed that greater number of combusted sample pieces influence total energy released.

For all cases, total energies released per unit weight converted vary between 31 and 40.6 kJ/g, which agree well with Dulong's empirical formula in the form:

$$\text{HHV} = 33.96 C + 141.890 (H-O/8) + 9.42 S \text{ kJ/g [74]} \quad (5-E1)$$

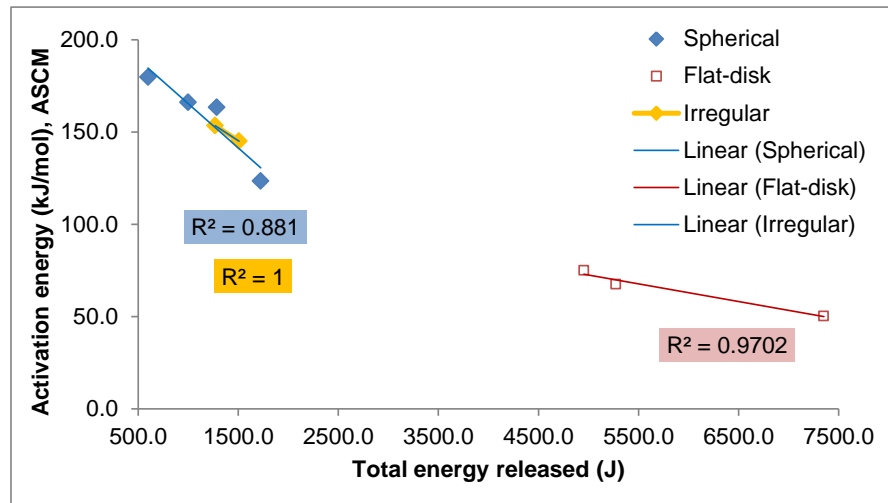
where: C, H, O and S are the weight fractions of carbon, hydrogen (H₂), oxygen (O₂) and sulfur for solid fuels.

Figure 5-10 provides the relationship of activation energy and total energy released. This plot suggests that decrease of activation energies of irregular and disk-shaped particles result to increase of total energy released. It is obvious that energy released for all shape cases studied here are strongly influenced by activation energy, i.e., lower activation energies provide greater total energy released. Interestingly, the disk-shaped particles provide greater energy releases than spherical and irregular shaped particles. This is expected because these particles are lesser in size (1.5 mm thick versus 4 to 6.8 mm diameter) as compared to spherical model particles.

Table 5-7. Peak and total energies releases

Case No.	Model Shape	Initial weight (g)	No. of Sample Pieces	Air flow (m ³ /h)	O ₂ flow (m ³ /h)	IT (°C)	Peak Power Released (J/s)	Total Energy Released per weight converted (kJ/g)	Ea (kJ/mol)	A (m/s)
1	Disk	0.151	1		4	644	116.0	33.0	74.9	3.5E+04
2	Disk	0.182	1		4	584	85.3	40.6	50.2	3.7E+03
3	Disk	0.161	1		4	504	134.5	32.8	67.5	1.9E+04
4	Spherical	0.075	1	6		800	18.5	31.5	179.7	2.1E+06
5	Spherical	0.075	1	6		850	32.0	33.3	166.0	1.0E+05
6	Spherical	0.076	1	6	2	800	45.0	31.0	163.3	2.8E+01
7	Spherical	0.078	1	6	2	850	69.2	34.9	123.4	4.2E+02
8	Irregular	0.047	3	4.5		900	33.1	35.6	145	2.20E+04
9	Irregular	0.047	2	8		900	20.8	35.2	153.4	4.70E+04

Legend: IT - injection temperature

**Figure 5-10.** Relationship of the activation energy and the total energy released

5.3.3 System thermal efficiencies

System thermal efficiencies are calculated for each case on the combustion and gasification of large char particles. Efficiencies for combustion conditions include input energy required to compress air from atmospheric conditions to 101.325 atm and heat energy input from the combustion of propane gas to initiate reactions. For gasification of irregular char particles, energy required to make CO₂ is not included in the system thermal efficiency calculations.

Case nos. 3, 7 and 8 provide the highest thermal efficiency for combustion of disk-shaped, spherical-shaped and irregular-shaped particles, respectively (see Table 5-8). Among disk-shaped particles, case no. 3 provides the highest thermal efficiency because it has the lowest injection temperature. However, for spherical shapes, highest injection temperature with enriched condition provides highest thermal efficiency. This indicates that under certain conditions, enriched conditions have some advantages on thermal efficiencies as opposed to pure air combustion. For irregular shaped particles, it is also indicated that greater number of particles (i.e., up to 3 particles) has higher system thermal efficiency for the same initial weight and injection temperature conditions.

Table 5-8. Combustion system thermal efficiencies

Case No.	Model Shape	Initial weight (g)	No. of Sample Pieces	Air flow (m ³ /h)	O ₂ flow (m ³ /h)	IT (°C)	Peak Energy Released (J/s)	Total Energy Released (kJ/g)	System Thermal Effy (%)
1	Disk	0.151	1		4	644	116.0	33.0	0.1249
2	Disk	0.182	1		4	584	85.3	40.6	0.2959
3	Disk	0.161	1		4	504	134.5	32.8	0.3143
4	Spherical	0.075	1	6		800	18.5	31.5	0.0099
5	Spherical	0.075	1	6		850	32.0	33.3	0.0096
6	Spherical	0.076	1	6	2	800	45.0	31.0	0.0148
7	Spherical	0.078	1	6	2	850	69.2	34.9	0.0165
8	Irregular	0.047	3	4.5		900	33.1	35.6	0.0113
9	Irregular	0.047	2	8		900	20.8	35.2	0.0095

Legend: IT - injection temperature

For CO₂ gasification of irregular-shaped char particles, highest weight sample case (Test no. 9) provides the highest thermal efficiency. Under the same initial weight conditions with different injection temperatures, it is observed that higher injection temperatures provide higher system thermal efficiency. As shown in Table 5-9, Test no. 9 provides as high as 14.3 kJ/g of energy released per unit weight converted under CO₂ gasification. However, this provides only a char conversion of

0.25 for an injection temperature of 900 °C. The lowest injection temperature at 850 °C also provides a high total energy absorbed per unit weight converted at 13.7 kJ/g.

However, this only provides a low conversion of 17 %.

Table 5-9. Gasification system thermal efficiencies

Test Nos.	IT (°C)	Peak Energy Absorbed (J/s)	Total Energy Absorbed (J)	Total Energy Absorbed per Converted Weight (kJ/g)	Total Reaction Time (sec)	System Thermal Effy (%)
CO ₂ gasification (3 m ³ /h), Wo = 0.048 g < 0.05 g						
2	900	1.4	143.2	8.4	120.0	0.007
5	930	1.6	210.9	10.5	150.0	0.008
10	850	1.4	178.1	13.7	150.0	0.006
11	1000	2.6	288.5	10.7	120.0	0.008
CO ₂ gasification (6 m ³ /h), Wo = 0.055 g						
4	920	2.2	139.65	8.73	70.00	0.004
CO ₂ gasification (3 m ³ /h), Wo = 0.112 g						
9	900	1.4	199.8	14.3	150.0	0.015
Legend: IT - injection temperature						

Chapter 6: Conclusions

In this study, the gasification and combustion of the following large char particles and tar are investigated:

1. Carbon particles modeled as large disk-shaped char particles
2. Spherical shaped large oakwood char particles
3. Irregular shaped large coal char particles modeled as spherical particles
4. Phenol tar modeled as o-cresol (C_7H_8O)

In the absence of experimental data on reduction of large particles and phenol-based tar materials, experiments are undertaken to comprehend and characterize their conversion process behaviors when using air, CO_2 , O_2 , O_2 enriched conditions, steam and some combination of these oxidants. In the absence of modeling tools for reduction analysis, some models are developed (i.e., one-film ash segregated core model and simplified steady state energy equation for disk-shaped particles) in conjunction with already developed models from literature. These models are fitted to experimental data to further gain insight about conversion behaviors of large char particles. Key conclusions are emphasized for each material studied in this work for large disk, spherical and irregular (modeled as spherical) shaped char particles, including tar.

6.1 Large Disk-Shaped Char Particle Reduction

Packed tiny carbon particles with thicknesses between 1.52 and 5.5 mm are experimentally investigated with O_2 , steam, steam with air and steam with O_2 . A newly derived one-film ASCM for thin disk-shaped particle is used to analyze

experimental results for $C + O_2 \rightarrow CO_2$ and $C + CO_2 \rightarrow 2CO$ reactions. This model is derived based on the same assumptions made for derivation of existing one-film ASCM for spherical particles. This model is also compared with Arrhenius-type model and calculated activation energies are nearly identical for the same reduction conditions. A newly derived energy equation is also conjectured to calculate particle surface temperatures. The Arrhenius plot of experimental data that is generated with this new one-film model almost lie on the same location as those found in literature. Additional conclusions are as follows:

1. For $C + O_2$ reactions:
 - a. It took only 113, 140 and 640 sec to completely eliminate char sample with injection temperatures at 644, 584 and 504 °C, respectively.
 - b. The lowest reactor temperature at which carbon plus O_2 reactions occur is 584 °C.
 - c. The highest calculated char surface temperature in this study is 2333 K, which is nearly identical with calculated temperatures for combustion of tiny coal char particles under high enriched oxygen environments, i.e., between 2300 to 2400 K [17].
 - d. The ASCM on char combustion shows that all experiments are exhibited by $C + O_2 \rightarrow CO_2$ reactions. This confirms the claims of some authors that large particles tend to be dominated more by $C + O_2 \rightarrow CO_2$ as opposed to $C + \frac{1}{2} O_2 \rightarrow CO$ reactions at particle surfaces [11].

- e. The decrease both in activation energy and frequency factor values is observed to be influenced by higher values of rate of change of mass (\dot{m} , g/sec), average char surface temperatures and ash content during conversion.
 - f. It is demonstrated that one-film ASCM analysis on experimental data allows one to determine the regime of char reduction and kinetic parameters during preheating (with gasification at low temperatures) and combustion.
 - g. For higher S/V ratio, R_{kin}/R_{diff} is also higher but with lower activation energy value, implying also a faster diffusional rate.
2. For C + Vitiated Air (products of combustion of propane)
 - a. Modeling of the preheating of char with vitiated air (products of combustion from propane) via partial CO₂ gasification model provides a closer fit to the experimental data as compared to pure air gasification (stoichiometric coefficient =1.667) model. However, unlike combustion, this model did not yield any consistent kinetic parameter values which are probably caused by insufficient conversion ($X < 30 \%$).
3. For C + H₂O, C +H₂O + air and C+H₂O plus O₂:
 - a. The effect of 2 m³/h O₂ enrichment with steam mass flow at 0.1 g/s for gasification of 0.9 g char sample from 800 to 780 °C provides 96 % conversion. When compared to steam gasification alone, O₂ and steam mixture improved the conversion by 81 %.

- b. Oxygen enrichment with steam significantly increases conversion of 5.5 mm thick carbon particles up to 600 % under identical reactor temperatures.

6.2 Large Spherical Char Particles

Combustion of large spherical char particles with diameters between 6.7 to 6.8 mm at temperatures between 800 to 850 °C is investigated with air and O₂ enrichment under 1 atm for up to 40 seconds of reaction time. A one-film ASCM and RPM are used to analyze combustion behavior by fitting in experimental results. Thiele analysis is also performed to characterize surface reaction and pore diffusion rates. The following are experimental and modeling analyses results:

1. Particles are collapsing inside the pores during combustion. This implies that loss in the particle diameter during conversion is not exclusively caused by consumption of char external surface but also inside the pores. This is because the sample is highly porous at 82 %.
2. The effect of O₂ enrichment with as low as 25 % by mole fraction provides more significant contribution on conversion as compared to a 50 °C rise in reactor temperatures.
3. Thiele modulus analysis indicates that external chemical reaction rates are faster at higher reactor temperatures and O₂ enriched conditions. As reaction progresses further, external chemical reaction rates decrease with time in all cases.

4. O₂ enrichment provides higher calculated particle surface temperatures than those without enrichment. Also, as the reactor temperatures increase, surface particle temperatures also increase.
5. The estimated activation energies decrease with increase in temperature and O₂ enrichment per ASCM. However, estimated activation energies obtained with RPM do not provide consistent results. This is due to the fact that RPM does not account for the effects of diffusion and also assumes that conversion is purely kinetically controlled.
6. Based on the four cases investigated, the burning rate (\dot{m} , g/s), R_{kin}/R_{diff} , estimated surface temperatures and Thiele modulus values are inversely proportional to activation energies (based on the ASCM only).

6.3 Large Irregular Shaped Char Particles

Combustion and CO₂ gasification of irregular coal char (3.8 % volatile matter and 11.5 % ash) particles between equivalent diameters of 4 to 6.2 mm and at temperatures between 800 to 1000 °C are investigated under 1 atm for various reaction times. Experimental and data modeling analyses shows the following conclusions:

1. C + O₂ → CO₂ cases,
 - a. The maximum conversions for these experiments are between 77 and 91 %.
 - b. The average values of Thiele modulus (i.e. 1559 and 10,246) indicate that surface or external chemical reaction rates are significantly faster as compared to the particle's internal or pore diffusion rates. Also,

with the average effectiveness factors much less than 0.1, this implies that oxygen consumption rates at the pores are extremely low because most of the O_2 gas is consumed at the surface.

- c. The external diffusion rates are faster as compared to external chemical reaction rates as indicated by high values of R_{kin}/R_{diff} (39 and 48.2). This means that combustion is near kinetic-diffusion controlled (Zone II) regime.
- d. A decrease in activation energy increases values of R_{kin}/R_{diff} , char surface temperatures, Thiele modulus, X and conversion rates.

2. $C + CO_2 \rightarrow 2CO$ cases,

- a. Conversion rates increased five-fold when reactor temperature is increased from 850 to 1000 °C.
- b. For identical initial weights and no. of pieces (see Test Nos. 2 and 11), a rise in temperature from 900 to 1000 °C, provides a decrease in activation energy but increase in R_{kin}/R_{diff} , Thiele modulus, conversion (X), reduction rates and surface temperature.
- c. Most of these conditions are pore diffusion controlled and the external or surface chemical reaction rates are significantly faster than pore diffusion rates ($\phi \gg 1$ at 1559).
- d. The external diffusion rates are faster as compared to external chemical reaction rates as indicated by high values of R_{kin}/R_{diff} . This also means that most of these gasification processes are still chemical

reaction or kinetic controlled but nearer to kinetic-diffusion controlled regime.

- e. It seems that two series (primary and secondary) of tar releases are occurring at the early stages of reduction for reactor temperatures at 850, 900 and 1000 °C. At higher temperatures these releases tend to occur sooner as expected.
3. For both cases,
- a. When oxidant flows are not restricted, higher number of pieces provide greater conversions (see Test Nos. 1 and 3 from combustion case and Test Nos. 2 and 5 for gasification case).

6.4 Tar

The following conclusions are made from this experimental study with tar reduction for a continuously fed reactor that is operated non-isothermally using steam as oxidizing agent (non-catalytic):

1. Carbon conversion increases with greater residence time and temperature.
2. The production of CO and C_nH_m (mainly C₂H₂ with trace amounts of C₂H₄) increases when residence time is increased for S/T at 1.7.
3. C_nH_m production is detected during this experiment for high S/T at 1.7. However, for lower S/T at 0.865, C_nH_m production is nonexistent. This implies that increasing the amount of steam during tar reduction can increase the production of C_nH_m.
4. The production of CO and C_nH_m is higher for lower tar concentration (20 g/m³) and higher S/T ratio as compared to higher tar concentration (40 g/m³)

and lower S/T test condition for reactor temperatures between 821 and 873 °C, respectively.

5. The production of H₂ increases more at higher tar concentration as compared to lower tar concentration condition as reactor temperature increases.

6.5 Modeling Analysis Results

Diffusion parameters (i.e., Sherwood, effectiveness factor, Φ and $R_{\text{kin}}/R_{\text{diff}}$) of large particles are characterized and their relationships to kinetic parameters, conversion rates and energy parameters (released absorbed, total and peak). The natural logarithm of reaction rate coefficients for combustion of large char particles (near Zone II) lay below Zone I of small particles for identical T_s between 1390 and 1800 K. Data modeling analysis results further indicate the following conclusions:

1. Using derived simplified energy equation for one-film ASCM, highest peak power released is obtained with combustion of disk-shaped char particles for values ranging from 85.3 to 134.5 J/s. The greatest and least incidental peak power release are achieved at 504 °C (disk) and 900 °C (coal char with 8 m³/h air), respectively. The highest total energy release per unit weight converted is at 40.6 kJ/g when combusting disk-shaped char particles with O₂ at 584 °C. This shows that injection temperatures play an important role for efficient combustion of disk-shaped particles. For all cases studied, total energy release per unit weight converted vary between 31 and 40.6 kJ/g, which agree well with Dulong's empirical formula.
2. Based on average calculated energy distribution values of large disk-shaped particles, radiation provides the greatest energy lost during combustion with

values approaching 69 % followed by energy lost due to diffusion of product gases at 29 %. The energy lost due to conduction is very small at around 2 %. The greatest energy lost due to radiation occurs during the early part of reaction process when greatest energy is also released. This indicates that radiation heat transfer during reaction process has a strong importance on char surface temperatures as well as the values of kinetic parameters.

3. The natural logarithm of reaction rate coefficients of CO₂ gasified large char particles (with $d_p = 4$ mm) along with small particle diameters up to 0.2 mm from literature data [23, 24, 25] is provided. As indicated, CO₂ gasification of small particles has lower reaction rate coefficients as compared to large particles for identical temperatures between 1050 and 1270 K.
4. Resulting Sherwood numbers for these experiments with coal char CO₂ gasification experiments are very close with those in the literature, which both show that particle diameters are directly proportional to Sherwood numbers.
5. As expected, large particles generally have significantly less surface temperatures as compared to small particles under combustion processes. Additionally, it is observed that O₂ enriched conditions for combustion of large particles achieves higher surface temperatures than less enriched conditions for identical reactor temperatures and particle materials.
6. For oakwood char particles, it is clear that as R_{kin}/R_{diff} and Thiele modulus values increase with oxygen enriched conditions, activation energies also decrease.

7. For combustion of coal char particles, the Thiele modulus value (i.e. 10246) is significantly greater than those of oakwood char (i.e. 682.5 and 780.2) even with lower Sherwood numbers. This indicates that combustion rate of coal char particle external surfaces as compared to combustion rate of its internal pores is several orders of magnitude greater as compared to the oakwood char.
8. The apparent activation energies of irregular shaped coal char (modeled as spherical shapes) particles is 150 kJ/mol. For wood char particles, these vary between 144.5 and 171.5 kJ/mol. Based on these results, lower porosity coal char particles provide much higher Thiele modulus. This means that reaction rates at the surface of coal chars are much faster as compared to diffusion rates inside their pores relative to oakwood char particles. Additionally, relative external diffusion rates are faster ($R_{kin}/R_{diff} = 39$) for coal char particles versus oakwood char particles ($1.6 R_{kin}/R_{diff} < 2.2$).
9. Calculated frequency factors and activation energies based on the RPM did not provide consistent results as discussed and presented earlier in sections 4.3 and 4.4 for conditions operating mostly near kinetic-diffusion controlled regime or Zone II.
10. Combustion and gasification of large particles result to lower apparent activation energies as compared to smaller particles. This supports the claim of previous investigators [10,17].
11. For the combustion of coal char particles, the values of Thiele modulus vary between 1559 and 10246 with corresponding effectiveness factors varying between 0.002 and 0.0003.

12. The combustion of large coal char particles is mostly pore diffusion controlled and this is more severe as compared to combustion of wood char particles. It is interesting to note that because wood char (82 % porous) is significantly more porous as compared to coal char particles (14.3 % porous), effectiveness factor values for wood char particles are significantly greater than those of coal particles.
13. The activation energies of large particles are inversely proportional to total energy released or absorbed.
14. System thermal efficiencies are calculated with conjectured energy equation model for each case for combustion and gasification of large char particles.

Chapter 7: Contributions

This research effort contributed in improving the understanding of the combustion and gasification of large char particles and tar through the following:

1. Char combustion and gasification rates data are provided and characterized with air, steam, O_2 and their combinations. Specifically, this provided greater understanding of the following conditions:
 - a. There is significant advantage of combining O_2 (most especially) and air with steam in char reductions for up to 5.5 mm thick.
 - b. Ignition temperature of carbon particles starts as slow as 584 °C.
 - c. Diameter reduction of wood char particles are due to collapsing pores inside and consumption of external surface area.
 - d. There is huge advantage of O_2 enrichment versus increase in reactor temperature to increase conversion rate of large wood char (up to 6.8 mm in diameter) and carbon particles (up to 5.5 mm thick).
 - e. Provided experimental reduction data and Arrhenius parameters for particle sizes between 1.5 mm in thickness up to 6.8 mm diameter
2. Provided non-isothermal tar (o-cresol) reduction data using steam and vitiated air as oxidants between 800 to 900 °C and 1 atm for a continuously fed reactor.
3. Novel mathematical models are derived and developed to characterize combustion of disk-shaped and gasification of spherically-shaped large char particles. These models are compared with relevant existing literature data and calculated kinetic parameters and char surface temperatures agree.

4. It is demonstrated that random pore model method can be used to calculate apparent kinetic parameters for large particles greater than 4 mm. However, estimated kinetic parameters resulted to inconsistencies.
5. The relationships of calculated kinetic parameters with the following reduction conditions are characterized for each case investigated under non-isothermal and atmospheric conditions:
 - a. Energy parameters (thermal efficiencies, absorbed and released)
 - b. Ratio of resistances of kinetic rates to diffusion rates
 - c. Char surface temperatures
 - d. Processing or reduction rates
 - e. Ash contents for disk-shaped particles and oakwood particles
 - f. Thiele modulus and effectiveness factors
 - g. Sherwood Numbers for spherical and irregular shaped particles
 - h. Conversion rates
6. These analytical tools demonstrate that:
 - a. Disk-shaped particles provide higher system thermal efficiency than spherical or irregular shaped particles.
 - b. Tiny carbon particles arranged in disk-shaped configurations operate under pure kinetic regime up to 1.5 mm thick. Calculated intrinsic kinetic parameters also show catalytic effect of ash.
 - c. Partial CO_2 gasification model for the initial reactions during preheating with vitiated air for large disk-shaped char particles up to 1.5 mm thick under non-isothermal process is adequate.

7. One-film ASCM and steady state energy model equation are explored and applied at discrete time intervals for the first time to predict periodic nature of surface temperatures at various times. This approach allows a direct calculation of energy and kinetic parameter values with greatly reduced computational complexity such that Thiele modulus and effectiveness factors are also determined with changes in particle size and porosities.
8. One-film ash segregated (ASCM) model shows that reaction regime conditions as well as calculation of energy parameters and kinetic parameters can be applied for non-isothermal reduction of large char particles.
9. Sherwood number is also calculated at initial conditions as a comparative parameter to determine how well oxidants are transported into the particle surface. The values in this study simulate operation of literature data for large particles.
10. Photography imaging is used for the first time to determine the changes in particle diameters during conversion of nearly spherically-shaped large wood char particles. This technique introduced a novel approach on how to use one-film ASCM to calculate apparent kinetic parameters as an option.

Chapter 8: Recommendations for Future Work

8.1 Experimental Recommendations

Using atmospheric pressure with the same reactor temperatures, these are some of the recommendations that should be pursued to further advance the knowledge of estimating the intrinsic and apparent kinetic parameters as well as other key reduction parameters (i.e., energy and relative diffusional effects) of large particles (thickness or $d_p > 1$ mm) and tar:

1. Conduct an experimental study using disk-shaped particle with pure steam, pure air, pure O_2 and pure CO_2 gasification for oakwood and other biomass or solid waste (paper and cardboard) char particles. This may provide intrinsic kinetic parameters (Zone I) as long as thickness is maintained at 1.5 mm or less. Then compare the kinetic and energy parameter values obtained with spherical oakwood char analysis results that are operating near Zone II. The kinetic parameters should be determined using ASCM.
 - a. Repeat this test using thicker material up to 5 mm

To enhance greater understanding of Zone I and Zone II combustion and gasification regimes,

2. Conduct CO_2 and steam gasification for large spherical oakwood char particles using photo-imaging and compare results with kinetic and diffusion parameters that are obtained in this research.
 - a. Ensure that the Sherwood numbers are maintained within the bounds of literature data to enable meaningful comparison of results.

- b. Limit particle sizes between 4 mm to 7 mm.
3. Conduct an experimental data and compare obtained kinetic parameters and other factors (i.e., R_{kin}/R_{diff} , char surface temperatures, energy requirements, reduction rates, Sherwood nos., Thiele modulus and effectiveness factors) by using a larger bench scale CO_2 (> 0.75 gram per hour) gasifiers and combustors (> 3.32 grams per hour for disk-shaped particles, > 4.1 grams per hour for spherical shapes and > 1.3 grams per hour for irregular shapes).
4. Conduct pyrolysis investigations of large biomass (preferably oakwood) particles, coal, paper and cardboard for the same temperature conditions and estimate kinetic and energy operational parameters using ASCM, RPM and Arrhenius-Type models.
5. Extend some experimental work on reduction of multi-particles to investigate the effects of intra-particle and inter-particle phenomena.
 - a. Use appropriate containers to equally space particles and ensure that particles have the same Sherwood numbers
 - b. Determine the effect of system or overall porosity on conversion for these experiments
6. To improve calculation and evaluation of RPM, Thiele modulus and effectiveness factors and BET measurements, specific surface areas should be performed initially for all particle test samples. Also, it is possible that diameter of particles affect BET surface area measurement. Hence, scanning electron microscope should also be considered to visualize and measure porosity at various stages of conversion.

7. In the interest of converting char to CO, C_nH_m and H₂ gases, steam gasification combined with gas chromatography analysis should be pursued.

Also:

- a. To improve accuracy of gas measurements, electrically-actuated valves via programmable logic controllers in gas lines need to be used
 - b. Air or O₂ mixed with steam gasification should also be pursued and determine heating value of product gases
 - c. Determine char conversion and analyze results
8. For all above studies, analyze specific ash content of each sample char particles to be studied and determine ash content impacts on apparent or intrinsic kinetic data obtained as well as conversion.
 - a. Determine ash content impact on reduction rate
9. Continue tar reduction experiments using o-cresol as surrogate tar and determine reaction pathways.
 - a. Start reactor temperatures equal to or less than 1000 °C and perform experiments non-isothermally for a continuously fed reactor non-catalytically
 - b. To improve accuracy of gas measurements, electrically-actuated valves via programmable logic controllers in the gas lines need to be used
 - c. Develop a means to capture unconverted tar to determine tar conversion accurately

8.2 Modeling Recommendations

Additional modeling work is needed to explore thermo-physical and chemical properties as well as to characterize Zone I (intrinsic), Zone II and Zone III and their associated kinetic parameters for the following;

1. Repeat modeling work used in this study using double film (combustion processes only) theory via discrete time linear and nonlinear fit for Arrhenius equation solution
 - a. Use a suitable numerical method to solve kinetic parameters and then compare results obtained with one-film ASCM
2. Use shrinking core model (SCM) for reduction data analysis provided in this study and compare results with ASCM
3. Develop additional modeling tools to analyze multi-component gasification phenomena, particularly steam gasification of disk-shaped and spherical shaped particles
 - a. Calculate kinetic parameters of experimentally obtained data
4. Continue to explore the use of discrete time linear and nonlinear fit methods in solving kinetic and operating parameters for other models to be used for combustion and gasification processes of large char particles and tar
5. Develop a reduction model for cylindrical shaped char particles and obtain kinetic data
 - a. Relate reactivity to ratio of surface area-to-volume. Compare results with spherical and disk-shaped particles already determined in this work.

6. Calculate kinetic parameters using data provided in this work for reduction of o-cresol

8.3 Energy Balance Calculations

In the future, energy requirements via energy balance calculations for each of these cases should be evaluated in order to determine most efficient conditions for large char particle combustion and gasification. A new compact and well insulated reactor should be used for future experimental work suggested earlier with a bench scale system. Energy efficiency is a very important performance parameter because it gives an insight about potential energy production based on energy input requirements. Additionally, energy balance calculations and analyses should be performed to help in providing design guidelines for practical, compact and small scale efficient gasifiers and combustors, thereby, enhancing the advancement of biomass or solid waste energy resources when particles sizes (thickness or diameter) are greater than 1 mm.

Appendices

Appendix I. Derivation of One-film ASCM for Disk-shaped Char

This section provides the derivation of the one-film kinetic-diffusion equation for disk-shaped char configuration. Figure A-1 shows the oxidant flows as well as the desorbed gases when a char particle is attached with oxygen.

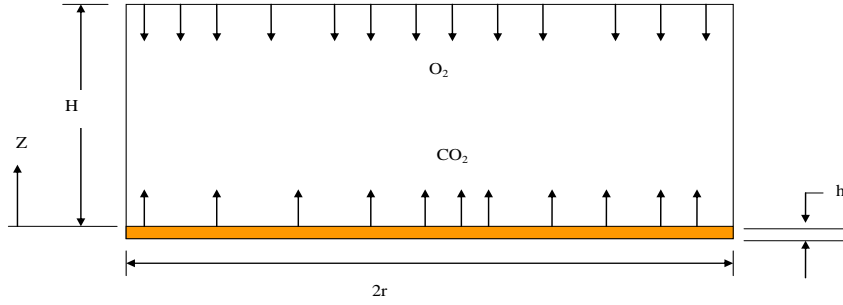


Figure A1-1. One film diffusion model combustion of disk-shaped char particle

For gasification reactions:



For combustion reactions:



$$\frac{\dot{m}_{\text{O}_2}''}{\dot{m}_{\text{C}}''} = v_I = \frac{32}{12} = 2.666 \quad (\text{A1-E7})$$

$$\dot{m}_{O_2}'' = v_I \dot{m}_C \quad (\text{A1-E8})$$

$$\frac{\dot{m}_{CO}''}{\dot{m}_C} = (v_I + 1) \quad (\text{A1-E9})$$

$$\dot{m}_{CO_2}'' = (v_I + 1) \dot{m}_C \quad (\text{A1-E10})$$

From Fick's law, for a one dimensional system,

$$\dot{m}_{O_2}'' = Y_{O_2} (\dot{m}_{O_2}'' + \dot{m}_{CO_2}'') - \rho D \frac{dY_{O_2}}{dz} \quad (\text{A1-E11})$$

Converting mass fluxes into mass rates,

$$\frac{-v_I \dot{m}_C}{\pi r^2} = Y_{O_2} \left(-\frac{v_I \dot{m}_C}{\pi r^2} + \frac{(v_I + 1) \dot{m}_C}{\pi r^2} \right) - \rho D \frac{dY_{O_2}}{dz} \quad (\text{A1-E12})$$

$$\frac{-v_I \dot{m}_C}{\pi r^2} = \frac{Y_{O_2} \dot{m}_C}{\pi r^2} - \rho D \frac{dY_{O_2}}{dz} \quad (\text{A1-E13})$$

Rearranging,

$$\frac{v_I \dot{m}_C}{\pi r^2} + \frac{Y_{O_2} \dot{m}_C}{\pi r^2} = \rho D \frac{dY_{O_2}}{dz} \quad (\text{A1-E14})$$

$$\frac{\dot{m}_C}{\pi r^2} (v_I + Y_{O_2}) = \rho D \frac{dY_{O_2}}{dz} \quad (\text{A1-E15})$$

$$\frac{\dot{m}_C}{\pi r^2} dz = \rho D \frac{dY_{O_2}}{(v_I + Y_{O_2})} \quad (\text{A1-E16})$$

Integrating from “0” to “H” and from char surface to freestream location,

$$\frac{H}{\rho D} \frac{\dot{m}_C}{\pi r^2} = \ln(v_I + Y_{O_2,\infty}) - \ln(v_I + Y_{O_2,s}) \quad (\text{A1-E17})$$

$$\frac{H}{\rho D} \frac{\dot{m}_C}{\pi r^2} = \ln\left(\frac{v_I + Y_{O_2,\infty}}{v_I + Y_{O_2,s}}\right) \quad (\text{A1-E18})$$

$$\dot{m}_C = \frac{\rho D \pi r^2}{H} \ln\left(\frac{v_I + Y_{O_2,\infty}}{v_I + Y_{O_2,s}}\right) \quad (\text{A1-E19})$$

Re-writing equation (A1-E19) and using transfer number, we have:

$$\dot{m}_C = \frac{\rho D \pi r^2}{H} \left[\frac{Y_{O_2,\infty} - Y_{O_2,s}}{v_I + Y_{O_2,s}} \right] \quad (\text{A1-E20})$$

$$B_{O,m} = \frac{Y_{O_2,\infty} - Y_{O_2,s}}{v_I + Y_{O_2,s}} \quad (\text{A1-E21})$$

$$\ln(1 + B_{O,m}) \approx B_{O,m} \quad (\text{A1-E22})$$

Now re-writing equation further with incorporation of transfer number we get:

$$\dot{m}_C = \frac{\rho D \pi r^2}{H} \left[\frac{Y_{O_2,\infty} - Y_{O_2,s}}{v_I + Y_{O_2,s}} \right] \quad (\text{A1-E21})$$

This is a new version after linearization, which is:

$$\dot{m}_C = \frac{\Delta Y}{H \left[\frac{v_I + Y_{O_2,s}}{\rho D \pi r^2} \right]} \quad (\text{A1-E22})$$

Therefore, the above equation is derived for the reduction of disk-shaped char.

Appendix II. Derivation of Energy Equation for Disk-Shaped Char Particle

This section provides the derivation of energy equation for a disk-shaped char particle inside the stainless steel pan. Considering the geometry of this problem, the energy fluxes at the surface of a disk-shaped char under an oxidizing environment are as follows (see Figure A-2):

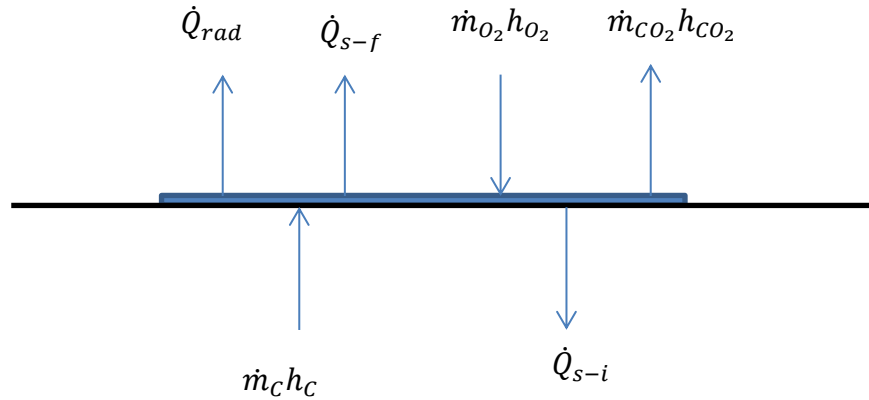


Figure A2-2. Energy flows at surface of burning flat-shaped char

Where:

\dot{Q}_{rad} = energy loss due to radiation to the surrounding medium

\dot{Q}_{s-f} = energy loss due to diffused gases into the oxidizing medium

\dot{Q}_{s-i} = energy loss due to conduction

$\dot{m}_c h_c$ = total energy content of carbon

$\dot{m}_{O_2} h_{O_2}$ = energy gain due to oxygen diffusion into the char surface

$\dot{m}_{CO_2} h_{CO_2}$ = energy loss due to the diffusion of CO_2 from the char surface

Δh_c = carbon-oxygen reaction heat of combustion, kJ/kg

However, the overall energy released due to carbon combustion can be expressed as:

$$\dot{m}_C \Delta h_c = \dot{m}_C h_C + \dot{m}_{O_2} h_{O_2} - \dot{m}_{CO_2} h_{CO_2} \quad (A2-E1)$$

And the energy loss due to diffused gases into the oxidizing medium and energy loss due to radiation is also expressed, respectively as:

$$\dot{Q}_{s-f} = H \rho c_p D (T_s - T_\infty) \quad (A2-E2)$$

$$\dot{Q}_{rad} = \varepsilon_s A \sigma (T_s^4 - T_{sur}^4) \quad (A2-E3)$$

The energy loss due to diffused gases into the oxidizing medium is derived by considering a one-dimensional steady-state energy analysis of energy conservation across a control volume above the flat-shaped char surface as follows (see figure A-3):

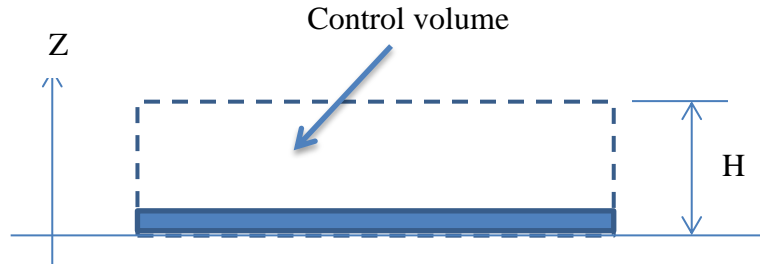


Figure A2-3. 1D steady-state energy analysis of energy conservation

where:

H = Height of the stagnant layer from the surface of the char to the freestream location

c_{pg} = constant pressure specific heat of diffused gases

ρ = density of diffused gases

D = mass diffusivity of gases

\dot{Q}_{s-f} = energy loss due to diffused gases into the oxidizing medium

Assuming that the energy loss due to transport by convection is negligible and no energy is released due to chemical reaction in the gas phase, the energy loss due to transport by diffusion for the released gases at the surface of the burning can be derived as follows:

$$\frac{d}{dz} \left(-\rho D \frac{d}{dz} \int c_p dT \right) = 0 \quad (\text{A2-E4})$$

Evaluating further the formula of the energy loss due to transport by diffusion as follows:

$$\frac{d}{dz} \left(\frac{dT}{dz} \right) = 0 \quad (\text{A2-E5})$$

Integrating once,

$$\frac{dT}{dz} = c1 \quad (\text{A2-E6})$$

Defining the temperature gradient as a function of heat flux due to transport by diffusion,

$$\frac{dT}{dz} = -\frac{\dot{Q}_{s-f}}{\rho c_p D} \quad (\text{A2-E7})$$

Integrating again,

$$T = -\frac{\dot{Q}_{s-f}}{\rho c_p D} z + c2 \quad (\text{A2-E8})$$

Applying boundary conditions, that is $z=0$ for $T = T_s$ and $z=H$ for $T = T_\infty$,

$$T_\infty = -\frac{\dot{Q}_{s-f}}{\rho c_p D} H + c2 \quad (\text{A2-E9})$$

$$T_s = c_2 \quad (\text{A2-E10})$$

Plugging the values of c_2 , the following equation for the energy loss due to diffused gases into the oxidizing medium is as follows:

$$\dot{Q}_{s-f} = H\rho c_p D(T_s - T_\infty) \quad (\text{A2-E11})$$

Appendix III. Sample of Numerical Method to Fit Models to Experimental Data

A3.1 Accounting mass changes at $t = k$ using Euler Explicit Method

Equation A3-E1 is used for disk-shaped as well as spherical and irregular shaped particles to calculate the new mass at $t = k+1$ via the ASCM. However, when using the RPM, the variable “ m ” is replaced with the variable “ X ”.

$$m_{k+1} = m_k + (t_{k+1} - t_k) \times \left. \frac{dm}{dt} \right|_k \quad (\text{A3-E1})$$

A3.2 Accounting of equivalent radius at $t=k$ using Euler Explicit Method

Starting with equation A3-E2, equation A3-E3 is derived and used for disk-shaped particles to calculate the rate of change of particle radius based on the rate of change of mass at $t = k$. Then equation A3-A4 is used to calculate the new particle radius due to weight loss as a result of reduction or conversion during gasification or combustions.

$$m = \rho_c \times \pi \times r^2 h \quad (\text{A3-E2})$$

$$\left. \frac{dr}{dt} \right|_k = \frac{1}{2\pi r_k \rho_c h} \times \left. \frac{dm}{dt} \right|_k \quad (\text{A3-E3})$$

$$r_{k+1} = r_k + (t_{k+1} - t_k) \times \left. \frac{dr}{dt} \right|_k \quad (\text{A3-E4})$$

With these equations, the char surface temperatures can now be calculated iteratively with the following equation for experimentally determined values of the rate of mass weights as indicated in equation (A3-E5) as follows:

$$\left. \frac{dm}{dt} \right|_k \Delta h_C = H \times \rho_g \big|_k C_{pg} \big|_k D \big|_k (T_S - T_\infty) \big|_k + \varepsilon_S \pi r^2 \big|_k \sigma (T_S^4 - T_\infty^4) \big|_k \quad (\text{A3-E5})$$

The values of activation energies are iteratively calculated to fit the models, using the weight for ASCM and dX/dt for RPM as shown in figures A3-4A and A3-4B, respectively for the combustion of coal char using 4.5 m³/h air for 0.05 g sample at initial temperature of 900 °C. Figures A3-4C and A3-4D provide the linear fits used for the Arrhenius equation to estimate the kinetic parameters (i.e. E_a and frequency factor) for the ASCM and RPM methods. Obviously from this figure, the RPM linear fit is not a suitable model. Nonetheless, the ASCM linear fit provides an R^2 value of 0.98, which implies how well the fit models the reaction rate coefficient data points.

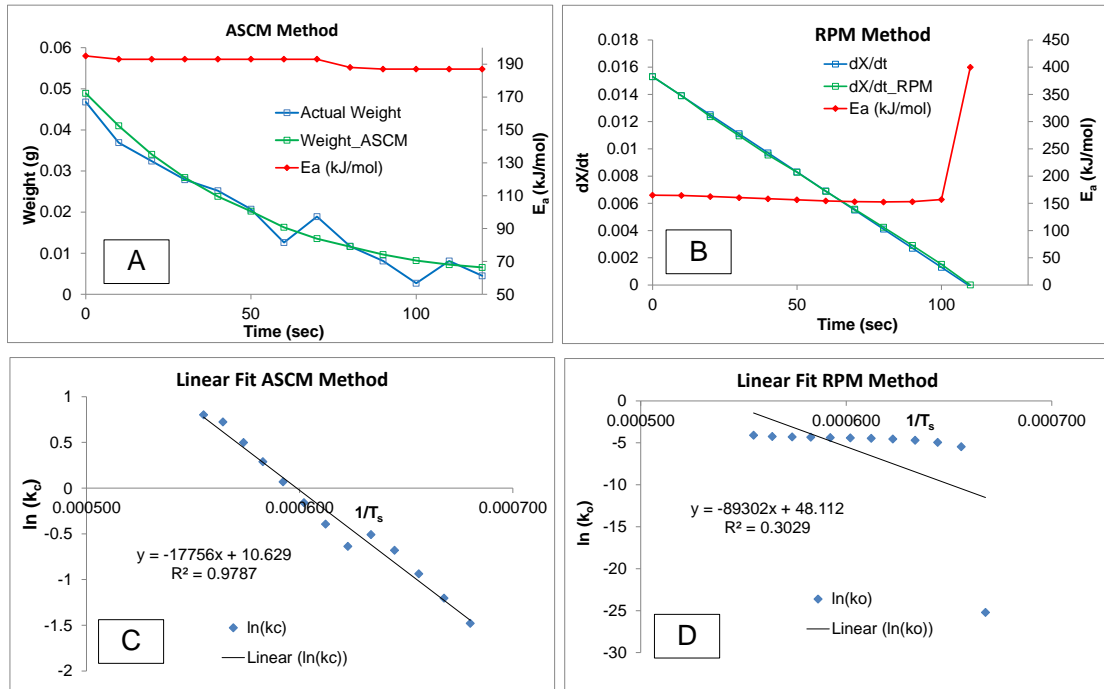


Figure A3-4. Nonlinear regression on experimental data

Appendix IV. Derivation of Energy Equation for Gasified Spherical Particle

This section provides the derivation of energy equation for the gasification of a spherical char particle. Considering the geometry of this problem, the energy fluxes at the surface of a spherical char under an endothermic oxidizing environment are as follows (see Figure A4-5):

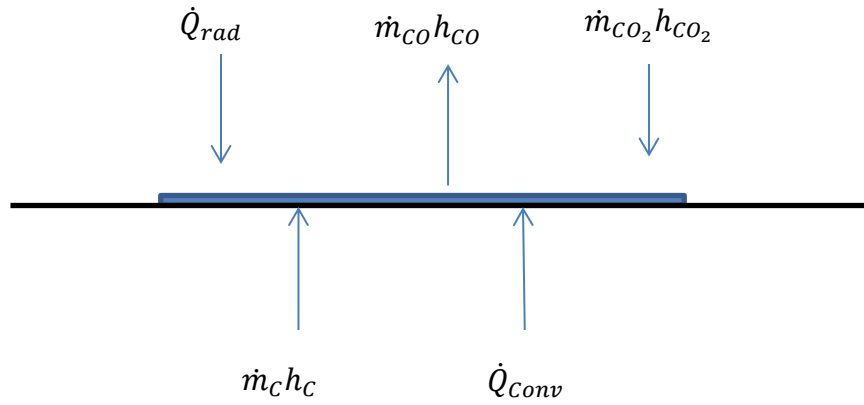


Figure A4-5. Energy flows at the surface of gasified particle

Where:

\dot{Q}_{rad} = energy gain due to radiation of the surrounding medium to the particle

\dot{Q}_{s-f} = energy loss due to diffused gases into the oxidizing medium

\dot{Q}_{conv} = energy gained due to convection of reacting CO_2 gases to the particle

$\dot{m}_C h_C$ = total energy content of carbon

$\dot{m}_{CO} h_{CO}$ = energy released due to the diffusion of CO from the char surface

$\dot{m}_{\text{CO}_2} h_{\text{CO}_2}$ = total energy content input of oxygen due to diffusion into the char surface

Δh_c = carbon-CO₂ reaction heat of formation, kJ/kg

However, the overall energy released due to carbon gasification reaction can be expressed as:

$$\dot{m}_c \Delta h_c = \dot{m}_c h_c + \dot{m}_{CO_2} h_{CO_2} - \dot{m}_{CO} h_{CO} \quad (A4-E1)$$

The radiation energy gain due to CO₂ gasification of char is taken as follows:

$$\dot{Q}_{rad} = \varepsilon_s 4\pi r^2 \sigma (T_\infty^4 - T_s^4) \quad (A4-E2)$$

Consequently, the energy gain due to heated CO₂ convection into the char particle is:

$$\dot{Q}_{conv} = h \times 4\pi r^2 (T_\infty - T_s) \quad (A4-E3)$$

Combining all the parameters in equations A3-E1 to A3-E3, the energy equation for CO₂ char gasification is as follows:

$$\dot{m}_c \Delta h_c = h \times 4\pi r^2 (T_\infty - T_s) + \varepsilon_s 4\pi r^2 \sigma (T_\infty^4 - T_s^4) \quad (A4-E4)$$

Assuming that the dynamic viscosities are identical at the freestream and particle surface, the Whitaker's equation can be used to calculate the convective heat transfer equation, h as follows [75]:

$$h = \frac{k_g}{2r} \left[2 + (0.4R_e^{1/2} + 0.06R_e^{2/3})P_r^{0.4} \right] \quad (A4-E5)$$

And the Prandtl number is calculated as:

$$Pr = \frac{c_p \mu}{k_g} \quad (A4-E6)$$

Solving equation A4-E4 shows that the char surface temperatures are very close to the reactor or freestream temperatures.

Appendix V. Sensitivity Analysis of Estimated Char Surface Temperatures

A sensitivity analysis of the calculated char surface temperatures for one of the cases is completed to determine the firmness of these values. This is done by varying the height of the stagnant layer (H), emissivity values and the evaluation of specific heat values based on how the distribution of the temperatures (char surface temperatures and reactor temperatures) are made to check the sensitivity of char surface temperatures. Figure A5-6 provides an illustration of a one-dimensional diffusion system for disk-shaped particles, showing the stagnant layer, H .

Based on this analysis, the average amount of deviation is 24.4°C when the emissivity is varied from 0.7 to 1.0 (see Table A5-1). As depicted in figure A5-7, the greatest amount of deviation with emissivity variations occurs at the beginning, which continues to decrease towards the end of the reduction period. The gas phase in the control volume is also assumed to be stagnant and convection is ignored in this analysis.

The second most sensitive case occurs when the height of the stagnant layer is varied, which subsequently provides an average temperature sensitivity value of 23.6°C . As indicated in figure A5-8, the greatest amount of deviation occurs after 80 seconds. It is also observed that as the height is decreased, the char surface temperature increases in value as expected.

The least deviation is 0.78°C as provided by changing the basis in calculating the gas constant pressure specific heat (see Figure A5-9). The greatest amount of deviation is obtained after 80 seconds in the reaction and the least amount of deviation occur towards the end between 120 and 180 seconds in the reaction.

Table A5-1 provides a summary of the sensitivity analysis result for these three cases investigated. The estimated char surface temperatures do not change drastically, and therefore, it is expected that the kinetic parameters that are calculated here will not also change as much. As discussed earlier in section, 2.5.1, Mitchell and his colleagues [76] suggested that the significant conversion of CO to CO₂ at the boundary layer could result to a significant particle surface temperature for large particles, which is obvious with these results as well. It is possible that the combustion of CO occur very close to the char surface because the surface temperatures tend to increase higher (see Figure A5-7) when the reference height is used to solve the energy equation for the values of T_s .

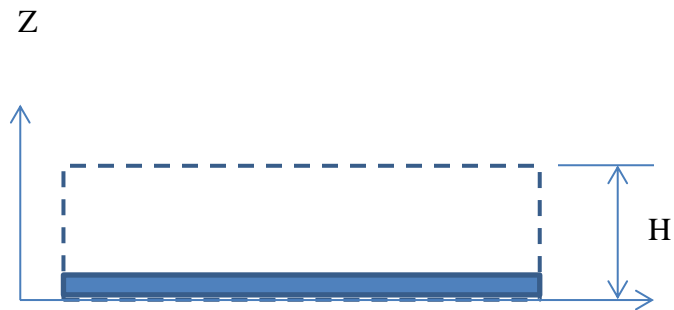


Figure A5-6. One-dimensional steady-state energy analysis

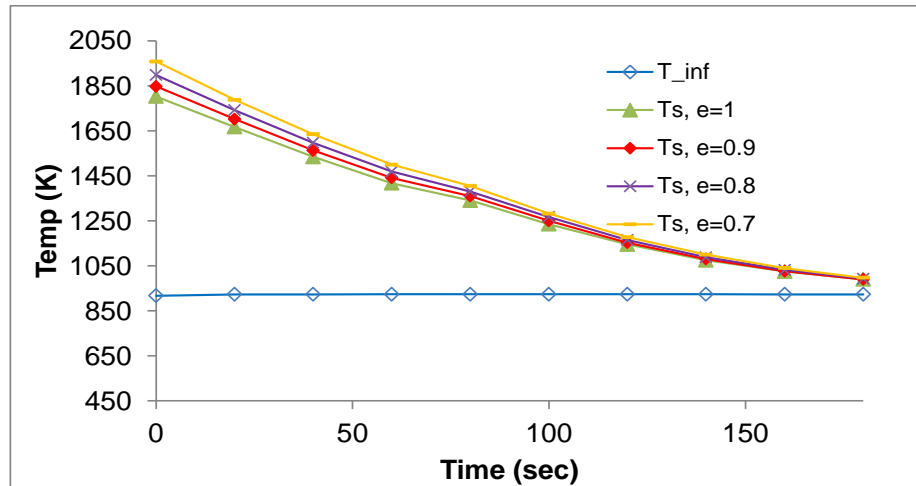


Figure A5-7. Estimated T_s based on emissivity from 0.7 to 1.0

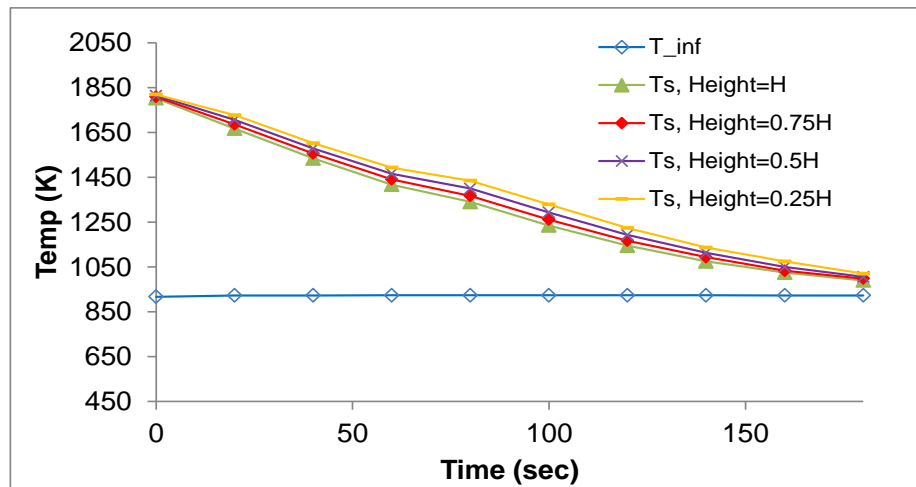


Figure A5-8. Estimated T_s based on H from $0.25H$ to H

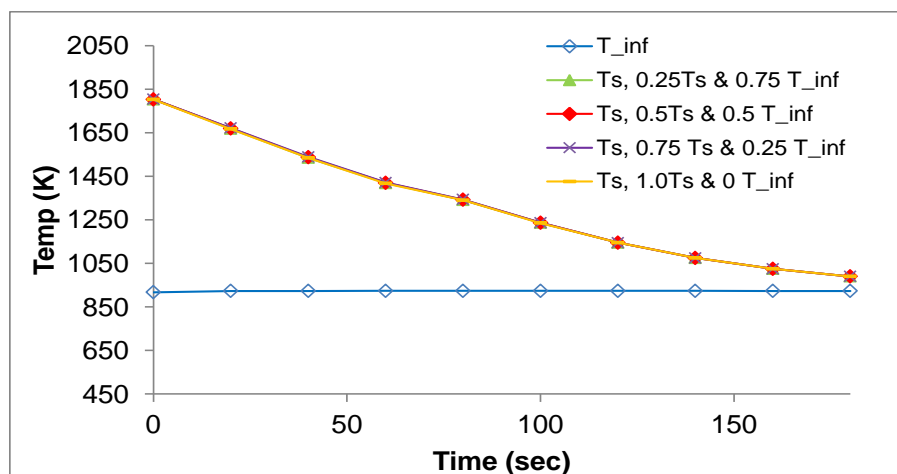


Figure A5-9. Estimated T_s based on the T_s (0.25 to 1.0) and T_{inf} (0 to 0.75)

Table A5-1. Sensitivity of calculated surface temperatures

Varied Parameters	Ave. SDs
Basis of Calculating k_g and c_{pg}	0.7767636
Emissivity (0.7 to 1)	24.405523
Height of SL (0.25 H to H)	23.574232
Legend: SL - Stagnant layer	

Based on average calculated energy distribution values, radiation provides the greatest energy lost during the reaction period with values approaching 69 % followed by the energy lost due to diffusion of product gases at 29 %. The energy lost due to conduction is very small at around 2 %. The greatest energy lost due to radiation occurs during the early part of the reaction process when the greatest energy is also released. This indicates that radiation heat transfer during the reaction process has a strong importance on char surface temperatures as well as the values of kinetic parameters.

Appendix VI. Standard Deviations of Experimental Data with Models

Standard deviation (SD) is used to analyze the modeling results as compared to the experimental data. The magnitude of standard deviation assigned with the symbol, sigma (σ) shows how much variation or dispersion exists from the average values between the experimental data with the modeling results both for the weights losses and the amounts of conversions. The ASCM predicts the weight losses while the RPM predicts the changes in conversions. A low standard deviation indicates that the data points tend to be very close to the mean, i.e. also called the expected value. Conversely, a high standard deviation indicates that the data points are spread out over a large range of values.

A6.1 Disk-shaped char

The injection temperature at 644 °C indicates that the second model case (partial CO₂ gasification) provides a closer value as compared to the first model case (air gasification) to the experimental data, especially during the first 200 seconds at the beginning of the preheating stage (see Figure A5-10). Between 200 to 340 seconds, these two models appear to produce about the same results that are also close to the experimental data. However, as the reduction time progresses further towards the end of the preheating stage, the trend deviates again increasingly for the first modeling case. After the preheating stage, the second model case still maintains more robust results except for three data points at $t = 600$ sec, 700 sec and 720 sec. As clearly indicated, the second modeling case provides more fidelity as compared to the first case.

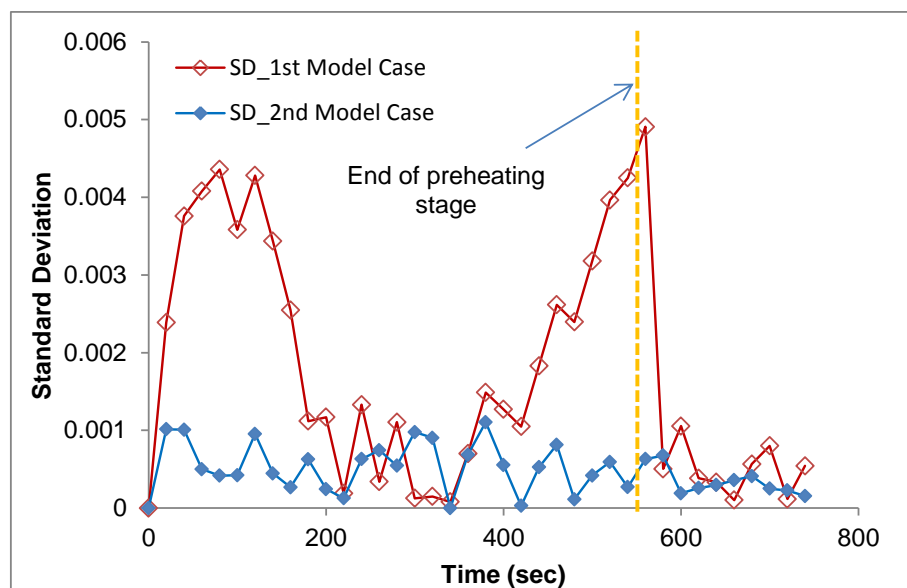


Figure A5-10. SDs of modeling results versus experimental data at 644 °C

For the injection temperature at 584 °C, the second model case also provides a closer value as compared to the first model case to the experimental data, especially between 25 to 145 seconds at the beginning of the preheating stage (see Figure A5-11). Between 165 to 205 seconds, these two models produce about the same results that are very close to the experimental data. However, as the reduction time progresses further towards the end of the preheating stage particularly between 245 and 355 seconds, these cases are nearly comparable. During the reaction period, the trend also deviates largely again for the first modeling case. Again, this clearly indicates that the second model case provides a better fit to the experimental data as compared to the first model case.

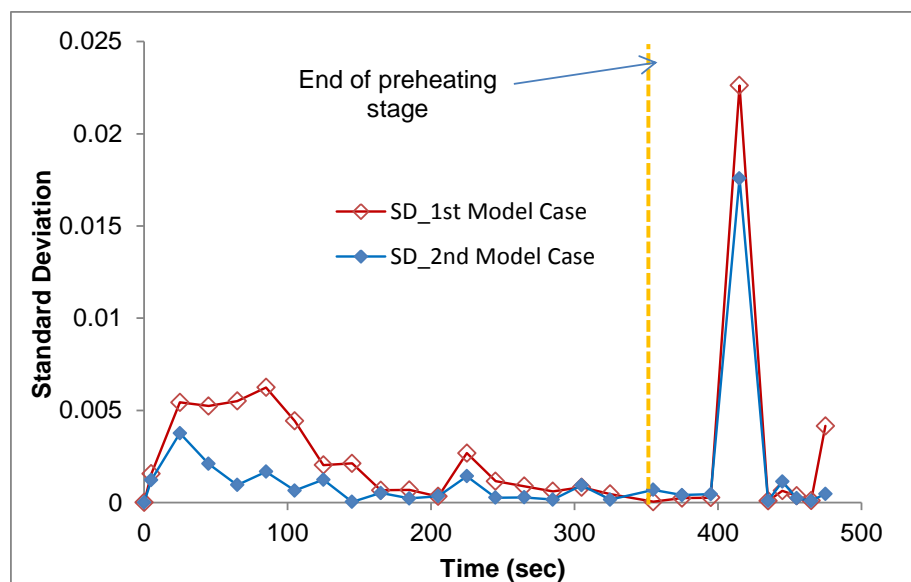


Figure A5-11. SDs of modeling results versus experimental data at 584 °C

For the injection temperature at 504 °C, the second model case also provides a closer value as compared to the first model case with the experimental data, especially between 27 to 187 seconds at the beginning of the preheating stage (see Figure A5-12). Between 226 to 227 seconds, the first model case produced a better fit to the experimental data as compared to the second case. However, at the combustion stage, the trend deviates largely again for the first modeling case between 287 and 430 seconds. This trend continued between 447 and 667 seconds. However, the result for the first case model rises significantly again towards the end of the reaction period between 827 and 867 seconds. Again, generally, this clearly indicates that the second modeling case provides a better fit as compared to the first case.

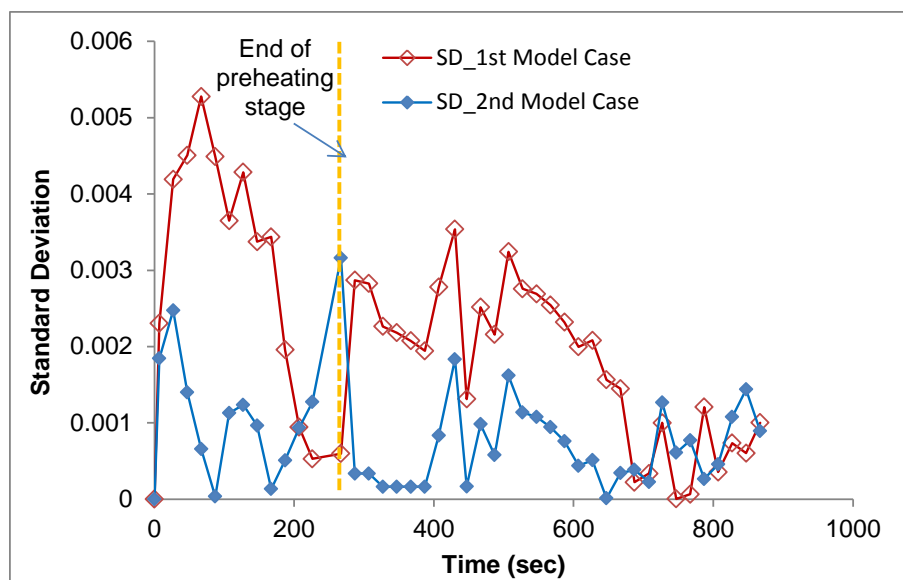


Figure A5-12. SDs of modeling results versus experimental at 504 °C

The calculation of kinetic parameters based on char surface temperature conditions provides more consistent and stable values as compared to the use of reactor temperatures. Therefore, efforts to improve the robustness of calculating the char surface temperature would provide a better assessment of kinetic parameters, especially between Zones I and Zone II combustion and gasification conditions.

A6.2 Spherical oakwood and coal char particles

Tables A5-2 and A5-3 provide the standard deviations of the average values of experimental data and the two models, i.e. the ASCM and RPM as used for coal and wood char particles. As discussed in sections 2.4.5 and 2.4.6, the ASCM uses the weight loss as a parameter to be modeled at each time interval. For the RPM, it uses the change of rate of conversion as the modeled parameter (see section 2.4.4) at each time interval. Figures A5-13 and A5-14 give the direct comparison between these two models, which shows that the RPM values are closer to experimental values as

compared to the ASCM predictions. Linear fit of the Arrhenius equation is used to calculate the kinetic parameters both for ASCM and RPM. It was found earlier that a linear fit to the Arrhenius equation provides more stable kinetic parameter results for ASCM as compared to those with RPM methods. Nonetheless, the standard deviations as predicted by the RPM are more consistent as compared to those predicted with ASCM.

Table A5-2. SDs of the average values for wood char

Test No.	Temp (°C)	Air (cmph)	O ₂ (cpmh)	ASCM	RPM
				Standard Deviations	
1	800	6		3.24E-04	5.81059E-05
2	850	6		6.24E-05	1.89574E-05
3	800	6	2	5.46E-05	8.09814E-05
4	850	6	2	1.70E-04	1.02E-04

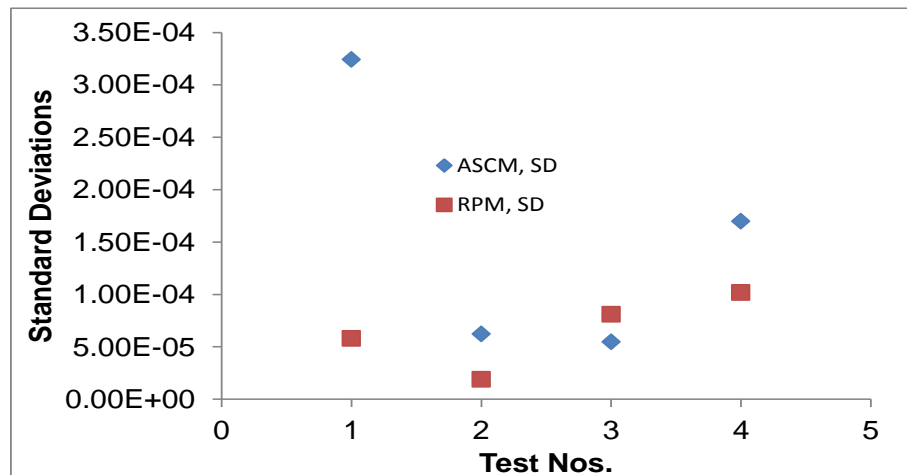


Figure A5-13. SDs of the exp. data and the two models used for wood char

Table A5-3. SDs of the average values for coal char

Test Nos.	No. of Pieces	IT (°C)	Total Weight (g)	Equivalent Diameter (mm)	ASCM	RPM
					Standard Deviations	
1	2	900	0.052	4.14	1.39E-04	1.04E-05
2	2	900	0.05	4.09	5.77E-07	1.18E-06
3	3	900	0.052	4.14	2.16E-04	1.60E-04
4	2	920	0.055	4.22	1.29E-04	8.35E-05
5	3	930	0.06	4.34	1.26E-03	1.29E-04
7	9	800	0.167	6.11	6.01E-05	2.19E-07
8	9	900	0.172	6.17	2.20E-06	5.80E-07
9	5	900	0.112	5.35	6.67E-06	1.14E-06
10	2	850	0.05	4.09	1.52E-04	2.74E-05
11	2	1000	0.048	4.03	1.42E-04	1.89E-05

Legend: ASCM - ash segregated core model, RPM - random pore model and IT - Injection temperatures

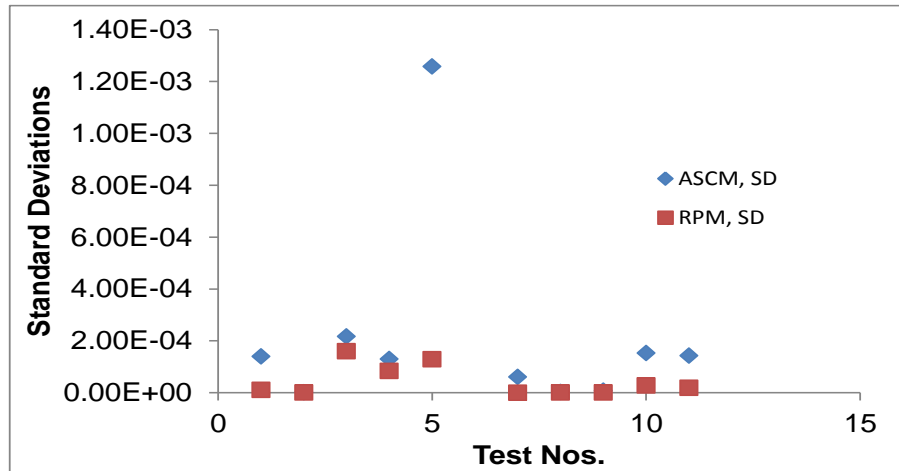


Figure A5-14. SDs of exp. data and the two models used for coal char

Appendix VII. Other Char Reduction Models for Zone I Regime Analysis

This section provides some information on various char reduction models that are used in literature to analyze char reduction experimental data. It also presents some analyses that were performed to investigate the applicability of such models such as the steam gasification of cardboard materials.

A7.1 Chemical equilibrium

The equilibrium modeling helps elucidate the role of various input and operational parameters for the gasification of carbonaceous materials. The results from the equilibrium model calculations provide only an estimate on the magnitude and the trends of various evolved compounds which can also aid in developing startup experimental test mixtures. These calculations are based on infinite residence times of reaction and involve the minimization of the Gibbs energy for the simulation of various processes (e.g., combustion, gasification, or pyrolysis). Some of the useful parameters that can be calculated with this model include: (1) the mass flow requirements of gasifying or oxidizing agents per unit mass of carbonaceous materials, (2) corresponding syngas product mole fractions under specified operating conditions of temperatures and pressures, and (3) total higher heating values of product syngas [77]. A comparison with experimental data was also made over a limited range of conditions by Molintas and Gupta [77]. The predicted synthesis gases enabled the comparison of calculated product species with experimental data for steam gasification. The equilibrium calculations showed a reasonably good agreement with gasification experiments on the actual behavior of CO and CO₂ at certain mass ratios when operating under fixed bed reactor conditions in a batch mode

at 1173 K and 1 atm conditions. Although equilibrium calculations neglect the effects of transport phenomena, solid-gas interactions, reactor geometry, reactor conditions, particle size, heating rates, and reactor residence times, the predicted results show that equilibrium models can provide a good approximation on the gasification process.

A7.2 Coats and Redfern Model and its modifications

Non-isothermal reactions are usually analyzed with Coats and Redfern (CR), four pairs Coats and Redfern (FPCR) and Reich and Stivala (RS) methods which all consider a rate law in the form of equation (A7-E1):

$$\frac{dX}{dt} = k(1 - X)^n \quad (\text{A7-E1})$$

Where, X is the char conversion degree, t is the reaction time, n is the reaction order and k is the reaction rate constant. Generally, the reaction rate constant for chemical reactions is represented by the Arrhenius equation (A7-E2):

$$k = A \exp\left(\frac{-E_a}{RT}\right) \quad (\text{A7-E2})$$

where, E_a is the activation energy, A is the frequency factor, R is the universal gas constant and T is the temperature of interest expressed in absolute terms [31]. In equation (A7-E2), the frequency factor (A) for the ASCM is replace with k_o , the frequency factor of the RPM. Regarding char gasification kinetic studies, char conversion (dry-ash free consideration) is generally estimated at various temperatures and times with the following expression in equation (A7-E3) [31]:

$$X = 1 - \frac{W}{W_o} \quad (\text{A7-E3})$$

Where, W and W_o are weights of the remaining sample at time t and initial dry ash-free (daf) weight of char at $t = 0$, respectively. Volatile matter is also removed from the dry-ash free weight to obtain W_o .

The FPCR and the RS methods are commonly used to estimate the values of KPs undergoing non-isothermal reactions [31]. Non-isothermal reactions can simulate in the changes of real world gas phase temperatures and heat transfer mechanisms that are common in most types of reactors. The FPCR [31] is an interesting variation of the Coats and Redfern (CR) method. This method uses the two-point form of the CR method. As shown in equation (A7-E4), four pairs of temperature and char conversion allow one to directly calculate the activation energy (E_a) and order of reaction (n). Alternatively, equation (A7-E5) is used for a two temperature data set.

$$\frac{\ln \left[\frac{1 - (1 - X_1)^{1-n}}{1 - (1 - X_2)^{1-n}} \times \left(\frac{T_2}{T_1} \right)^2 \right]}{\frac{1}{T_2} - \frac{1}{T_1}} = \frac{\ln \left[\frac{1 - (1 - X_3)^{1-n}}{1 - (1 - X_4)^{1-n}} \times \left(\frac{T_4}{T_3} \right)^2 \right]}{\frac{1}{T_4} - \frac{1}{T_3}} \quad (\text{A7-E4})$$

$$\frac{\ln \left[\frac{1 - (1 - X_1)^{1-n}}{1 - (1 - X_2)^{1-n}} \times \left(\frac{T_2}{T_1} \right)^2 \right]}{\frac{1}{T_2} - \frac{1}{T_1}} = \frac{E_a}{R} \quad (\text{A7-E5})$$

Where, X_j represents the fraction of char converted, T_j is the temperature matching the conversion at j , E_a is the activation energy, R is the universal gas constant and n is the

order of reaction. The recommended procedure of using this method is to make sure that $X_1 < X_2 < X_3 < X_4$. This method is most accurate when the fractions of char conversion are selected within the range when these are progressively accelerating at a maximum rate [1]. This method has been extensively used in the kinetic studies of thermal decomposition of coal and biomass [52].

Another variation of the CR method is the RS method. This method is developed by Reich and Stivala [78] to obtain KPs iteratively. The RS [3] as shown below is used for numerous pairs of temperature and degree of char conversion to directly calculate the activation energy and order of reaction as follows in equation (A7-E6):

$$\ln \left[\frac{1 - (1 - X_j)^{1-m}}{1 - (1 - X_{j+1})^{1-m}} \times \left(\frac{T_{j+1}}{T_j} \right)^2 \right] = \frac{E_a}{R} \times \left(\frac{1}{T_{j+1}} - \frac{1}{T_j} \right) + B \quad (\text{A7-E6})$$

Where, X_j represents the fraction of char converted, T_j is the temperature matching the conversion at point j , E_a is the activation energy, R is the universal gas constant, m is the order of reaction and B is taken as the y intercept. The recommended consideration in using this method is to make sure that $X_j < X_{j+1}$ is satisfied [31]. The left-hand side term of equation (A7-E6) is taken as the y vertical coordinate and the difference of the temperature reciprocal term on the right-hand side of the equation is taken as the x coordinate. Generally, the RS method is used for two data pairs to obtain kinetic parameters. However, to provide a more meaningful comparison of calculated KPs, it is recommended to use the same four data pairs of X and T selected in calculating KPs with the FPCR method. The RS method is performed with the

iterative linear regression approach on all x and y points by varying the reaction order until the value of B (second term on the right hand side of the equation) equals zero.

A7.3 Homogenous model

Another model that is usually used with non-isothermal char reduction modeling is the homogenous model shown in equation (A7-E7). This model assumes that the gasifying media (i.e., air, O_2 and CO_2) is reacting with char at all points (both outside at the surfaces and inside the particle surface). Therefore, this assumption can be represented with the following equation [78]:

$$\frac{dX}{dt} = Ae^{-\frac{E_a}{RT}}(1-X) \quad (A7-E7)$$

Since the temperature programmed reaction (TPR) is applied to samples at constant heating rate (i.e., a), the temperature (T) can be expressed in terms of time (t) in equation (A7-E8) as:

$$T = T_0 + bt \quad (A7-E8)$$

Where, T_0 is the starting temperature of reaction, b the heating rate and t is the time in seconds, respectively. Integrating equations (A7-E7) and (A7-E8) and then linearizing the result gives equation (A7-E9) [51]:

$$f_v = \ln \left[\frac{1}{T^2} \ln \left(\frac{1}{1-X} \right) \right] = \ln \left(\frac{AR}{bE} \right) - \frac{E_a}{RT} \quad (A7-E9)$$

which can be estimated by plotting the relationship of equation (A7-E9) in the left hand side and the reaction temperature.

The char reactivity is generally defined in equation (A7-E10) as follows [78]:

$$R_{reac} = \frac{1}{1-X} \frac{dX}{dt} \quad (\text{A7-E10})$$

And based on the homogeneous model, char reactivity can be estimated with equation (A7-E11):

$$R_{reac} = Ae^{-\frac{E_a}{RT}} \quad (\text{A7-E11})$$

A7.4 Arrhenius-type model

Other combustion model that is used to analyze small particle reduction data is the Arrhenius-type model as shown in equation (A7-E12) below:

$$-\frac{dm}{dt} = A \exp\left(-\frac{E_a}{R_u T}\right) m (P_{O_2})^n \quad (\text{A7-E12})$$

where m = mass of char, t = time, P_{O_2} = partial pressure of oxygen, A = pre-exponential factor (in 1/sec), E_a = activation energy, R_u = universal gas constant and T = char surface temperature [17] or reactor temperature [30] and n = reaction order of oxygen. This was used extensively by Jaramillo et al. [30] for the analysis of carbon particles assuming that the reduction is considered as Zone I regime.

Appendix VIII. Error Analysis

To reduce random errors, the experimental facility is mounted on a resilient rubber material to mitigate and absorb the external effects of weight disturbances around the vicinity. The weighing scale and thermocouples used in the experiments are also calibrated with 1 gram weight and bulb thermometers, respectively to reduce systematic errors on measurements. The weighing scale can precisely measure up to 0.001 gram and zero setting is always set before proceeding with any of the experiments. The estimated total percent error of calibration and measurement for the weighing scale is 0.15 %. The thermocouples have a measurement error of ± 5.0 °C. The thermocouple sensing probes are removed and cleaned periodically and most of the temperature measurements are very stable unlike the weight measurements.

The coal char particles possess the lightest weight as compared to the other test samples. As a result, this experiment is also expected to have the greatest measurement uncertainties and error analysis is focused and presented subsequently on this particular experiment. Figures A8-15 A and B provide the 5 % error bars for the coal char combustion experiments, which clearly show that random errors are present on most weight measurement. Figures A8-15 C and D provide the exponential regression curve fits of the experimental data. Because of the lack of knowledge about the exact value of the weight measurements, the exponential regression curve fit values are used for numerical modeling and calculation of kinetic data. Assuming that the exponential regression curve fit values are the exact weight values, a percent error calculation is performed to compare curve best fit values to experimental values and the plot is shown in Figure A8-16. Based on Figure A8-16, the percent errors

tend to increase as reaction time is increased, which is also expected because the char weights are much less, resulting to an increase of random errors. Also, from Figure A8-16, it indicates that the percent error is less for the higher air flow injection (i.e. 8 cmph or m^3/h) possibly because the higher lifting forces help to stabilize the particle during the experiment.

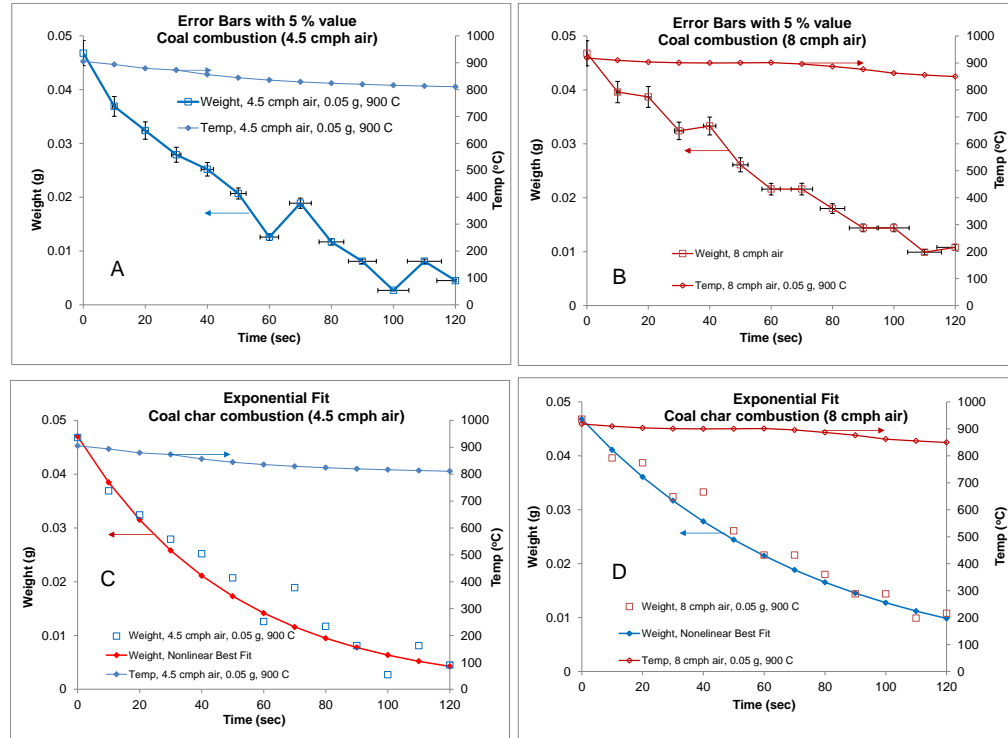


Figure A8-15. 5 percent error on measured values and exponential fits

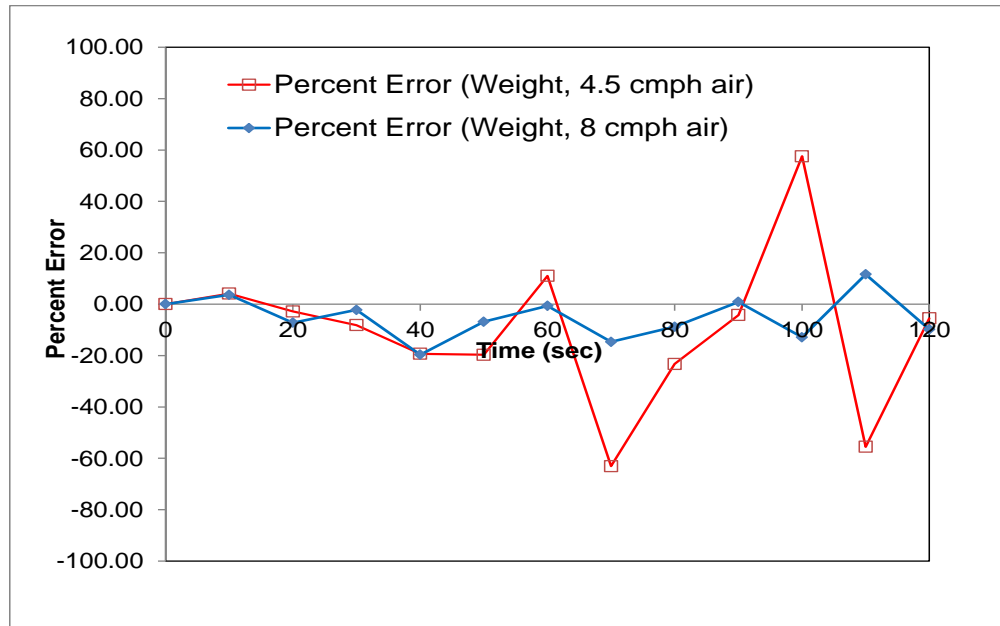


Figure A8-16. Percent error based on nonlinear best fit

In the succeeding section, some of these errors are further explained and discussed both for systematic and random errors.

A8.1 Systematic errors

Systematic errors are errors due to uncertainties with experimental measurements. These errors directly affect the true value or accuracy of the measured quantity. For the weighing scale used in this experiment, these may be caused by the following conditions:

1. Hardware defects such as wear and tear on the scale mechanism
2. Failure to calibrate
3. Weighing scale is wrongly used

Usually there are two systematic error types for a linear or a non-linear response. These could be attributed to the following:

1. Offset or zero setting error when the weighing scale does not read exactly zero when the quantity is supposed to be zero.
2. Multiplier or scale factor error when the instrument consistently reads changes in the quantity to be measured greater or less than the actual changes.
3. Poor contact between thermometer sensing and the substance being measured.
4. Instrument drift for electronic instruments that occur over time.
5. Lag time and hysteresis especially with temperature measurements when the system has not reached thermal equilibrium conditions.

A8.2 Random errors

These errors are caused by unknown and predictable changes in the measured values. These errors directly affect the precision of measurements. Precision of measuring instrument is described as the closeness of a number of measurements of the same quantity in agreement with each other. Some potential errors with the weighing scale are:

1. Electronic noise in the electrical circuit of digital measuring instruments.
2. Environmental factors of the working environment such as vibrations, changing temperatures or effects from nearby other experimental apparatus.

So far in all the experiments performed, electronic noise in the electrical circuits has not been observed. The presence of these errors is easily detected if the measurements abruptly drift during the experiments.

Bibliography

1. Williams, A., Pourkashanian, M. and Jones, J. M., “Combustion of Coal and Biomass”, *Progress Combustion Energy*, Vol. 27, No.6, 2001, pp. 587–610
2. Yang, Y. B., Sharifi, V. N., Swithenbank, J., Ma, L., and Darvell, L., “Combustion of a Single Particle of Biomass”, Vol. 22, No.1, *Energy & Fuels* 2008, pp. 306–316
3. Higman, C. and Van Der Burgt, M., “Gasification”, Elsevier Inc., Copyright 2008
4. Milne et al, “Biomass Gasifier: Tars, Their Nature, Formation and Conversion”, National Renewable Energy Laboratory Report, NREL/TP-570-2537, November 1998
5. Van Paasen and Kiel, J., “Tar Formation in a Fluidized Bed Gasifier: Impact of Fuel Properties and Operating Conditions”, Energy Center of the Netherlands – C – 04 – 013, March 2004
6. Shurtz, R. C., “Effects of Pressure on the Properties of Coal Char Under Gasification Conditions at High Initial Heating Rates”, Brigham Young University, PhD Dissertation, 2011
7. Schill, S. R., “Biomass Provides 10 Percent of Global Energy Use”, *Biomass Energy Magazine*, September 2013
8. Turns S. R., “An Introduction to Combustion”, McGraw Hill Book Co., Second Edition, 2000, pp. 656-658
9. Thiele, E.W., “Relation between Catalytic Activity and Size of Particle”, *Ind. Eng. Chem.*, Vol. 31, No. 7, 1939, pp. 916-920

10. Smith, I.W., "The Combustion Rates of Coal Chars: A Review", Nineteenth Symposium (International) on Combustion, Vol. 19, No. 1, 1982, pp. 1045-1065
11. Dennis, J.S., Hayhurst, A. N. and Scott, S.A., " The combustion of large particles of char in bubbling fluidized beds: The dependence of Sherwood number and the rate of burning on particle diameter", Combustion and Flame, Vol. 147, No. 3, 2006, pp. 185-194
12. Elliot, D. C., "Relation of Reaction Time and Temperature to Chemical Composition of Pyrolysis Oils", ACS Symposium Series 376, Pyrolysis of Oils from Biomass, Denver, Colorado, 1987, April 5-10.
13. Amundson, N. R. and Caram, H. S., "Diffusion and Reaction in a Stagnant Boundary Layer about a Carbon Particle", Ind. Eng. Chem. Fundamentals, Vol. 16, No. 2, 1977, pp. 171-181
14. Smith, I. W., "The intrinsic reactivity of carbons to oxygen", Fuel, Vol. 57, No. 7, 1978, pp. 409-414
15. Kim, D., Choi, S., Shaddix, C. R. and Geier, M., "Effect of CO₂ gasification reaction on char particle combustion in oxy-fuel conditions", Fuel, Vol. 120, 2014, pp. 130-140
16. Field, M. A., "Rate of Combustion of Size-Graded Fractions of Char from Low-Rank Coal Between 1200 and 2000 K", Combustion and Flame, Vol. 13, No. 3, 1969, pp. 237-252

17. Murphy, J. J. and Shaddix, C. R. "Combustion Kinetics of Coal Chars in Oxygen-Enriched Environments", *Combustion and Flame*, Vol. 144, No. 4, 2006, pp. 710–729
18. Muller, R., Zedtwitz, P., Wokaun, A. and Steinfeld, A., "Kinetic Investigation on Steam Gasication of Charcoal under Direct High-flux Irradiation", *Chemical Engineering Science*, Vol. 58, No. 22, 2003, pp. 5111-5119
19. Paviet, F., Bals, O., and Antonini, G., "Kinetic Study of Various Chars Steam Gasification", *International Journal of Chemical Reactor Engineering*, Berkeley Electronic Press, Vol. 5, Article No. A80, 2007
20. Backreedy, R. I., Fletcher, L. M., Jones, J. M., Ma, L., Pourkashanian, M. and Williams, "Co-firing Pulverized Coal and Biomass: A Modeling Approach", *A. Proc. Combust. Inst.*, Vol. 30, No. 2, 2005, pp. 2955–2964
21. Gera, D., Mathur, M. P. and Freeman, M. C., "Effect of Large Aspect Ratio of Biomass Particles on Carbon Burnout in a Utility Boiler", *Energy Fuels*, Vol. 16, No. 6, 2002, pp. 1523–1532
22. Kajitani, S., Suzuki, N., Ashizama, M. and Hara, S., "CO₂ Gasification Rate Analysis of Coal Char in Entrained Flow Coal Gasifier", *Fuel*, Vol. 85, No.2, 2006, pp. 163-169
23. Goetz, G. J., Nsakala, N. Y., Patel, K. L. and Lao, T. C., "Combustion and Gasification Characteristics of Chars from Four Commercially Significant Coals of Different Rank", Final Report, Project 1654-6, Electric Power Research Institute, Palo Alto, CA, 1982

24. Osafune, K., and Marsh, H., “Gasification Kinetics of Coal Chars in Carbon Dioxide”, *Fuel*, Vol. 67, No. 3, 1987, pp. 384–388
25. Kajitani, S., Hara, S. and Matsuda, H., “Gasification Rate Analysis of Coal Char with a Pressurized Drop Tube Furnace”, *Fuel*, Vol. 81, No. 2, 2002, pp. 539–546
26. Lu, H., Robert, W., Peirce, G., Ripa, B. and Baxter, L., “Comprehensive Study of Biomass Particle Combustion”, *Energy and Fuels*, No. 22, 2008, pp. 2826–2839
27. Kouchaksaraeia, M., “Fundamental Study of Single Biomass Particle Combustion”, Aalborg University, PhD Dissertation, 2013
28. Gerun L., Paraschiv M., Vijeun R., Bellettre J., Tazerout M., Gobel, B., and Henriksen, U., “Numerical Investigation of the Partial Oxidation in a Two-stage Downdraft Gasifier”, *Fuel*, Vol. 87, No.7, 2008, pp. 1383-1393
29. Graboski, M., “Kinetics of Char Gasification Reactions”, Solar Energy Research Institute, Golden, Colorado, Chapter 7, 1981, pp. 154-182
30. Jaramillo, I. C., Levinthal, J., Lighty, J. S., Gaddam, C. K., and Vander Wal, R., "Oxidation kinetics and nanostructure of model carbons based on TGA data", 8th Organized by the Western States Section of the Combustion Institute U. S. National Combustion Meeting, May 2013
31. House, J., “Principles of Chemical Kinetics”, Academic Press, Second Edition, 2007, pp. 229-233
32. Kou, K. K., “Principles of Combustion”, John Wiley and Sons, First Edition, 1986, pp. 115-117

33. Mitchell, R. E., Hurt, R. H., Baxter, L. L. and Hardesty, D. R., "Compilation of Sandia coal char combustion data and kinetic analyses", Report No. SAND92-8208, Sandia National Laboratories, 1992
34. Molintas, H. and Gupta, A.K., "Kinetics of Char Reduction of Residual Char Particles Using Air and O₂", Applied Energy Journal, Vol. 88, No. 1, January 2011, pp. 306-315
35. Gardiner, W. C., "Rates and Mechanisms of Chemical Reactions", Benjamin Benjamin-Cummins Publishing Co., Menlo Park, CA, 1972, pp. 284
36. Lide, D.R., "Handbook of Chemistry and Physics", CRC Press, Eighty-Sixth Edition, 2005, pp. 229-233
37. Jankowska, H., Swiatkowski, A., Choma, J. and Ellis, H., "Active Carbon", Prentice-Hall, Englewood Cliffs, NJ, 1991
38. S. Brunauer, P. H. Emmett and E. Teller, J. Am. Chem. Soc., 1938, 60, 309
39. Pastor-Villegas, J., Pastor-Valle, J. F., Meneses Rodriguez, J. M., and Garcia, M. G., "Study of Commercial Wood Charcoals for the Preparation of Carbon Adsorbents", Journal Analytical and Applied Pyrolysis, Vol. 76, No.1-2, June 2006, pp. 103-108
40. Gomez-Serrano, V., Valenzuela-Calahorro, C. and Pastor-Villegas, J., "Characterization of Rockrose Wood, Char and Activated Carbon", Biomass and Bioenergy Vol. 4 , No. 5, 1993, pp. 355-364
41. Ma, L., "Combustion and Gasification of Chars in Oxygen and CO₂ at Elevated Pressure", PhD Dissertation, Stanford University, 2006

42. Bhatia, S. K. and Perlmutter, D. D., "A Random Pore Model for Fluid-Solid Reactions: I. Isothermal, Kinetic Control," *AIChE J.*, 26, 1980, pp.379-386
43. Hurt, R. H., Sarofim, A. F. and Longwell, J. P., "Role of Microporous Surface Area in Uncatalyzed Carbon Gasification," *Energy and Fuels*, Vol. 5, No. 2, 1991, pp. 290-299
44. Lin, L., Gustafsson, E. and Strand, M., "High Temperature Kinetics of Fine Biomass Char Particles in Air and CO₂", 18th European Biomass Conference and Exhibition, Lyon, France, 2010
45. Su, J. L. and Perlmutter, D. D., "Effect of Pore Structure on Char Oxidation Kinetics, Vol. 31, No. 6, *AIChE Journal*, 1985, pp. 973-981
46. Singer, S. L. and Ghoniem, A., "Comprehensive Gasification Modeling of Char Particles with Multi-Modal Pore Structures", *Combustion and Flame*, Vol. 160, No. 1, 2013, pp. 120-137
47. Satterfield, C. N., *Mass Transfer in Heterogeneous Catalysis*, MIT Press, Cambridge, 1970
48. Griskey, R., "Transport Phenomena and Unit Operations", A John Wiley and Sons, Inc., 200 Turns S. R., "An Introduction to Combustion", McGraw Hill Book Co., Second Edition, 2000, pp. 656-6582, page 8
49. Thomson, W. J., "Introduction to Transport Phenomena", Prentice Hall, PTR, 2000, page 436
50. Wheeler, A., "Reaction Rates and Selectivity in Catalyst Pores," *Advances in Catalysis* 3, 1951, pp. 249-327

51. Miura, K. and Silveston, L. P., "Analysis of Gas-solid Reaction by use of a Temperature-programmed Reaction Technique", *Energy & Fuels*, Vol. 3., No.2., 1989, pp. 243-249
52. Cai, J., and Bi, L., "Precision of the Coats and Redfern Method for the Determination of the Activation Energy without Neglecting the Low-Temperature End of the Temperature Integral", *Energy and Fuels*, Vol. 22, No.4, 2008, pp. 2172-2174
53. Elliot, "Relation of Reaction Time and Temperature to Chemical Composition of Pyrolysis Oils", ACS Symposium Series 376, *Pyrolysis of Oils from Biomass*, Denver, Colorado, 1987, April 5-10.
54. Hasler P., and Nussbaumer T., "Gas Cleaning Requirements for Internal Combustion Engine Applications of Fixed Bed Biomass Gasification", *Biomass and Bioenergy*, Vol. 16, No.6, 1999, pp. 385-395.
55. Van Paasen and Kiel, J., "Tar Formation in a Fluidized Bed Gasifier: Impact of Fuel Properties and Operating Conditions", *Energy Center of the Netherlands – C – 04 – 013*, March 2004.
56. Milne et al, "Biomass Gasifier: Tars, Their Nature, Formation and Conversion", National Renewable Energy Laboratory Report, NREL/TP-570-2537, November 1998.
57. van der Hoeven, T., de Lange, A. and Steenhoven, A., "Analysis of Hydrogen-Influence on Tar Removal by Partial Oxidation", *Fuel*, Issue 85, Nos. 7 & 8, 2006, pp. 1101 – 1110.

58. Kube, M., Gfrieres, C., Waizmann, J., Michel, M., and Hein, K., “Hydrogen Rich Syngas Production from Steam Gasification of BCO in a FB Reactor: Gas Composition and Tar Formation at Various Conditions”, 2nd World Conference on Biomass for Energy, Industry and Climate Protection, Rome, Italy, May 2004.
59. Rath, J. and Staudinger, G., “Cracking Reactions of Tar from Pyrolysis of Spruce Wood”, Fuel, Vol. 80, No. 10, 2001, pp. 1379 – 1389.
60. Chen, J., “Kinetic Engineering Modeling of Co-current Moving Bed Gasification Reactors for Carbonaceous Material”, PhD Thesis, Cornell University, New York, 1987.
61. Di Blasi, C., “Dynamic Behaviour of Straified Downdraft Gasifiers”, Chemical Engineering Science, Vol. 55, No. 15, 2000, pp. 2931-2944.
62. Gerun L., Paraschiv M., Vijeun R., Bellettre J., Tazerout M., Gobel, B., and Henriksen, U., “Numerical Investigation of the Partial Oxidation in a Two-stage Downdraft Gasifier”, Fuel, Vol. 87, No.7, 2008, pp. 1383-1393.
63. Houben, M., De Lange, R. and Ouwers, C., “Low Tar Production by Pyrolysis Gas Recycling”, First World Conference on Biomass for Energy and Industry – Sevilla, Spain, pp. 1618-1621, June 2000.
64. Molintas, H. and Gupta, A., “Kinetics Study to Reduce Residual Char using Steam with Oxygen and Air Enrichment”, 49th AIAA Aerospace Sciences Meeting, Orlando, Florida, January 4 – 7, 2011, Paper AIAA 2011-0438.
65. Hong, L. and Luthy R., “Availability of Polycyclic Aromatic Hydrocarbons from Lampblack-Impacted Soils at Former Oil-Gas Plant Sites in California,

- USA”, Environmental Toxicology and Chemistry, Vol. 26, No. 3, 2007, pp. 394 – 405
66. Hong L., Ghosh U., Mahajan T., Zare R., and Luthy R., “PAH Sorption Mechanism and Partitioning Behavior in Lampblack-Impacted Soils from Former Oil-Gas Plant Sites”, Environmental Science and Technology, Vol. 37, No. 16, 2003, pp. 3625-3634
67. Leighton, D. and Acrivos, A., “The Lift on a Small Sphere Touching a Plane in the Presence of a Simple Shear Flow”, Journal of Applied Mathematics and Physics, Vol. 36, No. 1, January 1985, pp. 174-178
68. Stempniewicz, M. M., Komen, E. M. J. and de With, A., “Model of Particle Resuspension in Turbulent Flows”, Nuclear Engineering Design, Vol 238, 2008, pp. 2943-2959
69. Ahmed I. and Gupta A.K., “Syngas Yield During Pyrolysis and Steam Gasification of Paper”, Applied Energy, Vol. 86, No.9, 2009, pp. 1813 – 1821
70. Ahmed, I. and Gupta, A. K., “Evolution of Syngas from Cardboard Gasification”, Applied Energy, Volume 86, Issue 9, September 2009, pp. 1732-1740
71. La Nauze, R. D. and Jung, K., “The Kinetics of Combustion of Petroleum Coke Particles in a Fluidized-Bed Combustor”, Nineteenth Symposium (International) on Combustion, this vol., The Combustion Institute, Pittsburgh, PA, 1982, pp. 1087-1092

72. Branca, C. and Di Blasi, C., "Combustion Kinetics of Secondary Biomass Chars in the Kinetic Regime", *Energy & Fuels*, Vol.24, No.5, 2010, pp. 5741-5750
73. Mani, T., Mahinpey, N. and Murugan, P., "Reaction Kinetics and Mass Transfer Studies of Biomass Char Gasification with CO₂", *Chemical Engineering Science*, Vol. 66, No. 1, 2011, pp. 36-41
74. Keating, E. L., "Applied Combustion", CRC Press, 2007, pp. 206
75. Whitaker, S., "Forced Convection Heat Transfer Correlations for Flow In Pipes, Past Flat Plates, Single Cylinders, Single Spheres, and for Flow In Packed Beds and Tube Bundles", *American Institute of Chemical Engineers*, Vol. 18, No. 2, 1972, pp. 361-371
76. Mitchell, R. E., Kee, R. J., Glarborg, P. and Coltrin, M. E., "The Effect of Conversion in the Boundary Layer Surrounding Pulverized Coal Char Particles", *Proc. Combust. Inst.*, Vol. 23, 1990, pp. 1169–1176
77. Molintas, H. and Gupta, A., "Thermal Decomposition of Cardboard Wastes Using Steam Gasification", *International Thermal Treatment Technologies Conference*, No. 49, May 2009
78. Reich, L., and Stivala, S., "The Computer Method of Applying the Coats and Redfern Method Iteratively", *Thermochim Acta*, 36, 1980, p. 103